COMPARISON OF THE OXIDATION BEHAVIOR AND MICROSTRUCTURAL EVOLUTION OF NICOCRALY COATINGS PROCESSED VIA HVOF AND APS

by

Ali KALUSH

THESIS PRESENTED TO ÉCOLE DE TECHNOLOGIE SUPÉRIEURE
IN PARTIAL FULFILLMENT FOR THE DEGREE OF
DOCTOR OF PHILOSOPHY
Ph.D.

MONTRÉAL, 8 MAY 2025

ÉCOLE DE TECHNOLOGIE SUPÉRIEURE
UNIVERSITÉ DU QUÉBEC

BOARD OF EXAMINERS

THIS THESIS HAS BEEN EVALUATED

BY THE FOLLOWING BOARD OF EXAMINERS

Mr. Philippe Bocher, Thesis Supervisor
Department of Mechanical Engineering, École de technologie supérieure

Mr. Damien Texier, Thesis Co-supervisor
Department of Mechanical Engineering, École de technologie supérieure

Mrs. Ruxandra Botez, President of the Board of Examiners
Department of Systems Engineering at École de technologie supérieure

Mr. Vincent Demers, Member of the jury
Department of Mechanical Engineering, École de technologie supérieure

Mr. Walid Jomaa, Member of the jury
Department of Mathematic and Industrial Engineering, Polytechnique

Mr. Samir Mourad Chentouf, External Evaluator
Pratt and Whitney

THIS THESIS WAS PRENSENTED AND DEFENDED

IN THE PRESENCE OF A BOARD OF EXAMINERS AND PUBLIC

ON 14 APRIL 2025

AT ÉCOLE DE TECHNOLOGIE SUPÉRIEURE

ACKNOWLEDGMENT

I would like to express my deepest gratitude to Prof. Philippe Bocher, my director of research, for his invaluable guidance, support, and mentorship throughout this journey. His expertise and encouragement have been instrumental in the completion of this thesis. I am also profoundly grateful to Dr. Damien Texier for his assistance and insightful advice, which have greatly enriched my research experience.

I extend my sincere thanks to ETS University for providing me with the opportunity and resources to pursue this research. The academic environment and facilities have been crucial to my work.

Finally, I would like to thank my family for their unwavering support, patience, and love throughout these years. This achievement would not have been possible without their encouragement and sacrifices.

Comparaison du comportement à l'oxydation et de l'évolution microstructurale des revêtements NiCoCrAlY obtenus par HVOF et APS

Ali KALUSH

RÉSUMÉ

Cette étude approfondie examine le comportement d'oxydation à haute température des revêtements NiCoCrAlY déposés par les techniques de projection par oxycombustion à haute vitesse (HVOF) et de projection plasma atmosphérique (APS). Le comportement à l'oxydation de deux revêtements NiCoCrAlY, traités par APS et HVOF, a été examiné à haute température pendant une durée allant jusqu'à 500 heures. Les revêtements NiCoCrAlY ont été déposés sur des plaques en acier inoxydable 304. Les deux revêtements ont été déposés par PRAXAIR Surface Technologies pour cette enquête spécifique, en utilisant de la poudre NiCoCrAlY également fournie par PRAXAIR©. Les revêtements HVOF et APS, aussi bien à l'état enrobé que traités thermiquement, ont été oxydés pendant des périodes allant jusqu'à 500 heures à 1050 °C et 1150 °C en utilisant différents tests d'isotherme, interrompus et thermogravimétriques. L'étude a révélé que le taux d'oxydation des revêtements APS était indépendant de l'épaisseur, tandis que celui des revêtements HVOF augmentait avec l'épaisseur en raison d'une plus grande oxydation interlamellaire. Les spécimens APS d'une épaisseur inférieure à 60 µm ont subi une défaillance chimique intrinsèque (InCF) en raison de la consommation d'Al pour former Al_2O_3. Après 240 heures d'oxydation à haute température, le gain de masse de l'échantillon épais était neuf fois supérieur à celui du matériau coulé. Le taux d'oxydation des échantillons HVOF et APS suivait une loi de puissance avec un exposant proche de 3. Les défaillances InCF et MICF ont été observées pour les échantillons HVOF d'une épaisseur supérieure à 55 µm, tandis que les échantillons plus fins n'étaient sensibles qu'à l'InCF en raison de l'absence de décollement de l'oxyde. Par conséquent, l'intrusion d'oxyde et le décollement d'oxyde sont centraux dans la défaillance de l'Al_2O_3 et la durée de vie des produits NiCoCrAlY. Le revêtement HVOF a montré une résistance à l'oxydation médiocre par rapport au revêtement APS. L'analyse expérimentale a révélé des résultats critiques sur les transformations de phase, le gain de masse, la cinétique et les mécanismes d'oxydation, ainsi que sur la formation et le comportement de la couche TGO. L'étude souligne l'importance d'optimiser les techniques de dépôt et les processus de traitement thermique pour améliorer l'intégrité microstructurale et les performances des revêtements dans des environnements à haute température.

Mots-clés : Revêtements NiCoCrAlY, oxydation à haute température, HVOF, APS, défaillance chimique intrinsèque, défaillance chimique induite mécaniquement, effets de l'épaisseur, cinétiques d'oxydation

Comparison of the oxidation behavior and microstructural evolution of NiCoCrAlY coatings processed via HVOF and APS

Ali KALUSH

ABSTRACT

This comprehensive study investigates the high-temperature oxidation behavior of NiCoCrAlY coatings processed via High Velocity Oxy Fuel (HVOF) and Air Plasma Spray (APS) techniques. The research demonstrates how defects from these deposition processes can significantly impair the service life of MCrAlY coatings. The oxidation behavior of two types of NiCoCrAlY coatings, processed with APS and HVOF, was examined at high temperatures for up to 500h. NiCoCrAlY coatings were deposited by HVOF and APS processes on 304 stainless steel plates. Both coatings were deposited by PRAXAIR Surface Technologies for this specific investigation, using NiCoCrAlY powder (NI-191-4) also provided by PRAXAIR©. Both HVOF and APS, as coated and heat-treated coatings were oxidized for periods of up to 500h at 1050 °C and 1150 °C using different interrupted isothermal oxidation method. The study found that the oxidation rate of APS coatings was thickness-insensitive, while that of HVOF coatings increased with thickness due to greater intersplat oxidation. APS specimens thinner than 60 μm experienced intrinsic chemical failure (InCF) due to Al consumption to form Al_2O_3. After 240h of high-temperature oxidation, the mass gain of the thick sample was nine times that of the cast material. The oxidation rate of both HVOF and APS samples followed a power law with an exponent close to 3. InCF and MICF failures were observed for HVOF samples thicker than 55 μm, while thinner samples were only sensitive to InCF due to the lack of oxide spallation. Therefore, both oxide intrusion and oxide spallation are central to the Al_2O_3 failure and the service life of NiCoCrAlY products. The HVOF coating experienced poor oxidation resistance compared to the APS coating. The experimental analysis revealed critical findings on phase transformations, mass gain, oxidation kinetics, and mechanisms, as well as the formation and behavior of the TGO layer. The study underscores the importance of optimizing deposition techniques and heat treatment processes to enhance the coatings' microstructural integrity and performance in high-temperature environments.

Keywords: NiCoCrAlY coatings, high-temperature oxidation, HVOF, APS, intrinsic chemical failure, mechanically induced chemical failure, thickness effects, oxidation kinetics

TABLE OF CONTENTS

Page

LIST OF TABLES

Page

LIST OF FIGURES

Page

LIST OF SYMBOLS AND ABBREVIATION

Symbol	Description
kp	Parabolic rate constant
Δm, dW	Mass change
t	Time
h	Hours
β	βNiAl or Nickel Aluminide
γ	Gamma solid solution (γ-Ni)
γ′	Gamma Prime Solid Solution (γ'-Ni_3Al)
α-Al_2O_3	Alpha Alumina (Polymorphs)
θ-Al_2O_3	Theta Alumina (Polymorphs)
γ-Al_2O_3	Gamma Alumina (Polymorphs)
R_a, R_y	Roughness
S_a	Arithmetic average of the 3D roughness

Abbreviation	Definition
MCrAlY	Overlay BCs (M is a metal i.e. Ni or Co or in combinations)
TBC	Thermal Barrier Coating
TC	Top Coat
BC	Bond Coat
TGO	Thermally Grown Oxide
YSZ	Yttria-Stablised Zirconia
IDZ	Interdiffusion Zone
HVOF	High Velocity Oxy Fuel
APS	Air Plasma Spray
PVD	Physical Vapour Deposition
EBPVD	Electron Beam Physical Vapour Deposition
SEM	Scanning electron microscope
EDS	Energy Dispersive X-ray Spectroscopy
XRD	X-ray diffraction
TGA	Thermogravimetric Analysis
CTE	Coefficient of Thermal Expansion

INTRODUCTION

Background

The development of gas turbine engines for aircraft and power generation has seen notable progress since the mid-20th century. These engines function by burning fuel in a turbine, creating hot gas to drive the engine. The drive for improved efficiency, linked to cost reduction and decreased greenhouse gas emissions, has led to elevated turbine gas temperatures. To address challenges related to materials and oxidation at high temperatures, metallurgical designs have integrated superalloys with oxidation-resistant coatings on crucial components in the initial hot stage (such as turbine blades). This strategy guarantees strength and durability in challenging operational environments.

Coating of parts made of superalloys (as base material in turbine blade) are in most cases a necessary step of their manufacturing process as these alloys are specifically engineered to maintain their strength and integrity even under extreme conditions, especially at high temperatures. They play an indispensable role in many modern industries and applications.

The superalloys possess high-temperature load-bearing properties and they are frequently used in applications such as aero-engine turbine blades and power generation components. There have been notable advancements in the base materials of turbine blades, particularly with the shift from wrought alloys through Conventional Cast (CC) to directionally solidified (DS) and single crystal (SC) Nickel-based superalloys. The Figure 0.1 provides a comprehensive overview of the evolution in the temperature capabilities of superalloys used in turbine engine blades, charted from the 1940s through the present. It illustrates a progressive increase in the maximum temperature at which different alloys can sustainably operate under a specified stress (137 MPa) for a prolonged period (1000 h), indicative of their creep resistance. Initially, the wrought alloys (represented by circles) were prevalent, offering lower temperature capabilities. Over the decades, there has been a transition to more advanced casting methods and alloy systems. CC alloys, marked by squares, show a modest improvement over wrought alloys. A

significant advancement is observed with the introduction of DS alloys (upward triangles) and further with SC alloys (diagonals), which exhibit markedly higher temperature capabilities. This transition underlines the technological strides made in alloy processing and design, achieving superior high-temperature strength and creep resistance, essential for the demanding environments of modern turbine engines. (The notation "NIMS" next to some DS and SC categories indicates alloys developed by the National Institute for Materials Science in Japan, highlighting specific institutional contributions to material advancements).

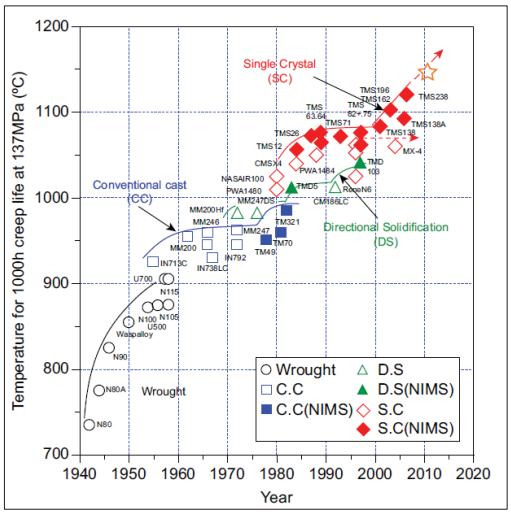

Figure 0.1 Progressive increases in temperature capabilities of superalloys for turbine engine blades taken from (David John Young, 2008)

However, despite the enhanced properties of these newer materials, in terms of strength and creep resistance, coatings are still essential. This is because surfaces in high-temperature applications need protection from harsh environments. By employing coatings, especially thermal barrier coatings system (TBCs), one can gain additional benefits. These include improved resistance to high-temperature oxidation, corrosion, and thermal insulation and crack growth hindering. The thickness of these layers is fine-tuned to efficiently tackle high-temperature oxidation and corrosion issues while keeping the rotating mass at a minimum to avoid affecting creep resistance. Therefore, using appropriate coatings thickness is important to ensure the reliability and performance of components in these demanding applications.

The TBC system is an example of a family of systems that have layers of different materials that contribute to enhanced performance and durability for each environmental or mechanical requirement. Such systems play a crucial role in many industrial applications. As a rule, engineering materials were made to have uniform properties, answering to an optimal performance requirement. However, the limitations of these materials led to the development of new ones to overcome these limitations. In certain industries, such as aerospace, automotive and biomedical industries, materials with gradually changing properties are need as they meet a gradient of requirements.

Specifically, in the aerospace industry where the superalloys are the industry-accepted material, the primary limitation is the inadequate oxidation resistance of such alloys, stemming from their chemical composition. To address this limitation, TBC system was introduced. They not only enhance the oxidation resistance performance of parts but also improves their ability to handle mechanical loads at higher temperatures. The gradient in properties, such as thermal conductivity and expansion coefficients across the TBC, critically impacts the coating's ability to withstand thermal stresses and maintain its integrity over time (Padture, 2016). Employing TBCs significantly reduces the surface temperatures of the turbine blades substrate, leading to improved component service life and higher fuel efficiency due to higher possible working temperature (Chandio, 2015). Research in such systems focuses on the detailed characterization, their interrelated properties and to predict their evolution under service conditions (D. R. Clarke, Oechsner, & Padture, 2012).

This thesis primarily focuses on coatings applied in parts used in gas turbine aircraft engines, particularly gas turbine blades. Specifically, our focus was on the NiCoCrAlY as bond coat obtained through two thermal spray coating process High Velocity Oxy-Fuel (HVOF) and Air plasma spray (APS). When these coated superalloys are exposed to high temperatures, they form unprotective oxides composed of various phases, including spinels.

Problem definition

TBC systems offer a noteworthy advantage by significantly lowering the surface temperatures of turbine components, reducing them in the range of 100−300 °C (Ren & Pan, 2014). This temperature reduction contributes to enhancing the durability and longevity of the respective parts. Yet, the application of TBC system hasn't been without its challenges. Two primary issues trouble TBC during their operational life:

1. Thermally Grown Oxide (TGO): The interface between the ceramic topcoat (TC) and bond coat (BC) sees the rapid formation and growth of the TGO layer. Originating from the oxidation of the BC at temperatures exceeding 1000 °C, the TGO layer's continuous thickening can result in TBC failure.

2. Interdiffusion Activities between TBC layers: At elevated temperatures, there's a concerning diffusion of elements between the BC and the superalloy substrate. This interchange leads to microstructural changes and phase transformations. Consequently, the interface's mechanical and adhesion properties between the topcoat/TGO, TGO/BC and BC/substrate deteriorate, paving the way for potential TBC delamination or cracking.

Both these challenges underscore the BC's important role in TBC system integrity. Hence, current research is primarily geared towards discovering innovative BC materials and refining techniques to improve adhesion between various layers of TBC system (a ceramic topcoat made from Y_2O_3-stabilized ZrO_2 (TC), Al_2O_3 oxide (TGO), MCrAlY (BC) and Ni-based superalloy).

Several studies seek to explain the underlying causes of TBC failures, ranging from deformations due to thermal expansion mismatches, chemical transformations within the TBC layers, and microstructure and interface morphology variations. Central to these studies is the BC's performance.

While mechanical damages to the topcoat can be ruled out in many instances, the importance of TBC failures can be traced back to poor BC performance. As a result, the BC has been the focal point of extensive research. Notably, the materials combination for the BC has progressed from initial NiAl coatings to those modified with platinum (Pt), like Pt-modified NiAl or PtAl coatings (Xie, Liu, Hu, Guo, & Zhu, 2024).

Presently, the successful implementation of MCrAlY coatings represents the latest advancement with each iteration contributing to enhanced oxidation resistance and more comprehensive mechanical properties in the BC.

However, diffusion aluminide BCs face a unique challenge– interface roughness (TGO thickness and interface roughness) induced by thermal stresses or manufacturing process. This introduces out-of-plane tensile stress at the TGO/BC boundary, leading to the emergence of interfacial cracks and subsequent TBC failure. Moreover, the associated processing techniques, like Electroplating and Chemical vapour deposition (CVD), come with a hefty price tag.

Problem statement

Although TBCs aim to improve superalloys performance in high temperature service environment, they face their own challenges: the defects originating from deposition processes negatively impact the service life of MCrAlY coatings on superalloys during their service life and the growth of the TGO layer and element interdiffusion at high temperatures, both of which compromise the TBC's structural integrity. Current BC materials make these problems more challenging by additional issues like surface 'rumpling' and high processing costs.

Thesis objectives

The thesis objective is to focuses on the relationship between the thickness of the coating and its service life for the NiCoCrAlY coating comparing two specific deposition methods: High-Velocity Oxy-Fuel (HVOF) and Atmospheric Plasma Spray (APS).

The objective is to:

1. Understand how the size (thickness) of the NiCoCrAlY coating affects the longevity of the blade.

2. Compare the life of blades coated using two different processes: HVOF and APS.

Significance

The outcome of this research will provide insights into which deposition method (HVOF or APS) is more suitable for maximizing the service life of TBC in high-temperature turbine blade. This study holds significant importance for several key reasons:

1. Optimization of Deposition Processes: By analyzing how HVOF and APS deposition techniques influence the microstructure and coating properties, this research seeks to optimize coating application methods. The resulting advancements will lead to more durable coatings, extending the service life of coated blade and enhancing performance under high-temperature conditions.

2. Improved Efficiency: A deeper understanding of the oxidation types occurring in the BC during service allows for enhancements in the protective properties of the coating. These improvements will lead to greater stability of the TBC layers, optimizing thermal insulation and improving the turbine's overall efficiency.

3. Enhanced Safety: Investigating the oxidation behavior of the NiCoCrAlY BC over various operational periods and documenting the onset and progression of breakaway oxides can help mitigate the risk of catastrophic turbine blades failures. By addressing the mechanisms behind TBC degradation, the study contributes to safer and more reliable operation of high-temperature application.

4. Environmental Impact: By increasing turbine engine efficiency through enhanced TBC performance, this study supports the reduction of fuel consumption and

greenhouse gas emissions. These environmental benefits align with global efforts to mitigate climate change, making this research relevant not only to industry but also to broader sustainability goals.

In summary, the findings of this research have the potential to improve the safety, efficiency, and environmental impact of turbine engines by advancing the understanding and application of TBC systems.

CHAPTER 1

LITERATURE REVIEW

1.1 Introduction

This literature review serves multiple purposes. Firstly, it provides a comprehensive background of thermal spray technologies, offering insight into their development, operation, and applications. Secondly, it explores the metallurgy of these coatings, both mechanically and physically. This involves understanding the fundamental properties that govern these coatings' performance, such as tensile strength, hardness, and roughness. It also involves the more microscopic properties, including crystallography and phase transformations, crucial to understanding the behavior and capabilities of these coatings on a deeper level. Thirdly, the characterization methods used to investigate these coatings are presented. Detailed knowledge of these techniques is essential for comprehending how these coatings are investigated and studied. Finally, as reported thermal coatings often operate in high-temperature environments, understanding the chemistry of high-temperature oxidation and corrosion is crucial to predicting and managing the coatings' long-term performance.

1.2 Thermal Barrier Coatings (TBC)

TBCs are multi-layered protective solutions widely employed in the high-temperature sections of gas turbines. Figure 1.1 illustrates the layered structure of TBCs used in turbine blades to manage high temperatures. The four layers in the current TBC systems are made of different materials with specific properties and functions. These layers are (i) the substrate, (ii) the BC, (iii) the TGO, and (iv) the ceramic topcoat. The side exposed to hot gas is the ceramic topcoat, typically made from zirconium oxide (ZrO_2) stabilized with Yttrium, ranging from 100 to 400 microns thick. It serves as the primary barrier against heat and corrosion. Beneath this is the TGO, usually alumina (Al_2O_3), about 1-10 microns thick, which forms naturally from the oxidation of the BC during service. The BC, around 100 microns thick, usually a MCrAlY

alloy or Pt-Al alloy, helps adhere the topcoat to the underlying substrate and imparts oxidation resistance. Finally, the superalloy substrate supports these coatings and provides the mechanical strength required for operation. The heat gradient across the TBC from the hot gas side to the cooled substrate side is also plotted in the figure by a blue thick line revealing the TBC's role in thermal management.

The primary objective of TBCs is to enhance engine efficiency by allowing gas turbine engine components, such as blades, vans, and seals to function optimally at more elevated gas temperatures. By insulating these parts, coated blades can sustain higher operating temperatures without compromising their integrity or performance. This translates to higher efficiency and diminished fuel consumption.

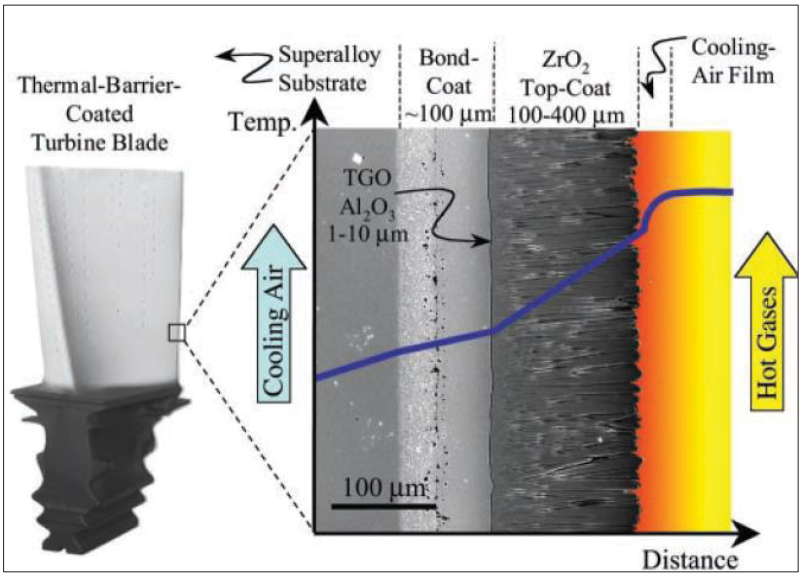

Figure 1.1 Schematic of TBC layers system,
taken from (Padture, Gell, & Jordan, 2002)

The effectiveness of these engines is closely tied to the temperature capability of the turbine blades. Between 1965 and 1985, there was an advancement in temperature capability of about 80 °C, achieved through the development of successive generations of nickel-based single crystals that showed increasing resistance to creep and fatigue. However, since the introduction of TBC on turbine blades in the early 1980s, the operational temperature capability of the

systems has been elevated by up to 200 °C (to about 1200 °C) as shown in Figure 1.2. The graph compares the temperature capabilities of wrought alloys, conventionally cast alloys, directionally solidified alloys, and single crystal alloys over time, alongside the temperature limits set by metal substrates and Yttria-stabilized zirconia (YSZ) TBCs, highlighting the thermal benefits provided by these innovations. The immediate advantages of temperature reduction resulting from TBC are evident in decreased oxidation. It has been shown that n components that rotate, damage caused by creep phenomena can be significantly diminished (Uwe Schulz et al., 2003).

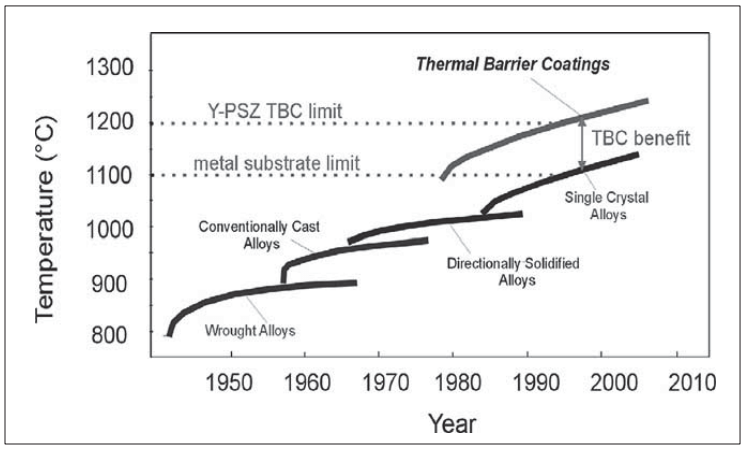

Figure 1.2 The advancements in turbine component materials from 1950 to 2010 taken from (Uwe Schulz et al., 2003)

Apart from the direct advantages TBCs have the tendency to decrease local temperature fluctuations, resulting in reduced distortion and an enhanced resistance to fatigue caused by temperature variations. Furthermore, TBCs impact how components react to sudden changes in temperature. These abrupt shifts arise from rapid alterations in energy input to high-temperature parts, like turbine blades, during aircraft takeoff, ascent, and landing. These shifts often have adverse impacts on the fatigue caused by temperature variations in metallic components. Because ceramic coatings have lower thermal conductivity, their response to sudden temperature spikes is considerably slower than that of metals. Consequently, TBCs to some extent mitigate these sudden shifts, leading to an improvement in resistance to fatigue caused by temperature variations.

In conclusion, the efficacy of protective coatings is underpinned by two essential components: the topcoat and the BC. The topcoat acts as the primary barrier against environmental exposures, while the BC secures this protective layer to the substrate. Facing extreme temperatures and harsh operational conditions, these materials are specifically engineered to be inherently durable, ensuring they maintain their protective qualities throughout their service life.

1.2.1 The ceramic topcoat

In gas turbines, temperatures can reach up to 1500 °C. Generally, a ceramic layer is employed as the topcoat coating, known for its stability up to 1200 °C. Beyond this temperature, the coating begins to degrade, leading to a reduction in the turbine's service life at elevated temperatures.

The ceramic topcoat, typically made of zirconium oxide stabilized with Yttrium (YSZ), plays a key role in protecting the superalloy substrate in demanding applications. Typically, topcoats of YSZ exhibit low stiffness columnar microstructures with fine microcracks and pores as shown in Figure 1.3. Its primary function is to act as an insulator, preventing the degradation of the superalloy during operation. Beyond this core protective role, the ceramic layer (with young's modulus up to 250 GPa) offers a shield against various external threats as result from the hot fuel stream environment (D. D. Hass, 2000). Leveraging the high heat resistance of ZrO_2 to further reduce heat transfer, the ceramic topcoat ensures that the superalloy substrate maintains a more stable and lower temperature. This thermal resistance is indispensable in sectors where maintaining specific temperature thresholds is vital. There are several key aspects that highlight its importance and intricacies:

- **Material selection**: YSZ, a ceramic layer imbued with 7-8 wt. % yttria Y_2O_3-stabilized ZrO_2, is the material of choice because of its optimal thermal properties, including its low conductivity and high melting point. The yttria ensures that the zirconia remains in the insulating cubic phase (Zhao, Yu, Bennett, & Wadley, 2006). Moreover, high

fracture toughness and better thermal matching (Padture, 2016; Thakare, Pandey, Mahapatra, & Mulik, 2021) have contributed to the increasing utilization of YSZ in TBCs.

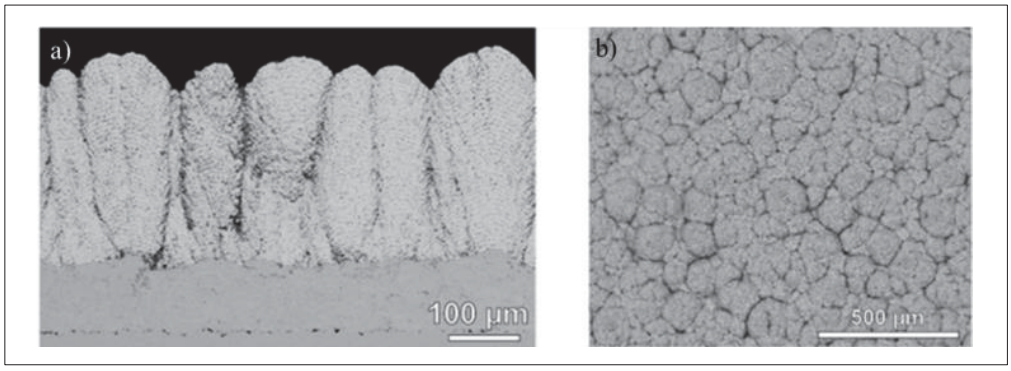

Figure 1.3 a) Cross-section and b) topographical backscattered electron (BSE) images of the coating of YSZ ceramic topcoat taken from (Lokachari et al., 2024) showing the columnar arrangement of YSZ particles during partial melting and re-solidification.

- **Thermal gradient**: In operation, the ceramic topcoat encounters high operating temperatures, while the layers beneath -the metallic BC and substrate- should remain relatively in lower temperature. Due to the presence of defects such as cracks and pores in the YSZ topcoat, the thermal conductivity of the YSZ coating is typically lower than that of other types of coatings. Actually, YSZ exhibits one of the lowest thermal conductivity among other ceramics at elevated temperatures. Therefore, its thermal conductivity is around 2.2-2.9 W/(m.°K) at 1000 °C (Klemens & Gell, 1998; Zhao et al., 2006) and the coated blade surface experienced a temperature decrease of up to 200 °C through the utilization of the YSZ topcoat with the advanced cooling system (Nagabandi, Mills, Zhang, Toal, & Keane, 2017).

- **The deposition method**: The deposition method for the ceramic topcoat significantly affects thermal conductivity of topcoat layer of YSZ. It has been shown that the ceramic topcoat Electron Beam Physical Vapor Deposition (EB-PVD) of YSZ with a columnar coating morphology exhibits higher thermal conductivity than APS YSZ with a splat morphology (D. Hass, Slifka, & Wadley, 2001).

- **Thermal expansion coefficient compatibility**: The thermal expansion coefficient of the ceramic top coat should closely match that of the TBC system: TGO, the BC and substrate. This compatibility minimizes potential stresses and strains from thermal mismatches during operational cycles. To prevent TBC system failure caused by a mismatch in the thermal expansion coefficients of various TBC layers, several strategies enhance durability. Firstly, reducing thermal conductivity in the top coat layer lowers the amount of heat transferred to the subsequent layers. This insulation effect reduces the thermal gradients that occur across the TBC system. With smaller thermal gradients, each layer undergoes less differential expansion, resulting in reduced thermal stresses between the layers. Secondly, the topcoat minimizes oxygen permeation therefore reducing the formation of the TGO layer, which, while protective, grows thicker over time and introduces stress and it can lead to cracking, delamination, or spallation. These measures improve the high-temperature oxidation and thermal shock resistance within the coating system (Shi et al., 2020).

- **Durability & service life challenges**: Multiple factors influence the YSZ's service life. One of the most importance factors is the formation of a TGO layer. The TGO, primarily composed of alumina, at the interface can be a stress point, potentially leading to delamination. The YSZ topcoat, with a porous microstructure and its fine microcracks, offers a balance of low stiffness and adequate strength, making it particularly suitable for rotating components like turbine blades. This combination not only enhances the performance and durability of gas turbine parts but also provides a cost-effective solution for extending their service life. (Jang & Matsubara, 2005).

- **Optimized porosity**: The overall porosity characteristic of the ceramic coating is significantly influenced by the column size and density, intercolumnar gaps, and inter pass porosity bands. Porosity in the ceramic topcoat is a double-edged sword. While it enhances thermal insulation, finding the right balance is crucial to maintaining both structural integrity and effective protection. Insufficient porosity increases thermal

conductivity and creates a stiffer layer causing delamination and also impairs TGO formation due to limited oxygen permeation. Conversely, excessive porosity weakens the topcoat structure and also allows too much oxygen to permeate, potentially accelerating TGO growth causing the decrease in the coating's durability. For instance, researchers such as R. Vaßen et al. (Vaßen, Kerkhoff, & Stöver, 2001) have identified that the porosity range for ceramic topcoat (YSZ) falls within 10% to 20% showing that this range of pore volume is advantageous because it facilitates strain tolerance while minimizing thermal conductivity. Therefore, a higher thermal conductivity is associated with lower pore percentages, resulting in reduced strain tolerance. In contrast, an elevation in pore volume fraction raises the likelihood of oxygen penetration and augments the growth rate within the TGO layer (D. Hass et al., 2001). Recently, Yang et al. (Yang et al., 2024) investigated stress and temperature distribution at the TGO/TC interface with varying porosities and TGO layer thicknesses employing finite element numerical simulation. They verified the layer thickness and porosity level to document heat insulation properties and surface residual stress in TBCs produced through APS. Their findings revealed that optimal thermal insulation performance and maximum von Mises stress in the coating layers occurred when the ceramic coating had a porosity of approximately 24-35% and the TGO layer thickness was 2.1 micrometers. This discovery presents a promising solution to address ceramic peeling issues, potentially extending the service life of TBCs.

- **Application techniques**: Topcoats are commonly applied using air plasma spray (APS) for large, stationary components and electron beam physical vapor deposition (EB-PVD) for rotating parts like high-pressure turbine blades. While EB-PVD offers durability with a columnar microstructure, it has a slow deposition rate and high costs, exceeding 15 million pounds per unit due to expensive vacuum chambers and installation (Chow, 2016; D. Clarke & Levi, 2003; Feuerstein, Hitchman, Taylor, & Lemen, 2009; Jude, Jappes, & Adamkhan, 2022; Padture et al., 2002). Thus, the

decision should consider both the operational requirements and budgetary limitations to optimize performance and cost effectiveness.

1.2.2 The BC layer

The BC layer is an indispensable component of TBC systems, playing an important role in their durability and reliability. Typically composed of either an aluminide (AlNi) diffusion coating or an MCrAlY overlay coating (where M = Co, Ni, or a combination of both), the BC offers several benefits (Uwe Schulz, Saruhan, Fritscher, & Leyens, 2004):

1. **Oxidation protection**: The BC safeguards the substrate material by forming a dense and continues oxide scale, specifically alumina (α-Al_2O_3). This protective oxide layer not only prevents the substrate from oxidizing but also acts as a diffusion barrier. It restricts atomic movement between the substrate and the coating, further inhibiting diffusion. The BC also preserves the protective Aluminum from both the substrate and itself, serving as an Aluminum reservoir. This enhancement in oxidation resistance is important in prolonging the life of the coated blade. A central part of its protective strength comes from the Al and Cr in the coating. These elements help form a TGO layer, which acts as a barrier. This layer limits the movement of oxygen and slows down the oxidation process. Especially important is the formation of Al_2O_3, mainly because of Al's reactivity. This reactivity, paired with its stability over Cr_2O_3, results in a dense Al_2O_3 layer. This protective layer effectively inhibits oxidation, enhancing the overall oxidation resistance of the coated system (H. Evans & M. Taylor, 2006; W. G. Sloof & T. J. Nijdam, 2009).

2. **Adhesion**: Acting as a bridge, the BC ensures a firm adhesion between the ceramic topcoat and the substrate through multiple mechanisms, including chemical bonding, mechanical interlocking, thermal compatibility, and diffusion. The chemical bonding involves the formation of a stable TGO layer. Additionally, the BC's rough surface enables mechanical interlocking with the ceramic layer, resisting shear stresses, while diffusion bonding strengthens and stabilizes the interface. This tight bond prevents

potential delamination or peeling of both TGO oxides and the ceramic topcoat (Padture et al., 2002).

3. **Thermal insulation**: The BC, while not a primary insulator and primarily designed for oxidation protection and adhesion, also contributes indirectly to thermal insulation. The BC enhances the insulation performance by providing a transition layer that supports the stability and integrity of the ceramic topcoat (D. Clarke & Levi, 2003). Additionally, the BC's TGO layer, acts as a secondary barrier to heat transfer because of its relatively low thermal conductivity and stable structure, which limits heat flux to the underlying substrate Schulz (Uwe Schulz et al., 2004).

4. **Stress relief**: Differences in the coefficients of thermal expansion between the substrate and the ceramic topcoat can introduce residual stresses when exposed to high temperature working conditions. The BC acts as an essential stress-relief layer, primarily due to its intermediate coefficient of thermal expansion (CTE), which lies between that of the YSZ topcoat and the metallic substrate. This gradient in CTE helps accommodate thermal mismatch and reduces residual stresses during thermal cycling (D. Clarke & Levi, 2003). Without this relief, direct bonding of the YSZ topcoat to the substrate would lead to high stress at the interface due to significant CTE disparities, which could result in spallation or cracking (Feuerstein et al., 2009). Furthermore, the BC can undergo limited plastic deformation, allowing it to absorb and dissipate thermal stresses and reduce strain on the ceramic topcoat, thus contributing to the overall structural integrity and durability of the TBC system (Uwe Schulz et al., 2004).

By serving these multiple functions, the BC layer significantly extends the surface life, safeguarding it from high-temperature environments and maintaining the substrate's pristine condition.

1.2.3 Thermally Grown Oxides (TGO)

The TGO layer stands as an essential part of TBC systems, especially in high-temperature applications such as gas turbines and jet engines. One of its main functions is to enhance the adhesion between the ceramic topcoat and the metallic BC. This firm bond is essential in preventing the ceramic layer from delaminating, ensuring the longevity of the TBC system. The TGO layer serves as a stable barrier against oxidation, especially at elevated temperatures. This protective barrier protects the underlying metallic BC, thereby prolonging the operational life of the entire TBC system. To optimally serve its purpose, the TGO layer must have several important criteria: it should maintain a consistent thickness, ensure thermodynamic stability to prevent the formation of non-protective oxides, and display a restrained growth rate on the BC surface. These collective attributes equip it to withstand the intense stress and temperatures on turbine blades.

TGO layer oxide system

The TGO layer is regarded as a complex oxide system. These oxides can be broadly classified into two categories: α-Al_2O_3, known for its superior protective properties, and mixed oxides such as Cr_2O_3, NiO, and spinel (Ni, Co) $(Cr, Al)_2O_4$ (C. Giggins & F. S. Pettit, 1971; Padture et al., 2002). A TGO layer composed of pure α-Al_2O_3 is preferred due to its low effective diffusion rates for oxygen and metal ions, along with high chemical and thermal stability (W. Chen, Wu, Marple, Nagy, & Patnaik, 2008). The growth of the TGO layer, identified as a major contributor to TBC failure, is proportionate to time and temperature (Rabiei & Evans, 2000).

TGO scale adherence is influenced by multiple aspects, including kinetics of oxide growth, defect formation, the interfacial segregation of elements, and residual stresses. The composition and structure of the BC play an important role in these influencing points. Analyzing aerospace alloys, Barrett et al. (Barrett, 1992) revealed a connection between alloy composition and spallation behavior during high-temperature oxidation. Similarly, Brandl et al. (Brandl, Grabke, Toma, & Krüger, 1996) investigated the oxidation behavior of TBCs with

varying aluminum content in the BC, observing homogeneous TGO oxide scaling with higher levels of aluminum even after prolonged operation.

Reactive elements such as Y, when present in low concentrations (less than 0.3 wt.%), prove beneficial for improving scale adhesion of MCrAlY coating. However, at high concentrations, these elements can be detrimental due to their tendency to form intermetallic phases, promoting the growth of unprotective oxides (Smialek, 2000).

The formation and stability of the TGO are significantly influenced by the interdiffusion of elements within the TBC layers. The interdiffusion phenomenon in TBC system leads to a reduction in the concentration of aluminum within the BC. Consequently, this diminishes the coating's capability to sustain exclusive Al_2O_3-scale growth, leading to localized detachment or cracking. The interdiffusion also introduces conditions that can potentially encourage the spallation of oxide scales (Basuki, Crosky, & Gleeson, 1997).

The evolution of the TGO layer in TBCs is influenced by some factors, including aluminum contents, the temperature, hold time, and the diffusivity of oxygen through the TBC thickness. In a study by Che et al. (Che, Wu, Qi, Huang, & Yang, 2009), the imbalanced growth of the TGO layer and the resulting stress distribution in TBCs were examined. The findings revealed that irregular TGO interfaces and thicknesses could lead to a substantial 200% increase in interface stress. Dong et al. (Dong, Yang, Li, Luo, & Li, 2014) identified a critical TGO thickness threshold, beyond which TBCs are prone to spalling. This critical thickness depends on the stress levels within the oxide, which can vary based on factors like oxidation rate, temperature, and the material's thermal expansion mismatch.

Moreover, the insulating capacity of the TGO layer is noteworthy. Its lower thermal conductivity compared to the metallic BC ensures minimal heat transfer to the underlying substrate, aiding in temperature regulation of the coated surface. This inherent property not only keeps the component relatively cooler but also stalls the progression of cracks in the

ceramic topcoat. By halting these cracks before they reach the metallic BC, the TGO layer plays an important role in mitigating substantial damages to the TBC system.

TGO thickness

Examining the effect of TGO thickness on thermal shock resistance and cyclic loading behavior, Kaveh Torkashvand et al. (Torkashvand, Poursaeidi, & Mohammadi, 2018) discovered a positive influence with a TGO thickness of about 3μm in terms of service life. Shen et al. (Shen et al., 2018) advanced a coupled mechanical-oxidation model, unveiling the link between changing TGO thickness, stress alterations, and the chemical reaction governing TGO layer formation. The rapid growth of mixed oxides within the TGO layer, coupled with significant volume expansion, can induce cracks in the ceramic topcoat, hastening premature spallation failure of TBCs (W. Chen, Irissou, Wu, Legoux, & Marple, 2011).

Oxide coverage

Research has demonstrated an inverse relationship between the thermal cyclic service life of TBCs and the coverage ratio of the spinel and Cr_2O_3 oxides in the TGO layer. The coverage ratio was defined as the ratio of the covered areas by the mixed oxides on the BC surface to the whole layer surface using backscattered electron microscopy imaging. A higher coverage ratio is associated with early spalling of the ceramic topcoat (Y. Li, Li, Zhang, Yang, & Li, 2010).

TGO growth mechanisms and crack propagation

Chen et al. investigated the impact of TGO growth on the cracking behavior of atmospheric plasma-sprayed (APS) TBCs, revealing a three-stage phenomenon in TGO thickening and linearly proportional crack propagation with increasing TGO thickness (W. Chen, Wu, Marple, & Patnaik, 2006). At the initial stage which happens during the first 10h, the formation of oxides mainly depended on the diffusion rate. Thus Cr and Co are oxidized before Al. At the second stage which is a steady oxidation stage between 10 h to 120 h, the thermodynamics takes a dominant role and the main oxides are Al_2O_3. At the third stage which occurs after 120 h of exposure, Cr and Co are oxidized with the consumption of Al at the TGO/BC interface.

Both the replacement reaction of Cr_2O_3 and the phase conversion of Al_2O_3 lead the TGO thickness to decline at this stage. Later, Chen et al. demonstrated that exposure to oxidation in a low-oxygen environment can reduce crack formation during the initial stage of Al_2O_3 oxide layer formation and extending the steady-state phase, thereby enhancing durability (W. Chen, Wu, Marple, Lima, & Patnaik, 2008).

Zhi-Yuan et al. (Wei, Cai, Meng, Tahir, & Zhang, 2020) introduced a model coupling TGO growth and crack propagation mechanisms to understand the effect of TGO growth on crack propagation. The study showed that the stress concentration always occurs near the pore and the lamellar interface crack also changes the stress distribution within the topcoat/BC interface. It has been shown that the lamellar crack steadily propagates at the early stage and the crack length sharply increases before the occurrence of coating spallation which was in line with the experimental result.

1.2.4 Superalloy substrate

At the heart of the TBC system lies the substrate made from nickel- or cobalt-based structural superalloys. These superalloys are not only passive backers; they actively contribute to the system's thermal management. Made specially to withstand extreme conditions, they are internally air-cooled, either from within their core or through designed hollow channels. Their design consideration helps establish a temperature gradient across the component's thickness, ensuring that even under intense external heat, the inner regions remain relatively cooler.

Using advanced manufacturing techniques like investment casting, these components can be rendered in single-crystal forms for unparalleled grain uniformity, or polycrystalline structures that harness the collective strength of multiple grain orientations. The superalloy's intricate composition, often containing a combination of 5 to 12 additional elements, is purposefully chosen (Donachie & Donachie, 2002). Each added element has a specific effect: some enhance high-temperature strength, others improve ductility, and still others amplify attributes like oxidation resistance, hot-corrosion resilience, creep, and castability. For instance, nickel-based

superalloys exhibit outstanding high-temperature creep resistance attributed to microstructure characterized by a significant proportion (around 70%) of cuboidal precipitates of γ'-Ni_3(Al, Ta, Ti) phase within the γ-Ni matrix (Reed, 2008).

However, as with many high-performance materials, superalloys in TBC systems are not without their challenges. At the soaring temperatures typical of gas turbine engine operations, these superalloys can increase elemental diffusion. Elements, especially those in high relative concentrations within the superalloy, might migrate towards the BC. This migration doesn't stop at the BC; occasionally, these diffusing elements move further, marking their presence in the TGO and even the ceramic topcoat. Such interdiffusion, while microscopic, can have macroscopic effects. It can severely impact the TBC's adhesion, potentially leading to spallation failure. The interdiffusion of substrate superalloy results in the formation of topologically close-packed (TCP) phases, like σ, μ, and R on its interface. The plate-like or needle-like morphology of these TCP-phase precipitates is recognized as detrimental to the strength and toughness of the coating/alloy system. Even a small volume percentage of TCP phase formation is considered detrimental, with this process being promoted by deformation and the presence of refractory elements like Cr, Ta, and Re (Ritzert, Arenas, Keller, & Vasudevan, 1998).

Thus, one cannot merely view these superalloys or the TBC as static entities; they evolve constantly and change compositions. In the crucible of service conditions, thermal barrier-coated superalloys change, both in composition and properties, demanding that they be approached as dynamic engineering systems (Padture et al., 2002; Sato, Chiu, & Reed, 2011; M. Taylor, Evans, Gray, & Nicholls, 2011; Terry, 1999).

1.3 Thermal spray science & technologies

Thermal spray is a coating technique in which fine particles of a material are applied to the surface of a prepared substrate in a molten or semi-molten state (Chagnon & Fauchais, 1984). In this process, a torch transforms these particles into a hot gas stream, utilizing electric power

for plasma generation and chemical energy for combustion (Cizek & Matejicek, 2018). The coating material, heated through combustion or plasma generation, transforms into a molten state, and is driven by the high-velocity, high-temperature gas stream onto the substrate. The material to be coated can exist in various forms, such as wire, powders, rods, suspension, or molten state (Sampath et al., 2004). As these particles adhere to the substrate's surface, they form discrete layers known as "splats." Subsequent particles arriving at the surface amalgamate to create multiple splat layers, ultimately completing the coating structure (Fanicchia et al., 2017). Figure 1.4 illustrates the thermal spray coating process. When selecting a coating material, it is crucial to ensure compatibility in thermal expansion coefficients between the substrate and the coating material (Kang et al., 2018).

These coating processes are indispensable in various industries due to their ability to improve or restore a material's surface properties such as high temperature oxidation, resistance to wear, erosion, corrosion, and thermal cycling (Bose, 2007).

These processes can be classified based on their power consumption and deposition rate. Figure 1.5 offers a comprehensive overview of the diverse thermal spray techniques, with the exception of cold spray.

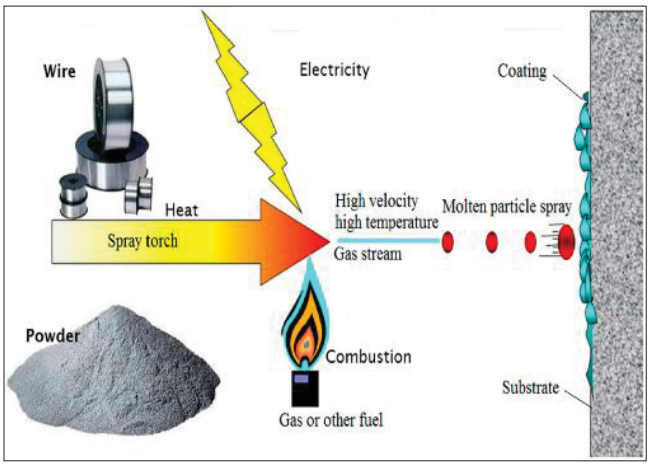

Figure 1.4 Thermal spray process taken from (Bose, 2007)

In the following pages, several important types of thermal coating will be briefly reviewed (Abhijith, Kumar, & Kalyansundaram, 2022; R. Kumar, Kumar, & Kumar, 2018; S. Kumar, Prasad C, & Hanumanthappa, 2024).

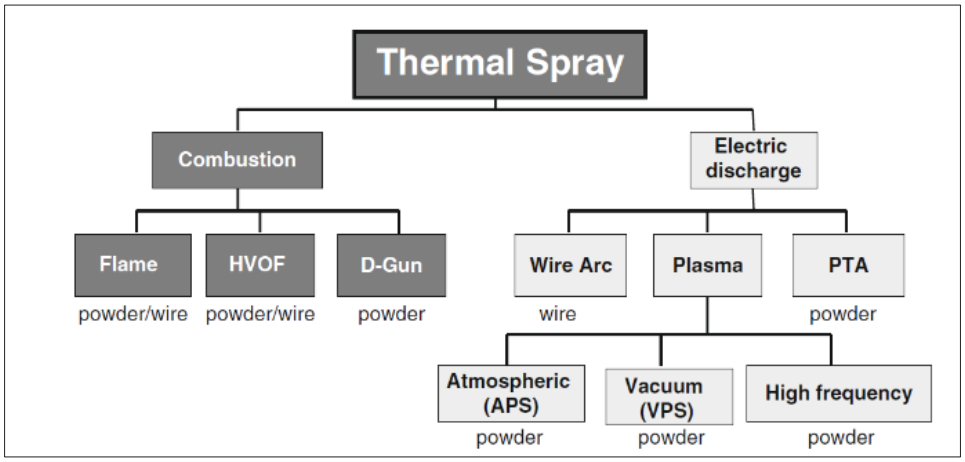

Figure 1.5 Thermal spray technology classification (Maher I. Boulos, Fauchais, & Pfender, 2023)

1.3.1 High-Velocity Oxy Fuel process (HVOF)

High-Velocity Oxy-Fuel (HVOF) is a thermal spray coating process that is commonly used for applying wear, corrosion and oxidation-resistant coatings, amongst other applications. The process operates by creating a combustion reaction between a fuel and oxygen to produce a high-temperature, high-pressure flame. The coating material, typically in powder form, is then injected into this flame, where it melts and is propelled towards the substrate at high velocity. This results in a dense, strong coating with high adhesion to the substrate (Oksa, Turunen, Suhonen, Varis, & Hannula, 2011). The HVOF coating process can apply coatings up to 1.5 mm thick, playing a crucial role in reducing residual stress, particularly when considering the control of the cooling rate during depositing process.

HVOF process mechanics

In the HVOF process, a fuel (hydrogen, kerosene, propane, or propylene) and oxygen are mixed and combusted in a high-pressure combustion chamber. This produces a hot gas stream

that is ejected from the chamber through a converging-diverging nozzle, reaching velocities that can exceed Mach 1. The coating material, generally in the form of a powder, is injected into this hot gas stream where it rapidly heats up and melts. The molten particles are then propelled towards the substrate at high velocities. Upon impact, the particles flatten and rapidly solidify to form the coating as shown in Figure 1.6. The high particle velocities and rapid cooling rates result in coatings that are dense (0.5-2% porosity) with strong adhesion to the substrate(Vats, Kumar, Patnaik, & Meena, 2021).

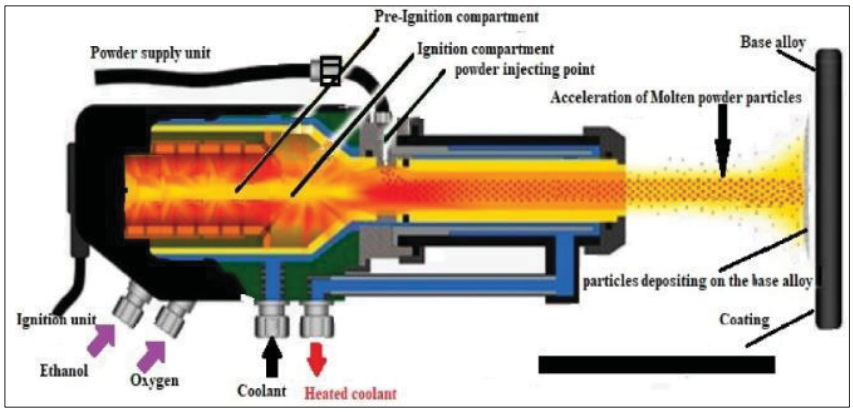

Figure 1.6 Diagram illustrating HVOF spraying system taken from (Alnaser, Yunus, Alfattani, & Alamro, 2021)

HVOF material considerations

In the HVOF process, ceramic material feedstock is predominantly utilized in wire and cord configurations, diverging from the conventional practice of using metal powder feedstock in its powdered state. This choice stems from the innate rigidity of ceramics. Throughout the process, the liquefied powder is atomized into fine particles and propelled forward by supplementary gas through the spray gun. while in case of the wires, rods, or cords form are consistently advanced at an appropriate pace, facilitating the spray jet's efficient melting of their ends(C.-J. Li & Yang, 2013). The HVOF process can be used to spray a wide range of materials, including metals, alloys, ceramics, and ceramics. The choice of material depends on the desired properties of the coating. For example, MCrAlY alloys (where M = Ni, Co, or both) are used to produce coatings that can resist high-temperature oxidation and hot corrosion, while

the WC-Co (tungsten carbide-cobalt) CERMETS are often sprayed using HVOF to produce hard, wear-resistant coatings. Szala et al. (Szala, Walczak, & Świetlicki, 2021) utilized three coatings—NiCoCrAlY, CoNiCrAlY, and NiCrAlMoNbTa—applied via HVOF onto an Inconel 617 substrate to examine their effects on tribological and cavitation erosion performance as shown in Figure 1.7. Their findings indicate that the NiCrMoNbTa coating exhibits superior resistance to wear, and cavitation erosion compared to the other coatings (NiCoCrAlY, CoNiCrAlY). Additionally, their results underscore the effectiveness of the HVOF method in providing a wide array of coating options to fulfill specific demands in demanding operational environments.

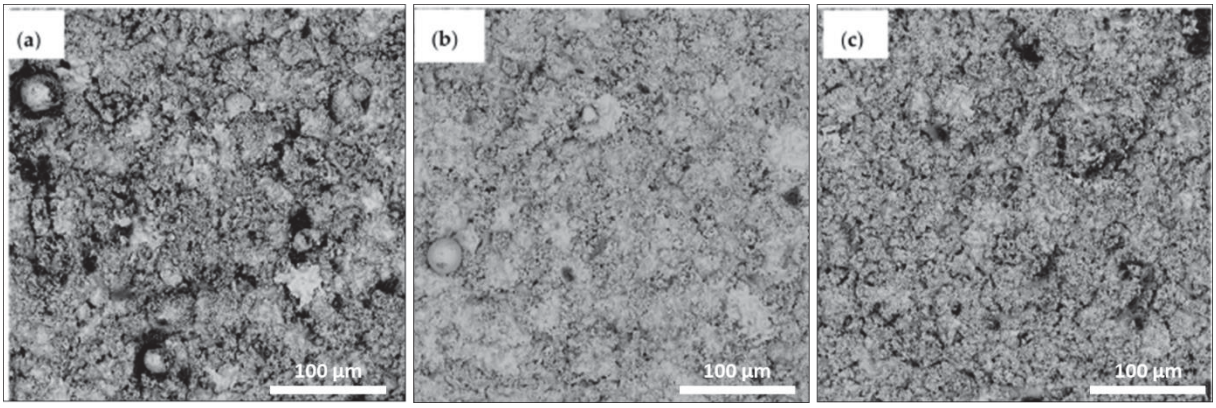

Figure 1.7 Surface morphology of as-sprayed HVOF-coatings: (a) CoNiCrAlY; (b) NiCoCrAlY and (c) NiCrMoNbTa taken from (Szala et al., 2021)

HVOF process parameters

The HVOF method, which functions under atmospheric conditions and involves roughly one tenth of the investment costs compared to other thermal spray methods such as VPS, emerges as the most suitable and optimal choice for applying MCrAlY coatings (Vats et al., 2021). To safeguard the microstructure of the powder within the coating, it's possible to spray the particles in a plastic state instead of melting them, thanks to the high velocities of the powder particles, which can reach up to 800 m/s. Therefore, the potential for oxidation during particle flight and flattening is minimized, as oxidation can only occur through relatively sluggish diffusion processes (Voggenreiter, Huber, Beyer, & Spies, 1995). Despite being in a plastic state, the high kinetic energy of the particles enables deformation-driven flattening, resulting

in thick and entirely pore-free coatings (with a coating porosity of less than 1%) (Sidhu, Prakash, & Agrawal, 2005). Figure 1.8 shows the ideal model of the HVOF-NiCoCrAlY coating structure after spraying process.

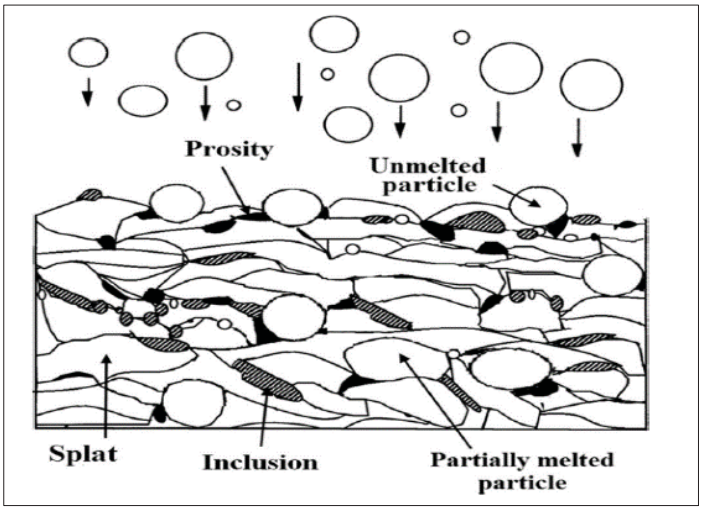

Figure 1.8 Schematic representation of the HVOF-NiCoCrAlY coating
taken from (Doolabi, Ghasemi, Sadrnezhaad, Habibolahzadeh, & Jafarzadeh, 2018)

Erich Lugscheider et.al., (Lugscheider, Herbst, & Zhao, 1998) conducted a study to examine how various process parameters affect the microstructure and oxygen content of MCrAlY coatings. The investigation revealed that several factors, including spray distance, the ratio of fuel to oxygen, powder feed rate, and substrate temperature, played a crucial role in influential both the microstructure and oxygen levels in the coatings. Moreover, Doolabi et al., (Salehi Doolabi, Ghasemi, Sadrnezhaad, Habibolahzadeh, & Jafarzadeh, 2018) explored how different oxygen/fuel ratios affect NiCoCrAlY coatings made by conventional HVOF spraying. They assessed oxidation behavior, bond strength, hardness, and microstructure, finding that higher ratios decrease inclusion but may increase porosity and unmelted particles. Mechanical properties like bond strength and hardness initially rise, then decline with the ratio. Optimal ratio, determined through AHP-VIKOR methods, is 2.27 coatings due to its improved oxidation resistance.

Applications of HVOF coatings

Due to its ability to produce dense, high-quality coatings, the HVOF process is used in a wide range of applications. These include wear and corrosion protection in the oil and gas industry, high-temperature oxidation resistance in the aerospace and power generation industries, and biocompatible coatings in the medical field.

Advantages and disadvantages of HVOF Process

The HVOF process offers several advantages over other thermal spray processes. These include the ability to produce dense, hard coatings with high bond strength and low porosity. In addition, the high particle velocities result in coatings that have a smoother surface finish compared to those produced by other thermal spray processes. However, these projected coatings are much more prone to internal defects such as unmelted particles, pores, internal oxides and/or nitrides, inter-splats. Oxygen ingress along these open channels causes oxide intrusions within the coating. Oxidation-induced expansion of the coating creates tensile stress in the outer layer, which can result in the cracking and shedding of the scale.

Moreover, the HVOF process also has some inherent disadvantages. The high-temperature, high-velocity nature of the process can cause challenges with controlling the coating process parameters, and the equipment can be more expensive compared to other thermal spray processes (Mondal, Nuñez III, Downey, & Van Rooyen, 2021; Pawlowski, 2008).

1.4 Atmospheric plasma spray process (APS)

Intermetallic coatings are on the rise as a means of safeguarding engineering alloys, and as a result, numerous deposition techniques have been devised (Cinca, Lima, & Guilemany, 2013). Among these methods, air plasma spraying (APS) has gained popularity due to its versatility across industrial applications and its compatibility with commercial usage (Handbook, 2004; Pawlowski, 2008). These processes use an electric arc to generate a plasma, which in turn melts the coating material that is then propelled onto the substrate. This process is typically used to produce coatings that can resist wear, corrosion, and high oxidation temperatures.

1.4.1 APS process mechanics

In the APS process, a high-frequency electric arc is established between a cathode (usually made of tungsten) and an anode, located at the exit of the plasma torch as shown in Figure 1.9. A flow of plasma-forming gas, such as argon, nitrogen, or hydrogen, is introduced around the cathode and through the arc, where it becomes ionized to form a plasma. This plasma forms a high-temperature jet as it exits the torch nozzle. The coating material, typically in powder form, is injected into this plasma jet where it is rapidly heated and melted. The molten particles are then propelled towards the substrate where they solidify to form the coating.

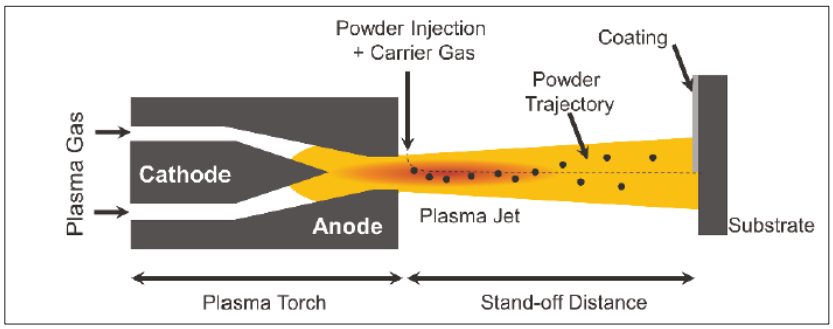

Figure 1.9 Illustration of the APS process taken from (Pierre Fauchais, Heberlein, & Boulos, 2013)

1.4.2 APS material considerations

The APS process is extremely versatile in terms of the types of materials that can be sprayed. These include metals, alloys, ceramics, and CERMETS. For example, Yttria-Stabilized Zirconia (YSZ) is often used to produce TBCs that can resist high-temperature oxidation and thermal shock. Other materials, such as Al_2O_3 and TiO_2, are used to produce wear- and corrosion-resistant coatings.

1.4.3 APS prosses parameters

The APS process can be influenced by several factors, including the plasma gas composition, electrode setup, spray gun design, spraying distance, surrounding environment, torch speed,

substrate temperature, and the type and size of the powder used (Bounazef, Guessasma, Montavon, & Coddet, 2004; Nouri & Sola, 2019; Prochazka, Khor, & Cizek, 2006). The plasma gas used in this procedure usually contains Argon (Ar), Argon with Hydrogen (H_2), Argon with Helium (He), Argon with Nitrogen (N_2), as well as Nitrogen or a mixture of the two. Argon stabilizes the electric arc in the nozzle, whereas Nitrogen or Hydrogen's strong thermal conductivity enhances heat transfer to the sprayed particles (Janisson et al., 1999). APS plasma torch temperatures may reach 13000 degrees Celsius (T. Liu, Zheng, & Zhang, 2016), resulting in particle velocities at the nozzle outflow of 500 meters per second, depending on particle size (P Fauchais, 2004) and plasma jet velocity and enthalpy depend on plasma gas composition (X. Chen et al., 2016). In atmospheric plasma spraying, particle characteristics like velocity and temperature are critical for coating quality. Kwon et al.(Kwon et al., 2023) investigated how variations in process gas composition affect in-flight particle characteristics and coating deposition. They found that a higher hydrogen ratio improved deposition efficiency, reduced porosity, and enhanced bonding between splats by controlling droplet superheating.

The substrate temperature is important when applying ceramic coatings to metal surfaces because it may cause residual stresses. Alumina coatings adhere best at substrate temperatures between 300 and 500 degrees Celsius (Mellali, Fauchais, & Grimaud, 1996). The spraying distance is usually 60 to 150 millimeters, and the environment is usually air (Ng & Gan, 2005).

1.4.4 Applications of the APS coatings

APS is used in a wide range of applications. Its ability to spray ceramic materials at high temperatures makes it particularly well suited for producing TBCs for gas turbine components in the aerospace and power generation industries. APS can also produce wear- and corrosion-resistant coatings for components in the oil and gas and automotive industries, and biocompatible coatings for medical implants(Lima & Marple, 2007).

1.4.5 APS advantages and disadvantages

APS has several advantages, including the ability to spray a wide range of materials, from metals to ceramics, and to produce thick coatings. In addition, the process operates at atmospheric pressure, simplifying the process equipment compared to other thermal spray processes that operate under vacuum. However, APS also has some disadvantages. The high temperatures involved can lead to the oxidation or decomposition of some coating materials, and the process can produce a relatively rough coating surface compared to other thermal spray processes.

1.4.6 HVOF vs APS

The main differences in parameters between HVOF and APS are visually illustrated in Figure 1.10 along with other processes (Oksa et al., 2011). The HVOF process uses particles travelling at speeds of 400 to 1000 m/s within a torch temperature of 3000 °C, while APS involves lower particle speeds, typically between 150 and 400 m/s, within a torch temperature of 12,000 °C.

The HVOF technique excels in producing coatings with low porosity and oxide content, providing dense microstructures with enhanced wear and oxidation resistance (Hong et al., 2016; Xiaofeng et al., 2015), while the APS technique, despite its cost advantages, tends to result in coatings with a porous structure and higher oxide levels due to its application in the open atmosphere (Y. Liu et al., 2017).

Karaoglali et al. (Karaoglanli, Ozgurluk, & Doleker, 2020) investigated the microstructures and TGO layers of MCrAlY coatings deposited via APS and HVOF spraying techniques, subjected to isothermal oxidation tests at 1000 °C for varying durations. The results indicate that APS coatings exhibit high microstructural porosity and oxide content, with a TGO layer forming on the NiCoCrAlY coating's surface during oxidation, increasing in thickness over time. Unlike alumina, other oxides, primarily Al_2O_3 and mixed/spinel oxides, become dominant in the TGO structure with prolonged exposure. In contrast, HVOF coatings demonstrate lower oxide and porosity content compared to APS, with limited observed oxide

content between splats. Increased oxidation time results in thicker oxide layers and visible locally internally oxidized regions. The slower aluminum depletion in the HVOF-coated structure leads to a higher formation of protective alumina phases on the surface compared to APS-MCrAlY coatings in later oxidation stages.

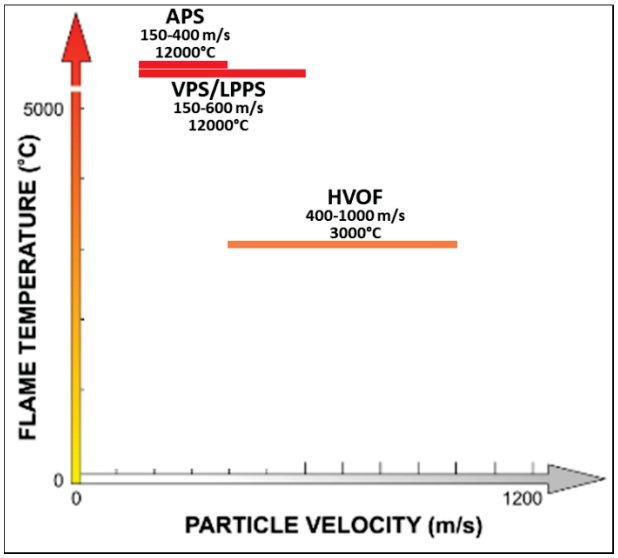

Figure 1.10 Illustrates the typical operational ranges of flame temperature and particle velocity for various thermal spray systems taken from (Oksa et al., 2011)

Moreover, the thermal responses of HVOF and APS techniques differ significantly. In a study by Waki et al. (Waki, Kitamura, & Kobayashi, 2009), the impact of thermal treatment on the high-temperature mechanical properties enhancement in HVOF and APS MCrAlY coatings was compared. The findings indicated that intensive thermal treatment effectively increased the bending strength and Young's modulus, particularly in HVOF coatings, which experienced approximately threefold increases in bending strength. In contrast, APS coatings showed a lower degree of enhancement, particularly those produced with fine powder sizes.

Therefore, while literature often highlights the potential of optimized HVOF processes to produce dense coatings with low oxide content and potentially superior oxidation compared to APS, it is crucial to note the specific context of the present study. The HVOF processing parameters employed here, selected partly to explore different deposition conditions, resulted

in a coating microstructure containing a significant volume fraction if unmelted particles (detailed in Chapter 3, Section 3.3 and Chapter 4, Section 4.2.1). As will be demonstrated in the experimental sections of this thesis, these process-inherited defects created pathways for significant intrusive oxidation, impacting the direct comparison with the APS coating evaluated within this specific research framework. This context, particularly the deviation from an optimized HVOF microstructure due to the chosen parameters, should be considered when interpreting the comparative performance results presented later.

1.5 Vacuum Plasma Spray process (VPS)

Vacuum Plasma Spray (VPS), also known as Low-Pressure Plasma Spray (LPPS), is a variant of the atmospheric plasma spray (APS) process, but as the name suggests, it's performed under vacuum conditions. The VPS process is often used for applications where high-purity coatings or thick deposits are required, such as in the aerospace and nuclear industries.

1.5.1 VPA process mechanics

Like APS, the VPS process also uses an electric arc to create a plasma. The plasma is generated in a similar manner, with a high-frequency electric arc established between a cathode and an anode. The plasma-forming gas, usually argon or helium, is ionized to form a plasma which generates a high-temperature jet when exiting the torch nozzle. The coating material, typically in powder form, is then injected into this plasma jet, where it rapidly melts. The molten particles are propelled towards the substrate under vacuum as shown in Figure 1.11, where they solidify to form the coating.

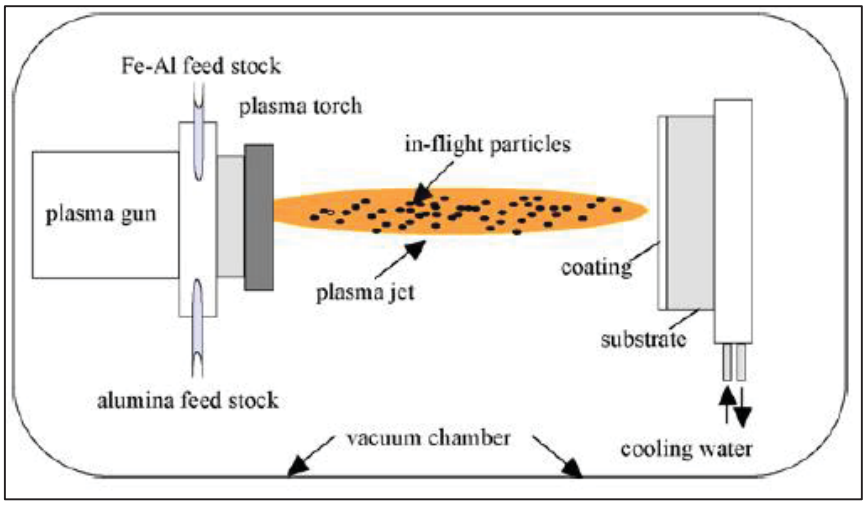

Figure 1.11 Illustrations of the VPS process

1.5.2 VPS material considerations

Like APS, VPS can spray a wide range of materials, including metals, alloys, ceramics, and CERMETS. The ability to control the atmosphere during spraying allows VPS to deposit materials that are sensitive to oxidation or contamination, such as titanium and some high-performance ceramics.

1.5.3 Application of the VPS coatings

VPS finds applications in a variety of industries where high coating purity, low oxide content, or thick deposits are required. For example, in the aerospace industry, it is used to produce thick TBCs for gas turbine components. VPS is also used in the nuclear industry for the encapsulation of radioactive waste.

1.5.4 VPS advantages and disadvantages

VPS has the advantage of spraying in a controlled environment, allowing the deposition of materials sensitive to oxidation or contamination, and enabling the production of high-purity coatings. It can also produce thick coatings and allows better control over coating microstructure compared to APS. However, the process is more complex and costlier due to

the need for a vacuum chamber and associated equipment. Moreover, the coating rate is generally lower compared to APS due to the smaller spraying distance in a vacuum chamber.

1.5.5 Comparison between HVOF and VPS

VPS and HVOF both can produce high-quality coatings, but each has its strengths depending on the application. HVOF typically generates coatings with lower porosity and higher bond strength due to higher particle velocities, making it well suited for wear and corrosion-resistant coatings. VPS, on the other hand, allows for the deposition of high-purity coatings and those from oxidation-sensitive materials, making it ideal for applications such as TBCs in aerospace and encapsulation in the nuclear industry (Maher I Boulos, Fauchais, & Heberlein, 2021; Davis, 2004; Pawlowski, 2008).

1.6 Defects of coating deposition

While thermal spray techniques offer numerous advantages, the deposition process can introduce a range of defects that can potentially compromise the functionality and longevity of the coating. These defects arise from various factors, including the intrinsic nature of the spraying process, equipment parameters, and the interplay between the coating material and substrate. Understanding these defects and their causes is crucial to optimize the spraying process and ensure the desired coating quality and performance (Davis, 2004; P. L. Fauchais, Heberlein, & Boulos, 2014; Pawlowski, 2008).

1.6.1 The porosity of the coating

The porosity refers to the presence of small holes or voids within the coating. These can compromise the integrity and performance of the coating. Causes of porosity often include gas evolution during the spraying process, improper spraying parameters, or the presence of contaminants that can trap gas within the coating.

The significant development of pores at the interface deteriorates the bond between the substrate and coating, potentially causing the coating system to failure. Interdiffusion between the BC and nickel-based substrate results in various effects, including the depletion of alloying elements, the creation of Kirkendall porosity, and the formation of intermetallic phases (as shown in Figure 1.12). Notably, the diffusion of aluminum from the coating to the substrate poses a particular problem by reducing the available aluminum for forming the alumina scale. This interdiffusion leads to the emergence of a β-phase depletion zone in the coating and a γ′-phase depletion zone in the substrate (Renusch, Schorr, & Schütze, 2008). Different diffusion coefficients of key alloying elements in the diffusion couple (substrate-BC) can cause vacancies to accumulate at the interface, leading to void coalescence (Nakajima, 1997). The extent of Kirkendall porosity formation depends heavily on the alloy composition of both the coating and substrate, as well as the coating deposition process. Substantial Kirkendall porosity can severely weaken the BC-substrate interface, potentially resulting in the ultimate failure of the coating system (Chyrkin et al., 2016).

Studies done by Moritz Elsab et al., (Elsaß, Frommherz, Scholz, & Oechsner, 2016) examined the impact of alloy composition and coating method on diffusion effects. They used different MCrAlY coatings on a Nickle superalloy via LPPS and HVOF techniques. After annealing at 1050 C, the microstructural and compositional analyses were performed on the coated specimens. LPPS-BCs displayed less Kirkendall porosity compared to HVOF-BC. The location of porosity shifted based on the depositing method, moving from substrate side (LPPS) to coating side (HVOF). This shift is attributed to accelerated element diffusion, particularly aluminum, influencing observations.

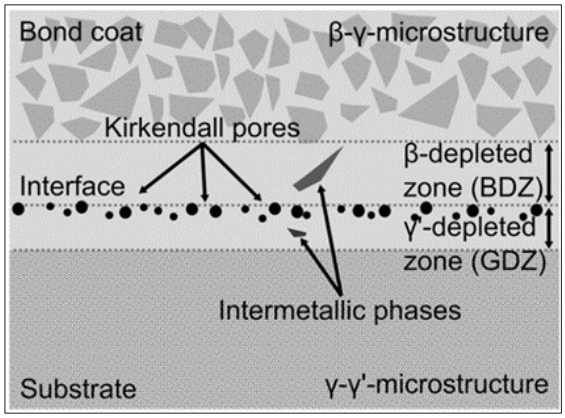

Figure 1.12 Schematic overview of the interdiffusion phenomena appearing at the BC substrate interface (Elsaß et al., 2016)

1.6.2 Oxidation of the coatings

Oxidation in coatings manifests as the formation of oxides in forms of regions, particle or layers. These oxides can degrade the properties of the coating, such as its electrical or thermal conductivity. Causes of oxidation include interaction of the hot coating particles with the atmosphere or substrate, particularly if there isn't an adequate shielding of during spraying or the temperature is not properly controlled. In MCrAlY, the majority of alloying elements are susceptible to oxidation, resulting in the creation of diverse oxide species. The formation of these oxides is influenced by numerous factors, such as surface condition during oxidation, coating microstructure, temperature, alloy composition, and more. These oxide varieties encompass Al_2O_3, spinel-type oxides, NiO, Cr_2O_3, and Y-oxides.

1.6.3 Splat shape

Splats are flattened, disk-like particles observed on the coating surface. They arise when molten droplets impact the substrate and spread out. Causes of splats can be natural, as a part of the process, but excessive or irregular splats can be due to inconsistent droplet sizes or irregular trajectories(Abbas, Smith, & Munroe, 2020; Kwon et al., 2023). In their study, Liu et al. (T. Liu et al., 2016)examined the morphology of splats deposited by comparing the performance of the APS process and the SPS process utilizing a solid shield. They observed

that the SPS process yielded more disk-shaped splats and significantly reduced oxygen concentration in the coating. These outcomes were attributed to the application of a solid shield, which resulted in higher flame temperatures and lower oxidation levels as shown in Figure 1.13.

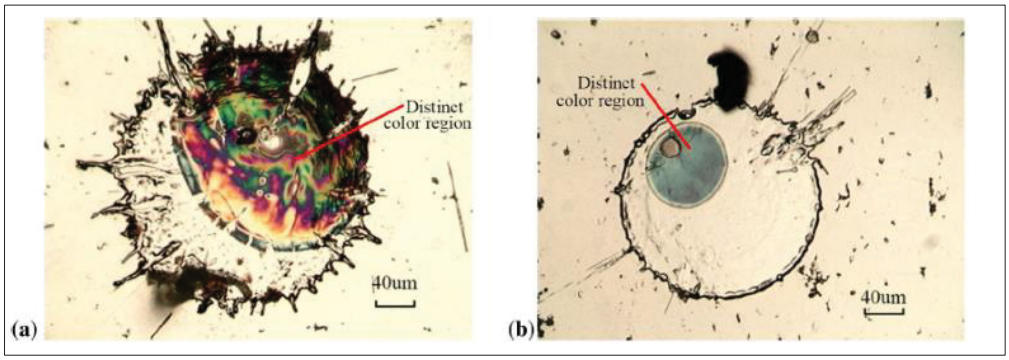

Figure 1.13 Illustrates optical micrographs depicting splat morphology. (a) Represents the APS process, while (b) illustrates the SPS 90 mm process taken from (T. Liu et al., 2016)

1.6.4 Unmelted particles

Unmelted or partially melted particles are a type of defect that can be present in thermally sprayed coatings, particularly affecting the coating's density, integrity, and performance. The extent to which particles melt during spraying depends heavily on the specific process (e.g., APS vs. HVOF) and the chosen parameters such as powder temperature, velocity, and projection distance (Léger, Wigren, & Hansson, 1998).

HVOF spraying, when optimized, has the potential to produce dense MCrAlY coatings with low porosity and minimal oxide content, leading to favourable oxidation behaviour. Research by Richer et al. demonstrated that HVOF coatings could exhibit microstructures and oxidation resistance (low oxide growth rates, stable $\alpha{-}Al_2O_3$ formation) comparable to or even better than other techniques like Cold Gas Dynamic Spray (CGDS), provided the processing achieves good particle deformation and bonding. Similarly, Shibata et al. found HVOF coatings showed low oxidation kinetics, comparable to LPPS and significantly better than APS, despite observing the presence of some unmelted particles in their HVOF structure. This suggests that

a limited quantity of such particles may not be severely detrimental if the overall coating matrix is dense and has low in-spray oxidation (Richer, Yandouzi, Beauvais, & Jodoin, 2010; Shibata et al., 2006).

However, the specific HVOF process parameters used for the coatings investigated in this thesis resulted in a microstructure containing a significant fraction of unmelted particles (approximately 21 ± 2%, as detailed in Chapter 3). These largely intact particles, often retaining their original powder microstructure, were poorly bonded to the surrounding matrix, creating voids and interconnected pathways within the coating. This contrasts with the denser, more consolidated structure achievable with optimized HVOF parameters.

The primary impact of these numerous unmelted particles and associated porosity in the thesis HVOF samples was the facilitation of oxygen ingress deep into the coating. This led to significant *intrusive oxidation* along the particle boundaries and within the voids, consuming the protective elements (like Aluminum) not just at the surface but also within the bulk of the coating. This internal/intrusive oxidation contributed significantly to the overall mass gain observed during high-temperature exposure and accelerated the depletion of the aluminum reservoir, ultimately impairing the coating's ability to maintain a protective α−Al2O3 scale compared to the APS samples studied in this work (see Chapter 3 results). While internal oxides, sometimes termed "island-like" oxides, are frequently noted in APS coatings due to in-flight oxidation, the numerous unmelted particles in the specific HVOF samples of this thesis created analogous pathways for detrimental internal oxidation. Therefore, the presence of a high volume fraction of unmelted particles, indicative of suboptimal processing for the specific HVOF samples in this research, critically undermined their potential high-temperature oxidation resistance (L Wang et al., 2014).

1.6.5 Cracks

Cracks can appear either within individual splats or as macro-cracks that traverse several splats. Causes for crack formation include thermal stresses generated during the rapid cooling of the

coating, mismatch in the coefficient of thermal expansion between different layers of TBCs, the substrate, the BC, oxide (TGO) and topcoat or the use of improper spraying parameters.

Several studies have been conducted on TBCs and found that the expansion of α-Al_2O_3 TGO leads to increased tensile stress near the interface between YSZ (yttria-stabilized zirconia) and the BC. This stress is responsible for cracking in ceramic materials. However, they also observed that the presence of mixed oxide can significantly shorten the service life of TBCs. Mixed oxide is characterized by localized growth and a much higher growth rate than α- Al_2O_3. Consequently, the rapid expansion of Mixed oxides leads to localized cracking in the ceramic. Nearly all types of mixed oxides can induce this local cracking. When these cracks caused by adjacent Mixed oxides gatherings connect, it results in YSZ spallation, further compromising the performance of the TBC (Y. Li, Li, Zhang, et al., 2010; Wei & Cai, 2020; Wei, Cai, & Zhao, 2022; R. Xu, Fan, Zhang, & Wang, 2014).

The primary cause of cracking around the interface of the yttria-stabilized zirconia (YSZ) and BC in TBCs is the development of TGO at elevated temperatures. In the work conducted by Wei et al., (Wei, Liu, Cheng, & Tahir, 2022) the researchers investigated the influence of TGO thickness on the local stress and cracking behaviour in TBCs. The findings revealed that the non-uniformity thickening and lateral growth rate of TGO had a substantial effect on the propagation of cracks in ceramic top layer (YSZ) and TGO as shown in Figure 1.14. Therefore, the optimization of the depositing process has the potential to delay the propagation of cracks and enhance the endurance and reliability of the coating system. This may be achieved by minimizing the non-uniformity and growth rate of the TGO layer.

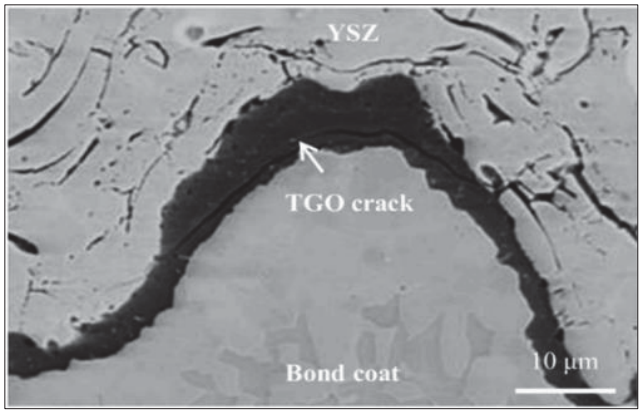

Figure 1.14 The ceramic topcoat/BC interface cracking due to non-uniform of TGO thickness (Wei, Liu, et al., 2022)

1.6.6 Delamination failure

Delamination is when the coating separates either from the substrate (bonding failure) or between different layers of the coating itself, as shown in Figure 1.15 (Krämer et al., 2008). Causes can include poor bonding due to surface contamination, inadequate surface preparation, or thermal stresses that arise during the cooling phase.

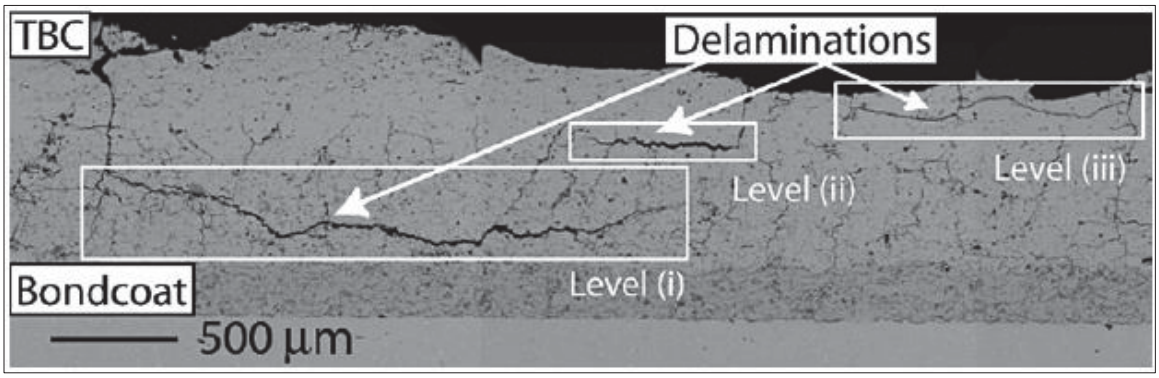

Figure 1.15 Illustrates the presence of delamination occurring at various locations within APS-TBC coatings taken from (Krämer et al., 2008)

More specifically, bonding failure results in poor adhesion of the BC to the substrate. Causes of bonding failures can be traced back to inadequate surface preparation, contamination of the substrate surface, or the use of improper spraying parameters which don't allow for good adhesion.

1.6.7 Bond coat roughness

BC roughness is a crucial factor affecting TBC service life, with variations arising from deposition methods, feedstock powder properties, and spraying parameters. Research by Eriksson et al. shows that higher BC roughness extends thermal fatigue life, and adjustments in Variable Pressure Plasma Spray (VPS) parameters impact Ra values. This increased roughness is thought to move the failure modes from primarily interface failure to topcoat failure due to high roughness (Eriksson et al., 2013). Additionally, Vassen et al. confirmed the significance of BC roughness, obtained through VPS spraying of MCrAlY feedstock powders with different particle sizes, using a model to describe crack growth and failure in thermally cycled TBC systems (Vaßen et al., 2001). Nowak et al. conducted a study with the aim of investigating how the morphology and roughness of BCs affect the durability of TBC systems. They examined BCs with identical chemical compositions that were applied using three different methods: high-velocity oxy-fuel (HVOF), vacuum plasma spraying (VPS), and a double-layered BC consisting of an HVOF base coating, and a thin outer layer known as the "flash coat" applied using APS. To assess longevity, cyclic oxidation testing was performed at a temperature of 1120 °C. To establish a link between the roughness of the BC and the service life of TBC systems, roughness parameters R_a and R_y were measured in the as-received TBCs samples. They made a noteworthy discovery, finding that TBC systems with a VPS-BC and the HVOF/APS-flash coat exhibited a service life roughly three times longer than TBC systems with the HVOF-BC (Nowak et al., 2014). Due to the fact that cracks can relatively more readily spread along the flat (lower roughness) topcoat/BC interface, but at greater roughness (VPS and HVOF with flash coat) BC the crack meets significant resistance to propagate along the interface.

1.6.8 Phase decomposition

Compounds such as AL_2O_3 and Cr_2O_3, upon cooling, might decompose into different phases rather than retaining their desired phase. Causes include rapid cooling rates or inherent phase

transformations in specific materials during cooling. Phase decomposition can weaken the adhesion between layers in the TBC system resulting spallation and degradations of TBC service life (Bogdan & Peter, 2024).

1.6.9 Retention of unwanted phases

Certain phases which are present in the molten or semi-molten state might remain as-is in the solidified coating. Causes include extremely rapid cooling that prevents the phase from transforming or separating out.

1.6.10 Inclusions

Inclusions, which are undesired foreign materials or impurities found within the coating, are primarily composed of metallic oxides. These inclusions typically arise from impurities present in the raw materials or the interaction between hot powder particles and their surroundings during flight, such as air and combustion products. This interaction results in the formation of inclusions between the splats or from contaminants introduced during the manufacturing process. According to Davis, the inclusion content in MCrAlY coatings is influenced by three main factors. First, the quality of the feedstock powder, including its purity and particle morphology, significantly affects the formation of inclusions, with impurities or irregular particle sizes leading to defects. Second, spray parameters, such as the angle, distance, and thermal energy during deposition, play a crucial role in determining how well the powder melts and solidifies, with suboptimal settings causing incomplete melting or excessive oxidation. Finally, environmental control, particularly oxygen levels, is vital as high oxygen exposure during the coating process can result in increased oxide inclusions (Davis, 2004).

Damien et al., (Damien Texier, Monceau, Hervier, & Andrieu, 2016) conducted a study involving a coating system that deposits a NiCoCrAlYTa coating to a Ni-based superalloy at high temperatures, reaching up to 1100 °C. Their research revealed that the manufacturing process for MCrAlY-coated nickel-based superalloys has a significant impact on the microstructure and mechanical properties of the system due to the existence of voids and non-

adherent grit-blasting particles in the coating/substrate interface. Consequently, the differences in substrate porosity may be attributed to the presence of grit-blasting particles originating from the fabrication process. These imperfections could potentially harm the material's behavior under high-temperature, high strain rate conditions, which may be responsible for problems like coating/substrate spallation.

1.6.11 Interdiffusion phenomenon

When exposed to prolonged high-temperature, coatings deteriorate through mechanisms like, hot corrosion, oxidation, and interdiffusion with the substrate. Interdiffusion involves elements like nickel (Ni), diffusing outward from the alloy and essential protective elements like aluminum (Al) diffusing inward toward the substrate. As coatings usually have a finer texture and contain more grain boundaries in comparison to the materials they are applied to as substrates, one can anticipate that diffusion rates within coatings will be higher than those within substrates of a similar composition (Campbell, Boettinger, & Kattner, 2002; Campbell, Zhao, & Henry, 2004).

Historically, interdiffusion between coating layers and the substrate was not considered a significant issue until MCrAlY alloys were introduced as BCs (J. Nicholls, 2000). However, even with the use of MCrAlY systems and advanced coating techniques, the diffusion of elements between the substrate and the coating, along with the loss of aluminum due to oxidation, can significantly reduce the coating's effectiveness. To ensure long-term stability, it is essential to develop diffusion barrier coatings that can prevent interdiffusion at the BC/substrate interface, preserving the coating's protective properties.

Role of α-Al_2O_3 in interdiffusion

It has been shown that the presence of α-Al_2O_3 in the TBC system can reduce interdiffusion with a dual function: it delays the outward elemental diffusion to the surface, while concurrently acting as a robust agent to restrict interdiffusion between the MCrAlY BC and

the superalloy substrate (Peng, Guo, He, & Gong, 2010). During the oxidation process, aluminum (Al) migrates to the interfaces of the coating, forming a protective layer of Al_2O_3.

However, over extended periods of oxidation, some aluminum can also diffuse into the substrate, depleting the coating of its aluminum content and reducing its ability to maintain the protective oxide layer. This process can weaken the coating's long-term performance and durability. As the Al_2O_3 layer gradually fails, more aluminum diffuses to the surface, promoting the growth and regeneration of the scale. This cycle continues until the aluminum concentration in the coating becomes insufficient to sustain a continuous Al_2O_3 layer. At this point, as the protective oxides diminish, less effective oxides of different alloying elements emerge, allowing oxygen infiltration into the coating, leading to the formation of internal oxides of the residual aluminum. The precise aluminum concentration marking this shift varies depending on factors such as substrate type, coating composition, and microstructure. For instance, during cyclic burner rig testing of a nickel-base alloy with a NiCoCrAlY coating, this transition typically transpires around 3.5% aluminum concentration (Bar-Cohen, 2014). The loss of aluminum due to oxidation leads to the recession of the β (NiAl) phase at the interface between the BC/oxide scale. This process is accompanied by a gradual phase transformation ($\beta \rightarrow \gamma' \rightarrow \gamma$). And the complete depletion of the β-phase is frequently regarded as the termination point of the chemical service life of the coating (P. Niranatlumpong, C. Ponton, & H. Evans, 2000).

Additionally, the coating acquires elements diffuse from the substrate, including detrimental ones like Ti, Mo, W and Ta as well as beneficial elements like Y and Hf. The diffusion of elements within the coating system, because of interdiffusion, can influence specific properties. For instance, in superalloys with high titanium content, the diffusion of titanium is recognized for providing remarkable strength at high temperatures and cost effectiveness. Although titanium improves the precipitation hardening effect, it also diminishes the high-temperature oxidation resistance of superalloys (Baik, Wang, Liaw, & Dunand, 2018; J. Chen et al., 2022; Teng et al., 2021).

Sun et al. (X. Sun et al., 2024) recently investigated interdiffusion between the NiCoCrAlY BC and Nickel-based superalloy substrate at 1100 °C. They found aluminum played a key role in initial phase transitions, and γ′ depletion in the substrate resulted from the loss of Ti and Ta. This interdiffusion led to microstructural degradation in both the BC and substrate in coating system as shown if Figure 1.16. Moreover, several investigations have noted that variations in elemental diffusion rates result in the development of Kirkendall voids near the interface of the coating and superalloy, thereby reducing the strength of their bond (Campbell et al., 2004; Chyrkin et al., 2016).

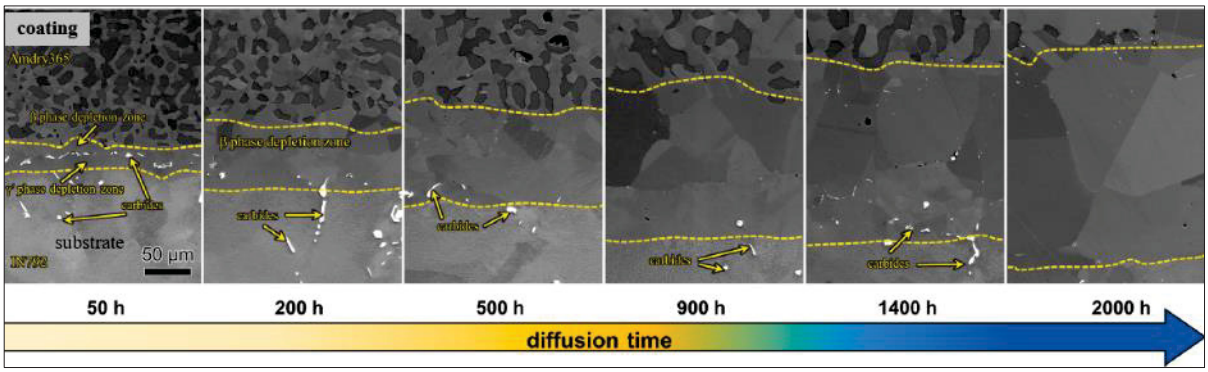

Figure 1.16 The cross-section microstructure evolution induced by interdiffusion between Amdry365 and IN792 after several of time exposure at 1100 ºC taken from (X. Sun et al., 2024)

Foreseeing these evolutions at the interdiffusion region is a fundamental consideration, given their direct control over the oxidation life expectancy. Moreover, one must bear in mind that alterations in alloy composition due to this phenomenon can potentially exert significant effects on the mechanical properties of the coating system (Damien Texier et al., 2016).

1.7 Mechanical testing methods for thermal spray coatings

Mechanical testing methods are essential in evaluating the performance of thermal spray coatings, as they help predict how these coatings will behave under various operating conditions. These methods provide crucial insights into a coating's hardness, tensile strength, roughness, and toughness.

1.7.1 Roughness measurement

The surface roughness of a coating significantly affects its tribological properties, adhesion to the substrate, and overall performance. Roughness is typically quantified using profilometers or advanced techniques like laser scanning confocal microscopy and atomic force microscopy (Whitehouse, 2002).

Surface roughness, often represented by $\mathbf{R_a}$ (arithmetic average roughness), is a key parameter in surface texture analysis. $\mathbf{R_a}$ measures the average deviation of the surface profile from the mean line over a sampling length and is widely used due to its simplicity and standardization. Other roughness parameters, such as $\mathbf{R_z}$ (average peak-to-valley height) and R_q (root mean square roughness), can provide additional insight into surface characteristics. These parameters are defined in standards like ISO 4287:1997 and ASME B46.1-2009, which offer guidelines for consistent measurement and interpretation (Standard, 1998; Whitehouse, 2002).

There are several methods to measure roughness, often involving specialized tools and techniques:

- **Contact Profilometry**: This method uses a diamond stylus that is moved vertically against the surface and then dragged across the surface at a constant speed. As the diamond stylus moves up and down along the surface irregularities, a sensor measures the vertical deflection, and a surface profile is created.

- **Non-Contact Profilometry**: Laser scanning, white-light interferometry, and confocal microscopy are examples of non-contact profilometry. They map the surface by analyzing how light reflects off it.

- **Atomic Force Microscopy (AFM)**: AFM probes the surface at the atomic level and can be used to measure nanoscale roughness.

The effect of roughness on oxidation

Surface roughness undeniably plays a significant role in the oxidation behavior and life of MCrAlY coatings. While certain roughness can offer benefits like enhanced oxide adherence, it can also introduce challenges like stress concentration. Optimizing the roughness level for specific applications is essential to ensure the best performance and longevity of the coating.

1. **Oxidation initiation**: Surface roughness can influence the initial stages of oxidation. Rougher surfaces provide more nucleation sites for oxide formation. This can lead to a quicker, but potentially more uneven, initiation of the protective oxide layer.

2. **Adherence of TGO layer**: A rougher surface can provide better mechanical interlocking between the MCrAlY coating and the TGO. This can enhance the TGO's adherence and reduce the likelihood of spallation. However, if the roughness is too high, the TGO can become mechanically strained, leading to early failure (A. G. Evans, Mumm, Hutchinson, Meier, & Pettit, 2001).

3. **Stress concentrations**: Surface irregularities can act as stress concentrators. During thermal cycling, these areas can experience elevated stresses, leading to the initiation and propagation of cracks, thereby reducing the life of the coating (Karlsson & Evans, 2001).

4. **Effects on protective oxide thickness**: Rougher surfaces might lead to thicker oxide layers in the valleys of the roughness profile, which could offer better protection. However, the peaks might become points of vulnerability where the oxide is thinner (Wright & Evans, 1999).

5. **Impedance to ion diffusion**: The irregularities of a rough surface can impede the diffusion pathways of ions, such as oxygen, during oxidation. This might slow down the overall oxidation rate. However, this effect may be less pronounced over

extended periods, as the oxide layer's growth might level out these surface disparities (Weiser, Chater, Shollock, & Virtanen, 2019).

1.7.2 Hardness test

Hardness testing is a widely used method for rapidly assessing the mechanical properties of materials. Hardness in materials science refers to a material's ability to resist localized deformation, such as scratching, denting, or indenting. It measures how well a material can withstand wear, abrasion, or other mechanical stresses, making it a critical property for applications requiring durability and resistance to damage. Hardness testing involves applying a known force to an indenter, which penetrates the material’s surface. The depth or size of the indentation is measured during a hardness test, and the hardness value is determined either by calculation or by referencing a predefined scale specific to the test method. Harder materials produce smaller or shallower indentations under the same load, while softer materials show larger or deeper indentations.

The choice of testing method depends on factors like material type, thickness, and precision requirements. Hardness testing methods like Rockwell, Vickers, and Knoop are widely used for evaluating material properties, each with specific applications, advantages, and limitations. The Rockwell test is fast and simple, making it ideal for production settings and bulk materials, but it requires thicker samples and careful indenter selection. The Vickers test offers high precision and is suitable for thin materials or coatings, though it is slower and subject to errors in optical measurement. The Knoop test is specialized for microhardness measurements on very thin samples or coatings, requiring minimal material, but it is limited by the small loads it uses and its focus on localized properties rather than bulk behavior. The choice of method depends on the material, the testing environment, and the required accuracy, ensuring suitability for specific industrial and research applications (Whitehouse, 2002). Vickers hardness is commonly used for MCrAlY coatings due to its applicability to a broad range of hardness values, within the thickness of the coating and its ability to provide a continuous scale

of hardness. Vickers hardness values for MCrAlY coatings can vary significantly depending on the coating process and heat treatment.

Hardness of MCrAlY coatings

MCrAlY coatings are characterized by their moderate hardness, ranging from 400 HV to 800 HV, which plays a critical role in their ability to resist wear, deformation, and erosion at high temperatures. The hardness of these coatings is mainly determined by their microstructure and composition. Their hardness can be affected by a number of factors including the phase composition (γ'-Ni_3Al as a ductile phase, and β-NiAl as a brittle phase), grain size, presence of defects, and the distribution of elements (Cr, Al, Y) within the coating.

It should be noted that the hardness of these coatings can change significantly during service at high temperatures due to phenomena such as oxidation, phase transformation, and recrystallization. For example, a study by Ghadami et al., reported Vickers hardness values for HVOF-sprayed NiCoCrAlY coatings of around 500 HV (F Ghadami, Aghdam, Zakeri, Saeedi, & Tahvili, 2020; F Ghadami, Zakeri, Aghdam, & Tahmasebi, 2019) when another study by Tao et al. found that APS-sprayed NiCoCrAlY coatings had hardness values of about 400 HV (Tao, Wang, & Song, 2017). These variations demonstrate that although hardness measurements are valuable for assessing the impact of factors and process parameters for samples with similar initial conditions, they are not suitable for directly comparing coatings with different initial states.

1.7.3 Tensile properties of MCrAlY coatings

Tensile testing involves applying a force to a material until it breaks or fractures. This test helps evaluate the strength of the bond between the coating and the substrate, as it provides information on how well the coating adheres to the underlying material (Damien Texier et al., 2016). This test is usually carried out indirectly via bond strength tests, such as the pull-off test or the tensile adhesive test.

The tensile properties of MCrAlY coatings can be influenced by a variety of factors, including the coating process, microstructure, composition, and testing temperature. The coatings typically exhibit lower tensile strength and ductility compared to the substrate material due to the presence of defects (pores, cracks, oxides) inherent in the thermal spray process. However, the coatings can still provide sufficient mechanical integrity for their intended high-temperature protective function.

The elongation to failure of MCrAlY coatings can be significantly lower than that of the substrate material, again due to the microstructural defects and the brittleness of the coating. However, in service, the coatings operate under compressive stresses due to thermal expansion mismatch with topcoat, reducing the significance of the low tensile properties (Alam, Parlikar, Chatterjee, & Das, 2017; He, 2022; International, 2016).

1.8 Relationships between the composition, structure, and performance of MCrAlY coatings

We begin with an overview of the composition of MCrAlY coatings, focusing on the roles of different elements in the coating and how they contribute to the coatings' high-temperature resistance. We then examine the phase diagrams of these materials, which serve as maps guiding us through the transformations of these coatings undergo under their formation thermal conditions.

Next, we delve into the crystallography and structure of these materials. Understanding the structure at different length scales, from the atomic to the macroscopic, is crucial for comprehending the coatings' physical and mechanical properties.

Moving on, we take a closer look at the thermal spray coating process parameters. The characteristics of the coatings are profoundly affected by process conditions, and we will explore processes such as fusion, phase changes, oxidation, solidification, and adhesion, which play significant roles in the final coating properties.

By the end of this section, we will have an in-depth understanding of the physical metallurgy of MCrAlY coatings, equipping us with the necessary tools to investigate the behavior of the samples used for this project.

1.8.1 Microstructure evolution of MCrAlY coatings

A study by Gheno et al. examined the phase equilibria and microstructural evolution of NiCoCrAlY coatings during oxidation, focusing on the relationship between their behavior and phase diagrams. They analyzed various chemical compositions and found excellent agreement between calculated and measured phase compositions for the β–γ equilibrium, as well as good agreement for the three-phase β–γ–σ and β–γ–α equilibria. However, their results showed that the microstructure of the alloy can vary significantly with composition and temperature, as illustrated in Figure 1.17. These findings highlight the complex interplay between chemical composition, temperature, and phase stability in MCrAlY coatings (Gheno, Liu, Lindwall, Liu, & Gleeson, 2015).

It has been shown that for MCrAlY coatings, the typical maximal temperatures range from 1100–1150 ◦C, whether they are overlaid with a ceramic topcoat for TBCs applications or not. The formation of the Al_2O_3 scales and intrusions, combined with the interdiffusion with the substrate, results in the depletion of aluminum in the coating. Especially in thinner products, this can reduce the Al concentration to a critical threshold where Al_2O_3 becomes unstable. Consequently, other oxides might develop extensively at both the oxide/gas and metal/oxide interfaces (Damien Texier et al., 2021).

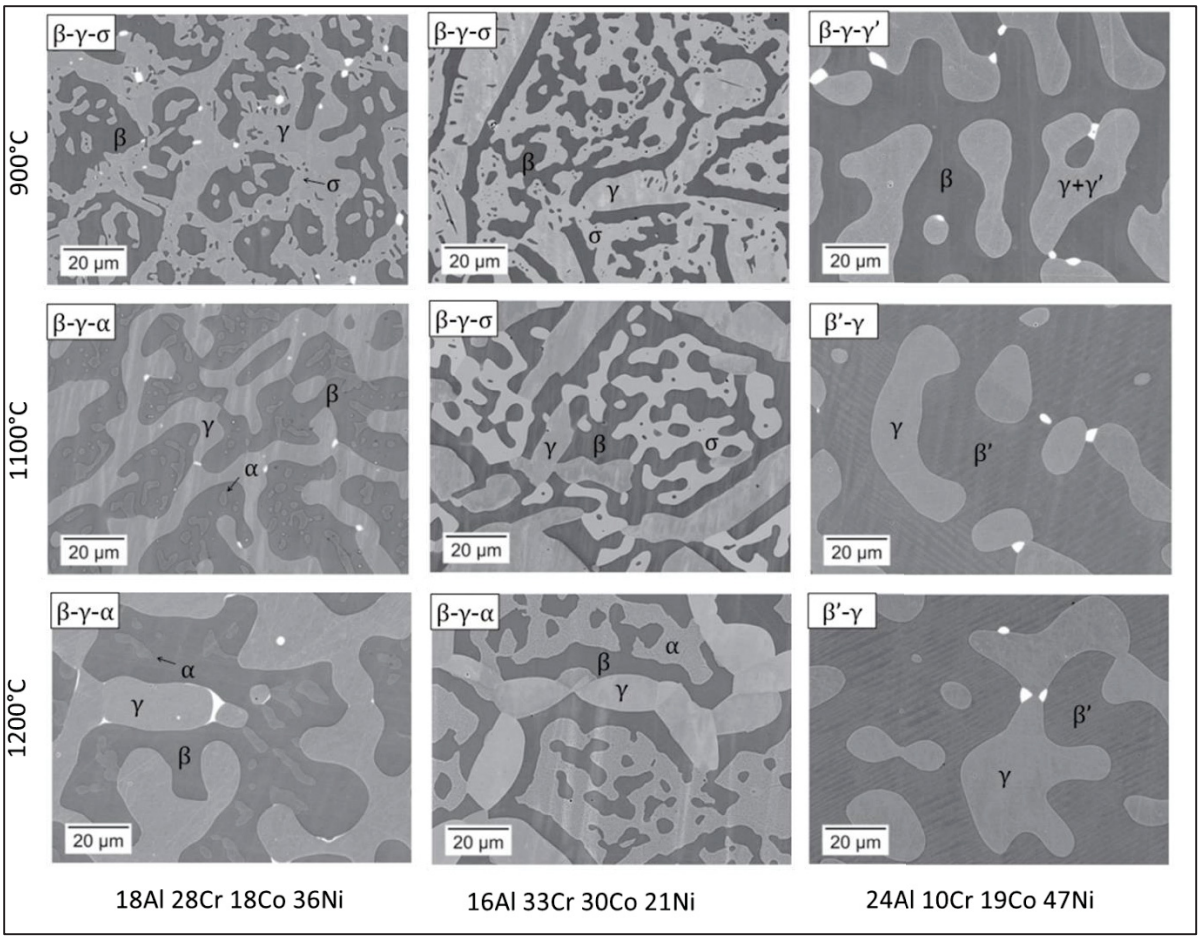

Figure 1.17 Microstructure of three alloys equilibrated at 900 °C, 1100 °C and 1200 °C. Bright precipitates are yttrium-rich compounds taken from (Gheno et al., 2015)

1.8.2 Phase diagram of coatings

In the context of MCrAlY coatings, phase diagrams are important for understanding the high-temperature behavior of these materials. The MCrAlY system involves several elements, making their phase diagrams complex. The main elements in NiCoCrAlY are Nickel (Ni), Cobalt (Co), Chromium (Cr), Aluminum (Al), and Yttrium (Ni-Y), with Ni and Co often forming the base of the alloy.

NiCoCrAlY coatings, as an example of MCrAlY coatings, exhibit a complex crystallography and structure, consisting of multiple elements and phases. The microstructure and phase stability are key factors that researchers and engineers consider when designing and evaluating these coatings for applications in demanding environments.

Goti et al., (Goti, Bétaille-Francoual, Hourcastagné, Viguier, & Crabos, 2014) investigated the oxidation behavior of NiCoCrAlY coatings at temperatures up to 1150 °C for varying durations. Their study involved a detailed analysis of phases and chemical compositions, resulting in the development of a phase diagram (Figure 1.18). During oxidation test, the aluminum-rich β phase in the coatings transformed progressively from grains to islands of the γ' phase and eventually to the γ phase as aluminum was consumed. This transformation was attributed to both oxide scale formation and interdiffusion near the coating/superalloy interface.

This phase diagram revealed that the microstructures and phases of the oxidized coatings depended on exposure temperature and duration. Lower temperatures and shorter exposure times led to a three-phased structure (γ, β, γ'), while higher temperatures caused complete conversion to a single γ phase. Intermediate conditions resulted in two-phased microstructures (γ, β) or (γ, γ').

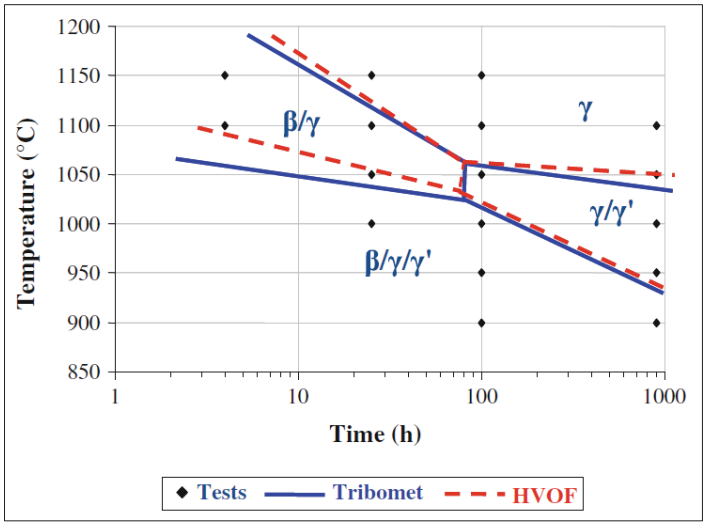

Figure 1.18 NiCoCrAlY coating microstructure diagram, function of temperature and exposure duration taken from (Goti et al., 2014)

Significantly, the γ’ phase was observed only below 1050 °C, allowing the dominance of the β and γ phases which are aligned with the Ni-Cr-Al ternary phase diagram proposed by Taylor and Floyd (A. Taylor & Floyd, 1951).

1.8.3 Roles of alloying elements in MCrAlY coatings

The adding of minute quantities of alloying elements (typically below 1 wt%) has the potential to impact various aspects of MCrAlY coating, including its microstructure, mechanical properties, and thermal behavior. Reactive elements are crucial to improving the adherence of the protective scales in MCrAlY coatings. This enhancement is achieved by their ability to form stable oxides at the interface between the protective scale and the coating. Notable examples of such reactive elements include Yttrium (Y), Hafnium (Hf), Lanthanum (La), Scandium (Sc), Cerium (Ce), Zirconium (Zr), and others. The role of the main alloying elements of MCrAlY Coatings is described as follows:

Nickel (Ni)

Nickle plays a fundamental role in both MCrAlY coatings and nickel-base superalloys, contributing significantly to the enhancement of oxidation resistance, thermal stability, creep resistance, and overall mechanical properties in applications with high temperatures. It forms various high-melting-point phases, including γ-Ni, γ’-Ni3Al, and the oxidation-resistant β-NiAl. In addition to its role in phase formation, nickel's similarity in coefficient of thermal expansion to many superalloys is crucial, especially when using the nickel to an alloy Al-Co-Cr as overlay coating or BC in the TBC system. This similarity aids in minimizing thermal stresses between the coating and the substrate, playing a vital role in preventing delamination and cracking of the coating during thermal cycles. Furthermore, nickel contributes to the enhanced creep resistance of the coating, particularly at elevated temperatures (Tamarin, 2002).

Aluminum (Al)

Aluminum significantly influences the resistance to oxidation by promoting the formation of the stable protective oxide α- Al_2O_3, known for its slow growth. The impact of aluminum on oxidation resistance tends to strengthen with increasing concentration. However, an excessive elevation in aluminum content can lead to a substantial decrease in the ductility of MCrAlY. Despite this concern, it is essential to maintain aluminum content at a sufficiently high level to foster the creation and preservation of an alumina layer, preventing subsequent breakaway oxidation. Typically, aluminum content falls within the range of 10-12 wt.%. Moreover, aluminum forms phase with Co or Ni, resulting in the creation of β-(Co,Ni)Al phase. This phase forms the protective α-alumina scale and acts as a reservoir for re-precipitate the alumina scale.

Chromium (Cr)

MCrAlY alloys, characterized by substantial chromium content complemented by minor yttrium additions contributing to solid solution hardening, exhibit a solid solution effect that acts as a barrier, impeding dislocation movements along grain boundaries and effectively bolstering the inherent creep resistance of MCrAlY alloys (Tancret, Bhadeshia, & MacKay, 2003). Chromium plays a dual role in enhancing both hot corrosion resistance and the activity/diffusivity of aluminum. This dual effect reduces the amount of aluminum required to form and maintain the protective alumina oxide scale, consequently increasing ductility. Furthermore, chromium effectively lowers the oxygen diffusion into the alloy by reducing the oxygen activity at the oxide-coating interface. Additionally, the Cr element stabilizes α- Al_2O_3 over γ- Al_2O_3.

Yttrium (Y)

Enhancing the overall protective mechanisms of MCrAlY coatings is a critical function of incorporating yttrium. Yttrium contributes to stability by forming robust oxides, serves as a diffusion barrier, promotes adhesion, and exerts influence on microstructure. The segregation of yttrium to the grain boundaries of TGO induces a notable "block effect," effectively

inhibiting the outward transport of aluminum and thereby reducing the TGO growth rate. These combined features make MCrAlY coatings containing yttrium highly effective in extending the service life and improving the performance of materials in high-temperature environments. To optimize these beneficial effects, it is imperative to achieve a uniform distribution of yttrium in MCrAlY alloys (Lu et al., 2019).

Cobalt (Co)

In coatings that contain cobalt, the formation of cobalt oxides such as CoO is possible at high temperatures. The presence of these oxides can significantly alter the protective layer's overall characteristics. Additionally, the interaction of cobalt with chromium and oxygen can lead to the creation of complex oxides, such as spinel (for instance (Ni, Co) (Cr, Al)$_2$O$_4$). These specific compounds play a crucial role in minimize both the thermal stability and the protective qualities of the coating (Vicente-Mendoza, Mora-García, Muñoz-Saldaña, & Juárez-López, 2023).

Reactive elements

Elements like Y, Hf, La, Sc, Ce, and Zr are termed oxygen-reactive elements due to their oxides being more stable than those formed on most alloys in high-temperature oxidizing conditions. The presence of a reactive element enhances the adherence of Al_2O_3 and Cr_2O_3 scales to alloy substrates. Proper doping transforms the α-Al_2O_3 scale from poorly adherent, buckled, and void-filled structures to more protective scales that are flatter, denser, and better adherent. Overall, reactive elements exhibit significant effects, including enhanced scale adhesion, altered scale-growth mechanisms, reduced oxidation rates, modification of scale microstructure, and improved selective oxidation in alumina scale. Several proposed mechanisms shed light on the positive effects of reactive elements:

1. **Mechanical anchoring**: Reactive elements play a crucial role as mechanical anchors for the oxide scale. They achieve this by creating oxide pegs at the oxide–alloy interface, simultaneously acting as vacancy sinks to prevent void formation and scale buckling.

2. **Segregation and enhanced bonding**: Reactive elements segregate at the interface, contributing to an increased bond strength between the oxide scale and the alloy.

3. **Slow ion diffusion**: Reactive element ions exhibit slower diffusion compared to the native cation (Al). This inhibits the typical outward transport of cations along scale grain boundaries, with the new rate-limiting step being the inward transport of O ions. On a macroscopic scale, this alteration leads to a reduction in the parabolic oxidation rate constant.

4. **Altered growth mechanism**: Reactive elements induce a shift in the growth mechanism of alumina. This shift favors predominantly inward diffusion of oxygen, as opposed to the conventional combination of outward diffusion of aluminum or chromium and inward diffusion of oxygen. This alteration results in a decrease in lateral oxide growth and the associated residual stresses.

5. **Reduced scale grain growth**: The segregation of reactive elements has another effect of reducing scale grain growth. This is attributed to the solute-drag effect of the reactive element ions on the scale of grain boundaries. Therefore, α- Al_2O_3 scale exhibit a smaller average grain size. In reactive element-doped α- Al_2O_3 scales, the microstructure undergoes further modification, with the formation of columnar grains adjacent to the alloy due to the primary inward-growth mechanism and a preferred growth direction. (Bose, 2017).

1.9 High temperature oxidation of MCrAlY coating

The growth of the TGO during engine operation isn't just a casual occurrence—it's a fundamental event that dominates the coating's service life. The TGO's evolution, particularly the formation and expansion of the α-Al_2O_3 layer, directly leads to the depletion of aluminum in the bond coat. While this may seem like a routine chemical transition, the consequences are far-reaching. A substantial reduction in aluminum can results in the emergence of other, less desirable oxide phases. Elements like nickel and cobalt can combine to form spinel, and other

compounds like $Y_3Al_5O_{12}$ and Y_2O_3 may also materialize. Their presence can undermine the TGO's structural robustness. Moreover, these compounds can potentially accelerate oxidation processes, acting as highways for rapid oxygen diffusion. Such pathways can amplify localized oxidation, turning minor vulnerabilities into weak spots.

It's for these reasons that studying high-temperature oxidation is paramount. Understanding the dynamics of TGO growth and the subsequent oxide formations can be the key to enhancing TBCs' resilience, ensuring that they perform optimally under the service conditions of engine operation. In essence, the quest for durable TBCs is inextricably linked to mastering the intricacies of high-temperature oxidation (Padture et al., 2002).

1.9.1 Fundamentals of high-temperature oxidation

Understanding the thermodynamics and kinetics of oxidation is fundamental to evaluating the behavior of coatings under high-temperature exposure. Thermodynamics provides insight into the driving forces behind oxidation, such as temperature and oxygen partial pressure, which determines the formation and stability of oxide compounds. Kinetics, on the other hand, explains the rate and mechanism by which oxidation progresses, influencing the formation and growth of thermally grown oxides (TGOs).

High-temperature oxidation is an important process that depends on the interaction of multiple factors or condition. When specific conditions of temperature and oxygen partial pressure are satisfied, they act as driving forces propelling the oxidation reaction. The driving force for oxidation is rooted in thermodynamics, specifically the free energy of formation, also known as Gibbs free energy (eq. 1). The formation energy stems from the intrinsic thermodynamic properties of the oxide compound involved.

$$2\Delta G = RT.\ln P_{O_2} \qquad \text{(eq. 1.1)}$$

where: ΔG (free energy of formation), R (the gas constant), T (temperature), and P_{O_2} (oxygen partial pressure). The Ellingham-Richardson diagram (Bürgel, Bürgel, Maier, & Niendorf, 1998) provides a direct means of obtaining the temperature and necessary oxygen partial

pressure for the oxidation reaction shown in Figure 1.19. For instance, at 1000 °C the formation of Al_2O_3, and Cr_2O_3 scale demands oxygen partial pressures of approximately 10^{-36} bar and 10^{-22} bar respectively, correlating with increasing ΔG values in the same order. Higher ΔG° values signify enhanced thermodynamic stability for the oxides.

The rate at which the reaction occurs (reaction kinetics) is also important in understanding or determining the outcome of the oxidation process. Through experimentation, it has been established that different rate laws can be discerned. This relationship discovered by Tammann and later explained by Pilling, Bedworth, and Wagner (Pilling, 1923; Tammann, 1920; Wagner, 1933) is often used to describe the oxidation process:

$$\left(\frac{\Delta m}{A}\right)^2 = k_p.t \qquad \text{(eq. 1.2)}$$

where "m" is gained mass, "A" is sample area, "k_p" is the rate constant, and "t" is time.

However, specific conditions must be met for the parabolic law to be valid. In practical scenarios, oxide layers don't align with these ideal conditions, causing a modified equation with an exponent "n" different than 2 (Stott, 1992):

$$\left(\frac{\Delta m}{A}\right)^n = k_p.t \qquad \text{(eq. 1.3)}$$

n is an exponent (k and t as in the previous equation).

It has been demonstrated that the exponent 'n' in the above formula can equal 1, indicating linear oxidation. This linear oxidation is often attributed to factors such as the formation of non-protective oxides and breakaway oxidation (Nesbitt, 1983). The Pilling-Bedworth ratio (PBR) (Pilling, 1923), which compares the volume of the oxide to the volume of the metal, plays a critical role in these cases. When the oxide volume is smaller than the metal volume (PBR < 1), the oxide scale becomes porous, resulting in linear metal oxidation (n = 1). Additionally, non-protective oxides can form when the alloy lacks essential elements required to create a stable, protective oxide layer. This leads to the formation of unstable outer oxides, causing the oxidation kinetics to follow a linear (n = 1) pattern after an initial period of parabolic growth.

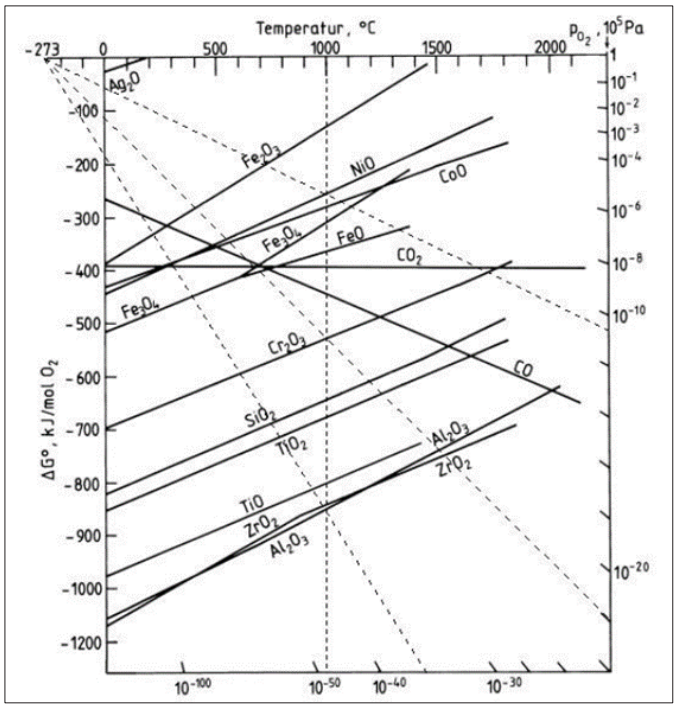

Figure 1.19 Diagram depicting the Ellingham-Richardson oxide formation taken from (Bürgel et al., 1998)

Breakaway oxidation involves stress-induced cracking or detachment of oxide. Stress can result from excess oxide volume (PBR > 1), oxide reaching a critical thickness, or thermal cycling. Cracked regions expose metal to gas, causing local oxidation. Some coating system under certain conditions conforms with both kinetics, initially parabolic law and then liner law such as repeated cracking and oxidation after period of parabolic oxide growth. Local oxidation adds stress, causing oxide spallation and potential sample weight loss (Nesbitt, 1983).

1.9.2 Oxidation process of MCrAlY coatings

The oxidation behavior of MCrAlY coatings is known to be influenced by various factors, including the chemical composition of the coatings (Naumenko, Pint, & Quadakkers, 2016), oxidation conditions (Brandl, Toma, Krüger, Grabke, & Matthäus, 1997; Nijdam, Jeurgens,

Chen, & Sloof, 2005; Toscano, Naumenko, Gil, Singheiser, & Quadakkers, 2008), and the coatings' microstructure. Additionally, studies have indicated that the surface roughness of MCrAlY coatings can affect the microstructure and composition of the TGOs (Gil et al., 2006).

When subjected to high temperatures, MCrAlY coatings stand out over a variety of high-temperature coatings for their exceptional ability to produce a dense scale from Al_2O_3 oxide (Hejrani et al., 2017). Consequently, temperatures exceeding 950 °C facilitate the development of a strong and protective alumina layer on the MCrAlY surface, effectively shielding components from extensive oxidation. During high-temperature exposure, various types of oxides can also grow atop the MCrAlY coating, with the specific oxides formed (e.g., Al_2O_3, NiO, CoO, Cr_2O_3, and spinel) contingent upon the composition of MCrAlY and the exposure temperature.

It is important to note that the condition of the surface significantly influences the rate of oxide growth in MCrAlY coatings. For instance, research has indicated that post-spray deposition treatments like grinding, and polishing can result in a higher oxidation rate when compared to the as-sprayed surface due to surface deformation mechanisms (Yuan, Peng, Li, Johansson, & Wang, 2015). Moreover, the inclusion of reactive elements in MCrAlY coating increases the potential to improve the adhesion of the oxide scale and provides the ability to modify the oxidation rate.

Furthermore, the deposition process itself exerts a substantial impact on the oxidation behavior of MCrAlY coatings. MCrAlY coatings deposited using the High-Velocity Oxygen Fuel method may exhibit enhanced resistance to oxidation and a slower rate of oxide growth at elevated temperatures in comparison to coatings produced through the Vacuum Plasma Spraying technique. This can be attributed to the presence of in situ Al_2O_3 oxide precipitates dispersed within the coating structure, which function as diffusion barriers (S. Zhou et al., 2014).

Oxidation during deposition process (as sprayed)

In this thesis, the conventional method of coating application on a substrate typically involves the utilization of thermal spraying techniques, particularly focusing on plasma or HVOF flame jet methods. The range of velocities and temperatures produced by DC-arc plasma and HVOF flame systems differs, thereby rendering each system suitable for specific applications. DC-arc systems generate plasma jets with high exit velocities and exceptionally high gas temperatures, whereas HVOF systems produce supersonic gas speeds and relatively lower, yet still elevated temperatures, contingent upon the particular fuel and oxidizer employed.

During the high velocity oxy fuel (HVOF) process, the ignition of fuel gas and oxygen produces a rapid jet flame, which then liquefies and propels the MCrAlY powder particles onto the substrate in the air condition. This powerful jetting force causes swift deformation of the particles and fast cooling, leading to their solidification and the creation of a coating. As a result, the HVOF-MCrAlY BC structure typically displays elevated oxide content and reduced density (H Chen et al., 2021; Farzin Ghadami, Sabour Rouh Aghdam, & Ghadami, 2021).

Compared to the HVOF process, MCrAlY powders used in the air plasma spray (APS) process are more susceptible to oxidation within the high-temperature flame flow, leading to higher oxide content in the resulting BCs. Furthermore, the low kinetic energy of the sprayed powders contributes to increased porosity in the BCs (Shibata et al., 2006). Borri et al. (Di Ferdinando et al., 2010) highlighted that this combination of elevated oxide content and porosity in APS BCs promotes the formation of mixed-oxide TGO layers on their surfaces..

Moreover, Meng et al. (Meng et al., 2019) found that the oxygen content in the as-deposited APS-MCrAlY BCs was three times higher than in the feedstock as shown in Figure 1.20, indicating a reaction with residual oxygen in the vacuum chamber. This formed an amorphous alumina film on the splat surface during deposition, as confirmed by Choi and Poza (Choi, Yoon, Kim, & Lee, 2002; Poza, Gómez-García, & Múnez, 2012). These oxides grew up by aluminum oxidation in feedstock during the deposition process (Meng et al., 2018a, 2018b).

Ultimately, the turbulent mixing of the spray jet with the surrounding atmosphere can significantly impact the oxide content of the coatings.

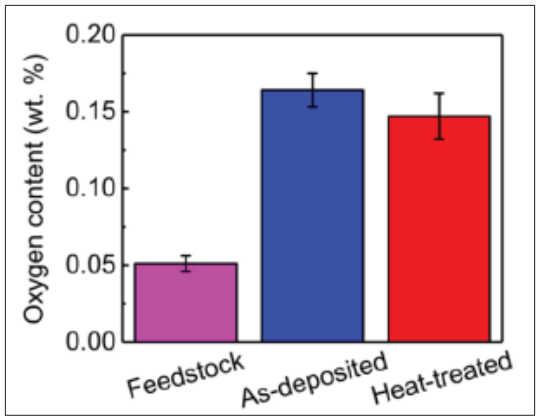

Figure 1.20 Illustrates the oxygen content in the APS-MCrAlY feedstock, as-deposited BCs, and heat-treated BCs
taken from (Meng et al., 2019)

Oxidation after heat treatments

Following coating deposition, the oxidation resistance of MCrAlY BCs can be further enhanced through post-treatment processes such as blasting, peening, and others (Naeimi, Rahimipour, & Salehi, 2016; Nijdam et al., 2005; Wellman et al., 2007; S. Zhou et al., 2016). However, these methods may introduce impurities or alter surface morphology. Among them, pre-heat-treatment is particularly effective in reducing porosity, ensuring uniform distribution of internal elements, and promoting the formation of a high-quality oxide scale, thus delaying BC failure. Importantly, pre-heat-treatment is cost-effective and easy to implement, making it a worthwhile option.

Meng et al. (Meng et al., 2018a) studied the effect of a controlled atmosphere pre-heat-treatment (10 h at 1100 ºC) on the microstructure of APS MCrAlY coating. Initially, the coating had numerous pores with continuous alumina films, hindering element diffusion and leading to mixed oxide formation as shown in Figure 1.21(a). After pre-treatment, the pores were healed, and the oxide scale broke into discontinuous particles, aiding rapid element

migration and suppressing mixed oxide formation during high-temperature oxidation as shown in Figure 1.21(b).

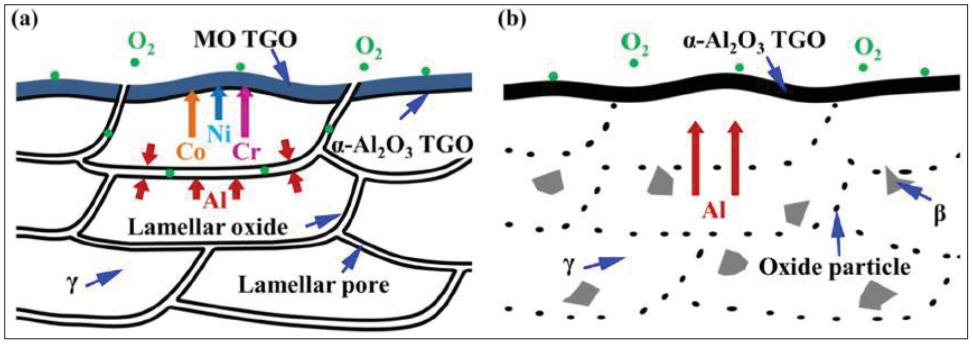

Figure 1.21 Microstructural changes in NiCoCrAlY BCs during isothermal oxidation depicted in schematic form: (a) untreated BC, and (b) heat-treated BC taken from (Meng et al., 2018a)

Ullah et al. (Ullah et al., 2020) applied arc ion plating to produce a NiCoCrAlY BC on a substrate. They then subjected this BC to a vacuum pre-heat-treatment at 1000 ºC for 4h. This treatment didn't change the BC's surface but healed its pores and improved coating density. this BC comprised a γ/γ′ matrix phase after depositing process (as deposited), but after treatment, the β-(Ni, Co)Al phase precipitated within the matrix.

Regarding surface effects, Saeidi et al. (Saeidi, Voisey, & McCartney, 2009) produced a MCrAlY BC using High velocity oxy fuel and HVOF methods, then subjected the BC to pre-treatment under low oxygen partial pressure at 1100 ºC for 3h. Following isothermal oxidation at 1100 ºC for 100h, the untreated BC surface exhibited a double-layer TGO, comprising an inner layer of alumina and an outer layer of mixed oxide. Conversely, the pre-treated BC surface displayed solely pure Al_2O_3 TGO.

In summary, BC pre-treatment focuses on evolving the initial oxide scale rather than forming a new one. This process significantly influences TGO growth behavior. To ensure superior BC performance and durability, careful attention to all preparation steps, including powder preparation, BC fabrication, and pre-treatment, is essential for optimal performance and durability.

In-service oxidation

In this section, the process of oxidation is divided into two primary categories: external oxidation, occurring on the coating's surface, and internal oxidation, which develops within the coating's structure.

Under high-temperature exposure, various oxides can form on the outer layer of the MCrAlY coating. The specific type of oxide, whether it's Al_2O_3, NiO, CoO, Cr_2O_3, or spinels (Y. Chen, Zhao, & Xiao, 2018; Richer et al., 2010; W. Sloof & T. Nijdam, 2009; Toma, Brandl, & Köster, 1999), can result in noticeable differences in oxidation kinetics, such as whether the growth of the oxide follows a parabolic or sub parabolic trend (Nijdam & Sloof, 2008; U Schulz, Menzebach, Leyens, & Yang, 2001). These differences may be attributed in part to variations in oxidation conditions, such as temperatures and oxygen partial pressures in the environment, as well as surface roughness (Gil et al., 2006; Toscano et al., 2008). Additionally, the composition of the coating, especially the presence of reactive elements like yttrium, could also play a role in these variations (Toscano et al., 2006).

The internal oxidation is commonly found in the BC layer of TBCs, especially those deposited through thermal spray processes. When exposed to high temperatures, internal oxides grow within the BC layer and can reach a significant proportion of the layer, leading to the depletion of aluminum and the formation of a TGO layer. However, the study by Patterson et al. suggests that the presence of internal oxides may extend the service life of TBCs during thermal cycling. This is because internal oxides can decrease the overall coefficient of thermal expansion of the BC layer, making it more similar to that of the topcoat layer. This reduces the thermal mismatch between the two layers, which is a common cause of TBC failure (Cen, Qin, & Yu, 2021).

Furthermore, referred to as Wang et al. (L Wang et al., 2014) used numerical calculations to demonstrate that the presence of internal oxides within the BC led to a reduction in stress levels in the TGO and a slower rate of crack propagation. These internal oxides were included in their finite element (FE) model and were assumed to have formed through static oxidation at high temperatures.

Formation of oxides causes a thin layer of TBC to form at the interface of the topcoat and BC in TBCs. This TGO layer grows dynamically and unevenly due to continuous precipitation, which significantly alters the interfacial morphology of BC/TC (T. Patterson, A. Leon, B. Jayaraj, J. Liu, & Y. Sohn, 2008; Richer et al., 2010). Additionally, internal oxides in the BC layer change the properties and microstructure of the BC layer. While several studies have focused on TGO layers and their stress concentrations that contribute to TBC failure (Aktaa, Sfar, & Munz, 2005; Jiang et al., 2017; V. Kumar & Balasubramanian, 2016; X. Li, Huang, Yang, & Tang, 2016), the swelling phenomenon caused by internal oxidation in the BC layer also significantly affects the residual stress and morphology of TBCs. Understanding the impact of internal oxides on the interfacial morphology (roughness)and stress state of TBCs can provide insight into the mechanisms behind TBC system failure (Zou et al., 2017).

However, studies (Thornton, Slater, & Almer, 2005; Zou et al., 2017) suggest that the presence of internal oxides with a high-volume fraction could have a negative effect on TBC service life. This is because the internal oxides can cause the BC layer to swell slightly and rumpling (Ahmadian & Jordan, 2014), leading to an increase in the interfacial roughness and residual stress (Jiang et al., 2017; L Wang et al., 2014).

1.9.3 The impact of high-temperature oxidation on MCrAlY coatings

This part of this thesis delves into the consequences of high-temperature oxidation on MCrAlY coatings, exploring their performance and stability under elevated temperature conditions. By analyzing the oxidation behaviour of these coatings, the part aims to uncover insights into their durability and protective capabilities in high-temperature environments.

Differences in k_p

The oxide scale in MCrAlY BCs, primarily composed of Al_2O_3, and potentially containing other phases and spinel TGO, depends on the oxidation process within the coating system (Lee, Kim, Choi, & Ahn, 2000; Tang, Ajdelsztajn, & Schoenung, 2004). Factors such as composition

(Brindley & Miller, 1990), deposition method (Saeidi et al., 2009), and oxygen content (C.-J. Li & Li, 2003) influence the growth of the TGO layer at the BC/topcoat interface. As discussed in Section 1.9.1, the k_p is a critical parameter for understanding the behavior of TGO layers in TBC systems. Nath et al. (Nath, Manna, & Majumdar, 2014) reported a growth rate constant k_p of (3.69 X 10^{-5} $\mu m^2/s$) for the TGO layer in YSZ TBC after oxidation at 1000 ºC. In contrast, Shi et al. (Shi et al., 2020) investigated TGO growth behavior within the MCrAlY-YSZ coating system and found a higher k_p of (4.03 X 10^{-5} $\mu m^2/s$) at the same temperature. This difference in oxide growth rate (k_p) could potentially be attributed to variations in the composition of the bond coating utilized in these studies.

Beyond the effect of composition, the coating method has also been shown to influence the oxidation rate. Several studies have explored the oxidation behavior of BCs and TGOs, with some findings suggesting that a NiCoCrAlY BC produced through HVOF exhibits slower oxidation compared to one produced using VPS (Brandl et al., 1997; Bürgel et al., 1998).

Besides the composition and coating method, the phase transformations of alumina oxides during oxidation also significantly impact oxidation behavior and coating stability of the TGO layer. The growth of alumina involves transitioning through metastable phases (γ-Al_2O_3, δ-Al_2O_3, and θ-Al_2O_3) before stabilizing as α-Al_2O_3 (corundum) (Wefers & Misra, 1987).. It has been demonstrated that γ-Al_2O_3, δ-Al_2O_3, and θ-Al_2O_3 phases form during the initial stages of oxidation, but the corundum structure (α-Al_2O_3) ultimately governs the overall kinetics (Pieraggi, 1987). Eventually, α-Al_2O_3 becomes the preferred phase due to its slower oxygen diffusion and reduced oxide growth rate (Brumm & Grabke, 1992; A. G. Evans et al., 2001).

Mixed oxides, particularly the spinel phase, are more detrimental to TBCs than Al_2O_3 due to their faster growth rate and increased porosity (Doleker, Ozgurluk, & Karaoglanli, 2018). Chen et al. (W. Chen, X. Wu, B. Marple, & P. Patnaik, 2005) discovered that mixed oxides like Cr_2O_3, Ni (Cr, Al)$_2O_4$, and NiO facilitate crack nucleation and growth, serving as pathways for oxygen ion diffusion and causing accelerated oxidation. These oxides also induce significant

volume expansion, leading to growth stresses that contribute to ceramic coating spalling (Saremi, Afrasiabi, & Kobayashi, 2008).

Intrinsic Chemical Failure (InCF)

The complex chemistry and thermodynamics of Intrinsic Chemical Failure (InCF) under oxidizing conditions were documented by Evans et al. (H. Evans, A. Donaldson, & T. Gilmour, 1999) studying the mechanisms of breakaway oxidation in chromia-forming steel. At its core, the oxidation of the reactive alloying element (chromium or Aluminum oxides) is determined by an equilibrium reaction that results in a shift in oxygen activity as the alloying element concentration changes at the oxide-metal interface. As the element continues to deplete from the system, there's an increased likelihood of reactions with other elements. This new reaction can result in the formation of oxide compounds, and the equilibrium of this process plays a role in determining the onset of InCF.

It has been shown that when the concentration of alloying elements at the oxide-metal interface falls below a critical threshold, the system becomes vulnerable to InCF. The dynamics of this process can be influenced by various factors, including the oxidation rate, effective diffusion coefficient, and interactions between the oxide layer and metal substrate. While certain equations and models can predict the depletion profiles, their accuracy depends on the actual concentrations reached during oxidation.

In the case of MCrAlY, the significant alloying element in InCF is the depletion of aluminum. The formation of a protective Al_2O_3 scale is a direct consequence of the aluminum present in the coating. As oxidation progresses, the aluminum concentration in the substrate near the TGO gradually decreases. Once this concentration falls below a critical threshold, the stability of the Al_2O_3 scale is compromised, increasing the risk of the protective layer peeling off.

A study by Texier et al. specifically investigated the Intrinsic Chemical Failure (InCF) mechanism in APS-processed NiCoCrAlY coatings at 1150 °C using ultrathin freestanding samples (16-240 μm) to accelerate the process. Their research, while related to the oxidation

behavior studied here, differed in that it focused solely on APS coatings and employed ultrathin freestanding samples (16-240 μm) specifically to accelerate the InCF process and establish it as a screening method. They confirmed that InCF occurred only after the complete consumption of the coating's aluminum reservoir. This failure resulted in the growth of a Cr_2O_3 layer beneath the original Al_2O_3 scale, accompanied by CrN precipitation at the new oxide/alloy interface. Interestingly, the overall mass gain did not accelerate significantly post-InCF, as the intact initial Al_2O_3 scale continued to limit diffusion rates, although mass loss was observed under airflow due to Cr_2O_3 volatilization. This work demonstrated that ultrathin samples provide a valuable method for rapidly screening and studying InCF mechanisms under isothermal conditions (Damien Texier et al., 2021).

Further insight into the stages following initial alumina scale failure (InCF) comes from studies on cast NiCoCrAlY alloys (defects free) using thin foils at 1150 °C by Gheno et al.. They observed a distinct sequence of oxide formation after the depletion of aluminum led to Al_2O_3 instability. First, a Cr_2O_3 layer formed at the alloy-scale interface. As chromium was consumed, this layer subsequently failed, leading to the formation of Ni- and Co-containing spinel oxides, which replaced the Cr_2O_3 at the alloy interface and converted the outer Al_2O_3 remnants. Finally, the remaining metallic Ni-Co alloy was converted to (Ni,Co)O. Significantly, this entire post-failure sequence occurred without a typical "breakaway" or sharp increase in oxidation rate, attributed to the diffusion-limiting effect of the remnant initial Al_2O_3 layer and the relatively small amount of metal remaining when fast-growing (Ni,Co)O began to form. This highlights that InCF does not always lead to immediate catastrophic oxidation if the initial scale maintains some structural integrity (Gheno, Rio, Ecochard, & Texier, 2021). Their research, although informative for understanding post-failure mechanisms, differed from the present work as it examined cast NiCoCrAlY alloys rather than sprayed coatings, utilized computational modeling, and specifically detailed the sequential oxidation stages following InCF.

Mechanically Induced Chemical Failure (MICF)

Mechanically Induced Chemical Failure (MICF) revolves around the intricate interactions between mechanical stress and chemical degradation. When the protective layer of a material experiences damage, such as spalling or cracking, it allows gases to penetrate and interact with the already depleted underlying alloy. This can lead to the rapid formation of less stable oxides beneath the surface, creating pit-like structures. Numerous studies have delved into this phenomenon, revealing the swift progression of the oxide front once the protective layer is compromised (H. Evans, 1995; H. Hindam & D. Whittle, 1982; Pollock, Laux, Brundidge, Suzuki, & He, 2011).

However, an interesting aspect to consider is the self-healing potential of the material. After such mechanical damage, the reformation of a protective oxide layer can occur once a specific local concentration of elements is reached. The critical concentration needed for this healing process is influenced by numerous factors: temperature, atmospheric composition, and the concentrations of other alloying elements.

It is essential to distinguish between this MICF process and traditional chemical failure. The latter often refers to the thermodynamic instability of protective layers. In the context of MICF, however, breakaway oxidation is a through section, non-protective oxidation. This can occur if the reactive alloying elements throughout the entire component fall below the critical concentration required for healing. This is especially true if the surface oxide layer subsequently experiences cracking or partial spalling (H. Evans et al., 1999).

Roughness and oxide formation

Czech et al. (Czech, Juez-Lorenzo, Kolarik, & Stamm, 1998) and Gil et al. (Gil et al., 2006) have conducted comparisons of the oxidation behaviors between MCrAlY coatings with rough surfaces and polished surfaces. Their findings revealed that on the rough coating surface, spinel such as $NiCr_2O_4$ and $CoCr_2O_4$, along with α-Al_2O_3 form, whereas only α-Al_2O_3 scale is observed on the polished coating surface. Furthermore, Gil et al. reported a correlation between

spinel formation and local surface curvature, with spinel developing in the convex regions of the coating surface (Gil et al., 2006).

The microstructure of the TGO is important in determining the BC's ability to withstand oxidation at elevated temperatures. With a composition solely comprising α-Al_2O_3, optimal service performance was found. Conversely, the presence of mixed oxides in TGO layer that growth on the BC surface detrimentally affects the service life of TBCs. Xu et al. (R. Xu et al., 2014) propose that mixed oxides can induce significant growth stress in the ceramic layer, hastening its cracking. Moreover, Maier et al. (Matsumoto et al., 2006) note that the growth rate on NiO exceeds that of α-Al_2O_3 by threefold, while (Ni, Co) (Cr, Al)$_2O_4$, a composite spinel-like oxide, typically undergoes rapid volume expansion, leading to a porous structure (Matsumoto et al., 2006).

Li et al. (Y. Li, Li, Zhang, et al., 2010) conducted thermal cycling experiments on TBC coatings consisting of YSZ topcoats and NiCoCrAlTa BCs with varying ratios of mixed oxides covering their surfaces. The results indicate that an increase in mixed oxide coverage correlates with heightened susceptibility of the ceramic layer to cracking, resulting in a notable reduction in the thermal cycling life of TBCs as shown in Figure 1.22. Thus, inhibiting mixed oxide formation and establishing a dense and continuous TGO layer composed of pure α-Al_2O_3 of specific thickness are crucial for enhancing the longevity of TBCs.

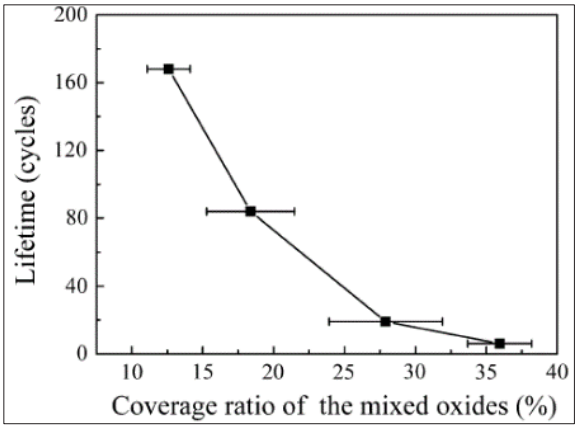

Figure 1.22 Illustrates the connection between the surface coverage of mixed oxides on the BC surface and the thermal cyclic service life following TBC failure
taken from (Y. Li, Li, Zhang, et al., 2010)

Combined effect of Cr_2O_3 and yttria

The oxidation behavior of NiCoCrAlY is dominated by the formation of Cr_2O_3, which acts as a protective layer that impedes the inward diffusion of harmful atoms, such as oxygen, into the coating.

The oxidation mechanism starts with the diffusion of chromium to the coating surface, where it reacts with atmospheric oxygen to form the Cr_2O_3 layer. This chromium-rich oxide layer is stable at elevated temperatures and maintains its protective properties over extended periods. The presence of yttrium further enhances the adhesion and cohesiveness of the Cr_2O_3 scale. Yttrium acts as a reactive element that segregates to oxide grain boundaries, thereby stabilizing the oxide layer and preventing spallation. The grain boundary segregation of yttrium ensures that Cr_2O_3 layer remains adherent and effective in its protective role, even after prolonged exposure to elevated temperatures (Gleeson, 2000; Reed, 2008).

The effect of TGO thickness on oxidation behavior

The thickness of the TGO layer is a crucial factor contributing to stress within TBCs, which can lead to cracking and failure (Ahrens, Vaßen, & Stöver, 2002; Dong et al., 2014; A. Evans, He, & Hutchinson, 2001; Padture et al., 2002; Rabiei & Evans, 2000; Yao et al., 2014). As the

TGO thickness increases during high-temperature operation, it induces significant growth stress in the adjacent ceramic layer, with greater thicknesses resulting in higher stress level (Y. Li, Li, Yang, & Xing, 2010). Once the TGO thickness surpasses a critical value, the ceramic layer begins to peel off, ultimately leading to failure (A. G. Evans et al., 2001; Rabiei & Evans, 2000).

The formation of a TGO layer can induce stresses through its lateral and normal growth mechanisms, as well as by causing mismatch stresses during thermal cycling (Rösler, Bäker, & Aufzug, 2004; F. Zhou, Wang, Wang, Cui, & Zhang, 2017). Sun et al. (J. Sun et al., 2015) investigated the thermal shock resistance of double-layer TBCs spanning temperatures from room temperature to 1200 °C revealing that as the number of thermal cycles increased, TGO thickness increased and the adhesion of the coating progressively decreased.

Torkashvand et al. (Torkashvand et al., 2018) explored how varying TGO thickness affects the service life of TBCs under thermal shock and cyclic loading conditions. They examined the relationship between TGO thickness and sample longevity. Their research revealed that TBCs with a TGO thickness between 2-3 μm exhibit enhanced resistance to thermal shock. Often researchers have noted that spallation at the interface between the TGO and topcoat can occur when the TGO scale exceeds a critical thickness of 10 μm (Lipkin & Clarke, 1996; Schlichting, Padture, Jordan, & Gell, 2003).

Dong et al. (Dong et al., 2014) studied how the thickness of TGO affects the thermal cyclic service life of TBCs. They applied a yttria-stabilized zirconia (YSZ) layer onto a NiCoCrAlTaY BC with varying initial TGO thicknesses, ranging from 1.3 μm to 7.7 μm. Following this, they subjected the TBCs to thermal cycling tests and revealed a noticeable decrease in the thermal cycle life of the TBCs as the initial TGO thickness increased, as illustrated in Figure 1.23.

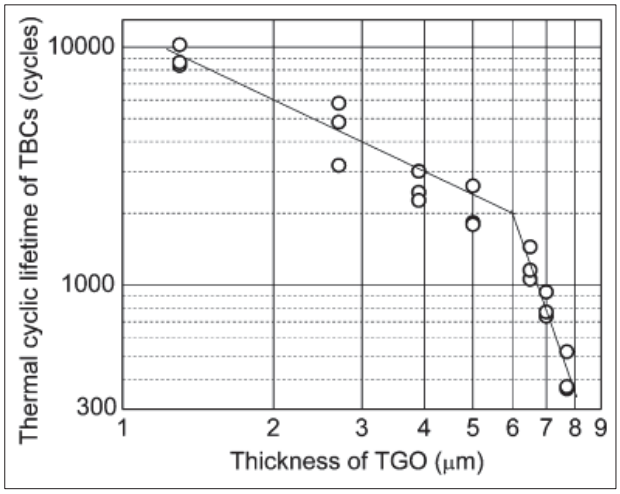

Figure 1.23 Illustrates the correlation between the thermal cyclic TBCs service life and the TGO thickness
taken from (Dong et al., 2014)

1.10 Summary

The literature review has provided a comprehensive overview of the existing research on TBCs, focusing on their composition, structure, and performance, as well as the critical processes involved in their application and degradation. The review explored the key layers of TBC systems, highlighting their individual roles and interdependencies. Additionally, common defects during coating deposition and their impact on performance were discussed in detail.

Significant attention was given to the oxidation behavior of MCrAlY coatings, with an emphasis on the mechanisms of high-temperature oxidation and its influence on TGO growth, phase transformations, and failure modes such as InCF and MICF.

This review identified the critical factors influencing TBC performance, providing a foundation for addressing current challenges in coating development and application. In the next chapter, the research objectives and proposed methodologies to advance the understanding of these systems will be detailed.

CHAPTER 2

MATERIALS AND METHODOLOGY

2.1 Introduction

This chapter presents the experimental methods and materials utilized in the present study of high-temperature oxidation of MCrAlY coatings, processed through Air Plasma Spray (APS) and High Velocity Oxy Fuel (HVOF) techniques. The fundamental objective of this chapter is to provide a comprehensive understanding of the experimental framework that underpins the research findings discussed in subsequent sections of the thesis.

The methodology outlined here is essential for investigating the degradation mechanisms of the coatings under simulated operational conditions, crucial for extending the service life of turbine components. Specifically, this chapter details the preparation and characterization of the coating materials, the experimental setup for oxidation testing, and the analytical techniques employed to assess the structural integrity and performance degradation of the coatings. Through this systematic exploration, the thesis aims to highlight the critical factors influencing the oxidation resistance and service life of these advanced material systems.

2.2 Sample preparation

2.2.1 Substrate materials

Instead of a nickel-based superalloy, 304 stainless steel plates with dimensions of 2 × 50 × 250 mm^3 was utilized as substrates. The most significant difference lies in their thermal expansion properties; however, their thermal expansion coefficient values are relatively similar (17.5 x 10^{-6}/°C for st.st. And 12.5 x 10^{-6}/°C for superalloys). These similarities were crucial as they allow the substrates to adequately support the coatings under investigation without influencing their intrinsic properties. The thickness of these coatings ensures that the substrate influence on the thermal and mechanical properties of the coatings is negligible. The selection of 304

st.st. allowed the research to focus exclusively on the behavior of the coatings themselves under high-temperature conditions.

2.2.2 Coating materials

The coatings investigated in this study are made from NiCoCrAlY alloy powder, specifically the NI-191-4 type. This powder is chosen for its high resistance to oxidation and corrosion at elevated temperatures, essential for applications such as turbine blades in gas turbines. Assuming typical characteristics for NI-191-4, the powder comprises a balanced composition of Nickel (Ni), Cobalt (Co), Chromium (Cr), and Aluminum (Al), with Yttrium (Y) added to enhance the oxide scale adhesion and stability.
Material Specifications:

- **Average particle size**: Approximately 45 ± 10 μm, suitable for thermal spray processes which require precise control over particle velocity and melting.

- **Chemical composition**: A rich matrix of Ni and Co, enhanced by Cr and Al for high-temperature capabilities, and a small but critical amount of Y to optimize high-temperature oxidation resistance. The powder chemical composition is given in Table 3.1.

- **Density and melting point**: The alloy's density and melting point are assumed to align with typical NiCoCrAlY alloys, which are crucial for predicting the deposition behavior and the final coating's structural integrity.

These characteristics ensure that the coatings can form a dense and adherent protective layer on substrates, crucial for their performance in harsh environments. The selection of NI-191-4 aims to leverage these properties to study the effects of different deposition techniques on the microstructural integrity and protective qualities of the coatings under high thermal stresses.

2.2.3 Deposition techniques

This research utilizes two advanced coating deposition techniques: Air Plasma Spray (APS) and High Velocity Oxy Fuel (HVOF). Both methods are well suited for applying the NiCoCrAlY coatings on stainless steel substrates but differ significantly in their operational parameters and the microstructural characteristics they impart to the coatings.

For this study, the use of both techniques allows a comparative analysis of how different spray parameters and resultant microstructures affect the high-temperature oxidation behavior of NiCoCrAlY coatings. This approach provides a broader understanding of the potential performance benefits of each technique under similar operational conditions, facilitating a more comprehensive evaluation of their suitability for protective applications in high-temperature environments.

HVOF

HVOF uses a mixture of oxygen and fuel to generate a high-velocity combustion flame into which the powder is injected. Typical parameters include a fuel-to-oxygen ratio of 1:1.2, with a total flow rate of 900-1000 SCFH and combustion pressures about 0.7-1.0 MPa. The particle velocities achieved are significantly higher than in APS, typically around 800-1000 m/s, which results in coatings that are denser and have lower porosity compared to APS. Figure 2.1 shows the HVOF gun used in this study.

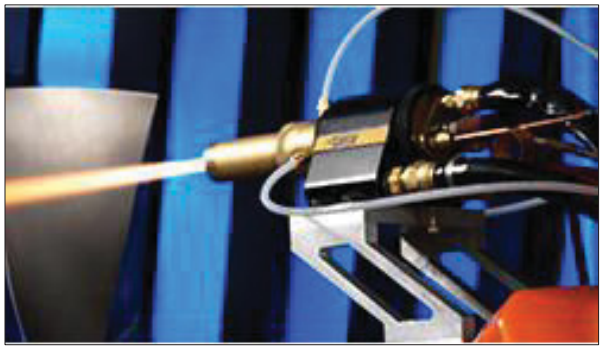

Figure 2.1 HVOF Gun TAFA Model 8300 HP (Praxair Co.)

APS

APS involves the melting of powdered material in a plasma jet, which then propels the molten particles onto the substrate (Figure 2.2). Typical parameters (assumed for this thesis) include a plasma gas flow rate of approximately 45-55 SCFH (Standard Cubic Feet per Hour), with a carrier gas flow rate around 5 SCFH, and a power input ranging from 40-50 kW. The spray distance is generally set between 100-150 mm, which facilitates the formation of coatings with moderate porosity and relatively high oxide content, suitable for high-temperature oxidation resistance.

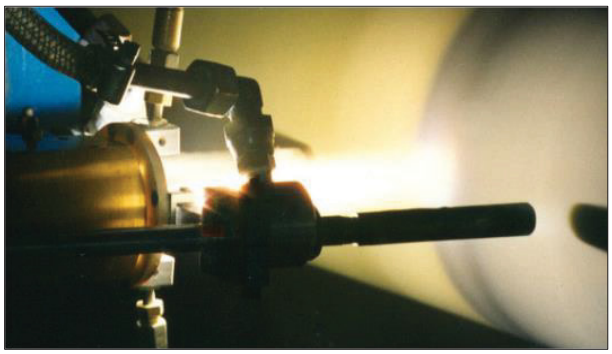

Figure 2.2 Plasma spray system with High-powered Plazjet II (Praxair Co.)

Samples received from the Praxair

Materials sourced from Praxair include stainless steel rectangular plates coated with NiCoCrAlY via two deposition methods (HVOF and APS) in as-sprayed condition 200x50 mm^2. Plate thickness differed by process; the HVOF coated sample measured 1 mm (without the substrate thickness), while APS and VPS coated samples were 600 mm thick (without the substrate thickness). The plates surface exhibited either a flat or tensile sample shape as shown in Figure 2.3.

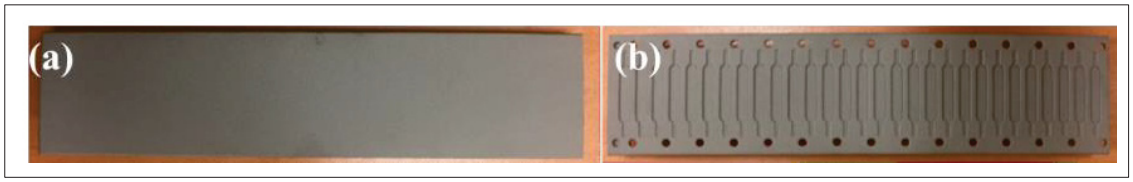

Figure 2.3 a) HVOF flat plate specimen (FP) b) HVOF tensile sample specimen (TP)

Preparation of free-standing coating sample (FCS)

Working with micrometre-thin samples presents considerable challenges and constitutes a pioneering facet of this thesis's experimental approach. The central objective was to create ultra-thin specimens with uniform thickness.

A range of techniques were employed to fabricate free-standing coating samples, with variations noted depending on the deposition method (high-velocity oxy-fuel or plasma spray), sample geometry (flat rectangular or ribbon-shaped), and the specified thickness, which, in some instances, was below 15µm.

Cutting the plate samples to shape

Each plate sample was cut using a precision cutter machine equipped with a silicon carbide cut-off wheel (HV 70-400) with dimensions of 150 mm in diameter, 0.5 mm in thickness, and a 12.7 mm bore size. The machine operated at a rotation speed of 3000 rpm and a feed speed of 0.045 mm/s to ensure precise and clean cuts.

For the rectangular samples, as illustrated in Figure 2.4, the plate was cut into dimensions of 8 mm by 10 mm. This precise cutting ensured that each sample-maintained uniformity for subsequent testing and analysis.

In the case of the tensile-shaped samples, the plate was initially cut into a rectangular shape larger than the final desired dimensions to facilitate handling and further processing. The initial rectangular cuts were larger than the overall length and width of the tensile-shaped samples, which were 5 mm by 35 mm, as shown in Figure 2.5. This approach allowed for precise final

shaping of the tensile samples, ensuring that they met the required specifications for mechanical testing.

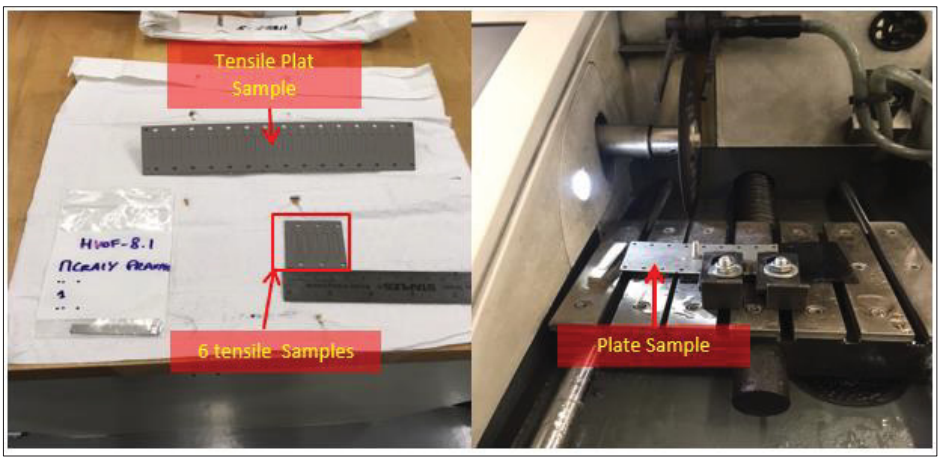

Figure 2.4 Cutting the plat using Precision cutter machine

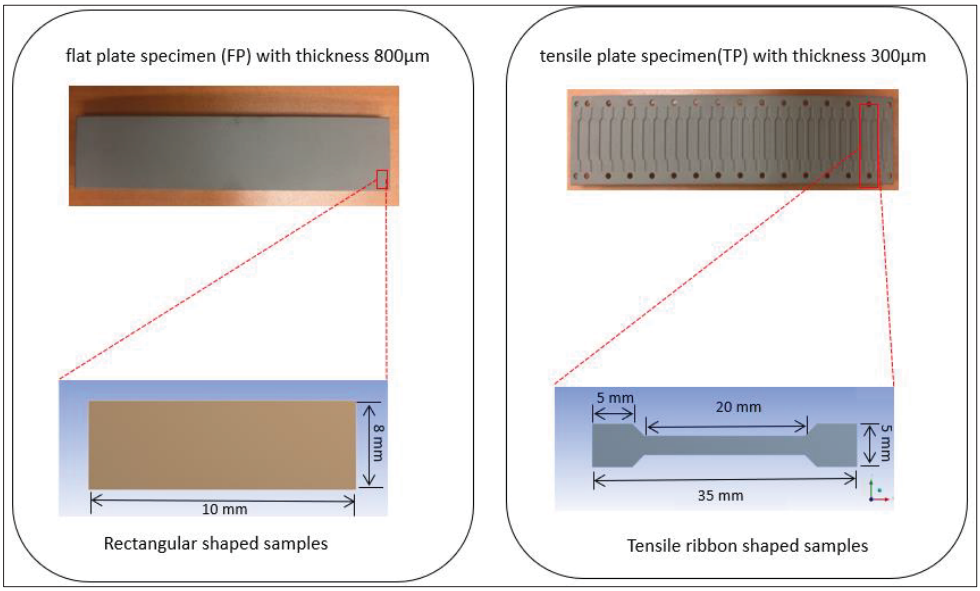

Figure 2.5 Micro samples cut from plate

Removing the substrate from coatings

Two methods were employed to separate the substrate from the coating, with the choice of method depending on the bonding strength between the substrate and the coating layer. By employing these two distinct methods, researchers can effectively separate substrates from

coatings regardless of the bond strength, facilitating further study and characterization of the coating layers.

Extracting the substrate from coating

This technique is suitable for cases where the bonding strength between the substrate and the coating is relatively weak. This phenomenon has been observed in samples deposited by air plasma spray (APS) but has not occurred in samples deposited by high-velocity oxygen fuel (HVOF) spray. The substrate was manually peeled away from the APS coating layer using a precision tool, the result was a coating 600 µm thick as shown in Figure 2.6. This method requires careful handling to avoid damaging the coating layer, ensuring that it remains intact for further analysis or testing. Manual extraction is typically faster and less labor-intensive than mechanical methods, provided the bond is not too strong.

Figure 2.6 APS-coating plat after separation of the substrate

Grinding the substrate

The grading was used in case of coating that has high bonding strength with substrate such as high velocity oxy-fuel coatings were adherent even for coating thicknesses of 1 mm. The stainless steel substrate (SS) was mechanically ground to roughly remove the whole substrate thickness. Several steps were used in this section to obtain samples without the substrate (FSCS).

- **First**: in order to save time, the automatic polishing Machin (Struers) and SiC P120 grate paper was used. Cylindrical holders of samples were made of Aluminum with dimensions of 30 mm length and 15 mm radius to fit the holder samples in a polishing

machine as shown in Figure 2.7. This step is limited to removing several micrometres of substrate because it was difficult for thickness control and polishing pressure, therefore the manual polishing jig was used for the rest of the substrate thickness.

- **Second**: stick the sample on the holder of the manual jig by heating the holder to temperature that does not affect on the microstructure of the coatings to about 70 °C not more. And then put the glue on the heated holder then fix the samples on the holder and leave until the holder get cold. Fixing the manual jig on the SiC P120 grate paper in the polishing machine and starting the grinding process as shown in Figure 2.7.

Figure 2.7 Using a Manual polishing jig on polishing machine

- **Third**: remove the most of the substrate thickness using the abrasive paper on the manual polishing machine with manual Jig. 4 to 6 samples fixed on the holder and grinding at the same time in this step. With appropriate speed of the polishing machine and using the pressure hand on the manual jig and changing the abrasive paper continually (5-10 minutes), the thickness reduces gradually till the last several micrometers of substrate (about 20µm) which still bonded with the coating reach the back coating surface.

- **Fourth**: the final stage involves substrate grinding to remove the last micrometres of the substrate and achieve the desired thickness for the coatings. To prevent sample damage, the disc grinder (GATAN 623), depicted in Figure 2.8, was utilized at this grinding stage, employing abrasive SiC P220 grade paper. This step is crucial for attaining precise control over sample thickness, ensuring uniform thinness with an accuracy of 5 µm.

Figure 2.8 The Disc Grinder 623

2.2.4 Thinning and polishing the samples

This step follows the removal of the entire substrate from the coating resulting in a free-standing coating sample (FSCS). It becomes necessary when the desired thickness has not been achieved, particularly for thin coatings that are challenging to obtain using manual polishing techniques with a Jig or disc grinder (less than 500 µm thick). In this thesis, the thinning and polishing process of the samples adhered to the protocol outlined in (D Texier, 2013; D. Texier, Monceau, Salabura, Mainguy, & Andrieu, 2016).

Reducing the thickness of the samples is essential to ensure the reliability of subsequent experimental procedures. To achieve this, a custom-built precision jig paired with a

BUEHLER© grinding/polishing machine employed as shown in Figure 2.9. The rotation speed of the machine was adjustable, ranging from 40 to 120 rpm, allowing for precise control during the diminishing process. This jig enables mechanical grinding without inducing significant residual stresses, ensuring the integrity of the samples. The samples are secured onto glass supports using Crystalbond 509 adhesive.

Usually more than one sample was processed simultaneously, to enhance efficiency and consistency in the diminishing process and maintain stability.

Before bonding, each sample undergoes measurement at several points along its length using a digital caliper to assess thickness deviation. The diminishing process involves using SiC papers of varying grades, with finer grains employed (from P120 up to P1200 grade) to minimize residual stresses.

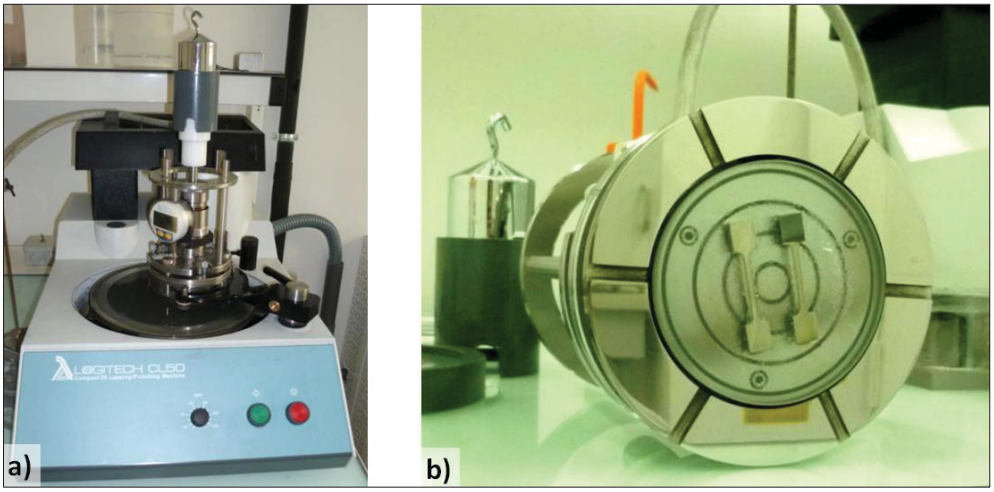

Figure 2.9 The diminishing the samples using precision polishing jig on polishing machine taken from (D Texier, 2013)

The diminishing process occurs in two stages: material removal and finishing. Initially, the load applied to the samples is adjusted to achieve a grinding rate of 1.67 μm/min until reaching a distance of 100 μm from the target thickness. Subsequently, the polishing machine rotates at 80 rpm, and the load is reduced by half to decrease the grinding rate.

To achieve parallelism between the coating and substrate surfaces, a 400 μm grinding or more is performed on the substrate side. Subsequently, the rough surface of the coating is polished on a P4000 grade paper without any load to eliminate 10-12 μm of significant coating roughness. Finally, the remaining substrate is removed to attain a coating thickness of under 40 μm.

The final stage of polishing the samples involved using SiC papers start from P1500 up to P4000 with minimal polishing load and speed to achieve a grinding rate of 0.34 μm/min. Manual finishing is then performed by applying 3 μm and then 1 μm diamond paste on a polishing cloth, ensuring a surface roughness is low enough (Ra = 0.005μm) which is both sufficient and consistent.

2.2.5 Cleaning the samples

To eliminate any residual glue and other contaminants that may adhere to the surface during sample fixation onto holders and polishing procedures, thorough cleaning of the samples is imperative to uphold the integrity of subsequent tests. The samples undergo multiple cleaning cycles with ethanol followed by drying. Subsequently, sample detachment is achieved through heating at 170 °C. A 15-minute treatment in an ultrasonic bath with an acetone solution facilitates the dissolution of residual glue. This process is succeeded by a final cleaning with ethanol.

2.2.6 Weighting the samples

The masses of the samples were meticulously measured using a high-precision balance, specifically the Sartorius MC5 model, which boasts an impressive precision of $\pm 1.0 \times 10^{-6}$ grams. This high level of accuracy ensures that even the smallest changes in mass can be detected, which is critical for precise experimental results. Each sample was weighed three times both before and after specified oxidation periods. This repeated weighing process helps to ensure the reliability and consistency of the measurements by accounting for any potential minor variations or errors.

The multiple measurements taken before and after the oxidation periods allow for a detailed and accurate quantification of the mass gain, denoted as $\Delta m(t)/S$. This parameter represents the change in mass per unit surface area of the sample over time, providing crucial data for understanding the oxidation behavior of the material. By conducting these repeated measurements with such a precise instrument, the study can achieve a high degree of accuracy in monitoring the oxidation process, thereby yielding valuable insights into the material's performance and stability under oxidizing conditions. This methodical approach to sample mass measurement underscores the importance of precision and consistency in experimental procedures, particularly when dealing with minute changes that can have significant implications for the study's findings.

2.2.7 High temperature oxidation

As received heat treatment

The FSCS (Full Scale Coated Specimens) underwent a heat treatment process to simulate the typical post-deposition heat treatments applied in industrial settings. Initially, the specimens were heat-treated at 1080 °C for 8h, followed by a second heat treatment at 870 °C for 20h. These specific temperatures and durations were chosen to replicate the conditions used to enhance the adhesion of the coating to the substrate through interdiffusion. This interdiffusion process is crucial as it helps in optimizing the mechanical properties of Ni-based superalloy substrates, which are commonly used in high-performance applications due to their excellent mechanical strength and resistance to thermal degradation.

In this context, although the specific conditions of heat treatment were not strictly necessary for the FSCS, the standard heat-treatment protocol was nonetheless carried out. The primary objective was to generate coating microstructures that accurately represent those found in service conditions. This step ensures that the experimental results and observations are relevant and applicable to real-world applications. The heat treatment not only improves coating adhesion but also mimics the operational environment, thereby providing insights into the long-term performance and reliability of the coated specimens under typical service conditions.

By adopting this standardized heat-treatment procedure, the study aims to produce results that are both reliable and comparable to industry standards.

Isothermal oxidation test

To simulate in-service conditions, as-sprayed HVOF free-standing coatings were subjected to isothermal oxidation at 1050 °C in air for various durations: 10, 30, 72, 120, and 240h.

The samples, each measuring 10×10 mm^2, were placed on insulating firebricks with their rough surfaces facing up. They were then carefully inserted into a muffle furnace preheated to 1050 °C. This furnace was equipped with a Type K thermocouple connected to a Graphtec mini-LOGGER GL900, ensuring accurate and reliable temperature measurements. These precise measurements were crucial for controlling and monitoring the experimental conditions during the exposure period.

Throughout the oxidation process, all necessary safety protocols were strictly followed. After the designated oxidation time, the samples were carefully removed from the furnace while still at high temperature and allowed to cool in laboratory air to room temperature (25 °C), as illustrated in Figure 2.10.

Interrupted oxidation test

Oxidation experiments were conducted at 1150 °C using interrupted furnace tests in a Nabertherm N 11/H furnace, performed in laboratory air without forced convection, for a cumulative duration of up to 500h. The study included two types of samples: HVOF-NiCoCrAlY coatings and APS-NiCoCrAlY coatings, each with varying thicknesses (started from tens of micrometres up to 367 μm). For each thickness condition, one sample was used to ensure detailed and specific observations.

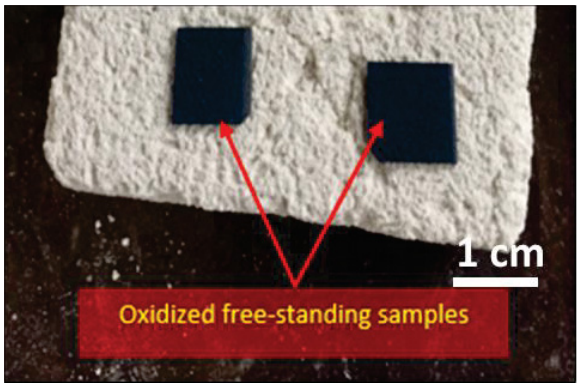

Figure 2.10 HVOF free-standing samples after isothermal oxidation at 1050 ºC, cooling in laboratory air at room temperature

During the oxidation tests, the samples were vertically suspended on alumina supports using platinum wire holders. This setup was designed to simulate service conditions while allowing for precise monitoring of oxidation behavior. Periodic interruptions were scheduled to observe local changes in the oxidation process, such as Al2O3 failure and oxide spallation, providing insights into the durability and integrity of the coatings under high-temperature conditions. The samples were weighed and examined using optical microscopy (OM) at various intervals: after 5, 10, 15, 20, 50, 100, 150, 250, 350, and 500 cumulative hours. These regular intervals allowed for a comprehensive analysis of the oxidation process over time. The primary focus of the optical observations was to detect and document instances of Al_2O_3 failure, characterized by the emergence of new oxidation products either on the surface of the external oxide scale or at the α-Al_2O_3/alloy interface. The semi-transparency of the α- Al_2O_3 scale in the visible spectrum facilitated these observations, enabling the identification of underlying changes in the oxide layer.

The data collected from these tests provided valuable information on the oxidation resistance and failure mechanisms of both HVOF and APS coatings. By comparing the performance of coatings with different thicknesses, the study aimed to identify the optimal coating parameters for enhanced durability and longevity in high-temperature environments.

Cross-sectional sample preparation

- **Nickel plating**

To protect the accumulated oxide scale from spallation during the cutting and polishing processes, a layer of nickel was deposited on both surfaces of the samples using an electroplating process. The electrolyte solution used was a Watts bath, which facilitated the plating of nickel from a nickel anode. The procedure followed was as outlined below:

- First, the surface area of the sample to be nickel-plated was determined to ensure accurate plating parameters. The sample was then immersed in hydrochloric acid (HCl) for 30 seconds to thoroughly clean the surface and remove any contaminants. Next, a voltage of 0.89 V was applied to the electrodes, with the current adjusted and maintained to keep the voltage steady at 0.89 V throughout the process. The electroplating process was conducted for 1 hour, resulting in a 50 μm thick nickel deposit on the sample surfaces (Figure 2.11).

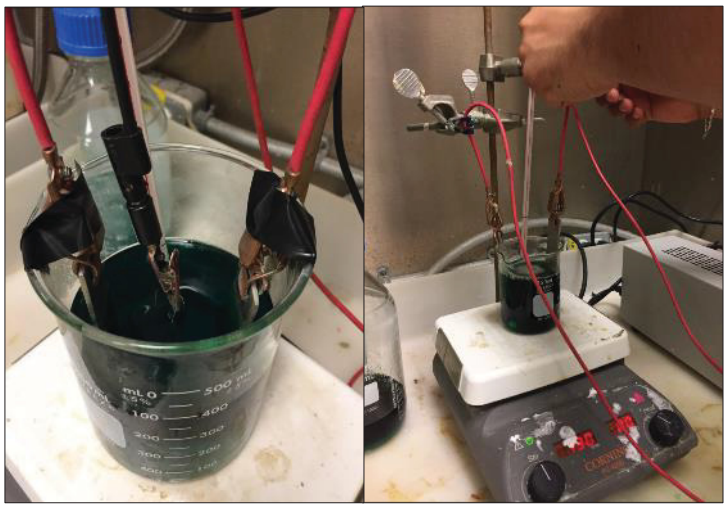

Figure 2.11 Nickel plating process

- **Mounting the samples**

Cold mounting was employed to prevent any temperature-related alterations to the sample surface. This technique ensures that the integrity of the sample is maintained by avoiding

exposure to high temperatures that could affect its microstructure or mechanical properties. The samples were embedded in a cold mounting resin, which cures at room temperature and provides a stable medium for handling and analysis.

The dimensions of the mounted samples were carefully chosen to facilitate ease of manipulation and subsequent analysis. Each mounted sample had a diameter of 30 mm and a thickness of 15 mm.

- **Cutting the mounted sample and polishing the cross-sectional surface**

The process of cutting the mounted sample involved a two-step approach to ensure precision and maintain the integrity of the sample, as shown in Figure 2.13. Initially, a carbon steel hacksaw was employed to remove the bulk of the copper mounting. This manual cutting step allowed for rough segmentation and prepared the mounted sample for more precise cutting.

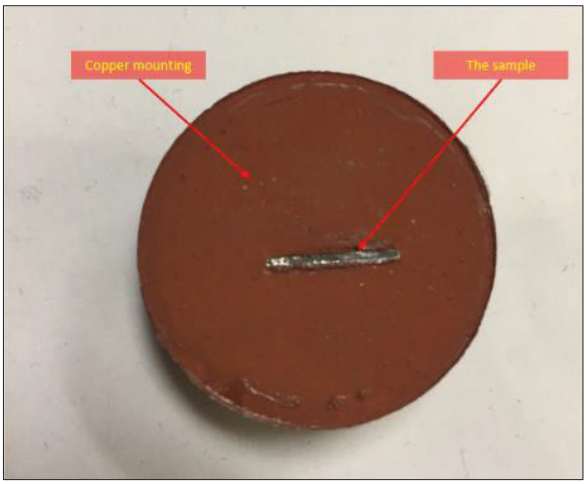

Figure 2.12 The copper mounting of samples for SEM analysis

Once the initial cut had been made, the sample was transferred to an automatic cutter for more accurate sectioning. The automatic cutter was equipped with a silicon carbide cut-off wheel, specifically the HV 70-400 type, with dimensions of 150 mm in diameter, 0.5 mm in thickness, and a bore size of 12.7 mm. This type of cut-off wheel was chosen for its durability and ability to produce clean, precise cuts through various materials, including metals and composites.

The automatic cutter operated at a high rotation speed of 3000 rpm, which, in combination with the sharp silicon carbide wheel, ensured efficient cutting with minimal thermal damage to the sample. The feed speed was carefully controlled at 0.045 mm/s, providing a steady and consistent cutting rate. This controlled feed speed was critical for avoiding excessive force that could potentially damage the sample or cause irregularities in the cut surface.

The final step in the preparation of the cross-sectional surface involved a meticulous polishing process to achieve a smooth and defect-free finish suitable for detailed microscopic examination. It began with SiC P600 grit waterproof paper. This coarse grit was used to remove any major surface irregularities and to level the surface of the cross-section. The process then gradually progressed through finer grits: P800, P1200, P2200, and finally P4000. Each successive grit removed the scratches left by the previous grit, resulting in a progressively smoother surface.

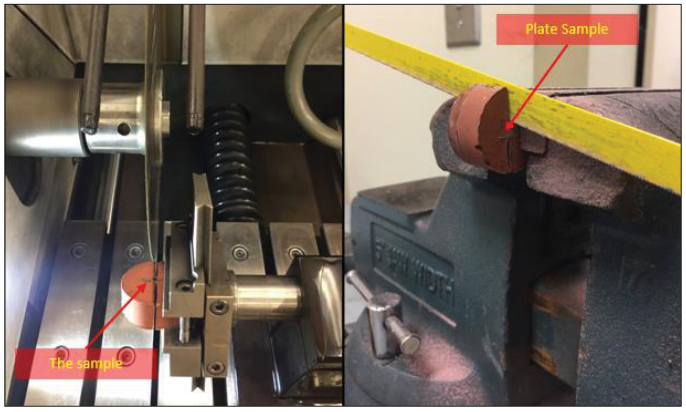

Figure 2.13 Cutting the cross-section samples manually and using automatic precision cutter.

After reaching the finest SiC grit, the surface was further refined using diamond paste. The polishing started with a 3 µm diamond paste, which helped to remove any remaining minor scratches and provided a more uniform surface. This was followed by 1 µm diamond paste for an even finer polish. This step ensured that the surface achieved a near-mirror finish, which was essential for high-quality cross-sectional observations.

The sample was thoroughly cleaned between each polishing stage to remove any abrasive particles that could cause scratches in the next step. Distilled water and an ultrasonic cleaner were used to ensure all residues were removed.

2.2.8 Characterization techniques

Microscopic analysis

Surface and cross-sectional observations of the oxidized samples were precisely conducted using two key microscopy techniques. Optical Microscopy (OM) was employed to perform a general examination of the surface integrity and the development of oxidation products. In addition, Scanning Electron Microscopy (SEM) in Backscattered Electron (BSE) mode was utilized for a more detailed analysis. This included using a Nova NanoSEM 450 field-emission gun SEM (FEG-SEM) from Thermo Fischer Scientific and a JSM 7800F Prime FEG-SEM from JEOL for in-depth cross-sectional observations.

Laser Scanning Confocal Microscopy (Olympus LEXT OLS5100) was also used to quantitatively document oxide intrusion in the materials, employing automatic stitching in laser intensity mode for comprehensive coverage and high-resolution imaging of large areas. Image segmentation was performed with Fiji [49] to differentiate between oxide intrusions and the remaining metal matrix.

Advanced imaging and analysis

To further characterize the coatings, CT-scans were employed on samples that had undergone 500h of oxidation. This method provided a three-dimensional quantification of oxide intrusion within the coatings. Two sample slabs from APS and HVOF coatings, respectively, were scanned using a v tome xs 240 scanner from GE, equipped with a DXR250 detector. The scans were conducted under specific parameters (numerical resolution of 1.75 µm/voxel, 100 kV voltage, 180 µA intensity, and a 1-second exposure time), and processed using the Phoenix datos-x reconstruction 2 software. Subsequent analysis involved Dragonfly 2021.3 [50], where

images were segmented using the Otsu algorithm, allowing for a precise assessment of the spatial distribution and concentration of intruded oxides.

Micro-tensile testing with DIC

Digital Image Correlation (DIC) is a non-contact, full-field displacement, and strain measurement method that is particularly effective in characterizing the mechanical behavior of materials subjected to loading, such as during tensile testing. DIC works by tracking the displacement of subsets or features within an image. The process begins with considering a speckle pattern on the surface of the material being tested. The speckle pattern serves as a virtual extensometer. The pattern is created such that each point on the sample's surface has a unique pattern subset. This pattern is then photographed under the initial, undeformed condition. As the material deforms under load, photographs of the speckle pattern are taken at regular intervals or at the end. The DIC software then compares these deformed images to the initial image, identifying the movement of each subset of the speckle pattern. By tracking these movements, the DIC software can calculate the full-field displacements and strains. The DIC software typically uses mathematical algorithms, such as cross-correlation and least-squares methods, to perform these calculations. It first divides the initial image into small subsets and attempts to find the same subset in the subsequent image. By comparing the displacement of each subset from the initial to the deformed image, it calculates the deformation gradient tensor, which can then be used to compute the strains in the material. The advantage of DIC over traditional strain gauges is that it provides a full-field view of strain, allowing for the observation of local variations in a strain that may be missed by point measurements. (Pan, Qian, Xie, & Asundi, 2009; Sutton, Orteu, & Schreier, 2009).

In terms of temperature dependence, the tensile strength of MCrAlY coatings usually decreases with increasing temperature. At elevated temperatures, the coatings may undergo phase transformations and grain boundary sliding, leading to a reduction in tensile strength. The exact temperature at which this occurs can depend on the specific composition of the coating (Damien Texier, Cadet, Straub, Eberl, & Maurel, 2020).

The elongation to failure of MCrAlY coatings can also be significantly lower than that of the substrate material, again due to the microstructural defects and the brittleness of the coating. However, in service, the coatings operate under compressive stresses due to thermal expansion mismatch with topcoat, reducing the significance of the low tensile properties (Alam et al., 2017; He, 2022; International, 2016).

Micro-tensile tests were conducted on the samples and recorded using the digital image correlation (DIC) technique. Surface features were utilized to calculate strain effects by comparing images taken before and after the strain application. The images used for DIC measurements were captured with a camera from Allied Vision Technologies (Figure 2.14). This setup enabled the analysis of the deformation process using a two-dimensional (2D) DIC technique (W.-M. Chen et al., 2016; Z. Chen et al., 2022). Furthermore, it is important to highlight that the dependability of the DIC setup was evaluated using a protocol outlined in a recent study. (Vanderesse, Richter, Nuno, & Bocher, 2018).

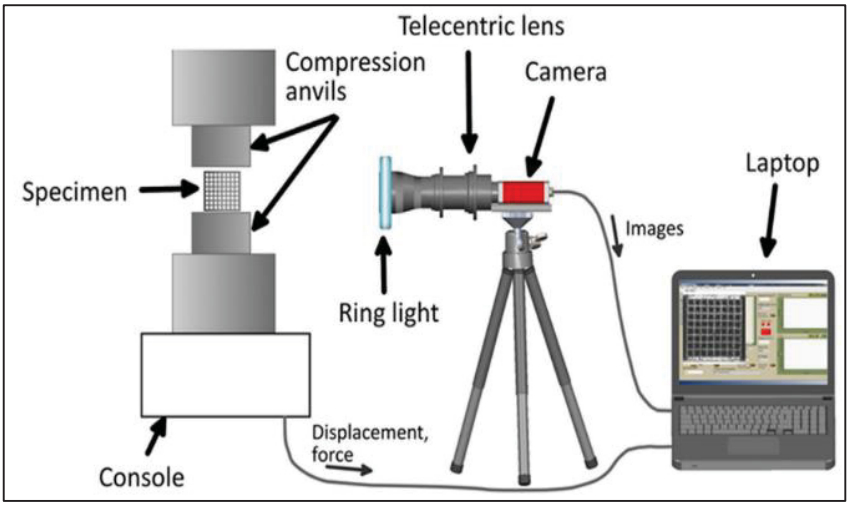

Figure 2.14 DIC setup to record images from cubic mesostructured taken from (Vanderesse et al., 2018).

After completing the tests, the digital image correlation software OpenDIC was used to process the BMP images. This software was developed at LOPFA, École de Technologie Supérieure, Montréal (Vanderesse, Lagacé, Bridier, & Bocher, 2013). In addition to the BMP images,

specific post-processing parameters were required for accurate analysis. The subset size and spacing parameters were set to 19 and 11 pixels, respectively. The output files from OpenDIC, including CSV files and log files, were then analyzed using Fiji software. This process generated strain fields, displacement fields, and quality index files, which were used to investigate strain distribution across the samples by examining the strain maps.

CHAPTER 3

ARTICLE: SIZE EFFECTS ON HIGH TEMPERATURE OXIDATION OF MCRALY COATINGS PROCESSED VIA APS AND HVOF DEPOSITIONS

Ali Kalush [a], Damien Texier [b], Maxime Ecochard [b], Quentin Sirvin [b], Karim Choquet [b], Thomas Gheno [c], Nicolas Vanderesse [d], Walid Joma [a], Philippe Bocher [a]

[a] Mechanical Engineering Department, École de Technologie Supérieure (ETS), 1100 Rue Notre-Dame Ouest, H3C 1K3 Montreal, Quebec, Canada
[b] Institut Clement Ader (ICA) - UMR CNRS 5312, Université de Toulouse, CNRS, INSA, UPS, Mines Albi, ISAE-SUPAERO, Campus Jarlard, 81013 Albi Cedex 09, France
[c] DMAS, ONERA, Université Paris Saclay, 92322 Chatillon, France
[d] PACEA - UMR CNRS 5199, Université de Bordeaux, 33615 Pessac Cedex, France

Paper published in *Surface & Coatings Technology*, April 2022

Abstract

The paper demonstrates how defects inherited from the deposition processes can severely impair the service life of MCrAlY coatings in service. The oxidation behavior of two NiCoCrAlY coatings was investigated at 1150 °C up to 500 h. The coatings had the same nominal composition but were processed by two different projection techniques: air plasma spray (APS) and high velocity oxy fuel (HVOF). Freestanding coating specimens were extracted from the coated system and thinned down to different thicknesses ranging from 520 to 15 μm in order to investigate size effects inherent to the oxidation response. The oxidation rate of the APS coating was found to be insensitive to the specimen thickness, while that of the HVOF coating increased with the specimen thickness, due to greater intersplat oxidation. APS specimens thinner than 60 μm experienced InCF due to Al consumption to form the Al_2O_3 scale. In comparison, HVOF specimens with a thickness of 367 μm were subject to InCF after 250-350 h oxidation. This first stage of InCF resulted in the formation of a Cr_2O_3 layer at the

Al_2O_3/metal interface once Al activity in the MCrAlY coating was low enough to thermodynamically allow Cr_2O_3 to form. In addition, thick HVOF specimens developed mechanically induced chemical failure (MICF) resulting in the formation of $(Ni,Co)(Cr,Al)_2O_4$ spinel on top of the Al_2O_3 scale and within oxide intrusions. The occurrence of MICF was associated with the concomitant effects of Al consumption due to intrusive oxidation and the spallation of the external Al_2O_3 scale.

3.1 Introduction

Structural materials operating at high temperature, such as Ni-based superalloys, are generally coated with MCrAlY (where M = Ni, Co or Ni/Co) or aluminide coatings to improve their protective resistance in severe environmental conditions (Bose, 2017; Mévrel, 1989; J. R. Nicholls, 2000; Rhys-Jones, 1989). MCrAlY coatings are widely applied to components exceeding 850 °C, such as first and second stage turbine blades and nozzle guide vanes, compressors, turbine shrouds. They are richer in Al (and Cr) than superalloy substrates, which promotes the formation of a continuous, slow-growing, compact and adherent α-Al_2O_3 scale at temperatures above ~1000 °C (H. E. Evans & M. P. Taylor, 2006; W. G. Sloof & T. J. Nijdam, 2009). The consumption of Al due to both oxide growth and interdiffusion with the substrate (Elsaß et al., 2016; Raffaitin, Monceau, Andrieu, & Crabos, 2006; W. G. Sloof & T. J. Nijdam, 2009; Vialas & Monceau, 2006) is central to the system service life, as it determines the integrity of the protective Al_2O_3 scale, and thus the delay until faster-growing oxides develop. The “Al reservoir” available in the coating can become a critical factor in aeronautical applications, where coating thicknesses are limited due to weight concerns.

MCrAlY coatings can be manufactured using various techniques depending on the geometry of the substrate to be overlaid (Tamarin, 2002). On the one hand, electroplating and electro-codeposition routes have the advantage of producing dense and oxide-free coatings on complex shapes because of their non-line-of-sight deposition capability (Raffaitin et al., 2006; D. Texier, Monceau, Crabos, & Andrieu, 2017; Zhang, 2015). For instance, CrAlY-based powders can be codeposited into a (Ni, Co) matrix during the electroplating process.

Appropriate post-plating heat treatments are then applied to allow for element interdiffusion between CrAlY-based particles and the matrix. This operation confers mechanical properties to the particle/matrix structure and forms the final MCrAlY microstructure. However, this deposition quality comes at the expense of the process price and productivity (Tamarin, 2002; Tejero-Martin, Rezvani Rad, McDonald, & Hussain, 2019). Line-of-sight deposition techniques, such as APS and HVOF deposition processes, are much more affordable and demonstrate a very interesting trade-off between a cost-efficient process and excellent protection for various industrial applications. However, these projected coatings are much more prone to internal defects such as unmelted particles, pores, internal oxides and/or nitrides, intersplats. Oxygen ingress along these open channels causes oxide intrusions within the coating (Belzunce, Higuera, & Poveda, 2001; H. Chen et al., 2021; W. R. Chen, X. Wu, B. R. Marple, & P. C. Patnaik, 2005; H. E. Evans & Taylor, 2001; Jiang et al., 2018; Léger et al., 1998; Ma & Schoenung, 2011; Meng et al., 2019; Meng et al., 2018a; Mutasim, Rimlinger, & Brentnall, 1997; P. Niranatlumpong, C. B. Ponton, & H. E. Evans, 2000; T. Patterson, A. Leon, B. Jayaraj, J. Liu, & Y. H. Sohn, 2008; Richer et al., 2010; Seo et al., 2008; Shibata et al., 2006; Damien Texier et al., 2020; L. Wang et al., 2014). This oxide intrusion, concomitant to external oxide scale growth, participates in the Al consumption. Therefore, the capability of the coating to form a continuous Al_2O_3 scale, which depends on the available Al reservoir, might be affected by the defect morphology (volume fraction, connectivity). Oxide intrusions were also found to participate in the coating swelling due to the Pilling-Bedworth ratio higher than 1 for Al_2O_3-forming MCrAlY alloys (Jiang et al., 2018). Oxidation-assisted swelling of the coating generates tensile stress in the external scale, which may lead to scale cracking and spalling (Damien Texier et al., 2020).

Thermal and environmental conditions can vary depending on the application of the coated components. Maximal temperatures of 1100–1150 °C are generally encountered for MCrAlY coatings, covered or not with a ceramic top coat for TBC applications. The formation of the Al_2O_3 scale and intrusions, together with the interdiffusion with the substrate, causes aluminum depletion in the coating. In thin products, this may bring the Al concentration down to a critical

level where Al_2O_3 is no longer stable (H. Chen et al., 2021; H. E. Evans, A. T. Donaldson, & T. C. Gilmour, 1999; Ishii, Kohno, Ishikawa, & Satoh, 1997; Damien Texier et al., 2021), (Gheno et al., 2021; Romain et al., 2021; Strehl et al., 2000; D. J. Young, Chyrkin, He, Grüner, & Quadakkers, 2013; D. J. Young, Chyrkin, & Quadakkers, 2012). Other oxides may then form at the oxide/gas and metal/oxide interfaces on large regions. This evolution of the protective Al_2O_3 scale is called intrinsic chemical failure (InCF (Strehl et al., 2000)) and is not necessarily associated with an increase of the mass gain (Gheno et al., 2021; Ishii et al., 1997; Strehl et al., 2000; Damien Texier et al., 2021). Mechanical, thermal cyclic and thermal transient loading promotes mechano-chemical coupling and the onset of early strain- and oxidation-assisted damage and cracking/spallation of the external oxide scale (H. E. Evans, 1995; H. Hindam & D. P. Whittle, 1982; Pollock et al., 2011). Repeated through-thickness cracking and/or spallation of the protective Al_2O_3 scale may bring the Al concentration in the vicinity of the oxide spalled and cracked region to a critical healing level. In comparison with InCF, this change in oxidation behavior is local: *i.e.*, where the damage of the oxide scale occurs. This phenomenon is called mechanically induced chemical failure (MICF (H. Evans et al., 1999)) and favors the rapid growth of oxides of the base elements (Ni, Co) (H. Evans et al., 1999; C. S. Giggins & F. S. Pettit, 1971; W. Sloof & T. Nijdam, 2009; Wilber, Bennett, & Nicholls, 2000). Localized and generalized Al_2O_3 failures are highly detrimental to the integrity of the coating itself, and even more damaging in TBC systems. Indeed, fast growing oxides at the bond coat/top-coat interface may cause the top-coat to spall, thereby exposing the metal parts to excessive temperatures (Busso, Evans, Qian, & Taylor, 2010; H. E. Evans & Taylor, 2001). The integrity of the coated system comes from its native protection against environmental stresses through the Al_2O_3 formation and its long-term chemical stability. Therefore, investigating the Al_2O_3 failure for coated components is central for high temperature applications.

In the present study, oxidation experiments were conducted at 1150 °C on ultrathin freestanding NiCoCrAlY coating specimens extracted from Air Plasma Spray (APS) and High Velocity Oxy Fuel (HVOF)-processed plates. The ultrathin specimens were prepared with a

dedicated precision jig (D. Texier et al., 2016) in order to activate InCF for short-term high temperature exposures due to through-thickness Al depletion. Interrupted oxidation tests were performed to document the onset and progression of the generalized breakaway as a function of the exposure time. Thermogravimetric analyses were conducted to study the mass variation associated with the formation of the oxidation products. The sensitivity to InCF was evaluated for both types of coatings and the macroscopic oxidation behavior was related to the oxide intrusion. X-ray micro computed tomography (micro-CT) and cross-sectional characterizations were conducted in order to assess the proportion of oxide intrusion in comparison with external scale. In order to document the intrusive oxidation within APS and HVOF materials, the oxidation behavior and service life of both the projected materials were directly compared to the ones of a "defect-free" cast material with a similar chemical composition solely developing and external Al_2O_3 scale (see specimen UT2 in Ref. (Gheno et al., 2021) for additional information on the microstructure, oxidation behavior and service life).

3.2 Experimental procedures

3.2.1 Materials

NiCoCrAlY coatings were deposited by HVOF and APS processes on 304 stainless steel (SS) plate[s] with dimensions of 2 × 50 × 250 mm^3. Both coatings were deposited by PRAXAIR Surface Technologies for this specific investigation. The NiCoCrAlY powder used in the present study was provided by PRAXAIR© (NI-191-4 powder). The powder diameter was about 45 ± 10 µm and its chemical composition is given in Table 3.1. Coatings with a thickness of 600 µm and 1 mm were deposited on the SS plates with the APS and HVOF processes, respectively. On the one hand, debonding occurred during the thermal spray deposition for the APS coating. Therefore, free-standing coatings samples (FSCS) were naturally obtained with this process. On the other hand, HVOF coatings were adherent even for coating thicknesses of 1 mm. Rectangular samples were then cut with a precision cutting machine and the SS substrate was mechanically ground to roughly obtain 800 ± 50 µm-thick HVOF FSCS.

Table 3.1 Nominal composition of the NI-191-4 powder used to deposit the NiCoCrAlY coating (in at.% and wt%)

Element	Ni	Co	Cr	Al	Y
x_i (at.%)	Balance	18.8	16.5	23.0	0.3
w_i (wt%)	Balance	22.0	17.0	12.3	0.5

The FSCS were heat-treated at 1080 °C for 8 h and then at 870 °C for 20 h to reproduce the post-deposition heat treatments that are routinely applied to improve the coating adhesion to the substrate by interdiffusion and consequently to optimize the mechanical properties of Ni-based superalloy substrates (Damien Texier et al., 2016). Neither was required here, but a standard heat-treatment was nonetheless conducted to generate coating microstructures representative of service conditions.

The microstructure of the APS and HVOF NiCoCrAlY coatings is illustrated in Figure 3.1. It contained β and γ phases with surface fractions about 58% and 42%, respectively (surface fractions obtained from image analyses). The β and γ phases appear in dark and light gray in BSE mode, respectively (see Figure 3.1). The microstructure of the APS and HVOF coatings presents features typical of thermal sprayed materials: melted and resolidified powder particles, unmelted powder particles, pores, dispersed alumina oxides and resolidified splats. Both surface and cross-sectional observations evidenced higher occurrence of unmelted powder particles for the HVOF coating (21 ± 2% using image analysis) for these deposition conditions compared to APS coating (5 ± 2%). The presence of unmelted powder particles is not related to the deposition process itself but to the chosen process parameters, *e.g.* the powder temperature, velocity, projection distance etc. (Léger et al., 1998). While the APS coating depicts a typical microstructure of high temperature projected coatings, the HVOF coating exhibits a rather cold processed microstructure.

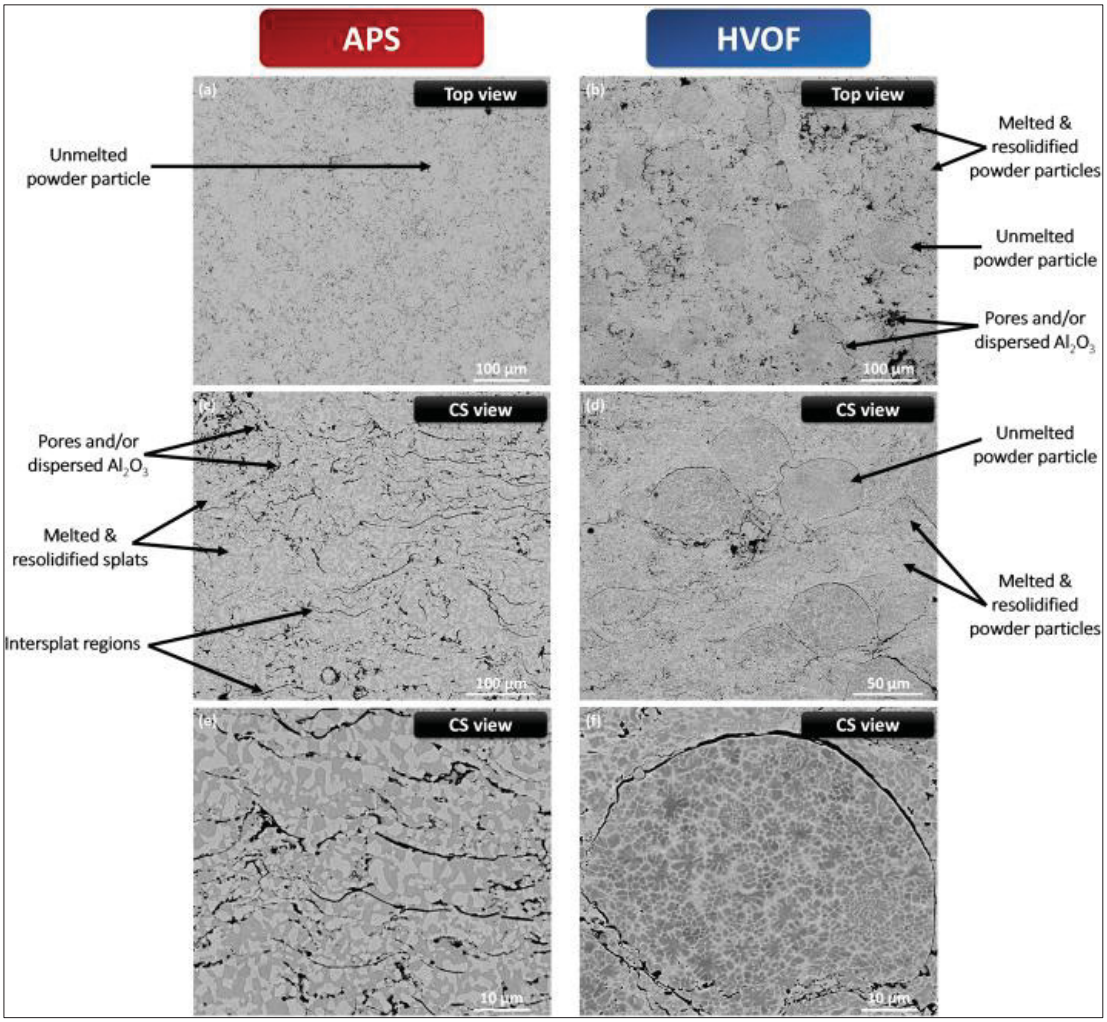

Figure 3.1 Microstructure obtained with a SEM in a BSE mode of the APS and HVOF coatings after standard heat treatment: (a) and (b) Top view observations of the samples (normal to the projection direction), (c) to (f) Cross-sectional (CS) observations of the samples showing melted and resolidified powder particles, unmelted powder particles, pores, dispersed alumina oxides and resolidified splats

3.2.2 Thin sample preparation

APS and HVOF FSCS were thinned down with a home-built precision Jig paired with a BUEHLER© grinding/polishing machine to obtain thin samples with different thicknesses. A particular care was paid on the precision jig stability to achieve low thickness variations over centimeter-size samples. The thinning procedure is fully detailed in Refs (D Texier, 2013; D. Texier et al., 2016). Samples with thickness ranging between 400 and 15 µm with less than ±3

μm in thickness variation were prepared. A surface finishing of P4000 SiC grit paper was applied on each sample face. In addition, both the projected materials were compared to a cast material with a similar chemical composition but exempt from process-defects (see specimen UT2 in Ref. (Gheno et al., 2021) for additional information).

3.2.3 High temperature oxidation

Thicknesses were measured using a micrometer with an uncertainty of ±1 μm, samples were photographed using a calibrated binocular magnifying glass (Leica DMS 300) to document the sample surface and measure the actual surface *S*. After preparation, samples were cleaned with acetone then ethanol using ultrasonic bath. Sample masses were measured with a precision balance (Sartorius MC5), with a precision of $\pm 1.0 \times 10^{-6}$ g. Samples were weighed three times before and after some oxidation periods allowing the mass gain $\Delta m(t)/S$ to be quantified.

Oxidation experiments were conducted at 1150 °C using interrupted furnace tests in a Nabertherm N 11/H furnace in laboratory air (no forced convection) for a cumulative time of up to 500 h. One sample was used for each thickness condition. Interruptions were done to observe local changes in the oxidation behavior, *e.g.* Al_2O_3 failure and oxide spallation. Samples were vertically hung on alumina supports using holders made of platinum wire during oxidation tests. Samples were weighed and observed using optical microscopy (OM) at different interruptions: after 5, 10, 15, 20, 50, 100, 150, 250, 350, and 500 cumulative hours. Optical observations aimed at capturing Al_2O_3 failure, *i.e.* new oxidation products either on top of the external oxide scale or at the α-Al_2O_3/metal interface owing to the semi-transparency of the α-Al_2O_3 scale in the visible spectrum.

3.2.4 Material characterization

Surface and cross-sectional observations of the oxidized samples were conducted using optical microscopy (OM) and scanning electron microscopy (SEM) in BSE mode. SEM observations were conducted using a Nova NanoSEM 450 field-emission gun SEM (FEG-SEM) from

Thermo Fischer Scientific and a JSM 7800F Prime FEG-SEM from JEOL for cross-sectional observations.

Optical observations were performed to quantitatively document oxide intrusion in the different materials using laser scanning confocal microscopy (Olympus LEXT OLS5100). Automatic stitching in laser intensity mode was conducted to cover large regions of interest with a resolution compatible with the oxide thickness (external oxide scale and oxide intrusion). The whole cross-section was imaged for each sample to analyze sample length compatible with the sparsely distributed intrusive oxides for the APS coating reported in a previous study (Damien Texier et al., 2020). Images were thus segmented using *Fiji* (Schindelin et al., 2012) in order to dissociate the oxide intrusions from the external oxide and the remaining metal.

CT-scans were performed on thick samples of APS and HVOF coatings oxidized for 500 h to quantitatively document oxide intrusion in three dimensions. Two slabs with dimensions of 1 × 2 × 0.2 mm^3 and 1 × 2 × 0.4 mm^3 were cut from the APS and HVOF samples, respectively. They were characterized with a v tome xs 240 scanner (GE) equipped with a DXR250 detector (2024 × 2024 $pixels^2$ with a dimensions of 200 × 200 μm^2). The scanning parameters were as follows: numerical resolution: 1.75 µm/voxel, voltage: 100 kV, intensity: 180 µA, exposure time: 1 s, filter: 0.1 mm thick Cu plate, 3 frames averaging, 2550 projections for 360° rotation. The projections were processed with the program *Phoenix datos—x reconstruction 2*. After reconstruction, the 3D images were analyzed with *Dragonfly 2021.3* (Object Research Systems, 2021). The images were segmented using the Otsu algorithm, enabling a quantitative and localized analysis of the intruded oxides within the matrix.

3.3 Results

3.3.1 Mass gain evolution

Mass gain evolution was investigated for both the APS and HVOF coatings up to 250 cumulative hours for all the coating samples, as depicted in Figure 3.2. The oxidation behavior

of a cast material with a similar chemical composition was added as a green dashed curve on the different graphs for direct comparison with a material without projection defects (results from Ref. (Gheno et al., 2021)). On the one hand, the mass gain of the APS coating was found nearly insensitive to the sample thickness and matched well with the one of the cast material. For short oxidation duration, the mass gain is slightly higher for the APS material in comparison with the cast material. The oxidation rate follows a power law with an exponent close to 3 similarly to the cast material, as observed on the log-log representation. More details on the oxidation of the APS coatings are reported in Ref. (Damien Texier et al., 2021). On the other hand, the mass gain evolution of the HVOF coating was found particularly sensitive to the specimen thickness. Thick samples demonstrate a greater mass gain for all the oxidation duration. For instance, the mass gain of the 367 µm-thick HVOF specimen after 250 h is nearly 9 times greater than the one of the cast material. Interestingly, the oxidation rate of the HVOF samples follows also a power law with an exponent close to 3 regardless of the specimen thickness (parallel linear trends in Figure 3.2 (d). In addition, the three thinnest HVOF specimens and the thinnest APS sample have a decrease in oxidation rate after 100 h.

The oxidation kinetics were analyzed with a power law:

$$\left(\frac{\Delta m}{S}\right)^{n} = k_n . t \qquad \text{(eq. 4.1)}$$

Where Δm is the mass gain, *S* is the external surface area, *n* and k_n and the oxidation exponent and constant, respectively, and *t* is the time. Values of *n* and k_n fitted on the mass gain data are reported as a function of the specimen thickness in Figure 3.3. The average value of the exponent was found to be 3.5 ± 0.6 for APS sample and 3.4 ± 0.4 for the HVOF ones. While k_n is insensitive to the thickness for the APS coating with a value of $6.9 \times 10^{-3} \pm 5.7 \times 10^{-3}$ $mg^{3.5} \cdot cm^{-7} s^{-1}$ (with $n = 3.5$), its value increases with the thickness for the HVOF coating from 1.0×10^{-3} $mg^{3.5} \cdot cm^{-7} s^{-1}$ to 4.2×10^{0} $mg^{3.5} \cdot cm^{-7} s^{-1}$ (with $n = 3.5$).

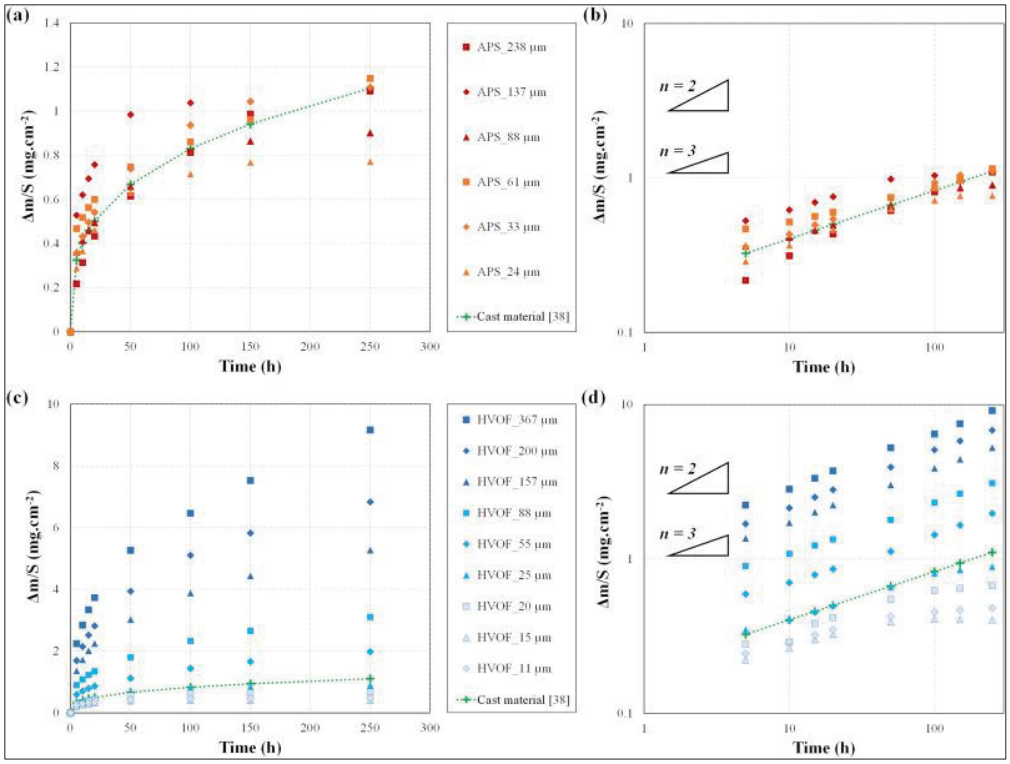

Figure 3.2 Mass gain evolution at 1150 °C for both the APS and HVOF free-standing coating specimens with various thicknesses: (a) and (c) Δm/S versus time representations, (b) and (d) log-log representations. The oxidation behavior of the cast material with a similar chemical composition was added as a green dashed curve on the different graphs for direct comparison (results from Ref. (Gheno et al., 2021))

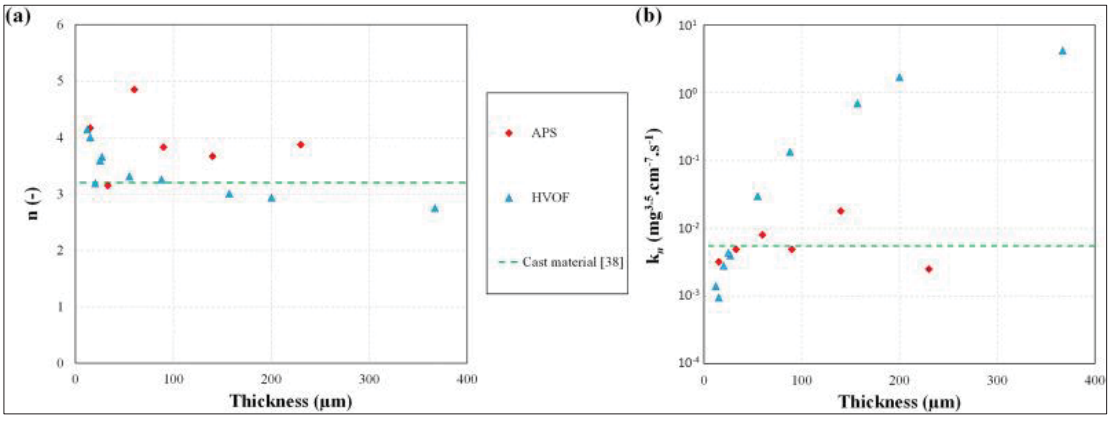

Figure 3.3 Evolution of the (a) oxidation rate exponent n and (b) oxidation constant k_n as a function of the specimen thickness. The oxidation behavior of the cast material with a similar chemical composition was added as a green dashed curve on the different graphs for direct comparison (results from Ref. (Gheno et al., 2021))

3.3.2 Evolution of the oxide scale

Macrographs were recorded for both the APS and HVOF materials at each interruption (Figure 3.4). After 5 h oxidation, all the specimens have a homogeneous and continuous light gray aspect, corresponding to the stable Al_2O_3 external oxide scale. For the APS coating, darker regions appear after 20 and 100 h on the 24 and 33 µm-thick specimens, respectively. These darker regions, highlighted with green arrows in Figure 3.4, correspond to the onset of InCF, as reported in Refs. (Gheno et al., 2021; Damien Texier et al., 2021). Specimens with a thickness of 61 µm or greater did not experience any InCF. For the HVOF coating, InCF was found to occur after 20 h on the 15 µm-thick specimen. Interestingly, Al_2O_3 failure was observed for all the specimens for oxidation duration lower than 250 h regardless of the specimen thickness (and even 150 h for specimens thinner than 200 µm).

Oxide spallation was found to occur for both materials (light gray regions in Figure 3.4 and Figure 3.5). It became significant after 50 h, and was more important in thicker samples. Thick APS coatings developed an external oxide scale with a homogeneous gray level (except oxide spalled regions) up to 500 h, corresponding to Al_2O_3 formation. Interestingly, thick HVOF coatings developed an external oxide scale with blueish islets spreading onto the surface. Blue oxide was mainly observed in regions where Al_2O_3 spalled at the previous cooling step (see *e.g.* supplementary materials Fig. S1 of (Kalush et al., 2022)). This local change in oxidation behavior preceded by Al_2O_3 spallation is consistent with MICF. Due to the increasing sensitivity to Al_2O_3 spallation with increasing specimen thickness, more than 10% of the sample surface is covered by MICF at 250 h and 150 h for specimens thinner and thicker than 150 µm, respectively. The blueish oxide scale covers the majority of the specimen surface after 350 h. While the APS specimens were only prone to InCF, HVOF specimens can be subject to InCF and MICF simultaneously. It is also important to note that specimens thinner than 30 µm did not experience any oxide spallation and were solely sensitive to InCF. In addition, the oxide scale was less prone to spall once InCF or MICF developed.

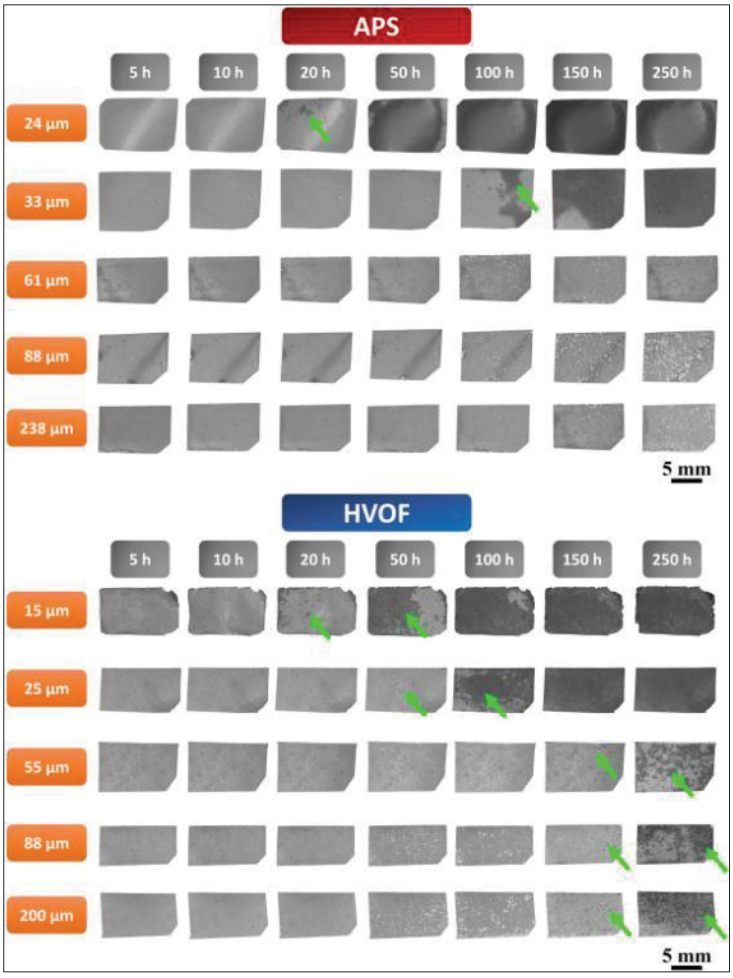

Figure 3.4 Macrographs showing surface evolution for both the APS and HVOF coatings at different oxidation cumulative time and specimen thicknesses. Green arrows highlight the onset of InCF. Please see the high-resolution version of the present figure for better details on InCF events. Partly reprinted from Corrosion Science, 184, Texier et al., Screening for Al_2O_3 failure in MCrAlY APS coatings using short-term oxidation at high temperature, 109334-4, Copyright (2021), with permission from Elsevier (Damien Texier et al., 2021)

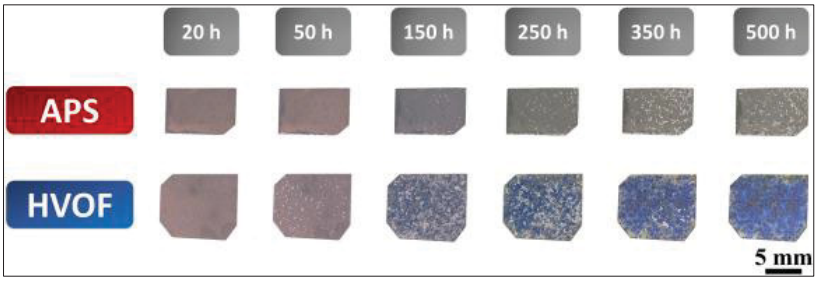

Figure 3.5 Surface macrographs of a 238 µm-thick APS and a 367 µm-thick HVOF coating samples, showing the evolution of oxide spallation and the development of the blue oxide

3.3.3 Cross-sectional observations

Cross-sectional observations were conducted on the APS and HVOF coatings after 250 h cumulative oxidation exposure for thick and thin samples, as illustrated in Figure 3.6 and Figure 3.7, respectively. Oxide intrusions were found in both materials, but extended deeper and developed thicker patterns in the HVOF coating. These intrusive oxides formed in intersplat and unmelted particle regions. For the APS coating, thin oxide stringers are observed and thick oxide intrusions are sparsely distributed on the cross-section views. Both the thick oxide intrusions and thin oxide stringers were characterized as Al_2O_3 using energy dispersive X-Ray (EDX) analyses. Some AlN precipitates were also observed within the bulk of APS coatings inherited from the deposition process (see ref. (Damien Texier et al., 2021) for additional information). $(Ni,Co)(Cr,Al)_2O_4$ spinels developed above the external Al_2O_3 scale but also in the specimen bulk of some HVOF specimens in the core of sub-surface intrusive oxides (white arrows showing lighter gray regions in the core of Al_2O_3 intrusions in Figure 3.6 (d)). These spinels were mainly found in a shallow region beneath and connected to the external oxide scale. The spinel formation was not necessarily associated with an advanced consumption of aluminum within the metallic material. These $(Ni,Co)(Cr,Al)_2O_4$ spinels were observed in regions of HVOF specimens with a β-γ microstructure in the specimen core. EDS analyses on the 200 and 367 µm-thick HVOF specimens revealed a large variability in Al content from regions to regions but Al content as high as 24 at.% was found far from regions developing $(Ni,Co)(Cr,Al)_2O_4$ spinels.

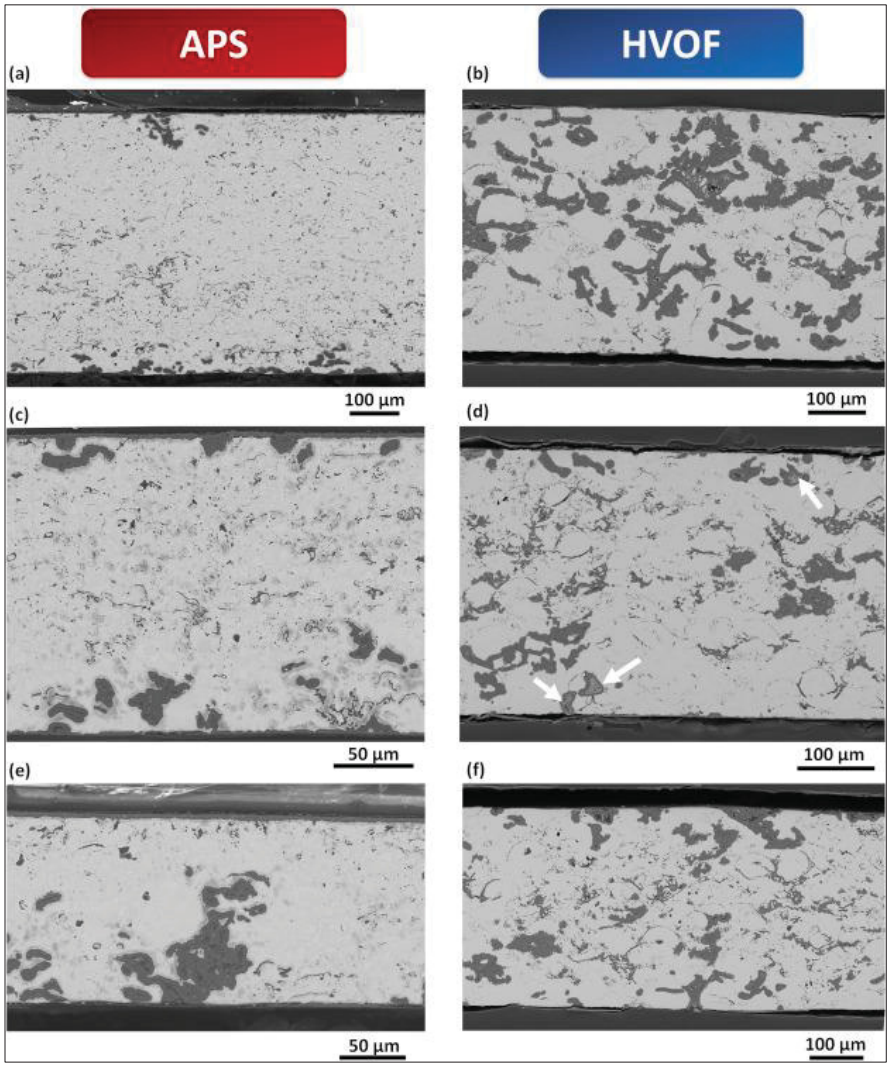

Figure 3.6 Cross-sectional observations of thick-samples after 250 h at 1150 °C showing difference in intrusive oxidation for a (a) 520 µm, (c) 200 µm, (e) 140 µm-thick APS and a (b) 367 µm, (d) 367 µm, (f) 367 µm-thick HVOF coatings

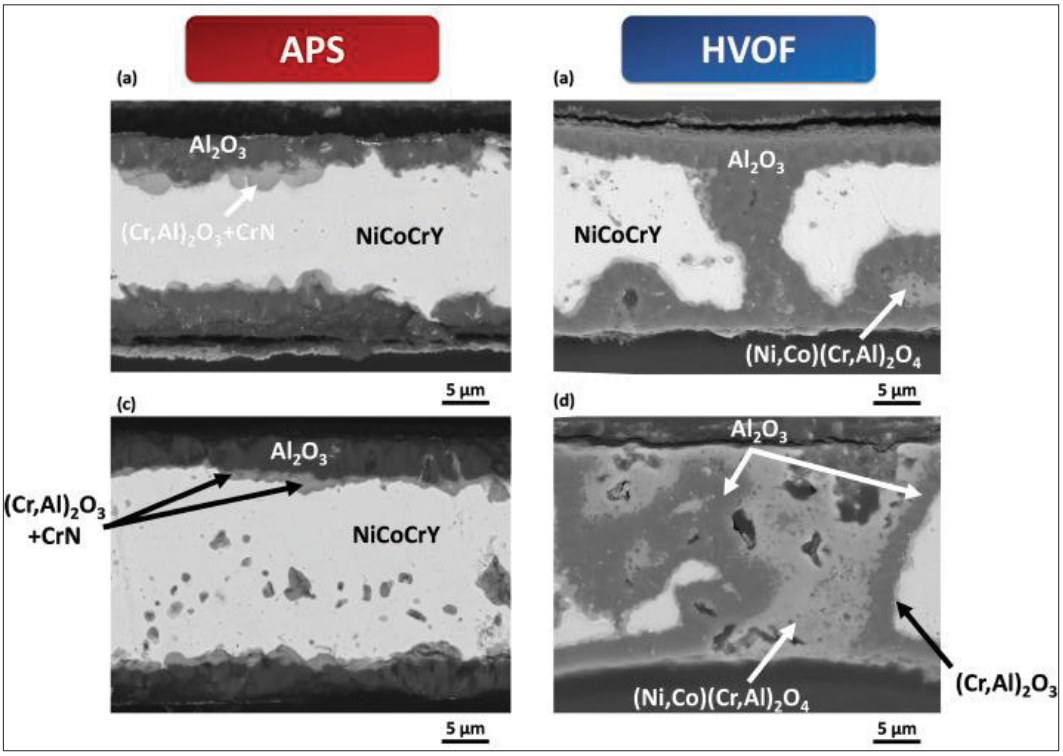

Figure 3.7 Cross-sectional observations of thin-samples after 250 h at 1150 °C showing difference in intrinsic chemical failure (InCF) for 24 µm-thick APS and 25 µm-thick HVOF coatings

In addition, a slight undulation of the surface was observed for thick HVOF samples, especially in the vicinity of sub-surface oxide intrusions. This undulation might result from growth stresses associated with the formation of the intense intrusive oxides. The Al_2O_3 would expand more than the metal it consumes to form the intrusive oxides (Pilling-Bedworth ratio of Al_2O_3 in Ni-based alloys nearly 1.8 (C. Xu & Gao, 2000)), thus deforming the material.

Cross-sectional observations of thin specimens experiencing InCF at 1150 °C for 250 h are depicted in Figure 3.7. For thin APS coatings, a $(Cr,Al)_2O_3$ layer was found to develop at the Al_2O_3/metal interface and CrN particles also formed in this region. For thin HVOF coatings, similar $(Cr,Al)_2O_3$ layer grew at the Al_2O_3/metal interface but $(Ni,Co)(Cr,Al)_2O_4$ spinels developed in the core of Al_2O_3 intrusions, as a second stage to InCF. This second stage of InCF, was not associated with a full consumption of Cr in the bulk of HVOF coatings.

Cross-sectional observations of thick specimens after 500 h exposure at 1150 °C are depicted in Figure 3.8. Al_2O_3 remained stable for the APS samples while $(Ni,Co)(Cr,Al)_2O_4$ oxides were observed as a continuous external layer for the HVOF samples, without the formation of the $(Cr,Al)_2O_3$ layer at the Al_2O_3/metal interface. $(Ni,Co)(Cr,Al)_2O_4$ oxides also formed in the core of intrusive oxides only for the HVOF samples even for the thickest samples (367 µm). $(Ni,Co)(Cr,Al)_2O_4$ spinels within intrusive oxides developed at depths shorter than 60 µm, *i.e.* at a depth less than 1.5 NiCoCrAlY particle size.

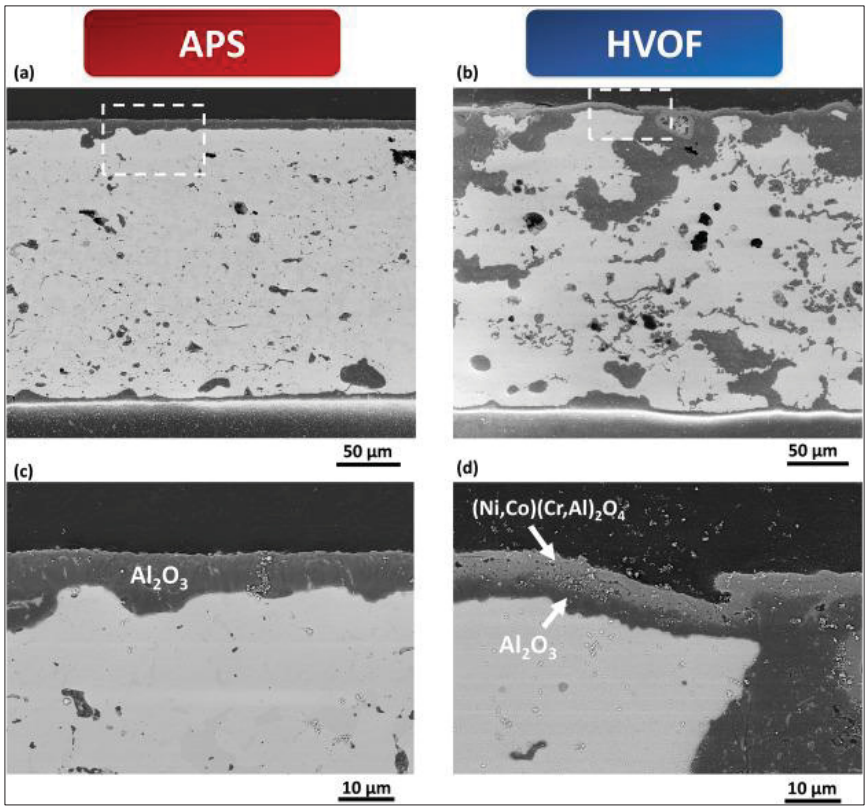

Figure 3.8 Cross-sectional observations of thick samples after 500 h at 1150 °C showing difference in external oxide scale composition between APS and HVOF coatings

3.3.4 Quantitative analyses of the intrusive oxidation

Large cross-sectional observations and CT-scans were investigated in order to dissociate the contribution of the external oxide scale and the oxide intrusion after 500 h at 1150 °C in two and three dimensions, respectively. While solely the thickest samples were investigated via

tomographic observations, different samples thicknesses ranging from 55 to 367 µm were analyzed using cross-sectional observations. Illustrations of the 3D macrographs are depicted in "*supplementary materials*" (Fig. S2, Fig. S3, Fig. S4, Fig. S5, Fig. S6 of (Kalush et al., 2022)). Intrusive oxides were thus segmented for both 2D and 3D characterizations to quantify their fraction and distribution within the sample and the fraction of intrusive oxidation compared to the external oxide scale. Segmented surfaces of the external oxide scale (S_{ext}), of oxide intrusions (S_{int}) and of the metallic region (S_{met}) were illustrated in "*supplementary materials*" (Fig. S7 of (Kalush et al., 2022)).

As aforementioned, intrusive oxides were segmented and compared to the external oxide scale, as shown by the S_{int}/S_{ext} ratio in Figure 3.9 (a). Both surface ratio (solid markers) and volume ratio (blank markers), respectively obtained from cross-sectional views and 3D CT-Scan results, were plotted for direct comparison. For the APS samples, the surface/volume occupied by intrusive oxides was found slightly lower than the one of the external oxide scale (S_{int}/S_{ext} ratio less than 1). The dark gray horizontal dashed line illustrates the $S_{int} = S_{ext}$ condition. For HVOF samples, the contribution of intrusive oxides is greater and the S_{int}/S_{ext} ratio increased with the sample thickness. Indeed, the surface occupied by intrusive oxides was more than ten times greater than the external oxide surface for the 367 µm-thick HVOF sample after 500 h at 1150 °C. Therefore, the contribution of oxide intrusions to the mass gain of the HVOF samples is further demonstrated, and explains the observed effect of the sample thickness on the oxidation kinetics. In addition, the fraction of intrusive oxide within the metallic material was considered as the cross-sectional surface (or volume from CT-scans) of intrusive oxide S_{int} divided by the cross-sectional surface (volume) of the sample except the surface (volume) of the external surface (S_{met}). Please refer to "*supplementary materials*" (Fig. S7 of (Kalush et al., 2022)) for illustration of S_{int} and S_{met}. Similarly, V_{int} and V_{met} are considered using 3D CT-Scan results. The fraction of intrusive oxide within the metallic material for the whole samples was depicted in Figure 3.9 (b). This fraction was roughly constant, regardless of the sample thickness for both the APS and HVOF materials. After 500 h at 1150 °C, the intrusive oxide

occupied 8 and 35% of the metallic sample for the APS and HVOF materials, respectively. 2D cross-sectional (CS) and 3D CT-scans (CT-S) results are consistent.

Oxide segmentation also aimed to evaluate the distribution of intrusive oxidation within the bulk of the metallic material. The fraction of intrusive oxide within the metallic material was calculated at different locations from the center of the sample, as illustrated in Figure 3.10. The profile of the intrusive oxidation fraction across the sample thickness has a "U"-shape regardless of the sample thickness and deposition process. The external oxide scale is not represented in this graph. Intrusive oxidation was greater in a shallow region beneath the external oxide scale then the fraction decreased in the sample core. Interestingly, fractions of intrusive oxidation greater than 40% were reported for both materials. This fraction decreased to a core value of nearly 4 ± 3 % and 24 ± 3 % for the APS and HVOF materials, respectively. Cross-sectional and CT-scan results are also consistent.

3.4 Discussion

The comparison between the high temperature oxidation of APS and HVOF coatings with similar nominal composition provides an opportunity to document how processed-inherited features affect the oxidation behavior, *i.e.* mass gain evolution and oxide formation, and ultimately the service life. Both projected materials developed an external oxide scale together with intrusive oxidation along intersplats and around unmelted particles, with a greater sensitivity for the HVOF coating. The greater sensitivity to intrusive oxidation is not attributed to the HVOF process but to the particular process parameters for the HVOF deposition used in the present paper. The comparison between APS and HVOF materials with the cast material with a similar chemical composition gives the opportunity to document the oxidation behavior when solely external oxidation takes place (Gheno et al., 2021), and enables to discuss on the contribution of oxide intrusions on InCF, MICF, and service life, *i.e.* time to Al_2O_3 failure.

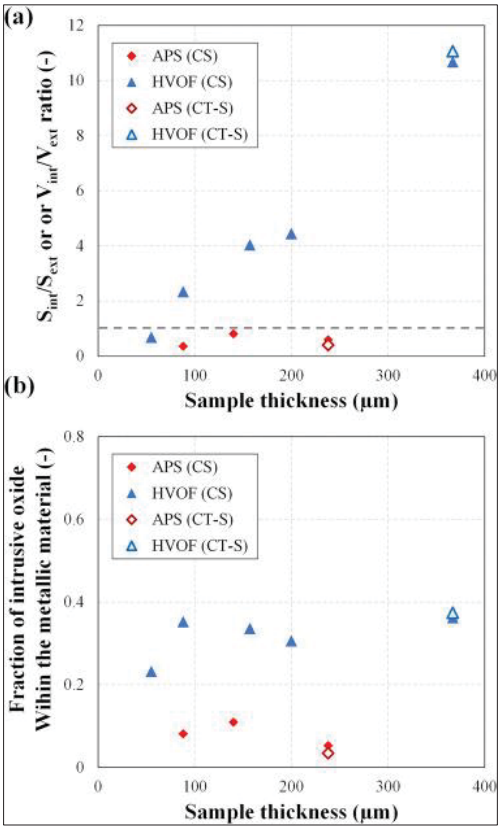

Figure 3.9 Evolution of the surface fraction of intrusive oxidation as a function of the sample thickness for both the APS and HVOF coatings after 500 h at 1150 °C. (a) Comparison with the external oxide, (b) Comparison with the metallic material

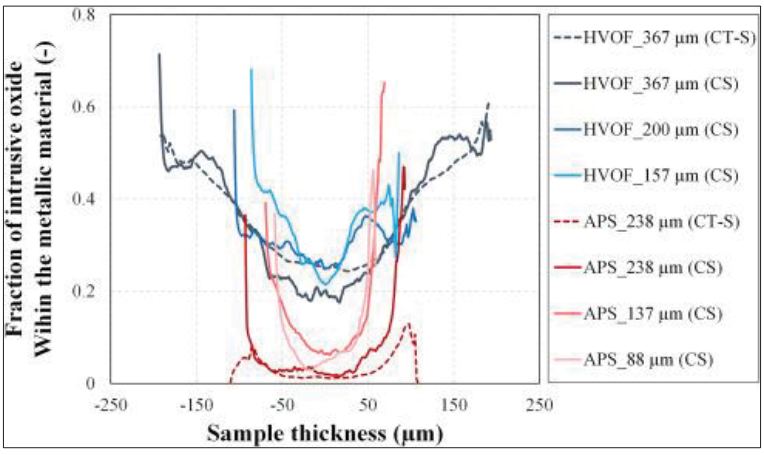

Figure 3.10 Distribution of the fraction of intrusive oxidation within the metallic material across the sample thickness for both the APS and HVOF after 500 h at 1150 °C. The external oxide scale is not represented in this graph

3.4.1 Origin of intrusive oxidation

As aforementioned, APS and HVOF materials developed intrusive oxidation along intersplats and around unmelted particles. Intrusive oxidation was found more pronounced for the HVOF material due to a high fraction of unmelted particles (see *e.g.* Figure 3.1). Intrusive oxidation was reported for different MCrAlY projected coatings, with a sensitivity not clearly associated to a deposition process (Belzunce et al., 2001; H. Chen et al., 2021; W. R. Chen et al., 2005; H. E. Evans & Taylor, 2001; Jiang et al., 2018; Léger et al., 1998; Ma & Schoenung, 2011; Meng et al., 2019; Meng et al., 2018a; Mutasim et al., 1997; P. Niranatlumpong et al., 2000; T. Patterson et al., 2008; Richer et al., 2010; Seo et al., 2008; Shibata et al., 2006; Damien Texier et al., 2020; L. Wang et al., 2014). For instance, several authors reported that HVOF MCrAlY coatings were less prone to intrusive oxidation compared to APS (or even low pressure plasma spraying (LPPS)) (Richer et al., 2010; Shibata et al., 2006; L Wang et al., 2014). The sensitivity to intrusive oxidation was found to be related to the presence and interconnection of unmelted powder particles. Process parameters such as powder temperature and velocity play a significant role on the fraction of unmelted powder particles in projected materials (Léger et al., 1998). Hotter process conditions for this specific HVOF material could improve its oxidation resistance and service life. Intersplat regions also participate in intrusive oxidation but in a less extensive manner due to morphological aspects. Intersplat regions for the APS material are more likely found orthogonal to the projection direction, *i.e.* orthogonal to the oxygen ingress direction/inward oxygen flux. The lack of adhesion of unmelted particles in the HVOF material generates continuous channels, whereas intersplat regions appear more discontinuous (see *e.g.* Figure 3.1). Therefore, defect connectivity from particles to particles seems greater for materials having unmelted particles, especially in depth, as depicted in Figure 3.1 (c) and (d). This particular defect morphology favors oxide intrusion in depth, thus affecting the core of the projected material due to deep open porosity. With these specific process conditions, the APS material is more likely to have closed porosity while the HVOF materials have a greater open porosity. Oxidation of intersplat regions and/or unmelted

particles can be significantly limited using additional surface treatments to close pores and channels (Wu et al., 2001).

3.4.2 Effect of intrusive oxidation on the Al_2O_3 failure

The motivation of the present paper is not to discriminate a deposition process but to investigate intrusive oxidation related to process-inherited defects and ultimately its service life based on the Al_2O_3 failure. Both external oxidation and intrusive oxidation participate in the mass gain evolution and in the consumption of metallic elements participating in the oxide formation. Different kinetics of oxidation and oxides in presence were found for the APS and HVOF materials due to the much more severe intrusive oxidation for the HVOF process. Two different oxidation mechanisms were reported to participate for the Al_2O_3 failure depending on the specimen thickness: (i) the intrinsic chemical failure (InCF) due to aluminum consumption, and (ii) the mechanically induced chemical failure (MICF) due to oxide spallation. These oxidation mechanisms are dependant on the specimen thickness since thin specimens are sensitive to reservoir effects and thick specimens are more prone to oxide spallation. Therefore, the competition between both the oxidation mechanisms will be discussed below for the APS and HVOF materials and compared to the cast material.

Based on the Pilling-Bedworth ratio of the metal/oxide system, development of oxide intrusions leads to swelling of the material or at least put the metal in a complex stress state. Such volume expansion can contribute to spallation of the external oxide scale, as observed in Ref. (Gheno et al., 2021) and can participate in the development of the intrusive oxidation. However, the coatings developed oxide intrusions before scale spallation started. Therefore, scale spallation was not the primary cause for intrusive oxidation.

APS materials with a thickness greater than 60 µm developed Al_2O_3 as external and intrusive oxides for samples up to 500 h. Despite oxide spallation, APS materials did not experience MICF in the time/temperature window. Samples as thin as 60 µm were necessary to activate InCF for the APS coating at 1150 °C up to 500 h oxidation, as depicted in Figure 3.4 (time to

InCF = 20 and 100 h for 24 and 33 μm-thick APS specimens). InCF was found associated with the formation of a $(Cr,Al)_2O_3$ layer and CrN precipitates at the Al_2O_3/metal interface (see *e.g.*Figure 3.7 and Ref. (Gheno et al., 2021) for more details). Similar results were reported for the cast material experiencing solely external oxidation, as reported in Ref.(Damien Texier et al., 2021). InCF resulted in the formation of a $(Cr,Al)_2O_3$ layer at the Al_2O_3/metal interface without precipitation of CrN. The cast materials experienced InCF after 20 and 200 h for 11 and 26 μm-thick specimens, respectively. These longer times to Al_2O_3 failure arise from the absence of intrusive oxidation, thus limiting the aluminum consumption compared to the APS material.

For the HVOF material, both InCF and MICF were observed in competition depending on the specimen thickness. Severe intrusive oxidation and oxide spallation for the HVOF material impaired the stability of Al_2O_3. A continuous $(Ni,Co)(Cr,Al)_2O_4$ spinel layer developed on top of the Al_2O_3 scale and within intrusive Al_2O_3 for specimens thicker than 55 μm (Figure 3.6). This second stage of oxidation is associated with the blueish coloration of HVOF samples. $(Ni,Co)(Cr,Al)_2O_4$ islets formed and spread from regions subjected to oxide spallation at previous interruptions (see *e.g.* supplementary materials, Fig. S1(Kalush et al., 2022)). The formation of $(Ni,Co)(Cr,Al)_2O_4$ spinels on top of the Al_2O_3 scale corresponds to MICF and was not associated with a particular increase in the oxidation rate due to the continued presence of the slow-diffusing oxide (Fedorova, Monceau, & Oquab, 2010; Ishii et al., 1997; Strehl et al., 2000; D. J. Young et al., 2013; D. J. Young et al., 2012). While both APS and HVOF materials were subject to Al_2O_3 spallation, solely HVOF formed large regions of $(Ni,Co)(Cr,Al)_2O_4$ spinels for specimens with thickness ranging from 55 to 367 μm. Meng et al. reported similar formation of $(Ni,Co)(Cr,Al)_2O_4$ spinels on top of the external Al_2O_3 scale after isothermal oxidation of an APS MCrAlY alloys developing severe oxide intrusion at intersplat regions (Meng et al., 2019; Meng et al., 2018a). In addition to MICF, InCF occurred for HVOF specimens regardless of the specimen thickness in this temperature-time window. Specimen as thick as 367 μm developed InCF since the fraction of intrusive oxides was found 10 times greater than the one of the external oxide scale (Figure 3.2 and Figure 3.9). Both InCF

and MICF were observed for HVOF specimens thicker than 55 μm while thinner specimens were only sensitive to InCF due to lack in oxide spallation. Therefore, both oxide spallation and oxide intrusion are central in the Al_2O_3 failure and service life of thin MCrAlY products.

3.4.3 Influence of oxide intrusion on the service life of projected MCrAlY materials

In an attend to predict the service life of material investigated in this work, the analytical model previously described in Refs. (Gheno et al., 2021; Damien Texier et al., 2021) is used. The assumption of flat diffusion profiles and mass balance equilibrium allows the analytical estimation of the Al concentration in the metallic MCrAlY as a function of the mass gain and thus the time. Time to InCF can thus be considered as the time necessary to consume all the Al content from the MCrAlY alloy due to external and intrusive oxidation. The model is based on the hypotheses detailed below:

- Composition profiles are nearly flat due to fast diffusion in both γ and β phase, relative to the oxidation rate;
- The quantity of non-oxidized elements, *i.e.* Co, Cr and Ni, remains constant in the metallic alloy during the Al_2O_3 growth stage;
- The alloy molar volume is considered constant;
- The specimen creep due to oxide growth is negligible;
- The kinetics of oxidation for the external and intrusive oxidation are comparable due to the open porosity associated to intersplat/unmelted particles regions.

The time to failure t_{InCF} can thus be expressed as follow (see Refs (Gheno et al., 2021; Damien Texier et al., 2021)):

$$t_{InCF=\frac{1}{k_n}} \left(\frac{3.M_O}{4.M_{Al}}.\rho_{MCrAlY}.\varepsilon_{MCrAlY}.w_{Al}\right)^n \quad \text{(eq. 4.2)}$$

with M_O and M_{Al} the molar mass of O and Al, ρ_{Al2O3} the density of Al_2O_3, ε_{MCrAlY} the thickness of the coating sample, and w_{Al} the weight fraction of Al in the MCrAlY alloy. Both model and experimental data were compared in Figure 3.11. For the HVOF material, k_n was found to increase with the specimen thickness and can be expressed as a power law function of the

specimen thickness (see *e.g.* Figure 3.3 (b)). Dashed lines correspond to the time to InCF for all the materials and colored domains correspond to time-thickness domain for which InCF is supposed to occur. While the time to InCF rapidly increases for the APS and cast materials for specimens thicker than 30 µm, time to InCF for HVOF specimens was found to linearly and slowly increase with the specimen thickness. For the experimental results, specimens covered by at least 10% by InCF or MICF were considered as affected by InCF or MICF, respectively. Both experiments and models were found to particularly match for the APS material. For the HVOF materials, the model tends to slightly overestimate the time to InCF for thick specimens. It is worth mentioning that oxide spallation at the different interruptions was not considered both in the experimental mass gain measurement and in the model, leading to faster consumption of Al. The distribution of oxide intrusion might also play a role on the local consumption of Al within the metallic MCrAlY alloy due to presence of residual β precipitates when both InCF and MICF occurred for thick HVOF specimens.

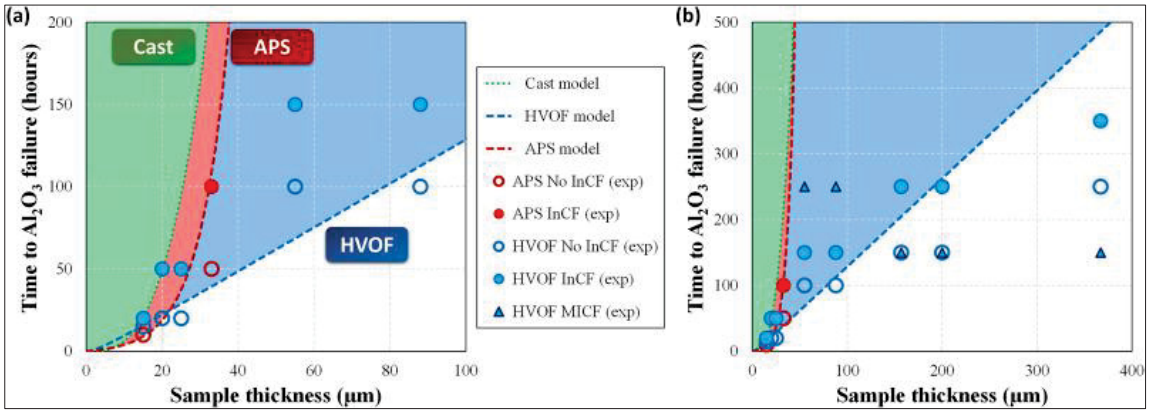

Figure 3.11 Service life prediction of the MCrAlY alloy as a function of the specimen thickness at 1150 °C for the APS, the HVOF and the cast materials

3.5 Conclusions

The oxidation behavior of two projected NiCoCrAlY coatings, *i.e.* APS and HVOF coatings, was investigated using thin freestanding specimens exposed at 1150 °C up to 500 h. A large amount of unmetled particles led to severe oxide intrusion for the HVOF coating. The main differences in oxidation behavior for both the coatings consist in:

- A greater mass gain for the HVOF coating condition investigated here compared to the APS coating and the model material;
- A mass gain increasing with the coating thickness for the HVOF coating due to severe oxide intrusion via oxygen transport through intersplat channels. The oxide intrusion was found more severe in the extreme surface compared to the specimen bulk due to oxygen transportation and/or diffusion via the intersplat channels. The oxidation rate of the APS coating was found insensitive to the specimen thickness as long as no intrinsic chemical failure (InCF) occurred. For APS coatings, the oxide intrusion was less pronounced and mainly connected to the external oxide scale;
- A greater sensitivity to oxide spallation for the HVOF coating, especially for thicker samples;
- A greater sensitivity to intrinsic chemical failure (InCF) for the HVOF coating. The first stage of InCF, *i.e.* the Al_2O_3 failure to form $(Cr,Al)_2O_3$ and/or CrN at the Al_2O_3/metal interface, occurred for thin APS specimens (samples thinner than 60 μm) and for all the HVOF samples (samples as thick as 367 μm) in the time/temperature window. A second stage of InCF resulting in the formation of $(Ni,Co)(Cr,Al)_2O_4$ spinels as an external oxide scale and within oxide intrusion occurred for all the HVOF samples.

It is worth noting that defects inherited from the deposition processes severely impair the oxidation resistance and service life of MCrAlY coatings under service. In the present study, the HVOF coating experienced a poor oxidation resistance compared to the APS coating. However, other deposition parameters could inverse this trend. The prediction of InCF occurrence based on the deposition process parameters and/or non-destructive analyses of microstructure is needed to better estimate the service life of coating system due to oxidation and interdiffusion. Additional surface treatments preventing oxygen transportation within intersplat channels could improve the reactivity of such projected coatings.

Data availability

The raw/processed data required to reproduce these findings cannot be shared at this time due to technical or time limitations.

CRediT authorship contribution statement

Ali Kalush: Methodology, Investigation, Data curation, Writing original draft. Damien Texier: Conceptualization, Methodology, Investigation, Data curation, Validation, Writing – original draft, Writing – review & editing, Funding acquisition. Maxime Ecochard: Investigation, Data curation, Methodology. Quentin Sirvin: Investigation, Methodology. Karim Choquet: Investigation, Methodology. Thomas Gheno: Methodology, Validation, Writing – original draft, Writing – review & editing. Nicolas Vanderesse: Investigation, Methodology, Data curation, Writing – original draft. Walid Jomaa: Conceptualization, Methodology. Philippe Bocher: Conceptualization, Methodology, Writing – original draft.

Declaration of competing interest

The authors declare the following financial interests/personal relationships which may be considered as potential competing interests: Damien TEXIER reports financial support was provided by French National Research Agency

Acknowledgements

This work was supported by the Agence Nationale de la Recherche (ANR) [ANR-18-CE08-003; ANR-JCJC-COMPAACT project funded from the AAPG2018].

CHAPTER 4

RESULTS AND DISCUSSION

4.1 Introduction

This chapter synthesizes the findings from the experimental investigations and some of the results presented in the published article outlined in Chapter 3 that needed more in-depth discussion. It aims to offer a comprehensive analysis of the properties and characteristics of the NiCoCrAlY coatings samples produced by HVOF methods with various conditions accompanying it with APS samples for comparison and analysis purposes. Further, it integrates additional experimental outcomes obtained after the publication of the article (Chapter 3), providing a holistic understanding of the behavior of NiCoCrAlY coatings under high-temperature oxidation conditions. This chapter seeks to contextualize these findings within the broader scope of the thesis, focusing on challenges of high-temperature protective coatings produced by HVOF.

4.2 Analysis and characteristics of as-coated HVOF samples

In this section, the characteristics of samples were examined immediately after coating. These samples were without the proceeding and routine heat treatment as being doing in actual coated parts. This investigation provides valuable insights into how the deposition process parameters, such as temperature, pressure, and particle velocity, influence the resulting surface characteristics and microstructure of the coating. By analyzing the sample at this stage, we can understand the initial characteristics of the coatings and the effects of the deposition techniques on the coating's morphology, including the distribution, the presence of defects such as pores or cracks, and the overall uniformity and adherence of the coating. This information is crucial for optimizing the coating process to achieve a certain level of desired coating properties before even subjecting it to any subsequent thermal treatments.

4.2.1 The microstructure of as-coated HVOF sample

Upon cross-sectional observation (Figure 4.1 and Figure 4.2), the Free-Standing HVOF Coating samples (FSCS-HVOF) shows a significantly higher occurrence of unmelted powder particles compared to APS. This difference in microstructure is attributed to the process parameters like powder temperature, velocity, and projection distance as the powders used were identical.

For the HVOF coating, the particles observed are round and measure around 45 μm in diameter. These particles are surrounded by alumina oxides and pores, consistent with the specifications of the NI-191-4 powder. Within these particles, a detailed, dendritic pattern can be observed (Figure 4.3). This microstructural characteristic is indicative of the high-temperature and rapid cooling conditions experienced during the HVOF process. The investigation revealed that the dark gray phase is enriched in aluminum, while the light gray phase contains more nickel. Since the γ-Ni phase is a solid solution with a higher mean atomic number, it appears light gray in BSE mode and is thus identified as γ. Conversely, the dark gray phase, with a lower mean atomic number in BSE mode, is identified as the β-NiAl intermetallic. The γ phase is predominant, with regions of β interspersed within it.

This microstructure analysis reveals that the unmelted particles maintain the original two-phase structure consisting of γ and β phases from the NiCoCrAlY powder even after the deposition process has been completed. This retention of the two-phase structure indicates that the particles did not undergo significant melting during deposition, thereby preserving their original microstructures to some extent.

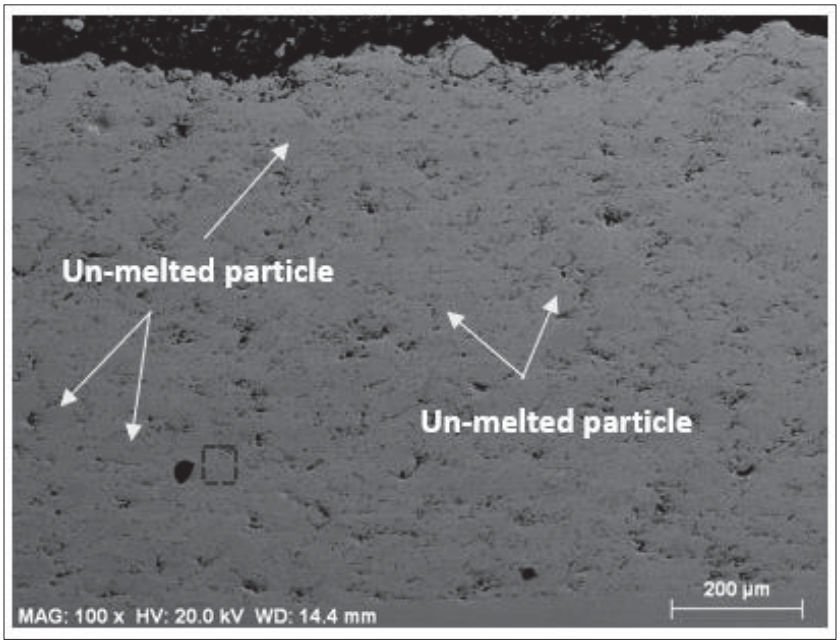

Figure 4.1 Microstructure of the As-Coated HVOF sample at 100x magnification

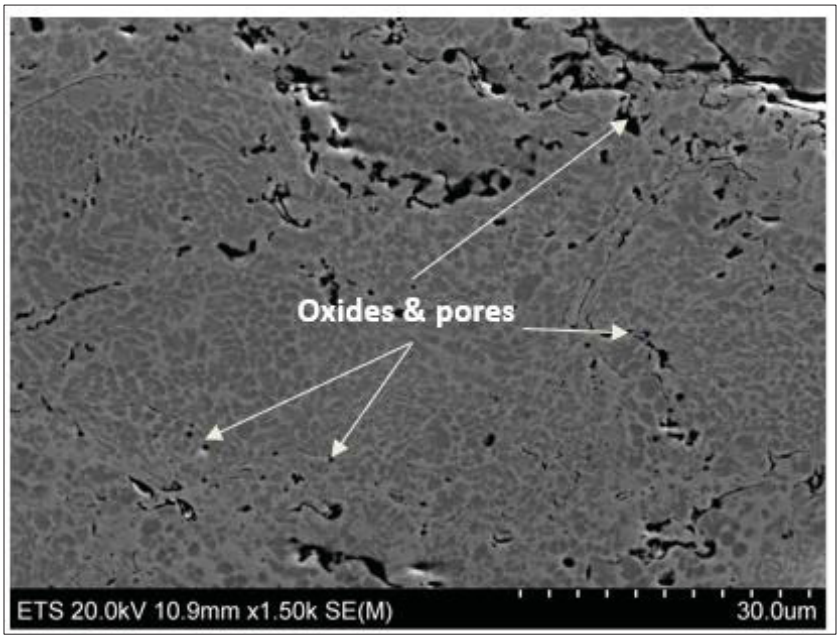

Figure 4.2 Microstructure of the As-Coated HVOF sample at 1.5k magnification

Figure 4.3 shows the micrograph of the as-coated HVOF sample. The re-solidified regions (identified by continuous light gray areas) engulfed the oxides and unmelted particles (identified by dark gray particles within the light gray background).

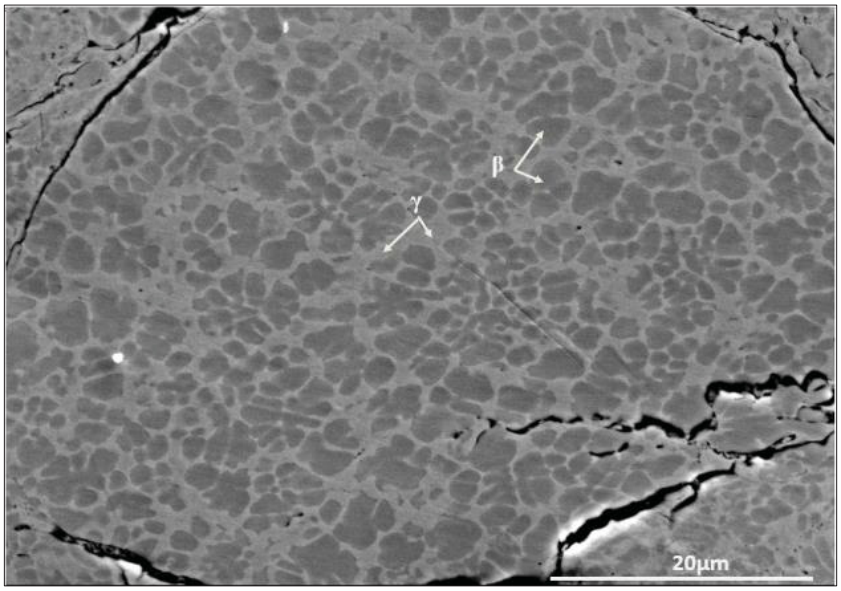

Figure 4.3 The phase distribution in unmelted particles of the As-Coated HVOF coating. The β-phase (bcc) is distinctly embedding the γ phase (fcc)

The presence of the oxides (Figure 4.4) within the coating shows the importance of coating process parameters. There are two primary oxidation mechanisms contribute to the oxygen content within the deposited coatings. The first mechanism, in-flight oxidation, occurs while the particles are heated and accelerated, exposed to the high temperature, oxidizing environment of the HVOF flame. This exposure leads to the formation of oxide layers on the surface of the particles before they impact the substrate. The second mechanism, post-deposition oxidation, takes place after the particles have adhered to the substrate. The high temperature of the substrate and the surrounding atmosphere further promotes oxidation of the particles. These combined mechanisms result in the characteristic oxidation features observed in the as-coated HVOF coatings, influencing the overall microstructure and performance of the coating. Throughout the spraying process, the surfaces of particles that have not fully melted are exposed to elevated temperatures, causing them to start melting. As these particles move

through the air, a thin oxide layer can form on their surfaces. This oxide layer later manifested as elongated oxide inclusions entrapped between semi- or unmelted regions as shown in Figure 4.4 (C.-J. Li & Li, 2003).

This occurrence of oxides and porosities is primarily due to the use of smaller particles, approximately 20 µm in diameter. Smaller particles are more prone to incomplete melting and oxidation during the spray process so the high temperature and rapid cooling involved in HVOF spraying can exacerbate the formation of such defects, leading to a more porous and oxide-rich structure compared to APS. The presence of pores and oxides affect the overall quality and integrity of the coating, underscoring the critical role of particle size and thermal management in the coating process.

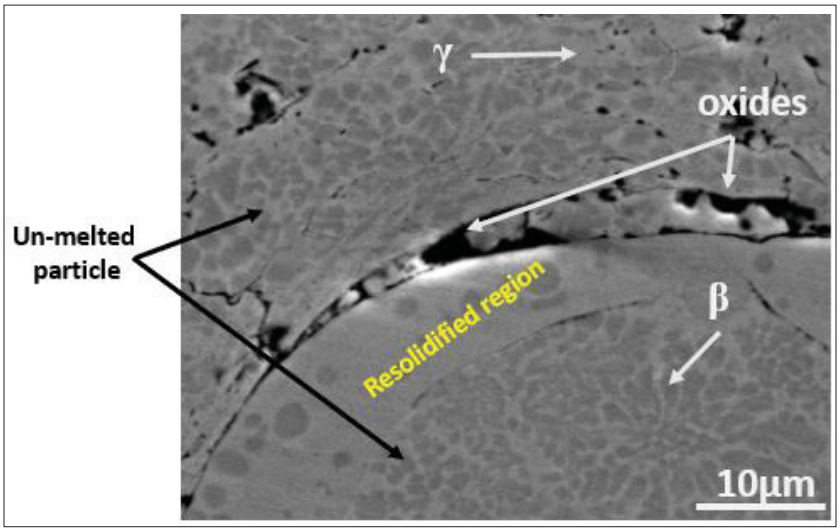

Figure 4.4 SEM micrograph of as-coated HVOF sample illustrating the structure of re-solidified region surrounding unmelted particles and oxides (black areas)

In addition to this, Figure 4.4 provides insight into the characteristics of the resolidified regions of the powder particles. These areas are typically devoid of distinct microstructural features, a condition attributed to the rapid cooling and solidification that occur when the molten material comes into contact with the substrate or previously deposited layers. The high cooling rates prevent the formation of large, distinguishable features within the resolidified material,

resulting in a featureless appearance. This rapid solidification is indicative of the high-energy nature of the deposition process, which leads to the quick transformation of the molten state to a solid state, thereby freezing the material in a nearly homogeneous structure.

4.2.2 Mechanical properties of FSCS-HVOF and FSCS-APS in as-coated condition

Due to the brittle nature of the coatings, obtaining reliable tensile data was challenging. Consequently, the focus of this research shifted to analyzing fracture surfaces and strain distribution on the coating surface using OpenDIC digital image correlation software.

Figure 4.5 presents the stress-strain curves, fracture surfaces, and strain maps of APS and HVOF samples immediately before fracture. This analysis offers valuable insights into the mechanical behavior and strain distribution uniformity of coatings produced by the two methods. As shown in Figure 4.5 (a) and (d), the stress-strain curve of the APS sample exhibits no plastic deformation, whereas the HVOF sample demonstrates slight plastic deformation prior to fracture. Despite this difference, both samples exhibit a similar fracture strength of approximately 190 MPa.

Strain map analysis

For the APS sample, the strain map shows a more uniform strain distribution across the coating. This uniformity suggests that the APS method produced a more homogenous coating, which could contribute to better mechanical performance under stress (Figure 4.5 (b)).

For the HVOF sample in contrast, the strain map reveals significant strain localization, indicating uneven distribution of mechanical stresses. This non-uniformity could lead to premature failure and reduced mechanical integrity of the coating (Figure 4.5 (e)).

Fracture surface analysis

The fracture surfaces of APS samples are smooth and uniform. This smoothness indicates that the coating material failed in a consistent manner, likely due to the homogenous microstructure

imparted by the APS process. The fracture surfaces of HVOF samples, however, are characterized by the presence of numerous unmelted particles, which appear as balls scattered across the surface. These unmelted particles suggest incomplete melting during the HVOF process, leading to a heterogeneous microstructure and, consequently, a more irregular fracture surface (Figure 4.5 (c) and (f)).

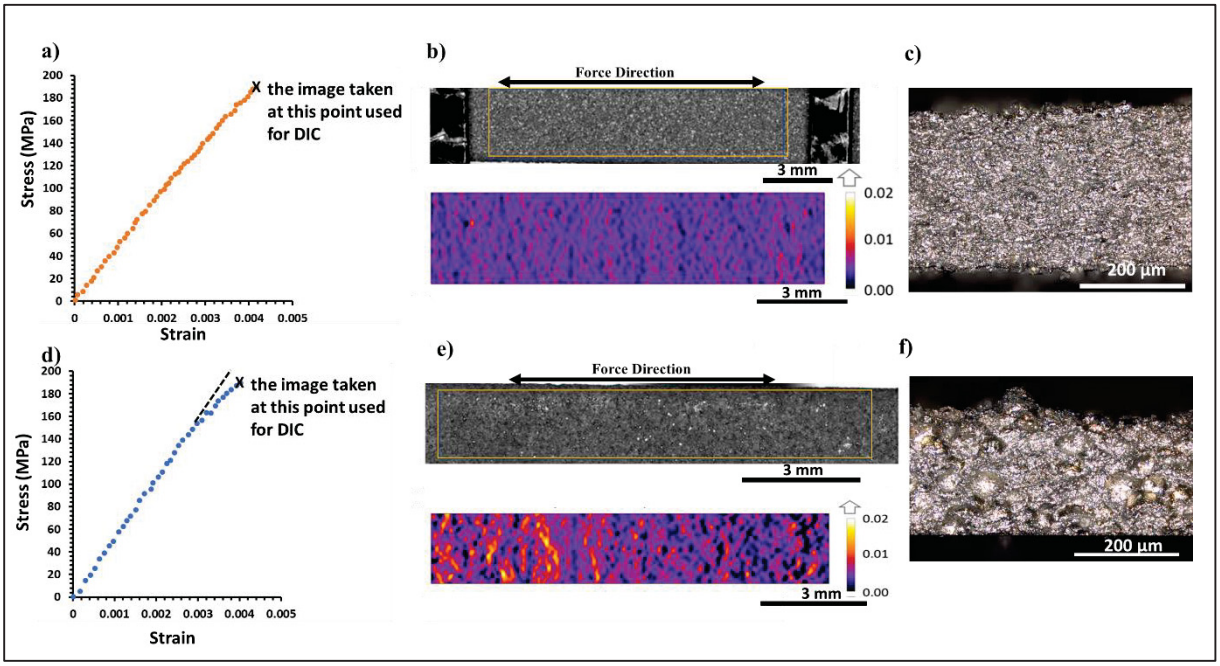

Figure 4.5 Stress-strain curves, strain maps (obtained using the OpenDIC digital image correlation technique), and corresponding fracture surface micrographs for APS and HVOF FSCS samples: (a) Stress-strain curve of the APS sample, (b) Strain map of the APS sample before fracture, (c) Fracture surface micrograph of the APS sample, (d) Stress-strain curve of the HVOF sample, (e) Strain map of the HVOF sample before fracture, (f) Fracture surface micrograph of the HVOF sample.

The differences in strain distribution and fracture surface morphology between APS and HVOF samples highlight the significant impact of the deposition method on the mechanical properties of the coatings:

- **Uniformity of strain**: The more uniform strain distribution in APS samples suggests that this method produces coatings with better mechanical cohesion and resistance to

localized stress concentrations. This uniformity can be beneficial for applications requiring consistent mechanical performance.

- **Fracture surface characteristics**: The smooth fracture surface of APS samples indicates a more cohesive material, whereas the irregular fracture surface of HVOF samples suggests potential weaknesses due to incomplete melting and the presence of unmelted particles. These weaknesses could compromise the overall mechanical integrity of the coating.

While a conclusive tensile testing of FSCS samples (coating samples without substrate) was not feasible due to their brittle nature, the use of digital correlation software to analyze strain maps and fracture surfaces provided valuable insights into the mechanical properties of APS and HVOF coatings. These findings underscore the advantages of APS in producing more uniform and mechanically robust coatings compared to HVOF with these predetermined parameters.

4.3 The oxidation of HVOF as-coated samples on 1050ºC at different exposure time

This section explores the behavior of HVOF samples under isothermal oxidation at 1050 °C. The samples studied include the as-coated sample and those exposed to oxidation for varying durations. To comprehensively analyze the oxidation effects, multiple characterization techniques were employed post-exposure, including X-ray diffraction (XRD), surface imaging using LEXT, scanning electron microscopy (SEM) of cross-sections, and energy-dispersive X-ray spectroscopy (EDX).

4.3.1 Effect of time of exposure to oxidation on surface

Figure 4.6 provides a detailed visual representation of the surface morphology of HVOF coatings subjected to high-temperature oxidation at 1050 ºC over varying exposure times. The

images captured through surface microscopy illustrate the progressive changes in the oxide layer and the associated color variations.

In the initial state, depicted in the panel (a) of Figure 4.6, the surface of the HVOF coating is free from oxides, presenting a uniform appearance. This condition serves as a baseline for understanding the subsequent oxidation behavior. After 30 h of exposure to high-temperature oxidation (Figure 4.6 b), significant changes are evident. A bluish tint begins to appear on the surface, indicating the formation of an oxide scale layer. The presence of both white and blue oxides is notable, suggesting the initial stages of oxide formation and the start of spallation. The visible spallation is consistent with MICF, which occurs due to the stress and structural changes induced by the oxidation process.

Prolonged exposure to oxidation, as shown in the image (Figure 4.6 (c)), reveals an extensive spread of the blue oxide layer across the specimen surface. This uniform bluish tint signifies the dominance of a specific oxide phase that forms over extended periods. The extensive coverage of the blue oxide indicates that the HVOF specimens are susceptible to both InCF and MICF simultaneously, demonstrating the complex and ongoing nature of the oxidation process in these coatings.

4.3.2 Effect of time of exposure on oxidation in cross-section

Subsequent exposure to high temperatures and oxidation significantly alters the morphology and surface of these samples, however, the effects are not limited to the surface and oxidation will penetrate to the depth of the sample. A notable observation is the gradual expansion of the Al depleted region and consequently the expansion of the TGO layer, which increases in thickness with prolonged exposure to oxidation conditions. Figure 4.7 displays the cross-section of the HVOF sample. The TGO layer in HVOF samples quickly reaches its maximum thickness within the initial hours and does not exhibit further significant changes. This rapid stabilization suggests that the TGO layer effectively seals off further oxidation, preventing deeper diffusion into the sample compared to the APS samples.

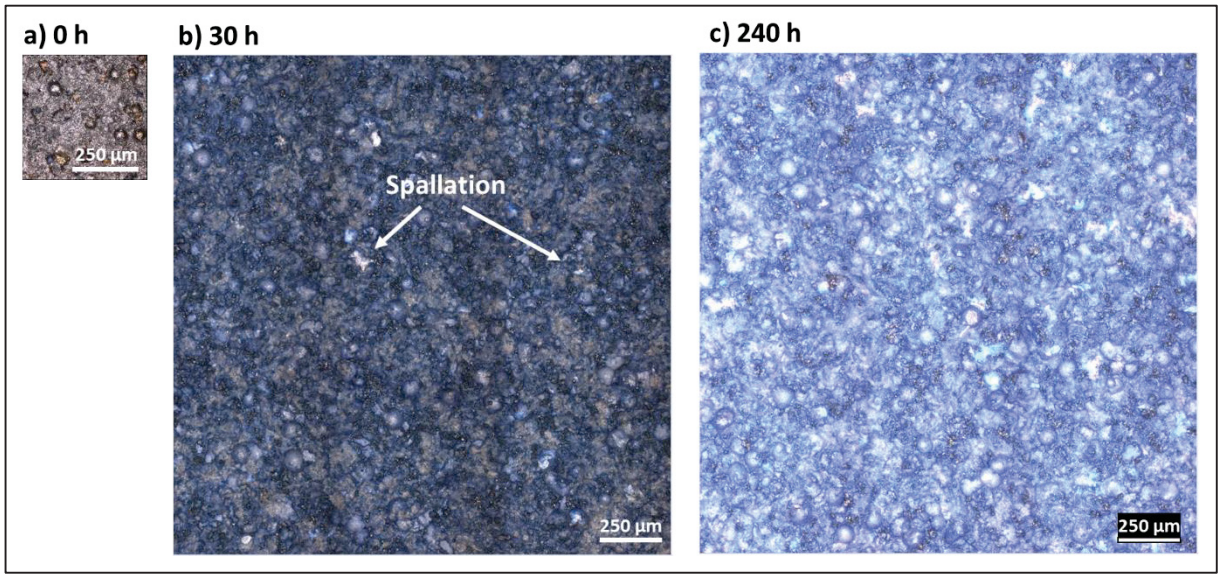

Figure 4.6 Surface microscopy images of HVOF coating post-oxidation at 1050 ºC: (a) As-coated, showing a pristine surface free of oxides; (b) After 30 h, exhibiting the initial formation of white and blue oxides with visible spallation, indicative of MICF; (c) After 240h, displaying extensive coverage of the blue oxide scale, demonstrating susceptibility to both InCF and MICF simultaneously

4.3.3 Effect of 1050 ºC oxidation exposure duration on HVOF coating

In this section, we examine the impact of oxidation exposure time on the thickness of the TGO layer, the extent of the aluminum-depleted region, the surface roughness and the weight change in FSCS-HVOF samples exposed to 1050 °C. Figure 4.8 provides a detailed graphical representation of these variables over time, illustrating four distinct curves: the growth of the TGO layer, the expansion of the Al-depleted region, the stability of samples roughness and the weight gains during the exposure.

- **Initial growth (first 10 hours)**: Within the first 10 h of exposure, the TGO layer quickly grows to approximately 4 microns. Concurrently, the Al-depleted region, which forms as the TGO layer consumes aluminum from the underlying material, expands to about 10 microns. This rapid initial growth phase highlights the aggressive

nature of the oxidation process at elevated temperatures, as the aluminum in the coating rapidly oxidizes to form the protective TGO layer.

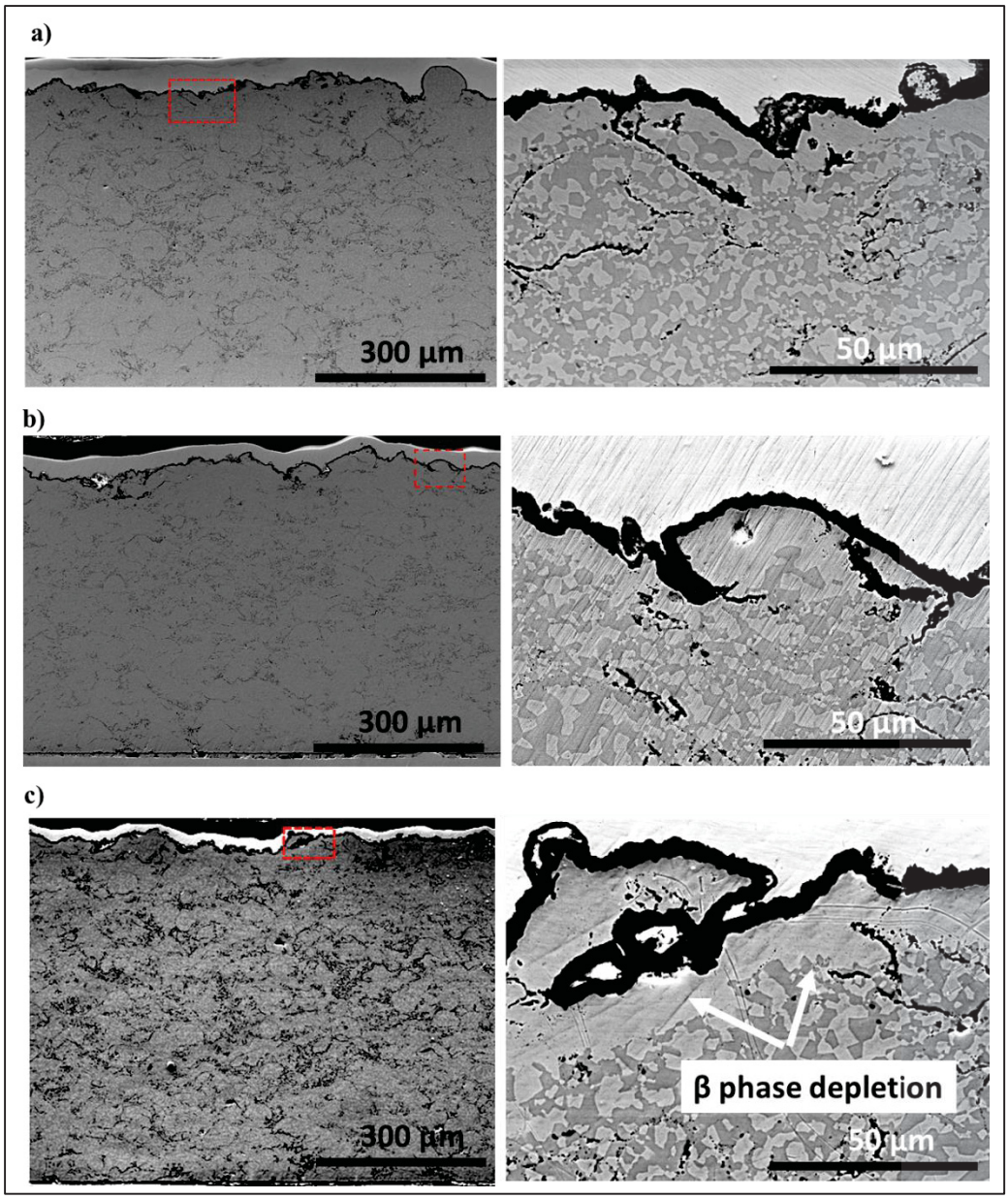

Figure 4.7 Effect of exposure time to high temperature oxidation on microstructure and morphology of HVOF samples (a) 30 h, (b)72 h, and (c) 240 h exposure to oxidation at 1050 °C. It can be seen that more exposure means more depletion of Al in areas close to the surface.

- **Stabilization / low growth rate of TGO thickness**: After the initial surge, the thickness of the TGO layer stabilizes, maintaining a relatively lower growth rate. This suggests that a protective oxide layer has been formed, which slows down further oxidation by acting as a barrier to oxygen diffusion. The stabilization of TGO thickness indicates that the protective mechanism is effective in preventing further rapid oxidation.

The Al-depleted region continues to expand slightly even after the initial phase. Over the course of 240 h, this region increases to about 14 μm. This continued growth indicates balancing diffusion of aluminum from the coating into the surface, which expands the dominant phase (γ) in the region and potentially weakens the coating over time.

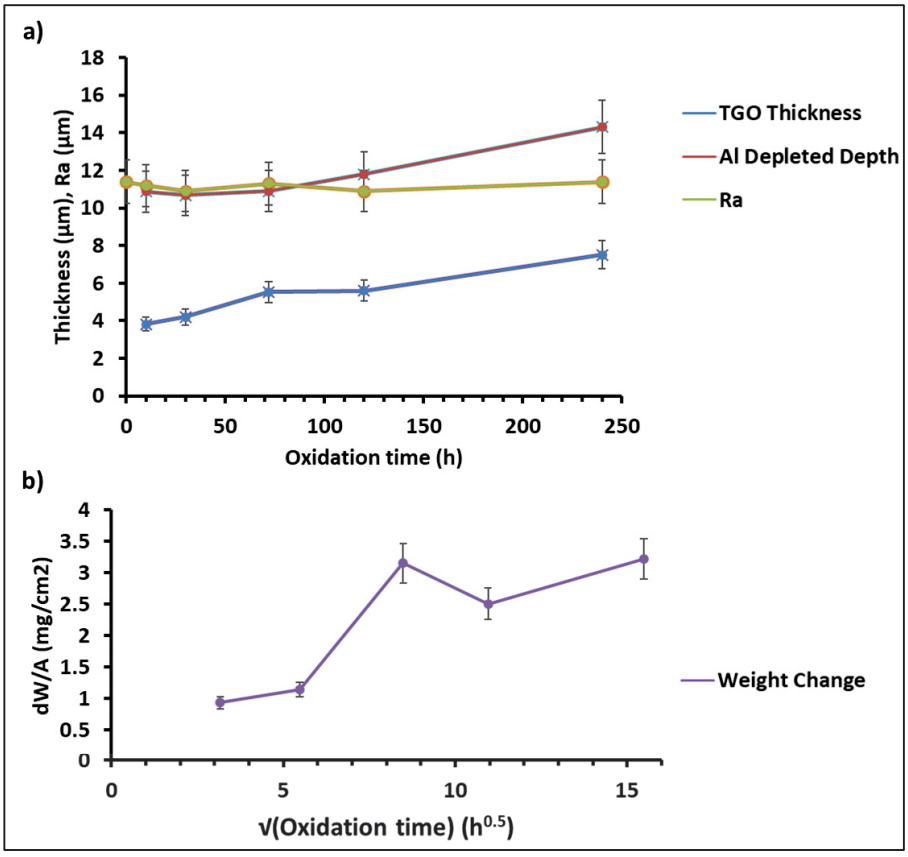

Figure 4.8 (a) TGO thickness, Al-depleted layer thickness, and surface roughness; (b) weight changes for FSCS-HVOF samples subjected to oxidation at 1050 °C over various exposure durations

Despite the significant changes in TGO thickness and the Al-depleted region, the surface roughness of the sample remains remarkably stable during all stages of oxidation. Throughout the whole exposure, the roughness fluctuates within a narrow range of ±1 µm. This stability suggests that the surface morphology is not affected by the formation of the TGO layer or the depletion of aluminum in this case. Over the extended oxidation period of 240 h, the surface roughness continues to exhibit minimal changes. This consistency in roughness indicates that the oxidation process, while affecting the subsurface regions, does not significantly alter the surface topography of the coating at this condition (1050 °C). The protective TGO layer likely provides a stable surface that resists morphological changes even as the underlying material undergoes transformations.

The graph in Figure 4.8 also provides a comprehensive overview of the changes in weight across various oxidation exposure durations which exhibits an overall increase with a distinct drop at the 120-hour mark. The weight change, represented by the violet curve in the figure, indicates the accumulation of oxides as the sample undergoes oxidation.

The initial phase of oxidation (up to 72 h) shows a steady increase in weight, which is consistent with the growth of the TGO layer and the formation of oxides. This increase is a typical indicator of the aluminum oxidation process, where the metal reacts with oxygen to form oxides, resulting in a gain in mass.

A significant drop in weight gain is observed after 120 h. This anomaly in the weight gain trend suggests a disruption in the oxidation process. As confirmed by the micrograph in Figure 4-8, spallation occurs at this stage, where portions of the oxide layer detach from the coating. Spallation is a common issue in high-temperature oxidation, where thermal stresses cause the oxide layer to crack and peel off, leading to a reduction in the overall weight.

After 120 h, the weight change curve resumes its upward trajectory. This indicates that post-spallation, the oxidation process continues, forming new oxides and increasing the sample's weight once again.

The weight change analysis during the oxidation of FSCS-HVOF samples highlights the dynamic nature of the oxidation process, influenced by the formation and spallation of oxide layers. The observed weight drops at 120 h underscores the significance of spallation in disrupting the protective oxide layer, leading to transient weight loss before the oxidation process resumes. This late-stage growth could be attributed to the breakdown of the protective oxide layer, leading to accelerated oxidation and formation of new unprotected oxides spallation.

4.3.4 Effect of 1050 ºC oxidation exposure on HVOF coating composition

Figure 4.9 provides a detailed microstructural analysis of an HVOF sample subjected to oxidation at 1050 °C for 120 h. The figure reveals critical insights into the oxidation behavior, elemental distribution, and microstructural changes occurring within the sample. In Figure 4.9 (a) BSE Image, a continuous black layer of oxides is visible between the nickel plating and the substrate (the dashed red line visually separating the Ni-plating that was applied to improve the polishing process and preserve the surface coating from polishing stress). A notable feature in this image is the spallation area, where the continuous oxide layer is broken, indicating regions where the oxide layer has been detached from the substrate.

The aluminum distribution map in Figure 4.9 (b) shows a bright TGO layer at the surface, indicating regions rich in aluminum oxides. Additionally, areas of aluminum depletion are visible in the substrate just beneath the TGO layer. This depletion suggests that aluminum atoms have diffused towards the surface to form the TGO layer.

Like the aluminum map, the oxygen distribution map in Figure 4.9 (c) highlights the TGO layer as bright areas, confirming the presence of aluminum oxides. The spallation area, encircled with a dashed oval, is evident in this map, indicating a region lacking the TGO layer.

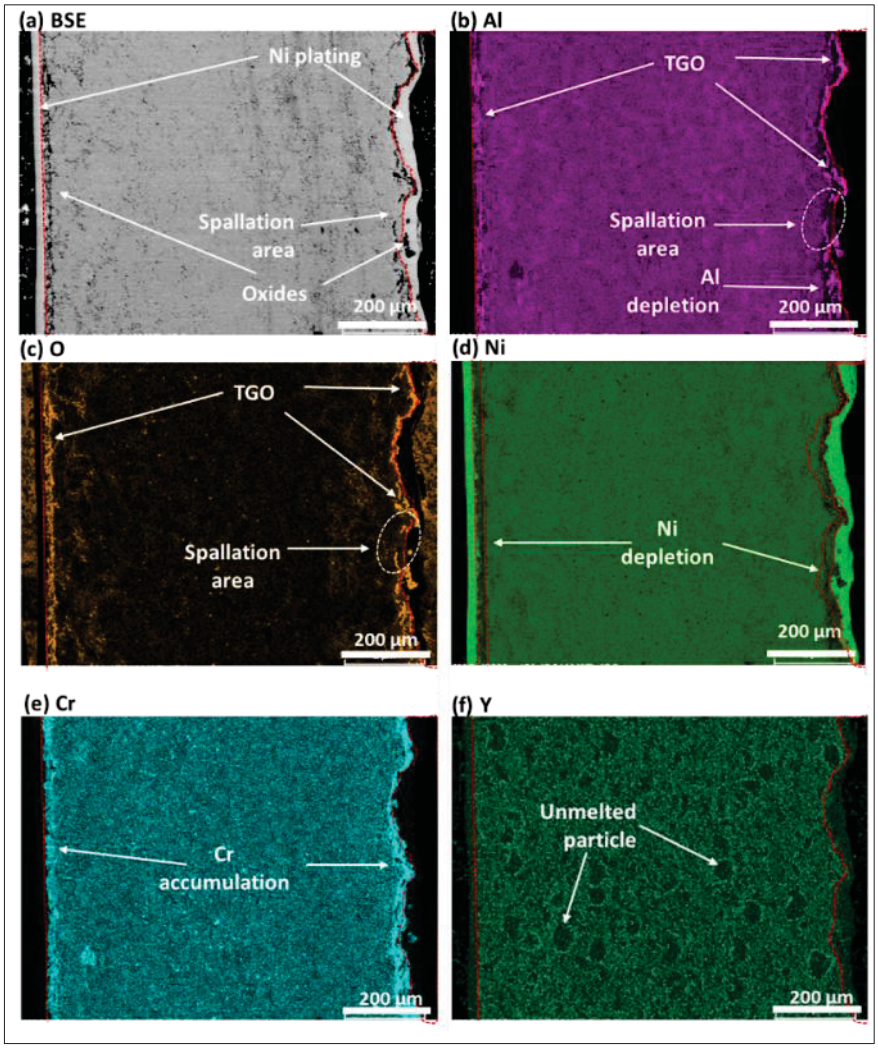

Figure 4.9 Microstructural analysis of an HVOF sample after 120 h of oxidation at 1050 °C. (a) BSE image showing the oxide layer, nickel plating, and spallation area; (b) aluminum distribution map; (c) oxygen distribution map; (d) nickel distribution map; (e) chromium distribution map; (f) yttrium distribution map. The analysis was conducted at 15 kV and a magnification of 130 x, clearly revealing the TGO layer, spallation regions, and detailed elemental distributions.

The nickel distribution map in Figure 4.9 (d) reveals a distinct area of nickel depletion adjacent to the TGO layer. This depletion indicates that nickel atoms have migrated away from the surface. The chromium distribution map (e) shows a contrasting behavior compared to nickel. Chromium atoms accumulate at the substrate surface and the TGO layer, similar to the behavior of aluminum atoms. This accumulation suggests the formation of chromium-rich

oxides within the TGO layer. The Yttrium map in Figure 4.9 (f) is showing the unmelted particles coated with Yttrium encircling areas with lower Yttrium contents. The depletion of nickel and the accumulation of chromium and aluminum at the surface indicate significant elemental migrations driven by the oxidation process.

Figure 4.10 provides an in-depth microstructural analysis of an HVOF sample after 240 h of oxidation at 1050 °C. The figure is revealing critical insights into the distribution of elements and the development of the TGO layer. The BSE image in Figure 4.10 (a) shows the overall structure of the HVOF sample. The oxides are visible as a black continuous layer between the nickel plating and the sample's surface. This TGO layer forms a clear distinction, indicating the oxidation front.

The aluminum distribution map in Figure 4.10 (b) highlights the TGO layer as brighter areas, indicating regions rich in aluminum oxides. Additionally, areas of aluminum depletion are visible in the substrate just beneath the TGO layer.

Similar to the aluminum map, the oxygen distribution map in Figure 4.10 (c) clearly shows the TGO layer as bright areas, confirming the presence of aluminum oxides. However, compared to the sample exposed 120 h to oxidation, the thickness of the TGO is visibly greater.

The nickel distribution map in Figure 4.10 (d) reveals a distinct area of nickel depletion inside and beneath the TGO layer. This depletion indicates that nickel atoms have migrated away from the surface, contributing to the formation of the TGO layer and possibly diffusing into the oxide scale.

The chromium distribution map in Figure 4.10 (e) shows that chromium atoms entirely diffuse from coating to beneath the TGO layer, accumulating at the substrate surface just beneath the TGO layer. This behavior suggests that chromium is unable to form oxides inside the TGO layer, leading to its accumulation in specific regions.

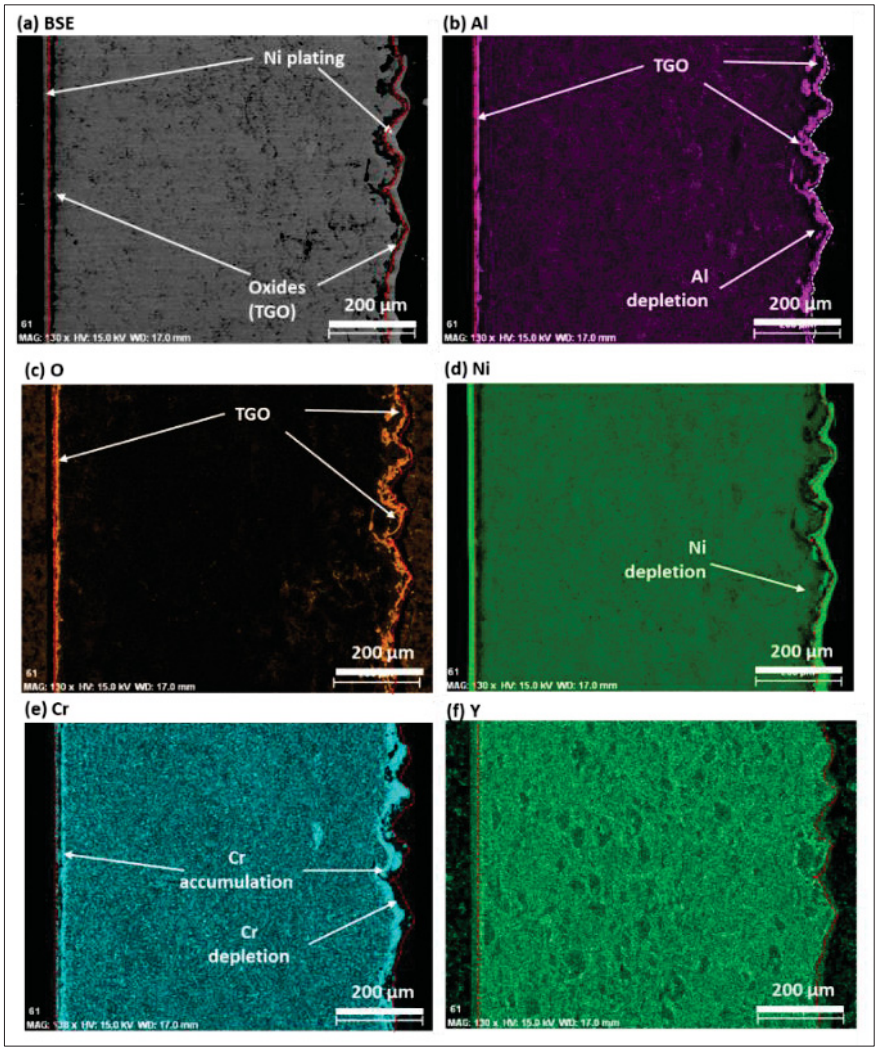

Figure 4.10 Microstructural Analysis of HVOF Sample After 240 h of Oxidation at 1050 °C. (a) BSE image showing the oxide layer and nickel plating; (b) Al distribution map; (c) O distribution map; (d) Ni distribution map; (e) Cr distribution map; (f) Y distribution map. The analysis was conducted at 15 kV with a magnification of 130x. The TGO layer, areas of elemental depletion, and accumulations are clearly visible

The yttrium distribution map in Figure 4.10 (f) indicates a slight accumulation of yttrium within the first few microns of the TGO surface a proof on how Yttrium's role in stabilizing the oxide layer and enhancing its protective properties.

4.3.5 The oxides formation in HVOF samples exposed to oxidation at 1050 °C

This section discusses the formation of oxides in HVOF samples exposed to 1050 °C, based on X-ray diffraction (XRD) analysis. Figure 4.11 displays the XRD results for different oxidation durations, highlighting the types of oxides detected over time.

Figure 4.11 shows the XRD patterns for HVOF samples after 0, 10, 30, 72, 120, and 240 h of exposure to high-temperature oxidation at 1050 °C. The key observations from these patterns are as follows:

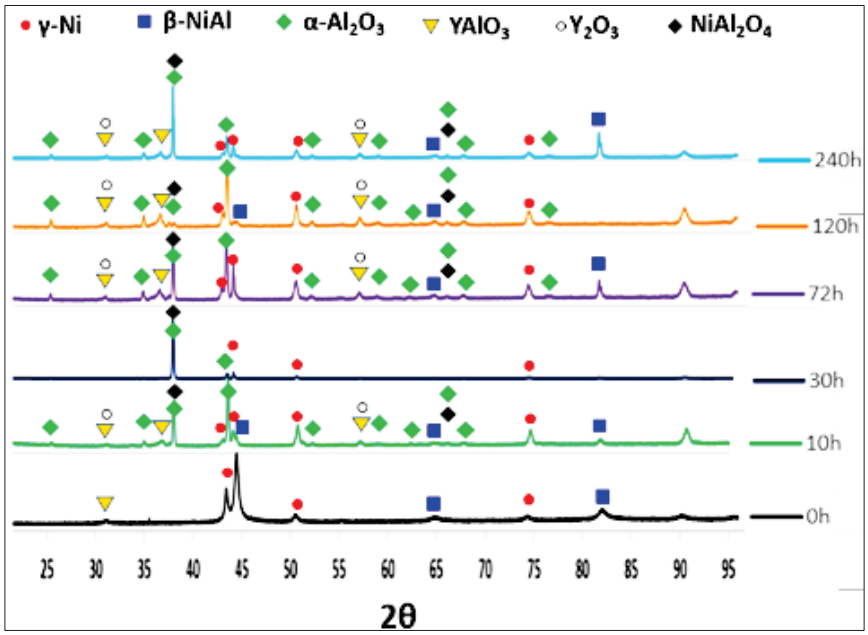

Figure 4.11 XRD Patterns Showing the Formation of Various Oxide Phases (γ-Ni, β-NiAl, α-Al_2O_3, $YAlO_3$, Y_2O_3, $NiAl_2O_4$) in HVOF Samples Exposed to 1050 °C for Different Durations (0 , 10 , 30 , 72 , 120 , and 240 h). The Data Illustrates the Immediate Formation of Oxides Upon Exposure and Their Persistence Over Time

All types of oxides, including α- Al_2O_3, $YAlO_3$, Y_2O_3, and spinel ($NiAl_2O_4$), form as soon as the samples are exposed to high-temperature oxidation. This indicates a rapid onset of oxidation processes upon exposure to 1050 °C, leading to the immediate formation of various oxide phases. The XRD patterns reveal that these oxide phases persist throughout the different oxidation durations, suggesting a stable formation of these oxides over time. The presence of

these phases from 10 h to 240 h highlights the continual oxidation and transformation processes occurring in the HVOF samples.

While the XRD data provides valuable qualitative insights into the types of oxides forming in the HVOF samples, it is important to note the limitations of this method. Due to the inherent constraints of the XRD method, such as high errors in phase percentage estimation and the sensitivity of parameter selection during phase calculation, the data cannot be reliably used for quantitative analysis. This means that while the presence of different oxide phases can be confirmed, their exact quantities or proportions cannot be accurately determined from these XRD patterns. Further quantitative analysis using complementary methods would be necessary to obtain a more detailed understanding of the oxide phase distributions and their implications on the material properties.

4.3.6 Microstructure evolution through the thickness of FSCS-HVOF

In this section, the analysis of the microstructural evolution through the thickness of freestanding HVOF (FSCS-HVOF) samples is done. The 120 h of oxidation at 1050 °C is selected as a representative of such evolution focusing on the distribution of beta (β), gamma (γ), and oxide phases from the surface to the core of the samples. The phase fractions were measured at various depths, providing insights into the changes occurring within the material due to prolonged high-temperature exposure.

Figure 4.12 illustrates the phase fractions of beta, gamma, and oxides at different depths from the surface of the FSCS-HVOF samples. At the surface, the beta phase is present in very small quantities, while the gamma phase constitutes approximately 75% of the material. The remaining 25% is composed of oxides. The low presence of beta phase at the surface is attributed to aluminum depletion, which is consumed during the formation of the oxide layer, predominantly consisting of aluminum oxide (Al_2O_3). Moving inward from the surface to a depth of about 100 microns, there is a significant shift in the phase fractions. The gamma phase drops rapidly to about 50%, while the beta phase increases to around 50%. The oxide content

decreases to about 5%. This transition reflects the depletion of aluminum stops at the surface, leading to the formation of the gamma phase and the transformation of the beta phase only at the surface and within the ranges of microns.

Beyond 100 µm, extending towards the center of the sample (up to 500 µm), the phase fractions of beta and gamma remain relatively stable, each constituting approximately 50% of the material. The oxide content further decreases slightly to 0-3%, indicating a reduced presence of oxidation products deeper within the sample.

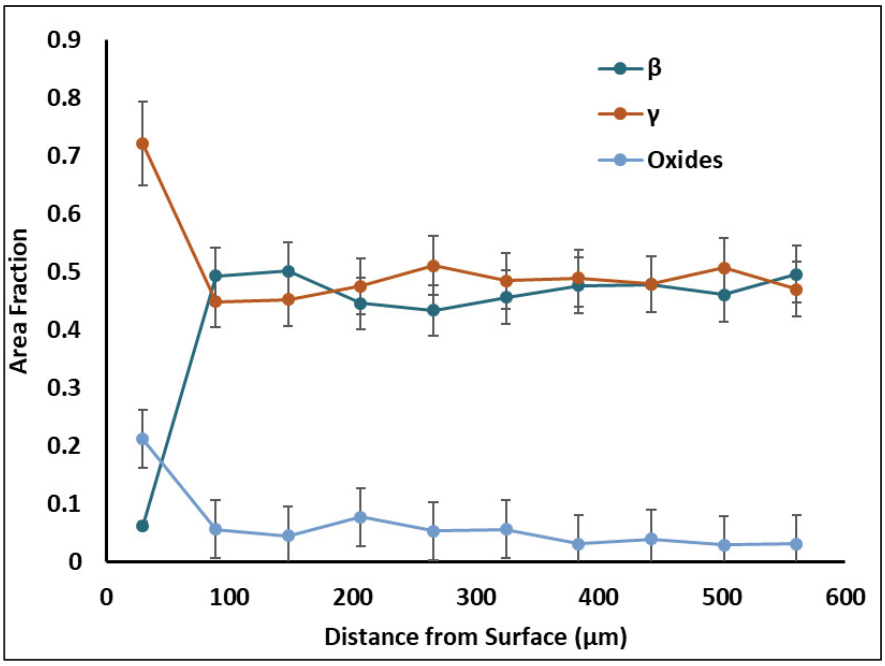

Figure 4.12 Microstructure Evolution in Thickness of FSCS-HVOF after 120 h of oxidation at 1050 °C in different distances from the surface.

The surface region shows a low beta phase and high gamma phase due to the consumption of Aluminum in forming the protective oxide layer. As Aluminum is depleted, the beta phase, which is Al-rich, diminishes, leading to an increase in the gamma phase. Deeper within the sample, the beta and gamma phases stabilize as the material reaches a region where aluminum depletion or oxygen diffusion are less pronounced. The protective oxide layer formed at the surface acts as a barrier, slowing down further inward diffusion of oxygen and aluminum depletion.

4.3.7 Effect of the initial surface roughness on oxidation of as-coated HVOF and APS samples at 1150 ºC

This section investigates the impact of the initial surface roughness on the oxidation behavior of samples produced by APS and HVOF methods. A total of eight samples were prepared for each method. The first sample in each set was left as-coated (level 0), while the remaining seven samples were polished to achieve specific roughness levels ranging from L0 (roughest) to L7 (smoothest) (Table 4.1). The initial roughness and weight of each sample were measured before exposure to high-temperature oxidation at 1150 °C for one hour (Figure 4.13). Post-oxidation measurements of roughness and weight were then conducted to assess the effects of the initial surface polishing. The figure presents the roughness change and weight changes for every initial roughness level after 1 h of oxidation for HVOF samples and APS samples as a comparison measure. There were minor changes in roughness not clearly visible in this figure; therefore, the next figure (Figure 4.14) exclusively presents the roughness changes as a function of the initial roughness (ΔS_a).

Table 4.1 Surface preparation levels (L0–L7) and their surface roughness values in µm.

Levels	L0	L1	L2	L3	L4	L5	L6	L7
APS	8.2	7.9	7.8	6.4	5.4	4.6	2.9	0.1
HVOF	11.6	11.1	9.9	8.7	7.3	7.8	5.5	0.2

The Figure 4.14 (a) indicates that lower initial roughness levels (smoother surfaces) result in a greater increase in roughness after oxidation for HVOF samples. This suggests that smoother surfaces are more prone to roughening during high-temperature exposure, however it is probable that this effect is due to the fact that relative roughness values have been used. The results of APS samples show a similar trend showing that this finding is not affected by coating method although, HVOF samples exhibited a more pronounced sensitivity to initial polishing. Highly polished HVOF samples ended up with slightly rougher surfaces post-oxidation compared to their APS counterparts. This indicates that HVOF coatings may have a higher susceptibility to surface degradation when initially polished to a smoother finish.

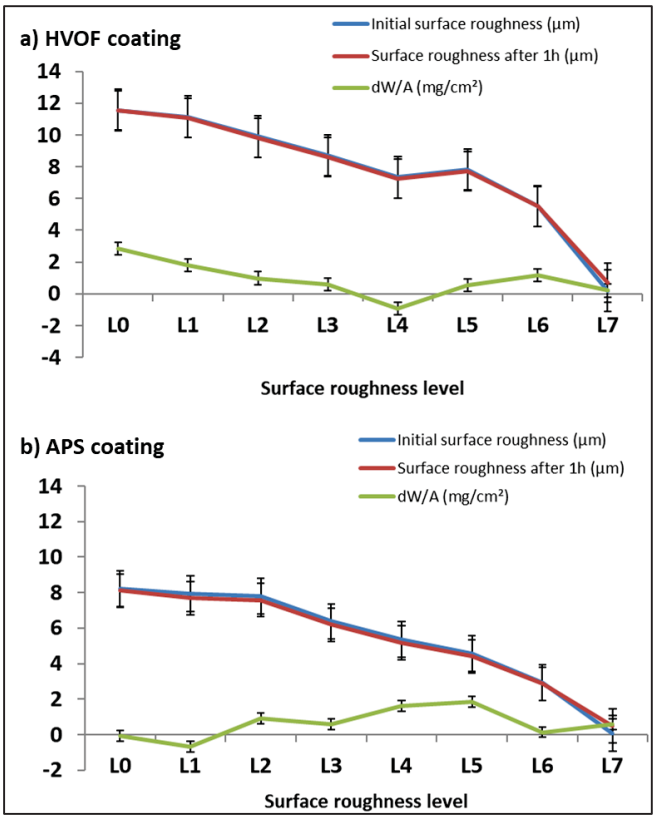

Figure 4.13 Changes in roughness and weight after 1h exposure to oxidation at 1150 °C: (a) HVOF coating, (b) APS coating.

HVOF samples demonstrated a decrease in terms of weight gain as the initial surface becomes smoother (Figure 4.14 (b)). This trend implies that smoother surfaces are less prone to oxidation-related weight gain in HVOF samples. For APS samples, a mid-roughness seems to have the highest weight gain as the roughest and smoothest surfaces have the lower weight gains.

At some initial roughness levels, spallation (weight loss) was more prevalent. This is evident from the steep drops in the weight gain curves, indicating that some surfaces experienced more frequent and severe spallation events. This suggests that polishing may lead to a less stable oxide layer, which is more likely to spall off during oxidation.

The results clearly demonstrate the significant role of initial surface roughness in the oxidation behavior of HVOF and APS coatings. The following key points summarize the findings:

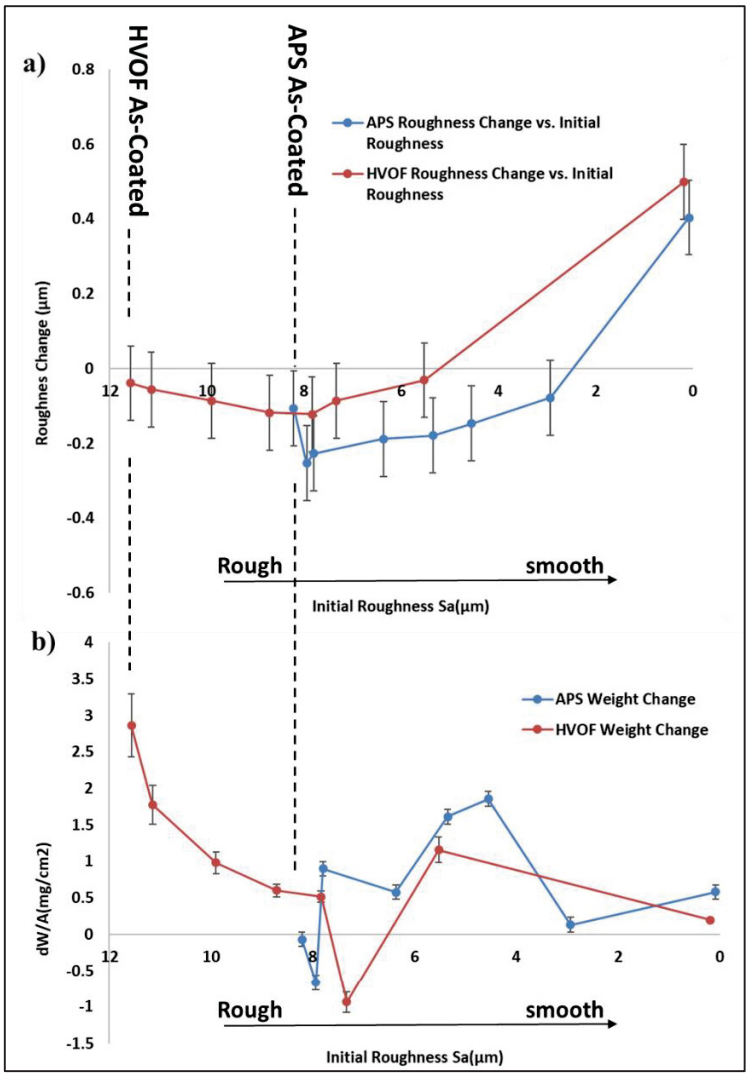

Figure 4.14 The effect of initial surface roughness on the roughness (a) and weight changes (b) after 1h exposure to oxidation at 1150 °C.

- **Surface Stability**: Smoother initial surfaces tend to become rougher after oxidation, indicating a destabilization process that may be attributed to the differential growth of oxide scales and underlying microstructural changes. Additionally, the polishing process removes the oxide barrier formed during the deposition process. This surface condition exposes and expands the channels and diffusion pathways, facilitating the outward diffusion of various element atoms to promote the growth of the oxide layer on the surface.

- **Oxidation Resistance**: The decrease in weight gain for smoother surfaces suggests that these surfaces may offer better resistance to oxidation. This could be due to fewer defects and cracks and a more uniform distribution of the protective oxide layer.

- **Method-Specific Sensitivities**: HVOF samples are more adversely affected by initial polishing than APS samples, resulting in rougher surfaces after oxidation. This highlights the need for careful consideration of initial surface treatments based on the coating method used.

Future research could extend the exposure time to oxidation to further explore the microstructural mechanisms driving these changes and develop strategies to mitigate adverse effects.

Figure 4.15 and Figure 4.16 display the surface micrographs of HVOF and APS samples in their as-coated conditions, with initial roughness levels of 11.6 μm and 8.2 μm (as-coated), 8.7 μm and 6.4 μm (intermediate roughness), and 0.2 μm and 0.1 μm (mirror-polished), respectively. Macrographs were obtained for both APS and HVOF coatings following oxidation interruption at 1150 °C. After one hour of oxidation, all specimens exhibited a continuous gray surface layer, with blue oxide regions prominently observed in areas of higher roughness, corresponding to the external oxide scale, as shown in Figure 4.15 and Figure 4.16.

This localized variation in oxidation behavior, which may have been preceded by oxide spallation, is consistent with the MICF mechanism observed in these thick specimens. Visible roughness changes were apparent across all samples, with the smoothest surfaces experiencing the most significant impact (high initial surface roughness change). For samples with intermediate roughness levels, initial surface roughness changes remained noticeable, particularly in the polished zones, while the least pronounced initial surface roughness changes were observed in samples with higher roughness level, as depicted in Figure 4.14 (a).

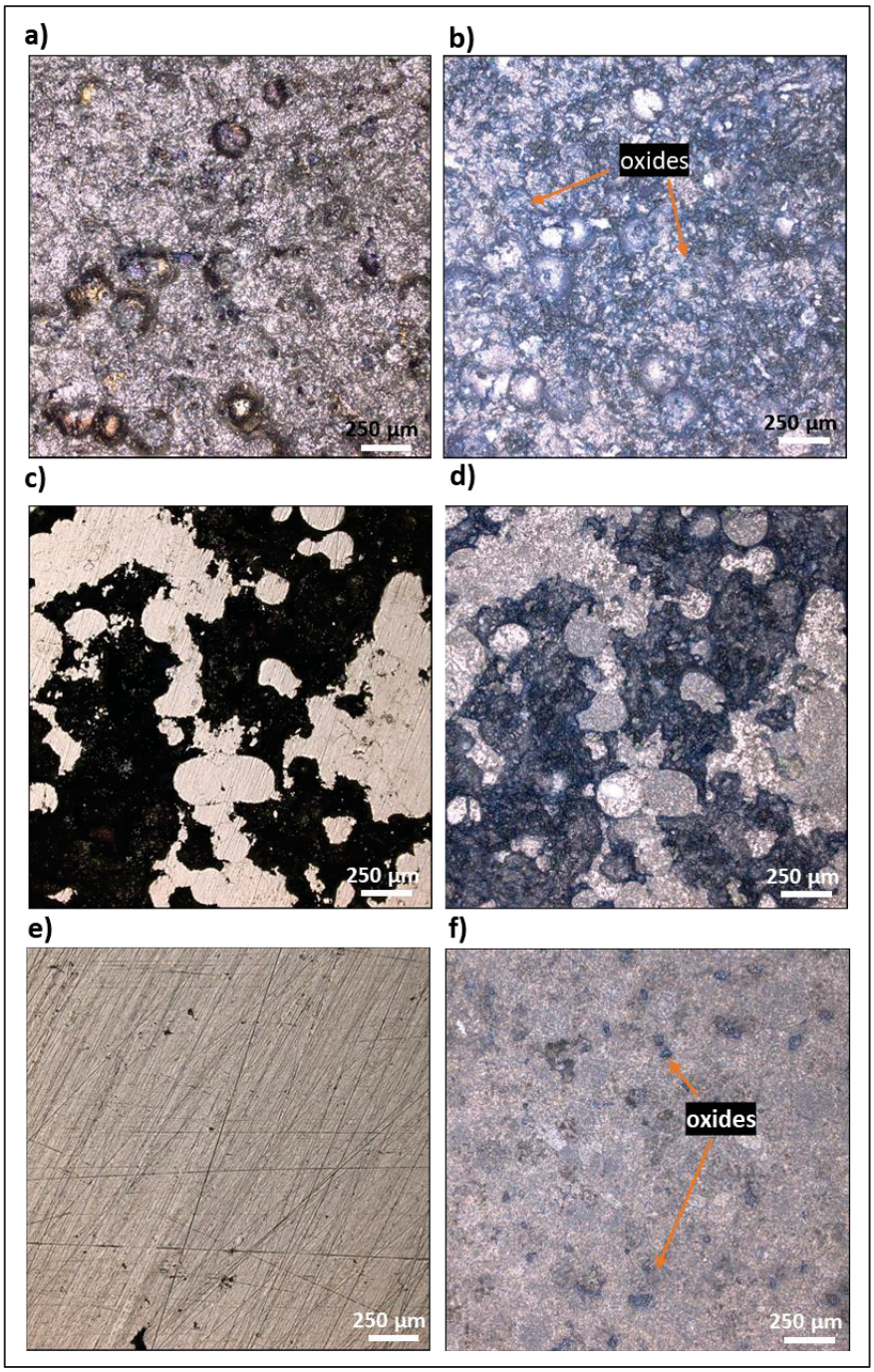

Figure 4.15 Surface micrographs of HVOF-coated samples in the as-coated condition and at initial roughness levels of L3 (8.7 µm) and L7 (0.2 µm). (a) HVOF as-coated; (b) HVOF as-coated after 1 h of oxidation; (c) HVOF with an initial roughness of 8.7 µm; (d) HVOF with an initial roughness of 8.7 µm after 1 h of oxidation; (e) HVOF with an initial roughness of 0.2 µm; (f) HVOF with an initial roughness of 0.2 µm after 1 hour of oxidation.

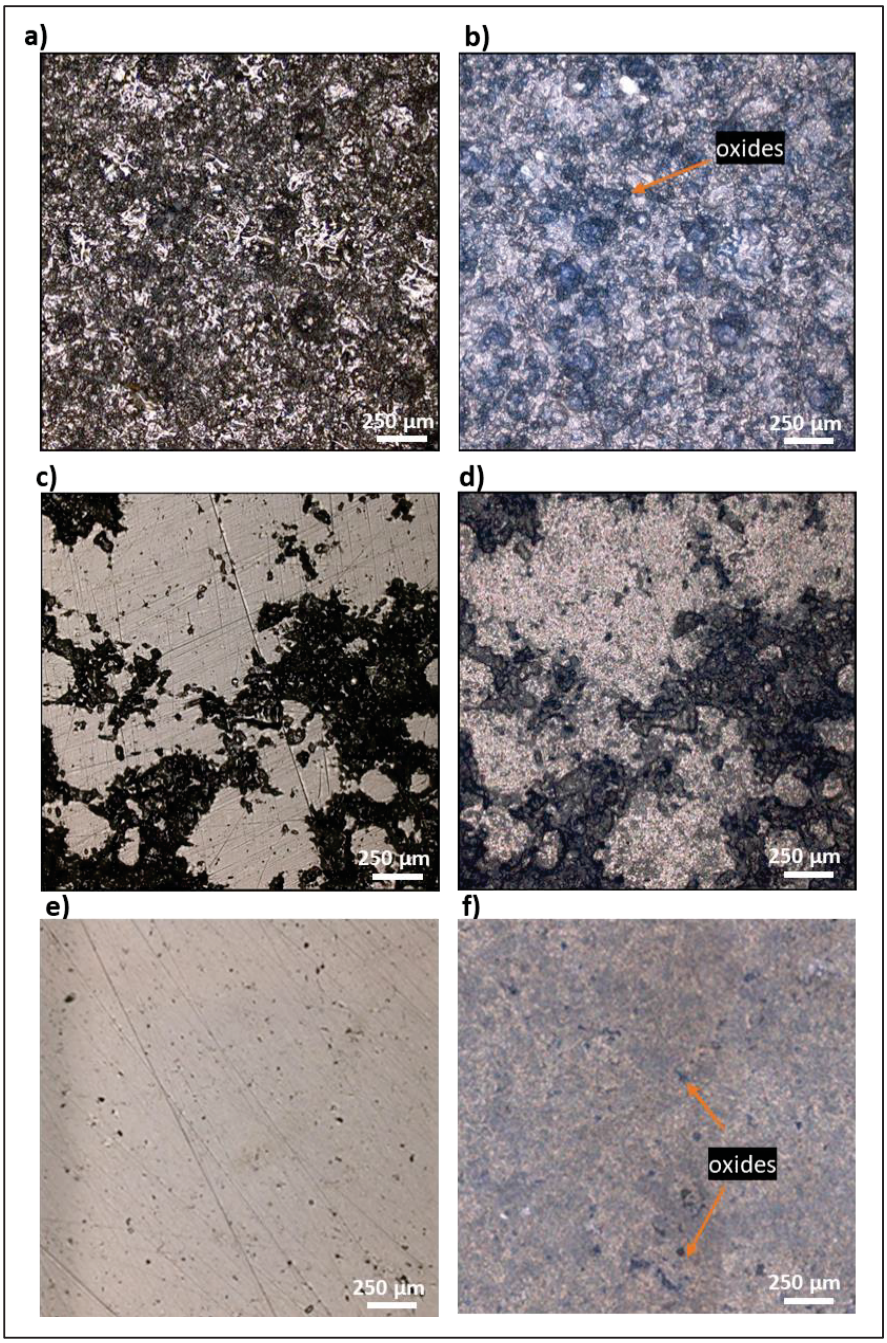

Figure 4.16 Surface micrographs of APS as-coated samples in the as-coated condition and at initial roughness levels of L3 (6.4 µm) and L7 (0.1 µm). (a) APS as-coated; (b) APS as-coated after 1 h of oxidation; (c) APS with an initial roughness of 6.4 µm; (d) APS with an initial roughness of 6.4 µm after 1 hour of oxidation; (e) APS with an initial roughness of 0.1 µm; (f) APS with an initial roughness of 0.1 µm after 1 h of oxidation.

4.4 The characteristics of as-received HVOF and APS samples and their oxidation after isothermal heat treatments

The so-called “as-received” samples used in this project had already undergone a standardized heat treatment, typically applied to high-temperature barrier coatings, before being received. This heat treatment consisted of two stages: an initial stage involving heating at 1080 °C for 8 h, followed by a secondary stage at 870 °C for 20 h. These post-deposition heat treatments are routinely applied to improve coating adhesion to the substrate through interdiffusion, thereby optimizing the mechanical properties of Ni-based substrates and it is expected to introduce a certain level of surface oxidation. The cross-sections of these samples were analyzed through metallographic examination both before and after undergoing additional isothermal oxidation at 950 °C and 1050 °C.

4.4.1 The microstructure of as-received HVOF and APS samples

The microstructure of the “as-received” HVOF and APS coatings (coating application + the two stage heat treatment), as shown in Figure 4.17, includes distinct β and γ phases, which can be identified in BSE mode by their dark and light gray appearances, respectively. Both coatings exhibit common characteristics of thermally sprayed materials, such as melted and resolidified powder particles, unmelted powder particles, pores, dispersed alumina oxides, and resolidified splats.

4.4.2 Evaluation of initial surface conditions on APS samples following additional oxidation heat treatment using TGA

The effect of initial surface conditions on the oxidation rate is a compelling subject in TBC applications, as surface conditions can be readily modified to enhance the oxidation resistance and longevity of coatings used in high-temperature applications. To achieve this, three surface conditions were examined: polished thick samples (referred to as 'Thick' samples), polished thin samples (referred to as 'Thin' samples), and as-coated rough surfaces (referred to as

'Rough' samples). The impact of these conditions on oxidation rates and coating reactions was studied during additional isothermal oxidation at 950 °C and 1050 °C.

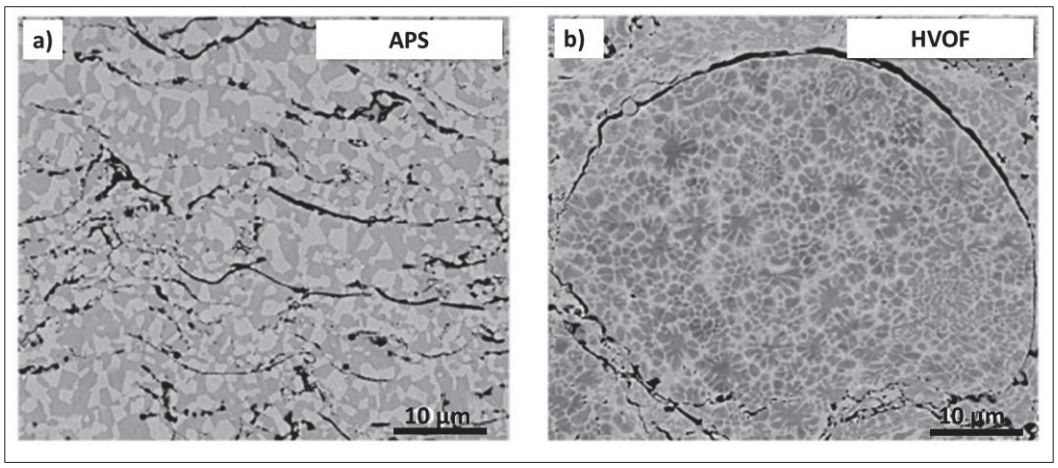

Figure 4.17 Microstructure of the as-received HVOF and APS coating (coating application + HT at 1080 °C for 8 h followed by a secondary HT at 870 °C for 20 h) showing the microstructure in two observation planes: (a) and (c) APS-NiCoCrAlY cross-sectional observation with two magnifications, (b) and (d) HVOF-NiCoCrAlY cross-sectional observation with two magnifications

TGA of oxidation at 950 °C

As mentioned above, the samples were categorized into three surface conditions:

- Rough sample: As-received with inherent surface roughness.
- Thick sample: Polished but maintaining substantial thickness.
- Thin sample: Polished and reduced in thickness.

TGA tests measure weight changes during heat treatment, providing quantitative data on the extent of oxidation. The TGA curves in Figure 4.18 (a) indicate that oxidation mas gain begins at approximately 400 °C. Beyond 400 °C, a significant increase in mass gain was observed, particularly in the rough samples. In contrast, the polished thick and thin samples exhibited similar oxidation behavior, indicating that the sample thickness did not influence the oxidation sensitivity at this temperature (950 °C). Over time, the oxidation rate of the Rough sample (shown in gray in (b)) remains significantly lower than that of the other two conditions, exhibiting noticeably lower mass gain. However, during the initial hours of exposure, the

oxidation behavior was almost similar for all samples. Over time the oxidation rate increased significantly in case of polished sample regardless to the sample thickness, in contrast, the rough sample exhibited more stable with low oxidation rate. The Rough Sample gains approximately one fourth the weight of the polished samples (0.008 mg/cm^2 compared to 0.016 mg/cm^2). This indicates that the surface inherently present in the as-received samples provides a level of resistance to oxidation, likely due to the strength of the oxides scale that formed during heat treatment processes, which reduces the pathways available for oxygen diffusion.

TGA of oxidation at 1050 °C

Figure 4.19 illustrates the oxidation behavior of APS samples at 1050 °C, shown as mass gain over time and temperature. Figure 4.19 (a) shows the weight percentage change per surface unit as the temperature increased up to 1050 °C. A significant rise in mass gain was observed starting at 400 °C, similar to the behavior seen during oxidation at 950 °C. However, differences in oxidation kinetics become apparent at higher temperatures. In Figure 4.19 (b), the figure represents the mass gain over 200 hours of isothermal exposure at 1050 °C. During the initial stages, the rough sample exhibited a higher oxidation rate compared to both polished samples. Despite this, the rough sample's oxidation behavior quickly stabilized and remained consistent throughout the test duration. Figure 4.19 (c), the log-log plot of the curves from Figure 4.19 (b) provides a detailed comparison of oxidation rates. The thin polished sample showed more stability compared to the polished thick sample; however, both polished samples displayed less stable oxidation rates than the rough sample.

These findings highlight that surface preparation significantly influences the oxidation stability of APS samples, with rough samples exhibiting more consistent behavior under prolonged isothermal conditions at 1050 °C. The TGA tests at 950 °C and 1050 °C revealed that rough APS samples exhibited greater oxidation resistance and stability due to the formation of a protective oxide scale. In contrast, both thick and thin polished samples showed higher oxidation rates and less stability, with no significant difference in behavior between the two

polished conditions. These findings highlight the critical role of surface roughness in enhancing oxidation resistance.

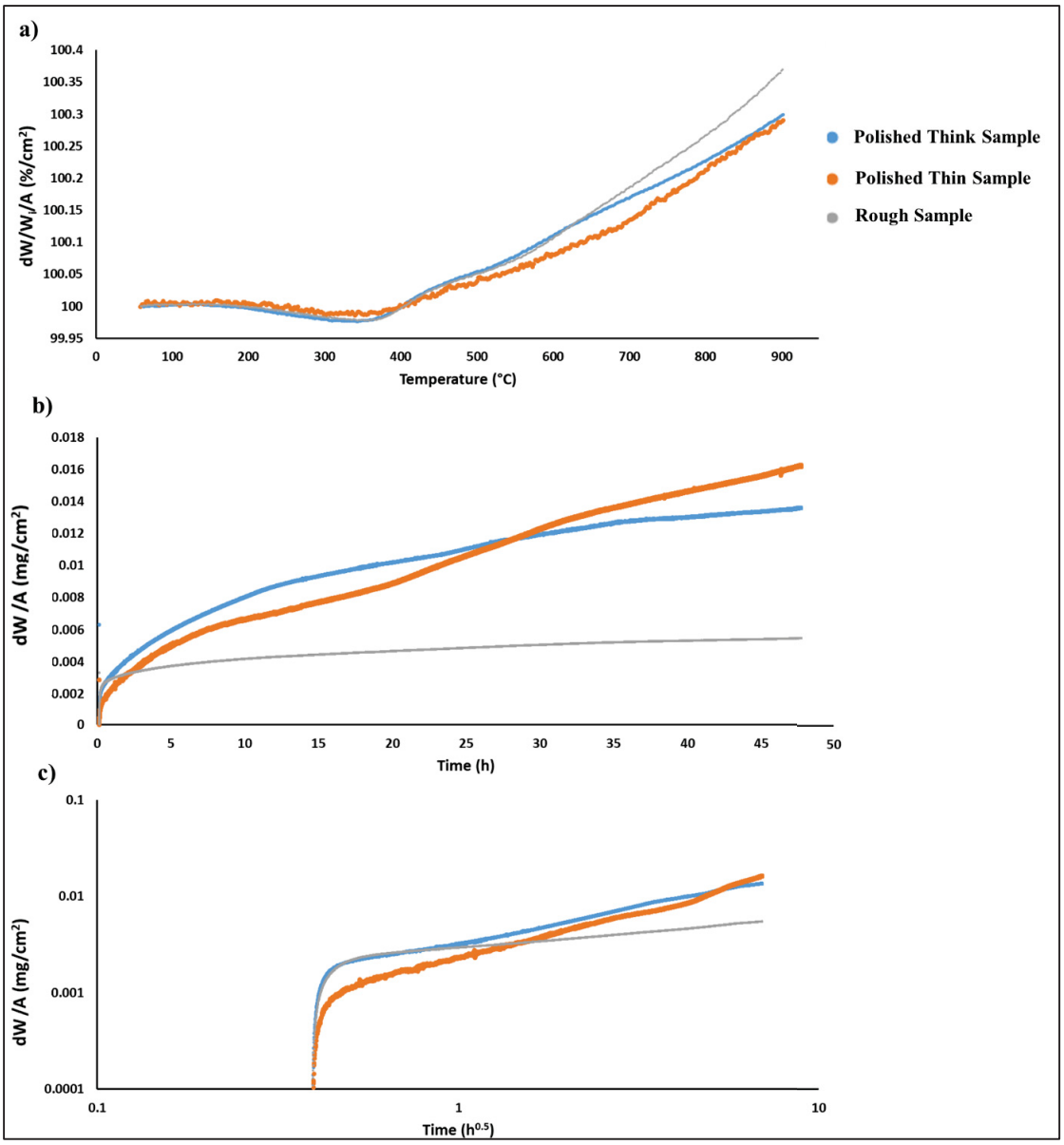

Figure 4.18 TGA curves showing oxidation as weight changes for APS samples at 950 °C. (a) Weight percentage change per surface unit during heating up to 950 °C, (b) weight change per surface unit over 50 h of isothermal exposure at 950 °C, and (c) log-log view of curves presented in (b)

4.4.3 Weight gain analysis of APS and HVOF coatings over various oxidation times at 1050 °C

The effect of oxidation times was investigated at 1050 °C but this time in an interrupted exposure. Figure 4.20 illustrates the weight gain per unit area (dW/cm^2) for HVOF and APS methods. The data reveals clear differences in the oxidation behavior and dynamics of the two deposition techniques. The APS coating exhibits a rapid initial weight gain, much higher than the HVOF coating within the first 30h of oxidation. This suggests that the APS method leads to fast oxidation at the beginning, possibly due to the immediate formation of a TGO layer.

Despite the initial rapid oxidation of APS coatings, the rate of weight gain begins to decrease as the TGO layer becomes established. This protective barrier effectively slows down further oxidation, maintaining a more consistent weight gain over time. The rapid initial formation of a protective TGO layer suggests that APS coatings are well suited for environments where quick stabilization of protective barriers is crucial. The relatively lower weight gain rate over time indicates reliable long-term performance with minimal oxide intrusion.

The HVOF coating, in contrast, exhibits a slower initial weight gain, indicating a lower initial oxidation rate. Although initially slower, it continues to oxidize at a constant rate, resulting in a higher overall weight gain by the 72 h. This consistent oxidation may lead to the formation of a thicker TGO layer or increased oxide intrusions within the coating. The significant drop in weight observed for the HVOF coating at 120 h is attributed to spallation, as discussed in detail earlier in Figure 4.9. Despite the initial setback, the oxidation rate remains robust, the HVOF coating resumes its oxidation process, leading to a significant weight gain by the 240 h. This suggests that HVOF coatings undergo continuous TGO growth and possible oxide intrusions which could imply greater overall oxidation protection but with potential vulnerabilities to spallation.

The comparison of APS and HVOF coatings reveals distinct differences in their oxidation behaviors. APS coatings demonstrate a rapid establishment of a protective TGO layer,

resulting in stable long-term performance. In contrast, HVOF coatings exhibit a more gradual oxidation process with higher overall weight gain, influenced by spallation events. These findings emphasize the importance of choosing the appropriate deposition technique based on the specific environmental and operational requirements of the coating application.

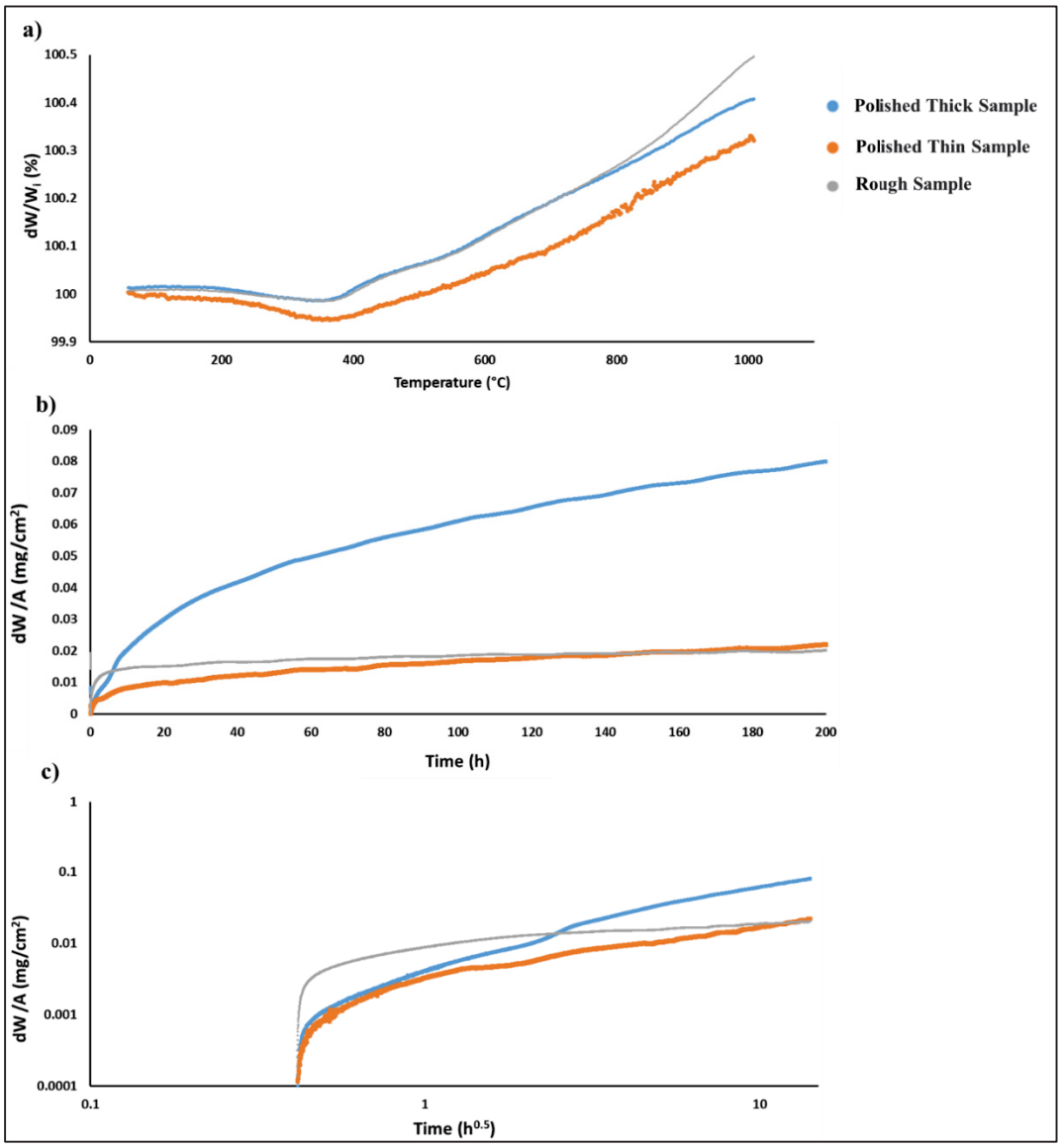

Figure 4.19 TGA curves showing oxidation as weight changes for APS samples at 1050 °C. (a) Weight percentage change per surface unit during heating up to 1050 °C, (b) weight change per surface unit over 200 h of isothermal exposure at 1050 °C, and (c) log-log view of curves presented in (b)

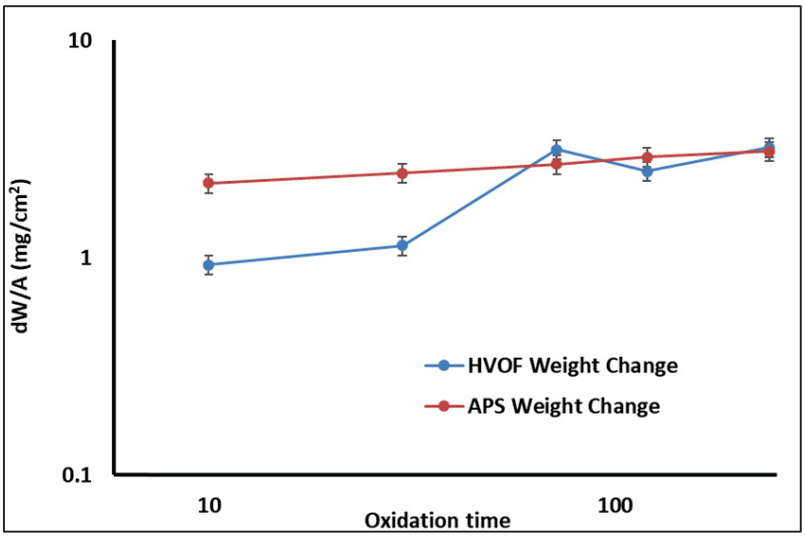

Figure 4.20 Weight gain per unit area (dW/cm^2) for APS and HVOF coatings over various oxidation times (the log-log presentation). The APS coating shows a rapid initial weight gain, stabilizing over time, while the HVOF coating demonstrates a consistent weight gain, interrupted by a spallation event at 120 h, followed by continued oxidation

4.5 Review of published results that needed in-depth discussion

While Chapter 3 presents the comprehensive article titled "Size effects on high temperature oxidation of MCrAlY coatings processed via APS and HVOF depositions," it is important to recognize the inherent constraints typical of journal publications. These constraints often necessitate a concise presentation and limit the depth of analysis that can be included within the scope of a single article. Consequently, certain observations and subtleties may not have been explored in detail, primarily due to the need to maintain a focused narrative.

In this section, we aim to expand upon the initial findings and drawing connections that contribute to a fuller understanding of the high-temperature oxidation behavior of MCrAlY coatings. This extended analysis is crucial for adding a significant layer of depth to the research presented in Chapter 3.

4.5.1 A comparison of oxidation rates in APS and HVOF coatings at 1150 °C

The comparative analysis of NiCoCrAlY coatings deposited using APS and HVOF techniques highlights notable differences in their oxidation rates, as reported in the published study by (Kalush et al., 2022). While this article presents oxidation mass gain for various thicknesses, this section specifically focuses on two thin specimen thicknesses 88 µm and 24-25 µm. The aim is to identify the most effective protective coating within a low thickness range, reconciling optimal oxidation resistance and durability with the goal of minimizing coating thickness to reduce the overall weight of gas turbine blades.

Although both methods show increased mass gain with greater thickness, their oxidation rates exhibit distinctive behavior under high-temperature conditions, demanding further investigation as shown in Figure 4.21.

Comparison of APS-88 µm and HVOF-88 µm Coatings

The APS-88 µm coating exhibited stable oxidation behavior with minimal mass gain throughout the 250-hour test. At 50 h, the APS sample showed a mass gain of approximately 0.64 mg/cm², reflecting a slow and steady oxidation process dominated by a uniform external Al_2O_3 scale. By 150 h, the mass gain increased to 0.82 mg/cm², maintaining its steady oxidation rate. After 250 h, the APS-88 µm sample reached a total mass gain of 0.84 mg/cm², indicating a slower oxidation process. This behavior, characterized by a power law exponent n approximately 3.5, highlights the APS coating's resistance to oxide intrusion and its dependence on stable external oxide scale formation.

In comparison, the HVOF-88 µm coating demonstrated significantly higher mass gain due to severe oxide intrusion facilitated by intersplat defects and unmelted particles. At 50 h, the mass gain for the HVOF-88 µm coating was approximately 1.85 mg/cm², nearly 2.89 times greater than that of the APS-88 µm sample. By 150 h, the mass gain increased to 2.9 mg/cm², over three times higher than the APS coating at the same time point. After 250 h, the HVOF coating reached a mass gain of 3.1 mg/cm², more than three times that of the APS sample, reflecting

the significant impact of process-induced defects. While the HVOF coating also followed a power law with n approximately 3.1, the oxidation constant k_n was substantially higher, demonstrating the more severe oxidation behavior driven by intrusive oxidation pathways and rapid aluminum depletion.

Comparison of APS-24 µm and HVOF-25 µm Coatings

For the APS-24 µm coating, the mass gain remained relatively low, even though intrinsic chemical failure (InCF) due to aluminum depletion occurred early in the oxidation process. At 50 h, the APS-24 µm coating exhibited a mass gain of approximately 0.61 mg/cm², indicating stable external Al_2O_3 formation with minimal intrusion. By 150 h, the mass gain increased gradually to 0.72 mg/cm², reflecting a steady and controlled progression of oxidation dominated by the formation of a stable external oxide scale. After 250 h, the APS-24 µm sample exhibited a mass gain of about 0.74 mg/cm², with oxidation kinetics primarily governed by the stable external Al_2O_3 scale and limited oxide intrusion.

In contrast, the HVOF-25 µm coating displayed a much more aggressive oxidation response, characterized by the occurrence of InCF. This mechanism accelerated aluminum depletion and led to the formation of $(Ni,Co)(Cr,Al)_2O_4$ spinel oxides within the oxide intrusions and on the surface of the Al_2O_3 scale. At 50 h, the HVOF-25 µm coating showed a mass gain of approximately 0.93 mg/cm², more than one and a half times higher than the APS-24 µm sample. By 150 h, the mass gain rose to 1.1 mg/cm², nearly 1.53 times greater than the APS coating. After 250 h, the HVOF-25 µm specimen reached a total mass gain of approximately 1.7 mg/cm², 2.3 times higher than the APS-24 µm coating. This higher mass gain reflects the severe oxide intrusion, interconnected porosity, and continued aluminum depletion, which significantly compromised the oxidation resistance of the HVOF coating.

Across both thickness ranges (88 µm and 24-25 µm), APS coatings demonstrated significantly lower mass gains and oxidation rates compared to HVOF coatings at all time points (50, 150, and 250 h). The HVOF coatings exhibited more aggressive oxidation behavior, with mass gains that were consistently 3 to 4 times higher than APS coatings due to their susceptibility to

intrusive oxidation and process-induced defects. For thin coatings (24-25 μm), both APS and HVOF specimens experienced intrinsic chemical failure (InCF); however, HVOF samples also underwent mechanically induced chemical failure (MICF), which exacerbated oxidation rates and mass gain. For thicker coatings (88 μm), the APS specimens maintained steady oxidation behavior comparable to defect-free cast materials, while HVOF specimens displayed accelerated aluminum depletion and greater sensitivity to defect-induced intrusive oxidation.

These findings underscore the greater oxidation resistance of APS coatings, particularly in minimizing mass gain and oxidation rates over extended exposure at 1150 °C. Additionally, the comparisons highlight the importance of deposition-related microstructure in determining the oxidation resistance of MCrAlY coatings, especially at elevated temperatures. The severe impact of process-induced defects, such as intersplat regions and unmelted particles, on the oxidation performance of HVOF coatings further emphasizes the critical role of deposition parameters in influencing coating behavior.

4.5.2 The evolution of oxide spallation and the development of MICF in HVOF samples

In the published article (Chapter 3), surface macrographs of the samples after various oxidation durations at 1150 °C were analyzed at intervals of 20, 50, 100, 150, and 250 h. However, the evolution of oxide spallation and the development of MICF could benefit from a more focused investigation, particularly emphasizing the formation and transformation of oxide phases over time. This deeper insight can be achieved by closely examining the images obtained from the sample with a thickness of 157 μm (Figure 4.22).

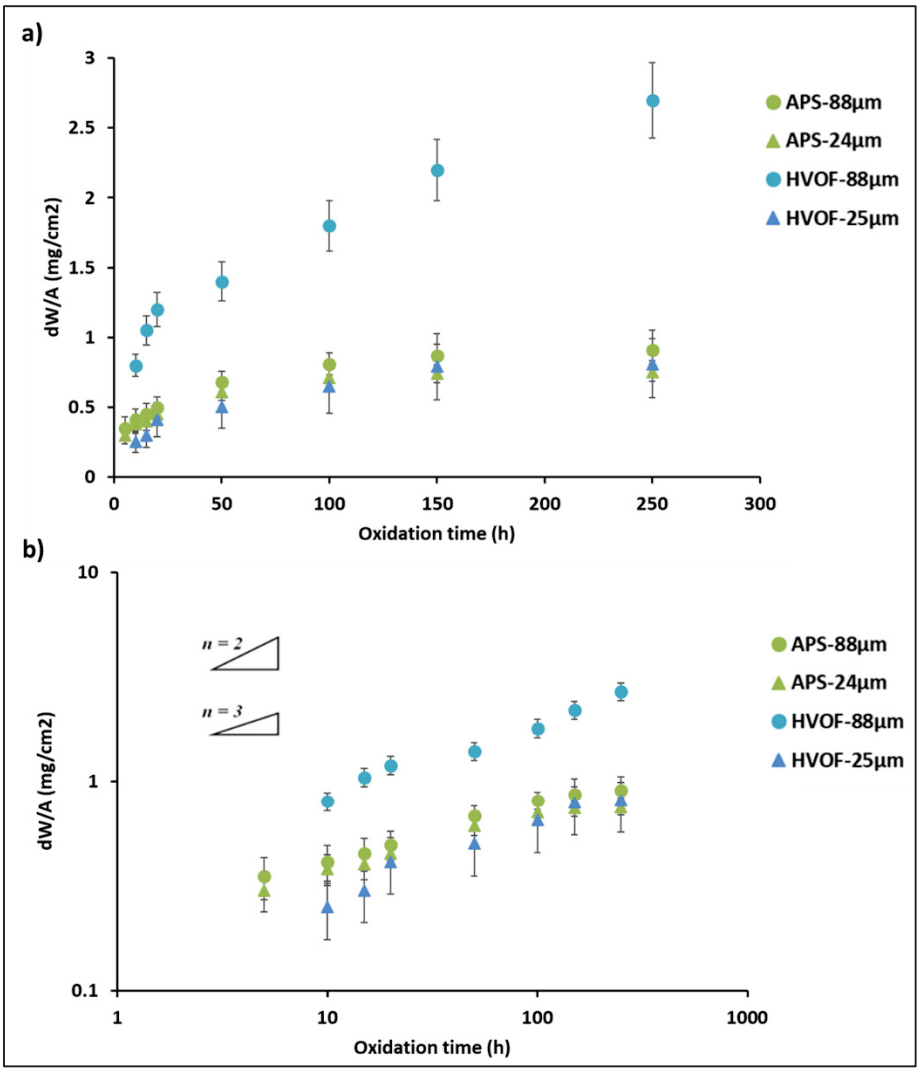

Figure 4.21 HVOF vs. APS mass gain for similar thicknesses of 88 microns and 24-25 microns at 1150 °C. (a) dW/A versus time representations, (b) log-log representations

After 20 h of oxidation (Figure 4.22 (a)), the surface of the HVOF coating shows initial signs of oxide formation. These oxides appear as small white dots scattered across the surface. The early stages of oxidation are marked by the nucleation of these oxides, indicating the beginning of the surface degradation process. By 50 h (Figure 4.22 (b)), the white dots are now larger white islands. Oxides begin to coalesce, forming larger and more prominent regions on the coating surface. The increasing size and number of these oxide islands reflect ongoing surface degradation and the progressive spread of oxidation across the sample. At 100 h of exposure

(Figure 4.22 (c)), MICFs start to manifest as blue spots distributed across the sample surface. The appearance of these blue oxide islands suggests a shift in the oxidation mechanism, marked by the formation of new oxide phases. This phase transformation highlights the growing complexity of the oxidation process as it progresses. by 150 h (Figure 4.22 (d)), the surface undergoes a significant transformation, with the previously white oxide islands largely converting to blue oxides, indicating the dominance of MICF oxides over the original oxidation products. By 250 h (Figure 4.22 (e)), the surface is extensively covered with blue oxides and the initial white oxides have been almost entirely replaced. The growth and spread of MICF oxides dominate the surface, highlighting the severe impact of prolonged high-temperature exposure. This observation indicates that in long exposures surface degradation is primarily driven by MICF rather than InCF, conclusively identifying MICF as the main factor contributing to the coating's surface instability.

The progression of surface oxidation in the 157-μm thick HVOF samples provides valuable insights into the underlying degradation mechanisms. Initially, oxidation starts with the formation of small, white oxide dots, which grow and merge into larger islands. As the oxidation process progresses, MICFs emerge, signalling a shift in the dominant oxidation mechanism and indicating the presence of significant stress. The transformation of white oxides to blue MICF oxides illustrates the interplay between mechanical stresses and chemical reactions in advancing the oxidation process. The extensive coverage of MICF oxides after 250 h underscores the need for strategies to mitigate such degradation in high-temperature applications, ensuring the longevity and performance of HVOF coatings under extreme conditions.

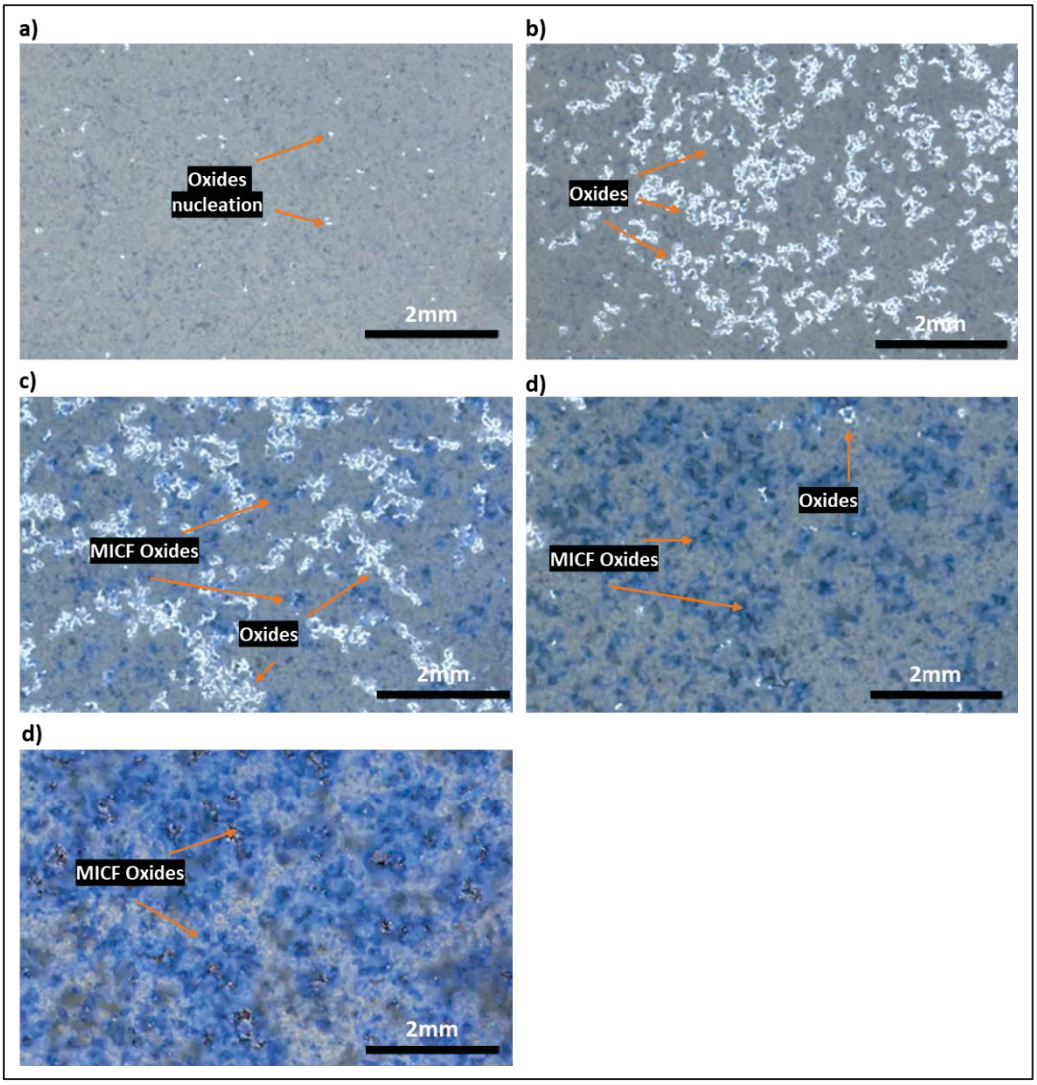

Figure 4.22 Surface macrographs of a 157 µm-thick HVOF coating sample at various oxidation times, illustrating the progression of oxide spallation and the formation of MICF (blue oxide islands). (a) After 20 h of oxidation, (b) 50 h, (c) 100 h, (d) 150 h, and (e) 250 h.

4.5.3 Oxidation profiles at different depths of HVOF coatings

The impact of oxidation at various depths of HVOF samples was included as supplementary material in the published article, but a detailed analysis could not be presented. To address this, a 367 µm thick HVOF sample was selected, and images at different depths after 500 h of oxidation were analyzed. Figure 4.23 presents these images, which were also used to derive the oxide percentages in the graph discussed in Figure 3.8 (of the published article).

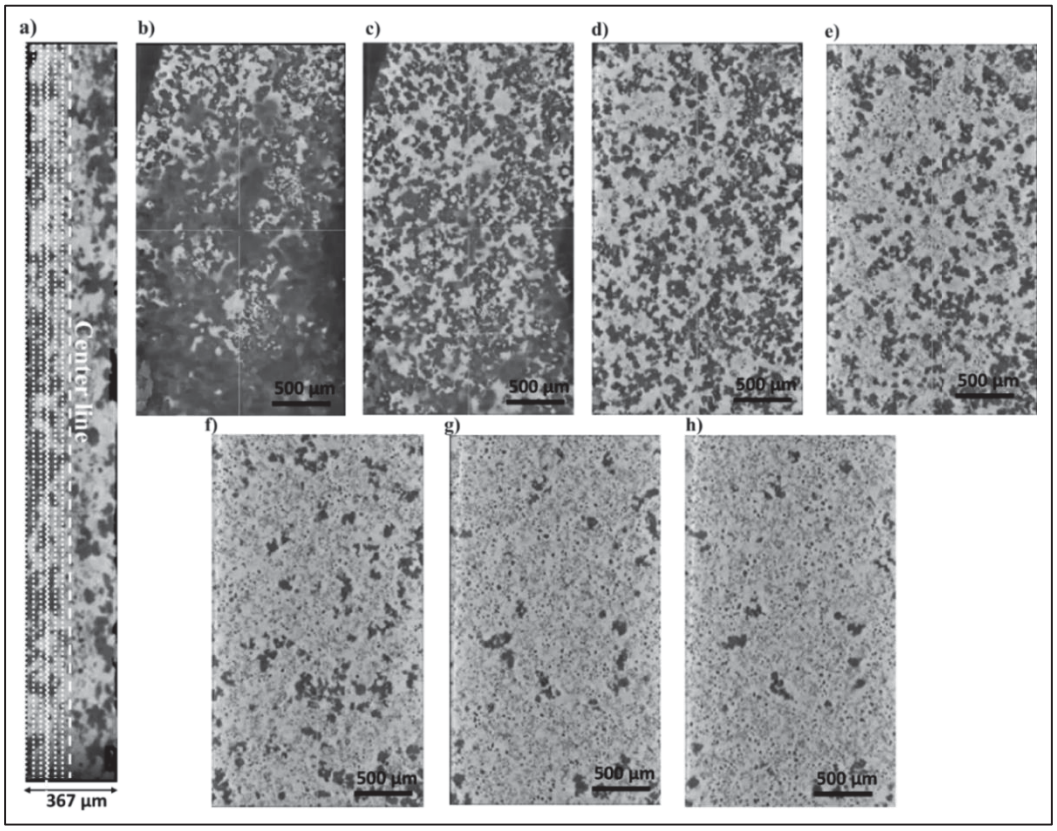

Figure 4.23 Depth profile images of a 367 µm thick HVOF sample, showing oxide distribution at various depths. (a) overview of the sample with a dotted white line schematically presenting the profile lines; (b) surface layer with 60–70% oxide content; (c) 20 µm depth with ~50% oxide; (d) 50 µm depth with ~40% oxide; (e) 90 µm depth with ~25% oxide; (f) 130 µm depth with ~22% oxide; (g) 160 µm depth with ~22% oxide; (h) 180 µm depth with ~22% oxide.

The outer edges of the sample exhibit high oxide percentages, reaching up to 60-70% (Figure 4.23 (b)). This indicates intense oxidation activity near the surfaces exposed to the oxidizing environment. Moving below the surface, the oxide percentages decrease significantly. In contrast, the central region of the sample exhibits fewer oxide intrusions, corresponding to the lower oxide. The metallic matrix remains more intact here, indicating limited oxidation progression toward the depth of the sample.

CHAPTER 5

CONCLUSION

This comprehensive study delved into the high-temperature oxidation behavior of NiCoCrAlY coatings processed via High Velocity Oxy Fuel (HVOF) and Air Plasma Spray (APS) techniques, providing critical insights into how these deposition methods influence the coatings' performance and durability.

5.1 Synthesis of Findings

This thesis undertook a comparative investigation into the high-temperature oxidation behavior and microstructural evolution of NiCoCrAlY coatings produced by Air Plasma Spray (APS) and High Velocity Oxy-Fuel (HVOF) deposition techniques. By employing a novel approach utilizing freestanding coating samples (FSCS) across a wide range of thicknesses (from ~15 μm up to several hundred μm), this study aimed to decouple substrate effects and directly assess the influence of coating properties and process-induced features on oxidation resistance and failure mechanisms at 1050 °C and 1150 °C.

The experimental results revealed significant differences in performance between the APS and HVOF coatings evaluated in this specific study. The HVOF coatings, processed using parameters chosen partly for experimental exploration, exhibited a high volume fraction (~21%) of unmelted particles. This defect structure contrasted sharply with the generally denser APS coatings which contained fewer (<5%) unmelted particles but exhibited typical APS porosity and oxide stringers.

This difference in initial microstructure critically influenced the subsequent oxidation behavior. The numerous unmelted particles and associated poor inter-splat bonding in the HVOF samples created extensive pathways for oxygen ingress, leading to severe intrusive oxidation that penetrated deep into the coating bulk. Consequently, the HVOF coatings

demonstrated oxidation kinetics highly sensitive to specimen thickness, with thicker samples showing significantly higher mass gain due to the larger volume available for internal oxidation. In contrast, the APS coatings showed oxidation rates largely insensitive to thickness (until very thin samples experienced reservoir depletion) and comparable to defect-free cast materials, indicating that oxidation was primarily controlled by the external scale growth with less contribution from internal defects under these conditions.

The prevalent intrusive oxidation in the HVOF samples accelerated the consumption of the aluminum reservoir, leading to earlier onset of Al2O3 scale failure compared to APS samples of similar thickness. Both Intrinsic Chemical Failure (InCF), marked by Cr2O3 formation, and Mechanically Induced Chemical Failure (MICF), associated with spallation and subsequent spinel formation, were observed in the HVOF samples, particularly thicker ones. The APS coatings were primarily susceptible to InCF only when thinned to below ~60 μm, where the aluminum reservoir was rapidly depleted. The mechanical analysis also reflected these microstructural differences, with the HVOF samples showing more strain localization potentially linked to the heterogeneous structure caused by unmelted particles.

5.2 Novelty and Contribution

A key contribution of this research lies in its methodology. This work represents one of the first systematic investigations using freestanding MCrAlY bond coat samples, prepared across a broad spectrum of controlled thicknesses (down to the tens of microns), to quantitatively study the distinct effects of coating thickness and inherent microstructural features, such as unmelted particles, on high-temperature oxidation behavior and failure modes (InCF/MICF). This approach effectively isolates the coating's intrinsic response from substrate interdiffusion effects, providing clearer insights into how process-specific defects influence degradation pathways like intrusive oxidation and subsequent chemical failure. The findings directly link the high prevalence of unmelted particles in the study's HVOF coatings to accelerated failure via intrusive oxidation, highlighting the critical impact of process parameter control.

5.3 Implications and Concluding Remarks

The findings underscore the importance of controlling process-induced defects in thermal spray MCrAlY coatings for reliable high-temperature performance. While literature suggests optimized HVOF can yield highly protective coatings, this study demonstrates how suboptimal parameters leading to defects like numerous unmelted particles can severely compromise oxidation resistance, making the coating susceptible to extensive intrusive oxidation and premature failure. In this specific comparison, the APS coatings exhibited superior performance due to their lower susceptibility to deep intrusive oxidation, despite being more prone to intrusive oxide content typical of the process.

This emphasizes that the choice between APS and HVOF should consider the achievable level of process control and the resulting defect population regardless of the deposition process. Minimizing defects like poorly bonded unmelted particles and interconnected porosity is crucial for maximizing the service life of MCrAlY bond coats by limiting detrimental internal/intrusive oxidation pathways.

5.4 Recommendations for Future Work

Based on this study, several avenues for future research are recommended:

1. **Optimized HVOF Study:** Conduct a similar comparative study using HVOF parameters specifically optimized to minimize unmelted particles and porosity, allowing for a comparison based on the inherent potential of a well-processed HVOF coating versus APS.

2. **Cyclic Oxidation:** Investigate the behavior of both APS and the thesis's defect-rich HVOF coatings under cyclic oxidation conditions, as thermal cycling introduces mechanical stresses that could interact differently with the distinct defect structures (e.g., influence on MICF vs. InCF).

3. **Quantitative Defect Analysis:** Employ advanced 3D characterization (e.g., high-resolution X-ray CT) across more samples and thicknesses to better quantify the connectivity of porosity and the distribution of unmelted particles and internal oxides, refining the link between specific defect morphologies and oxidation kinetics/failure.

4. **Substrate Interaction:** While FSCS isolates coating behavior, studies incorporating model substrates could investigate how the observed defect structures interact with interdiffusion phenomena.

5. **Mechanical Property Evolution:** Further investigate the evolution of mechanical properties (e.g., hardness, modulus) within the distinct defect structures (unmelted particles vs. APS splats) during high-temperature exposure using techniques like nano-indentation.

LIST OF REFERENCES

Abbas, M., Smith, G. M., & Munroe, P. R. (2020). Microstructural Characterization of HVOF-Sprayed Ni on Polished and Oxidized Stainless Steel Substrates. *Journal of thermal spray technology, 29*(5), 1093-1110. doi: 10.1007/s11666-020-01031-8. Repéré à https://doi.org/10.1007/s11666-020-01031-8

Abhijith, N. V., Kumar, D., & Kalyansundaram, D. (2022). Development of Single-Stage TiNbMoMnFe High-Entropy Alloy Coating on 304L Stainless Steel Using HVOF Thermal Spray. *Journal of thermal spray technology, 31*(4), 1032-1044. doi: 10.1007/s11666-021-01294-9. Repéré à https://doi.org/10.1007/s11666-021-01294-9

Ahmadian, S., & Jordan, E. H. (2014). Explanation of the effect of rapid cycling on oxidation, rumpling, microcracking and lifetime of air plasma sprayed thermal barrier coatings. *Surface and Coatings Technology, 244*, 109-116.

Ahrens, M., Vaßen, R., & Stöver, D. (2002). Stress distributions in plasma-sprayed thermal barrier coatings as a function of interface roughness and oxide scale thickness. *Surface and Coatings Technology, 161*(1), 26-35.

Aktaa, J., Sfar, K., & Munz, D. (2005). Assessment of TBC systems failure mechanisms using a fracture mechanics approach. *Acta materialia, 53*(16), 4399-4413.

Alam, M. Z., Parlikar, C., Chatterjee, D., & Das, D. K. (2017). Comparative tensile behavior of freestanding γ-γ′ and β-(Ni, Pt) Al bond coats and effect on tensile properties of coated superalloy. *Materials & Design, 114*, 505-514.

Alnaser, I. A., Yunus, M., Alfattani, R., & Alamro, T. (2021). High-Temperature Corrosion of APS-and HVOF-Coated Nickel-Based Super Alloy under Air Oxidation and Melted Salt Domains. *Materials, 14*(18), 5119.

Baik, S.-I., Wang, S.-Y., Liaw, P. K., & Dunand, D. C. (2018). Increasing the creep resistance of Fe-Ni-Al-Cr superalloys via Ti additions by optimizing the B2/L21 ratio in composite nano-precipitates. *Acta materialia, 157*, 142-154.

Bar-Cohen, Y. (2014). *High temperature materials and mechanisms* (Vol. 44). CRC Press Boca Raton, FL, USA:.

Barrett, C. A. (1992). *A statistical analysis of elevated temperature gravimetric cyclic oxidation data of 36 Ni-and Co-base superalloys based on an oxidation attack parameter*.

Basuki, E., Crosky, A., & Gleeson, B. (1997). Interdiffusion behaviour in aluminide-coated René 80H at 1150° C. *Materials Science and Engineering: A, 224*(1-2), 27-32.

Belzunce, F. J., Higuera, V., & Poveda, S. (2001). High temperature oxidation of HFPD thermal-sprayed MCrAlY coatings. *Materials Science and Engineering: A, 297*(1), 162-167. doi: https://doi.org/10.1016/S0921-5093(00)01239-9. Repéré à https://www.sciencedirect.com/science/article/pii/S0921509300012399

Bogdan, M., & Peter, I. (2024). A Comprehensive Understanding of Thermal Barrier Coatings (TBCs): Applications, Materials, Coating Design and Failure Mechanisms. *Metals, 14*(5).

Bose, S. (2007). High-temperature corrosion. *High temperature coatings*, 53-70.

Bose, S. (2017). *High temperature coatings*. Butterworth-Heinemann.

Boulos, M. I., Fauchais, P. L., & Heberlein, J. V. (2021). *Thermal spray fundamentals: from powder to part*. Springer.

Boulos, M. I., Fauchais, P. L., & Pfender, E. (2023). Plasma Spray Torches. Dans M. I. Boulos, P. L. Fauchais & E. Pfender (Éds.), *Handbook of Thermal Plasmas* (pp. 795-848). Cham: Springer International Publishing. doi: 10.1007/978-3-030-84936-8_49. Repéré à https://doi.org/10.1007/978-3-030-84936-8_49

Bounazef, M., Guessasma, S., Montavon, G., & Coddet, C. (2004). Effect of APS process parameters on wear behaviour of alumina–titania coatings. *Materials Letters, 58*(20), 2451-2455. doi: https://doi.org/10.1016/j.matlet.2004.02.026. Repéré à https://www.sciencedirect.com/science/article/pii/S0167577X04001843

Brandl, W., Grabke, H., Toma, D., & Krüger, J. (1996). The oxidation behaviour of sprayed MCrAlY coatings. *Surface and Coatings Technology, 86*, 41-47.

Brandl, W., Toma, D., Krüger, J., Grabke, H., & Matthäus, G. (1997). The oxidation behaviour of HVOF thermal-sprayed MCrAlY coatings. *Surface and Coatings Technology, 94*, 21-26.

Brindley, W., & Miller, R. (1990). Thermal barrier coating life and isothermal oxidation of low-pressure plasma-sprayed bond coat alloys. *Surface and Coatings Technology, 43*, 446-457.

Brumm, M., & Grabke, H. (1992). The oxidation behaviour of NiAl-I. Phase transformations in the alumina scale during oxidation of NiAl and NiAl-Cr alloys. *Corrosion Science, 33*(11), 1677-1690.

Bürgel, R., Bürgel, R., Maier, H. J., & Niendorf, T. (1998). *Handbuch Hochtemperatur-Werkstofftechnik*. Springer.

Busso, E. P., Evans, H. E., Qian, Z. Q., & Taylor, M. P. (2010). Effects of breakaway oxidation on local stresses in thermal barrier coatings. *Acta materialia, 58*(4), 1242-1251. doi: https://doi.org/10.1016/j.actamat.2009.10.028. Repéré à https://www.sciencedirect.com/science/article/pii/S1359645409007228

Campbell, C. E., Boettinger, W. J., & Kattner, U. R. (2002). Development of a diffusion mobility database for Ni-base superalloys. *Acta materialia, 50*(4), 775-792.

Campbell, C. E., Zhao, J.-C., & Henry, M. (2004). Comparison of experimental and simulated multicomponent Ni-base superalloy diffusion couples. *Journal of phase equilibria and diffusion, 25*, 6-15.

Cen, L., Qin, W., & Yu, Q. (2021). A three-dimensional finite element model for the oxide growth mechanism and growth-induced stress within thermal barrier system. *Materials Today Communications, 29*, 102790.

Chagnon, P., & Fauchais, P. (1984). Thermal spraying of ceramics. *Ceramics International, 10*(4), 119-131.

Chandio, A. D. (2015). *Processing, Characterisation and Oxidation Study of the Nickel Aluminides (βNiAl) for Thermal Barrier Coating Applications*. The University of Manchester (United Kingdom).

Che, C., Wu, G., Qi, H., Huang, Z., & Yang, X. (2009). Uneven growth of thermally grown oxide and stress distribution in plasma-sprayed thermal barrier coatings. *Surface and Coatings Technology, 203*(20-21), 3088-3091.

Chen, H., Fan, M., Li, L., Zhu, W., Li, H., Li, J., & Yin, Y. (2021). Effects of internal oxide contents on the oxidation and β-phase depletion behaviour in HOVF CoNiCrAlY coatings. *Surface and Coatings Technology, 424*, 127666.

Chen, H., Fan, M., Li, L., Zhu, W., Li, H. N., Li, J., & Yin, Y. (2021). Effects of internal oxide contents on the oxidation and β-phase depletion behaviour in HOVF CoNiCrAlY coatings. *Surface and Coatings Technology, 424*, 127666. doi: https://doi.org/10.1016/j.surfcoat.2021.127666. Repéré à https://www.sciencedirect.com/science/article/pii/S0257897221008409

Chen, J., Chen, J., Wang, Q., Wu, Y., Li, Q., Xiao, C., . . . Hui, X. (2022). Enhanced creep resistance induced by minor Ti additions to a second generation nickel-based single crystal superalloy. *Acta materialia, 232*, 117938.

Chen, W.-M., Xie, Y. M., Imbalzano, G., Shen, J., Xu, S., Lee, S.-J., & Lee, P. V. S. (2016). Lattice Ti structures with low rigidity but compatible mechanical strength: Design of implant materials for trabecular bone. *International Journal of Precision Engineering and Manufacturing, 17*(6), 793-799. doi: 10.1007/s12541-016-0097-6

Chen, W., Irissou, E., Wu, X., Legoux, J.-G., & Marple, B. (2011). The oxidation behavior of TBC with cold spray CoNiCrAlY bond coat. *Journal of thermal spray technology, 20*(1), 132-138.

Chen, W., Wu, X., Marple, B., Lima, R., & Patnaik, P. (2008). Pre-oxidation and TGO growth behaviour of an air-plasma-sprayed thermal barrier coating. *Surface and Coatings Technology, 202*(16), 3787-3796.

Chen, W., Wu, X., Marple, B., Nagy, D., & Patnaik, P. (2008). TGO growth behaviour in TBCs with APS and HVOF bond coats. *Surface and Coatings Technology, 202*(12), 2677-2683.

Chen, W., Wu, X., Marple, B., & Patnaik, P. (2005). Oxidation and crack nucleation/growth in an air-plasma-sprayed thermal barrier coating with NiCrAlY bond coat. *Surface and Coatings Technology, 197*(1), 109-115.

Chen, W., Wu, X., Marple, B., & Patnaik, P. (2006). The growth and influence of thermally grown oxide in a thermal barrier coating. *Surface and Coatings Technology, 201*(3-4), 1074-1079.

Chen, W. R., Wu, X., Marple, B. R., & Patnaik, P. C. (2005). Oxidation and crack nucleation/growth in an air-plasma-sprayed thermal barrier coating with NiCrAlY bond coat. *Surface and Coatings Technology, 197*(1), 109-115. doi: https://doi.org/10.1016/j.surfcoat.2004.06.027. Repéré à https://www.sciencedirect.com/science/article/pii/S0257897204004785

Chen, X., Kuroda, S., Ohnuki, T., Araki, H., Watanabe, M., & Sakka, Y. (2016). Effects of processing parameters on the deposition of yttria partially stabilized zirconia coating during suspension plasma spray. *Journal of the American Ceramic Society, 99*(11), 3546-3555.

Chen, Y., Zhao, X., & Xiao, P. (2018). Effect of microstructure on early oxidation of MCrAlY coatings. *Acta materialia, 159*, 150-162.

Chen, Z., Xu, G., Cao, Q., Ruan, M., Liu, S., Pan, H., & Liu, L. (2022). Deformation measurement in Al thin films at elevated temperatures by digital image correlation with speckles prepared by femtosecond laser. *Optics & Laser Technology, 155*, 108339. doi: https://doi.org/10.1016/j.optlastec.2022.108339. Repéré à https://www.sciencedirect.com/science/article/pii/S0030399222004960

Choi, H., Yoon, B., Kim, H., & Lee, C. (2002). Isothermal oxidation of air plasma spray NiCrAlY bond coatings. *Surface and Coatings Technology, 150*(2-3), 297-308.

Chow, B. J. (2016). *Forming infrastructural materials by mechanical compaction of lunar and Martian regolith simulants*. University of California, San Diego.

Chyrkin, A., Epishin, A., Pillai, R., Link, T., Nolze, G., & Quadakkers, W. (2016). Modeling interdiffusion processes in CMSX-10/Ni diffusion couple. *Journal of phase equilibria and diffusion, 37*, 201-211.

Cinca, N., Lima, C. R. C., & Guilemany, J. M. (2013). An overview of intermetallics research and application: Status of thermal spray coatings. *Journal of Materials Research and Technology, 2*(1), 75-86.

Cizek, J., & Matejicek, J. (2018). Medicine meets thermal spray technology: A review of patents. *Journal of thermal spray technology, 27*, 1251-1279.

Clarke, D., & Levi, C. (2003). Materials design for the next generation thermal barrier coatings. *Annual review of materials research, 33*(1), 383-417.

Clarke, D. R., Oechsner, M., & Padture, N. P. (2012). Thermal-barrier coatings for more efficient gas-turbine engines. *MRS Bulletin, 37*(10), 891-898. doi: 10.1557/mrs.2012.232. Repéré à https://www.cambridge.org/core/product/72FDF8FDDCD21040144D75579E3C1358

Czech, N., Juez-Lorenzo, M., Kolarik, V., & Stamm, W. (1998). Influence of the surface roughness on the oxide scale formation on MCrAlY coatings studied in situ by high temperature X-ray diffraction. *Surface and Coatings Technology, 108*, 36-42.

Davis, J. R. (2004). *Handbook of thermal spray technology*. ASM international.

Di Ferdinando, M., Fossati, A., Lavacchi, A., Bardi, U., Borgioli, F., Borri, C., . . . Scrivani, A. (2010). Isothermal oxidation resistance comparison between air plasma sprayed, vacuum plasma sprayed and high velocity oxygen fuel sprayed CoNiCrAlY bond coats. *Surface and Coatings Technology, 204*(15), 2499-2503.

Doleker, K. M., Ozgurluk, Y., & Karaoglanli, A. C. (2018). Isothermal oxidation and thermal cyclic behaviors of YSZ and double-layered YSZ/La2Zr2O7 thermal barrier coatings (TBCs). *Surface and Coatings Technology, 351*, 78-88.

Donachie, M. J., & Donachie, S. J. (2002). *Superalloys: a technical guide*. ASM international.

Dong, H., Yang, G. J., Li, C. X., Luo, X. T., & Li, C. J. (2014). Effect of TGO thickness on thermal cyclic lifetime and failure mode of plasma-sprayed TBC s. *Journal of the American Ceramic Society, 97*(4), 1226-1232.

Doolabi, M., Ghasemi, B., Sadrnezhaad, S. K., Habibolahzadeh, A., & Jafarzadeh, K. (2018). Evaluation and Selection of Optimal Oxygen/Fuel Ratio for Best Mechanical Properties, Oxidation Resistance and Microstructure of HVOF NiCoCrAlY Coatings Using AHP–VIKOR Method. *Oxidation of Metals, 89*. doi: 10.1007/s11085-017-9797-2

Elsaß, M., Frommherz, M., Scholz, A., & Oechsner, M. (2016). Interdiffusion in MCrAlY coated nickel-base superalloys. *Surface and Coatings Technology, 307*, 565-573.

Eriksson, R., Sjöström, S., Brodin, H., Johansson, S., Östergren, L., & Li, X.-H. (2013). TBC bond coat–top coat interface roughness: Influence on fatigue life and modelling aspects. *Surface and Coatings Technology, 236*, 230-238.

Evans, A., He, M., & Hutchinson, J. (2001). Mechanics-based scaling laws for the durability of thermal barrier coatings. *Progress in materials science, 46*(3-4), 249-271.

Evans, A. G., Mumm, D., Hutchinson, J., Meier, G., & Pettit, F. (2001). Mechanisms controlling the durability of thermal barrier coatings. *Progress in materials science, 46*(5), 505-553.

Evans, H. (1995). Stress effects in high temperature oxidation of metals. *International materials reviews, 40*(1), 1-40.

Evans, H., Donaldson, A., & Gilmour, T. (1999). Mechanisms of breakaway oxidation and application to a chromia-forming steel. *Oxidation of Metals, 52*(5), 379-402.

Evans, H., & Taylor, M. (2006). Oxidation of high-temperature coatings. *Proceedings of the Institution of Mechanical Engineers, Part G: Journal of Aerospace Engineering, 220*(1), 1-10.

Evans, H. E. (1995). Stress effects in high temperature oxidation of metals. *International materials reviews, 40*(1), 1-40. doi: 10.1179/imr.1995.40.1.1. Repéré à https://www.scopus.com/inward/record.uri?eid=2-s2.0-0029212260&doi=10.1179%2fimr.1995.40.1.1&partnerID=40&md5=45dc49259afaa9adfb4068ae3875e739

Evans, H. E., Donaldson, A. T., & Gilmour, T. C. (1999). Mechanisms of breakaway oxidation and application to a chromia-forming steel. *Oxidation of Metals, 52*(5), 379-402. doi: 10.1023/a:1018855914737. Repéré à https://www.scopus.com/inward/record.uri?eid=2-s2.0-0032655518&doi=10.1023%2fa%3a1018855914737&partnerID=40&md5=ff35ced71939c4e476459f2e31fb3bb4

Evans, H. E., & Taylor, M. P. (2001). Diffusion Cells and Chemical Failure of MCrAlY Bond Coats in Thermal-Barrier Coating Systems. *Oxidation of Metals, 55*(1-2), 17-34. doi: 10.1023/A:1010369024142. Repéré à https://www.scopus.com/inward/record.uri?eid=2-s2.0-0002565101&doi=10.1023%2fA%3a1010369024142&partnerID=40&md5=feb25bf65905a0971156d94172a63df7

Evans, H. E., & Taylor, M. P. (2006). Oxidation of high-temperature coatings. *Proceedings of the Institution of Mechanical Engineers, Part G: Journal of Aerospace Engineering, 220*(1), 1-10. doi: 10.1243/095441005X33420. Repéré à https://www.scopus.com/inward/record.uri?eid=2-s2.0-33645331281&doi=10.1243%2f095441005X33420&partnerID=40&md5=edab45de898fa01b659117406bbbaa83

Fanicchia, F., Axinte, D., Kell, J., McIntyre, R., Brewster, G., & Norton, A. (2017). Combustion flame spray of CoNiCrAlY & YSZ coatings. *Surface and Coatings Technology, 315*, 546-557.

Fauchais, P. (2004). Understanding plasma spraying. *Journal of Physics D: Applied Physics, 37*(9), R86.

Fauchais, P., Heberlein, J., & Boulos, M. (2013). *Thermal Spray Fundamentals: From Powder to Part*. doi: 10.1007/978-0-387-68991-3

Fauchais, P. L., Heberlein, J. V., & Boulos, M. I. (2014). *Thermal spray fundamentals: from powder to part*. Springer Science & Business Media.

Fedorova, E., Monceau, D., & Oquab, D. (2010). Quantification of growth kinetics and adherence of oxide scales formed on Ni-based superalloys at high temperature. *Corrosion Science, 52*(12), 3932-3942. doi: https://doi.org/10.1016/j.corsci.2010.08.013. Repéré à https://www.sciencedirect.com/science/article/pii/S0010938X1000404X

Feuerstein, A., Hitchman, N., Taylor, T. A., & Lemen, D. (2009). Process and Equipment for Advanced Thermal Barrier Coatings. *Progress in Thermal Barrier Coatings, 2*, 187.

Ghadami, F., Aghdam, A. S. R., Zakeri, A., Saeedi, B., & Tahvili, P. (2020). Synergistic effect of CeO2 and Al2O3 nanoparticle dispersion on the oxidation behavior of MCrAlY coatings deposited by HVOF. *Ceramics International, 46*(4), 4556-4567.

Ghadami, F., Sabour Rouh Aghdam, A., & Ghadami, S. (2021). A comprehensive study on the microstructure evolution and oxidation resistance of conventional and nanocrystalline MCrAlY coatings. *Scientific Reports, 11*(1), 875.

Ghadami, F., Zakeri, A., Aghdam, A. S. R., & Tahmasebi, R. (2019). Structural characteristics and high-temperature oxidation behavior of HVOF sprayed nano-CeO2 reinforced NiCoCrAlY nanocomposite coatings. *Surface and Coatings Technology, 373*, 7-16.

Gheno, T., Liu, X. L., Lindwall, G., Liu, Z.-K., & Gleeson, B. (2015). Experimental study and thermodynamic modeling of the Al–Co–Cr–Ni system. *Science and technology of advanced materials, 16*(5), 055001.

Gheno, T., Rio, C., Ecochard, M., & Texier, D. (2021). Alumina Failure and Post-failure Oxidation in the NiCoCrAlY Alloy System at High Temperature. *Oxidation of Metals, 96*(5), 487-517. doi: 10.1007/s11085-021-10060-9. Repéré à https://doi.org/10.1007/s11085-021-10060-9

Giggins, C., & Pettit, F. S. (1971). Oxidation of Ni-Cr-Al alloys between 1000 and 1200 C. *Journal of the Electrochemical Society, 118*(11), 1782.

Giggins, C. S., & Pettit, F. S. (1971). Oxidation of Ni - Cr - Al Alloys Between 1000° and 1200°C. *Journal of the Electrochemical Society, 118*(11), 1782. doi: 10.1149/1.2407837. Repéré à https://dx.doi.org/10.1149/1.2407837

Gil, A., Shemet, V., Vassen, R., Subanovic, M., Toscano, J., Naumenko, D., . . . Quadakkers, W. (2006). Effect of surface condition on the oxidation behaviour of MCrAlY coatings. *Surface and Coatings Technology, 201*(7), 3824-3828.

Gleeson, B. (2000). High-temperature corrosion of metallic alloys and coatings. *Materials Science and Technology: A Comprehensive Treatment: Corrosion and Environmental Degradation, Volumes I+ II, 1*, 173-228.

Goti, R., Bétaille-Francoual, M., Hourcastagné, E., Viguier, B., & Crabos, F. (2014). Isothermal oxidation behaviour of NiCoCrAlYTa coatings produced by HVOF spraying and Tribomet™ process. *Oxidation of Metals, 81*, 105-113.

Handbook, A. (2004). Handbook of Thermal Spray Technology: Chap.

Hass, D., Slifka, A., & Wadley, H. (2001). Low thermal conductivity vapor deposited zirconia microstructures. *Acta materialia, 49*(6), 973-983.

Hass, D. D. (2000). Directed vapor deposition of thermal barrier coatings. *Materials science and engineering. Ph. D. University of Virginia, 281*.

He, J. (2022). Advanced MCrAlY alloys with doubled TBC lifetime. *Surface and Coatings Technology, 448*, 128931.

Hejrani, E., Sebold, D., Nowak, W., Mauer, G., Naumenko, D., Vaßen, R., & Quadakkers, W. (2017). Isothermal and cyclic oxidation behavior of free standing MCrAlY coatings manufactured by high-velocity atmospheric plasma spraying. *Surface and Coatings Technology, 313*, 191-201.

Hindam, H., & Whittle, D. (1982). Microstructure, adhesion and growth kinetics of protective scales on metals and alloys. *Oxidation of Metals, 18*(5), 245-284.

Hindam, H., & Whittle, D. P. (1982). Microstructure, adhesion and growth kinetics of protective scales on metals and alloys. *Oxidation of Metals, 18*(5-6), 245-284. doi: 10.1007/BF00656571. Repéré à https://www.scopus.com/inward/record.uri?eid=2-s2.0-0020259269&doi=10.1007%2fBF00656571&partnerID=40&md5=d90965b72d34a87e1d774d384b9c8bcb

Hong, W., Lan, X.-d., Yong, L., Fei, L., Zhang, W.-d., Chen, Z.-j., . . . Han, Z. (2016). Fabrication, tribological and corrosion behaviors of detonation gun sprayed Fe-based metallic glass coating. *Transactions of Nonferrous Metals Society of China, 26*(6), 1629-1637.

International, A. (2016). *ASTM E8/E8M-16a: standard test methods for tension testing of metallic materials*. doi: 10.1520/E0008_E0008M-16A

Ishii, K., Kohno, M., Ishikawa, S., & Satoh, S. C.-s. (1997). Effect of Rare-Earth Elements on High-Temperature Oxidation Resistance of Fe-20Cr-5Al Alloy Foils. *Materials transactions, 38*, 787-792.

Jang, B.-K., & Matsubara, H. (2005). Hardness and Young's modulus of nanoporous EB-PVD YSZ coatings by nanoindentation. *Journal of Alloys and Compounds, 402*(1-2), 237-241.

Janisson, S., Meillot, E., Vardelle, A., Coudert, J. F., Pateyron, B., & Fauchais, P. (1999). Plasma spraying using Ar-He-H2 gas mixtures. *Journal of thermal spray technology, 8*(4), 545-552. doi: 10.1361/105996399770350232. Repéré à https://doi.org/10.1361/105996399770350232

Jiang, J., Xu, B., Wang, W., Adjei, R. A., Zhao, X., & Liu, Y. (2017). Finite element analysis of the effects of thermally grown oxide thickness and interface asperity on the cracking behavior between the thermally grown oxide and the bond coat. *Journal of Engineering for Gas Turbines and Power, 139*(2), 022504.

Jiang, J., Zou, Z., Wang, W., Zhao, X., Liu, Y., & Cao, Z. (2018). Effect of internal oxidation on the interfacial morphology and residual stress in air plasma sprayed thermal barrier coatings. *Surface and Coatings Technology, 334*, 215-226. doi: https://doi.org/10.1016/j.surfcoat.2017.11.040. Repéré à https://www.sciencedirect.com/science/article/pii/S0257897217311854

Jude, S., Jappes, J. W., & Adamkhan, M. (2022). Thermal barrier coatings for high-temperature application on superalloy substrates-A review. *Materials Today: Proceedings, 60*, 1670-1675.

Kalush, A., Texier, D., Ecochard, M., Sirvin, Q., Choquet, K., Gheno, T., . . . Bocher, P. (2022). Size effects on high temperature oxidation of MCrAlY coatings processed via APS and HVOF depositions. *Surface and Coatings Technology, 440*, 128483.

Kang, Y., Bai, Y., Fan, W., Yuan, T., Gao, Y., Bao, C., & Li, B. (2018). Thermal cycling performance of La2Ce2O7/50 vol.% YSZ composite thermal barrier coating with CMAS corrosion. *Journal of the European Ceramic Society, 38*(7), 2851-2862.

Karaoglanli, A. C., Ozgurluk, Y., & Doleker, K. M. (2020). Comparison of microstructure and oxidation behavior of CoNiCrAlY coatings produced by APS, SSAPS, D-gun, HVOF and CGDS techniques. *Vacuum, 180*, 109609.

Karlsson, A. M., & Evans, A. (2001). A numerical model for the cyclic instability of thermally grown oxides in thermal barrier systems. *Acta materialia, 49*(10), 1793-1804.

Klemens, P., & Gell, M. (1998). Thermal conductivity of thermal barrier coatings. *Materials Science and Engineering: A, 245*(2), 143-149.

Krämer, S., Faulhaber, S., Chambers, M., Clarke, D. R., Levi, C. G., Hutchinson, J. W., & Evans, A. (2008). Mechanisms of cracking and delamination within thick thermal barrier systems in aero-engines subject to calcium-magnesium-alumino-silicate (CMAS) penetration. *Materials Science and Engineering: A, 490*(1-2), 26-35.

Kumar, R., Kumar, R., & Kumar, S. (2018). Erosion Corrosion Study of HVOF Sprayed Thermal Sprayed Coatings on Boiler Tubes:A Review. *International Journal of Science and Management Studies (IJSMS)*, 1-6. doi: 10.51386/25815946/ijsms-v1i3p101

Kumar, S., Prasad C, D., & Hanumanthappa, H. (2024). Role of Thermal Spray Coatings on Erosion, Corrosion, and Oxidation in Various Applications: A Review. *Journal of Bio- and Tribo-Corrosion, 10*, 22. doi: 10.1007/s40735-024-00822-8

Kumar, V., & Balasubramanian, K. (2016). Progress update on failure mechanisms of advanced thermal barrier coatings: A review. *Progress in Organic Coatings, 90*, 54-82.

Kwon, H., Kang, Y.-j., Yoo, Y. W., Kim, D. H., Park, Y., Lee, S., & Park, H. (2023). Effect of process-gas composition on in-flight and deposition characteristics of atmospheric plasma-sprayed Ni particles. *Metals and Materials International, 29*(6), 1825-1840.

Lee, C., Kim, H., Choi, H., & Ahn, H. (2000). Phase transformation and bond coat oxidation behavior of plasma-sprayed zirconia thermal barrier coating. *Surface and Coatings Technology, 124*(1), 1-12.

Léger, A. C., Wigren, J., & Hansson, M. O. (1998). Development of a process window for a NiCoCrAlY plasma-sprayed coating. *Surface and Coatings Technology, 108-109*, 86-92. doi: https://doi.org/10.1016/S0257-8972(98)00615-X. Repéré à https://www.sciencedirect.com/science/article/pii/S025789729800615X

Li, C.-J., & Li, W.-Y. (2003). Effect of sprayed powder particle size on the oxidation behavior of MCrAlY materials during high velocity oxygen-fuel deposition. *Surface and Coatings Technology, 162*(1), 31-41.

Li, C.-J., & Yang, G.-J. (2013). Relationships between feedstock structure, particle parameter, coating deposition, microstructure and properties for thermally sprayed conventional and nanostructured WC–Co. *International Journal of Refractory Metals and Hard Materials, 39*, 2-17.

Li, X., Huang, X., Yang, Q., & Tang, Z. (2016). Isothermal and cyclic oxidation performance of vertically cracked and columnar thermal barrier coating structures produced using axial suspension plasma spraying process. *Journal of Engineering for Gas Turbines and Power, 138*(1), 012506.

Li, Y., Li, C.-J., Yang, G.-J., & Xing, L.-K. (2010). Thermal fatigue behavior of thermal barrier coatings with the MCrAlY bond coats by cold spraying and low-pressure plasma spraying. *Surface and Coatings Technology, 205*(7), 2225-2233.

Li, Y., Li, C.-J., Zhang, Q., Yang, G.-J., & Li, C.-X. (2010). Influence of TGO composition on the thermal shock lifetime of thermal barrier coatings with cold-sprayed MCrAlY bond coat. *Journal of thermal spray technology, 19*, 168-177.

Lima, R. S., & Marple, B. R. (2007). Thermal Spray Coatings Engineered from Nanostructured Ceramic Agglomerated Powders for Structural, Thermal Barrier and Biomedical Applications: A Review. *Journal of thermal spray technology, 16*(1), 40-63. doi: 10.1007/s11666-006-9010-7. Repéré à https://doi.org/10.1007/s11666-006-9010-7

Lipkin, D. a., & Clarke, D. (1996). Measurement of the stress in oxide scales formed by oxidation of alumina-forming alloys. *Oxidation of Metals, 45*, 267-280.

Liu, T., Zheng, L., & Zhang, H. (2016). Effect of solid shield on coating properties in atmospheric plasma spray process. *Journal of thermal spray technology, 25*, 1502-1515.

Liu, Y., Liu, Y., Lours, P., Sentenac, T., Vidal, V., Wang, Z., & Ding, K. (2017). Influence of isothermal aging conditions on APS TBC's interfacial fracture toughness. *Surface and Coatings Technology, 313*, 417-424.

Lokachari, S., Leng, K., Rincon Romero, A., Curry, N., Brewster, G., Norton, A., & Hussain, T. (2024). Processing–Microstructure–Properties of Columns in Thermal Barrier Coatings: A Study of Thermo-Chemico-Mechanical Durability. *ACS Applied Materials & Interfaces*.

Lu, J., Chen, Y., Zhao, C., Zhang, H., Luo, L., Xu, B., . . . Xiao, P. (2019). Significantly improving the oxidation and spallation resistance of a MCrAlY alloy by controlling the distribution of yttrium. *Corrosion Science, 153*, 178-190.

Lugscheider, E., Herbst, C., & Zhao, L. (1998). Parameter studies on high-velocity oxy-fuel spraying of MCrAlY coatings. *Surface and Coatings Technology, 108*, 16-23.

Ma, K., & Schoenung, J. M. (2011). Isothermal oxidation behavior of cryomilled NiCrAlY bond coat: Homogeneity and growth rate of TGO. *Surface and Coatings Technology, 205*(21), 5178-5185. doi: https://doi.org/10.1016/j.surfcoat.2011.05.025. Repéré à https://www.sciencedirect.com/science/article/pii/S0257897211005287

Matsumoto, M., Hayakawa, K., Kitaoka, S., Matsubara, H., Takayama, H., Kagiya, Y., & Sugita, Y. (2006). The effect of preoxidation atmosphere on oxidation behavior and thermal cycle life of thermal barrier coatings. *Materials Science and Engineering: A, 441*(1-2), 119-125.

Mellali, M., Fauchais, P., & Grimaud, A. (1996). Influence of substrate roughness and temperature on the adhesion/cohesion of alumina coatings. *Surface and Coatings Technology, 81*(2), 275-286. doi: https://doi.org/10.1016/0257-8972(95)02540-5. Repéré à https://www.sciencedirect.com/science/article/pii/0257897295025405

Meng, G.-H., Liu, H., Liu, M.-J., Xu, T., Yang, G.-J., Li, C.-X., & Li, C.-J. (2019). Highly oxidation resistant MCrAlY bond coats prepared by heat treatment under low oxygen content. *Surface and Coatings Technology, 368*, 192-201.

Meng, G.-H., Zhang, B.-Y., Liu, H., Yang, G.-J., Xu, T., Li, C.-X., & Li, C.-J. (2018a). Highly oxidation resistant and cost effective MCrAlY bond coats prepared by controlled atmosphere heat treatment. *Surface and Coatings Technology, 347*, 54-65.

Meng, G.-H., Zhang, B.-Y., Liu, H., Yang, G.-J., Xu, T., Li, C.-X., & Li, C.-J. (2018b). Vacuum heat treatment mechanisms promoting the adhesion strength of thermally sprayed metallic coatings. *Surface and Coatings Technology, 344*, 102-110.

Mévrel, R. (1989). State of the art on high-temperature corrosion-resistant coatings. *Materials Science and Engineering: A, 120-121*, 13-24. doi: https://doi.org/10.1016/0921-5093(89)90713-2. Repéré à https://www.sciencedirect.com/science/article/pii/0921509389907132

Mondal, K., Nuñez III, L., Downey, C. M., & Van Rooyen, I. J. (2021). Thermal barrier coatings overview: Design, manufacturing, and applications in high-temperature industries. *Industrial & Engineering Chemistry Research, 60*(17), 6061-6077.

Mutasim, Z., Rimlinger, C., & Brentnall, W. (1997). Characterization of Plasma Sprayed and Electron Beam-Physical Vapor Deposited Thermal Barrier Coatings. Dans *ASME 1997 International Gas Turbine and Aeroengine Congress and Exhibition* (Vol. Volume 4: Manufacturing Materials and Metallurgy; Ceramics; Structures and Dynamics; Controls, Diagnostics and Instrumentation; Education; IGTI Scholar Award). V004T12A026. doi: 10.1115/97-gt-531. Repéré à https://doi.org/10.1115/97-GT-531

Naeimi, F., Rahimipour, M. R., & Salehi, M. (2016). Effect of sandblasting process on the oxidation behavior of HVOF MCrAlY coatings. *Oxidation of Metals, 86*, 59-73.

Nagabandi, K., Mills, S., Zhang, X., Toal, D., & Keane, A. (2017). Surrogate Based Design Optimisation of Combustor Tile Cooling Feed Holes. Dans *Gas Turbine India Conference* (Vol. 58509, pp. V001T003A007). American Society of Mechanical Engineers.

Nakajima, H. (1997). The discovery and acceptance of the Kirkendall Effect: The result of a short research career. *Jom, 49*, 15-19.

Nath, S., Manna, I., & Majumdar, J. D. (2014). Kinetics and mechanism of isothermal oxidation of compositionally graded yttria stabilized zirconia (YSZ) based thermal barrier coating. *Corrosion Science, 88*, 10-22.

Naumenko, D., Pint, B. A., & Quadakkers, W. (2016). Current thoughts on reactive element effects in alumina-forming systems: in memory of John Stringer. *Oxidation of Metals, 86*, 1-43.

Nesbitt, J. A. (1983). *OVERLAY COATING DEGRADATION BY SIMULTANEOUS OXIDATION AND COATING/SUBSTRATE INTERDIFFUSION (NICKEL-CHROMIUM-ALUMINUM ZIRCONIUM)*. Michigan Technological University.

Ng, H. W., & Gan, Z. (2005). A finite element analysis technique for predicting as-sprayed residual stresses generated by the plasma spray coating process. *Finite Elements in Analysis and Design, 41*(13), 1235-1254. doi:

https://doi.org/10.1016/j.finel.2005.02.002. Repéré à https://www.sciencedirect.com/science/article/pii/S0168874X05000387

Nicholls, J. (2000). Designing oxidation-resistant coatings. *Jom, 52*(1), 28-35.

Nicholls, J. R. (2000). Designing oxidation-resistant coatings. *Jom, 52*(1), 28-35. doi: 10.1007/s11837-000-0112-2. Repéré à https://doi.org/10.1007/s11837-000-0112-2

Nijdam, T., Jeurgens, L., Chen, J., & Sloof, W. (2005). On the microstructure of the initial oxide grown by controlled annealing and oxidation on a NiCoCrAlY bond coating. *Oxidation of Metals, 64*, 355-377.

Nijdam, T., & Sloof, W. (2008). Effect of Y distribution on the oxidation kinetics of NiCoCrAlY bond coat alloys. *Oxidation of Metals, 69*(1), 1-12.

Niranatlumpong, P., Ponton, C., & Evans, H. (2000). The failure of protective oxides on plasma-sprayed NiCrAlY overlay coatings. *Oxidation of Metals, 53*, 241-258.

Niranatlumpong, P., Ponton, C. B., & Evans, H. E. (2000). Failure of protective oxides on plasma-sprayed NiCrAlY overlay coatings. *Oxidation of Metals, 53*(3), 241-258. doi: 10.1023/a:1004549219013. Repéré à https://www.scopus.com/inward/record.uri?eid=2-s2.0-0033875119&doi=10.1023%2fa%3a1004549219013&partnerID=40&md5=f467520d62426cc00ef310ed14209bc6

Nouri, A., & Sola, A. (2019). Powder morphology in thermal spraying. *Journal of Advanced Manufacturing and Processing, 1*(3), e10020.

Nowak, W., Naumenko, D., Mor, G., Mor, F., Mack, D. E., Vassen, R., . . . Quadakkers, W. (2014). Effect of processing parameters on MCrAlY bondcoat roughness and lifetime of APS–TBC systems. *Surface and Coatings Technology, 260*, 82-89.

Object Research Systems, I. (2021). Dragonfly 2021.3. Montreal, Canada. Repéré à https://www.theobjects.com/dragonfly/

Oksa, M., Turunen, E., Suhonen, T., Varis, T., & Hannula, S.-P. (2011). Optimization and characterization of high velocity oxy-fuel sprayed coatings: techniques, materials, and applications. *Coatings, 1*(1), 17-52.

Padture, N. P. (2016). Advanced structural ceramics in aerospace propulsion. *Nature materials, 15*(8), 804-809.

Padture, N. P., Gell, M., & Jordan, E. H. (2002). Thermal barrier coatings for gas-turbine engine applications. *Science, 296*(5566), 280-284.

Pan, B., Qian, K., Xie, H., & Asundi, A. (2009). Two-dimensional digital image correlation for in-plane displacement and strain measurement: a review. *Measurement science and technology, 20*(6), 062001.

Patterson, T., Leon, A., Jayaraj, B., Liu, J., & Sohn, Y. (2008). Thermal cyclic lifetime and oxidation behavior of air plasma sprayed CoNiCrAlY bond coats for thermal barrier coatings. *Surface and Coatings Technology, 203*(5-7), 437-441.

Patterson, T., Leon, A., Jayaraj, B., Liu, J., & Sohn, Y. H. (2008). Thermal cyclic lifetime and oxidation behavior of air plasma sprayed CoNiCrAlY bond coats for thermal barrier coatings. *Surface and Coatings Technology, 203*(5), 437-441. doi: https://doi.org/10.1016/j.surfcoat.2008.08.054. Repéré à https://www.sciencedirect.com/science/article/pii/S0257897208008219

Pawlowski, L. (2008). *The science and engineering of thermal spray coatings*. John Wiley & Sons.

Peng, H., Guo, H., He, J., & Gong, S. (2010). Cyclic oxidation and diffusion barrier behaviors of oxides dispersed NiCoCrAlY coatings. *Journal of Alloys and Compounds, 502*(2), 411-416.

Pieraggi, B. (1987). Calculations of parabolic reaction rate constants. *Oxidation of Metals, 27*, 177-185.

Pilling, N. (1923). The oxidation of metals at high temperature. *J. Inst. Met., 29*, 529-582.

Pollock, T. M., Laux, B., Brundidge, C. L., Suzuki, A., & He, M. Y. (2011). Oxide-Assisted Degradation of Ni-Base Single Crystals During Cyclic Loading: the Role of Coatings. *Journal of the American Ceramic Society, 94*, s136-s145.

Poza, P., Gómez-García, J., & Múnez, C. (2012). TEM analysis of the microstructure of thermal barrier coatings after isothermal oxidation. *Acta materialia, 60*(20), 7197-7206.

Prochazka, Z., Khor, K. A., & Cizek, J. (2006). Influence of input parameters on splat formation and coating thermal diffusivity in plasma spraying. *Advanced Engineering Materials, 8*(7), 645-650.

Rabiei, A., & Evans, A. (2000). Failure mechanisms associated with the thermally grown oxide in plasma-sprayed thermal barrier coatings. *Acta materialia, 48*(15), 3963-3976.

Raffaitin, A., Monceau, D., Andrieu, E., & Crabos, F. (2006). Cyclic oxidation of coated and uncoated single-crystal nickel-based superalloy MC2 analyzed by continuous thermogravimetry analysis. *Acta materialia, 54*(17), 4473-4487. doi: https://doi.org/10.1016/j.actamat.2006.05.034. Repéré à https://www.sciencedirect.com/science/article/pii/S1359645406003909

Reed, R. C. (2008). *The superalloys: fundamentals and applications*. Cambridge university press.

Ren, X., & Pan, W. (2014). Mechanical properties of high-temperature-degraded yttria-stabilized zirconia. *Acta materialia, 69*, 397-406.

Renusch, D., Schorr, M., & Schütze, M. (2008). The role that bond coat depletion of aluminum has on the lifetime of APS-TBC under oxidizing conditions. *Materials and corrosion, 59*(7), 547-555.

Rhys-Jones, T. N. (1989). Coatings for blade and vane applications in gas turbines. *Corrosion Science, 29*(6), 623-646. doi: https://doi.org/10.1016/0010-938X(89)90104-2. Repéré à https://www.sciencedirect.com/science/article/pii/0010938X89901042

Richer, P., Yandouzi, M., Beauvais, L., & Jodoin, B. (2010). Oxidation behaviour of CoNiCrAlY bond coats produced by plasma, HVOF and cold gas dynamic spraying. *Surface and Coatings Technology, 204*(24), 3962-3974.

Ritzert, F., Arenas, D., Keller, D., & Vasudevan, V. (1998). *The effect of alloying on topologically close packed phase instability in advanced nickel-based superalloy rene N6*.

Romain, C., Texier, D., Desgranges, C., Cormier, J., Knittel, S., Monceau, D., & Delagnes, D. (2021). Oxidation of Thin Nickel-Based Superalloy Specimens: Kinetics Study and Mechanical Integrity. *Oxidation of Metals, 96*(1), 169-182. doi: 10.1007/s11085-021-10075-2. Repéré à https://doi.org/10.1007/s11085-021-10075-2

Rösler, J., Bäker, M., & Aufzug, K. (2004). A parametric study of the stress state of thermal barrier coatings: Part I: creep relaxation. *Acta materialia, 52*(16), 4809-4817.

Saeidi, S., Voisey, K., & McCartney, D. (2009). The effect of heat treatment on the oxidation behavior of HVOF and VPS CoNiCrAlY coatings. *Journal of thermal spray technology, 18*, 209-216.

Salehi Doolabi, M., Ghasemi, B., Sadrnezhaad, S., Habibolahzadeh, A., & Jafarzadeh, K. (2018). Evaluation and selection of optimal oxygen/fuel ratio for best mechanical properties, oxidation resistance and microstructure of HVOF NiCoCrAlY coatings using AHP–VIKOR method. *Oxidation of Metals, 89*, 429-451.

Sampath, S., Jiang, X., Matejicek, J., Prchlik, L., Kulkarni, A., & Vaidya, A. (2004). Role of thermal spray processing method on the microstructure, residual stress and properties of coatings: an integrated study for Ni–5 wt.% Al bond coats. *Materials Science and Engineering: A, 364*(1-2), 216-231.

Saremi, M., Afrasiabi, A., & Kobayashi, A. (2008). Microstructural analysis of YSZ and YSZ/Al2O3 plasma sprayed thermal barrier coatings after high temperature oxidation. *Surface and Coatings Technology, 202*(14), 3233-3238.

Sato, A., Chiu, Y.-L., & Reed, R. (2011). Oxidation of nickel-based single-crystal superalloys for industrial gas turbine applications. *Acta materialia, 59*(1), 225-240.

Schindelin, J., Arganda-Carreras, I., Frise, E., Kaynig, V., Longair, M., Pietzsch, T., . . . Cardona, A. (2012). Fiji: an open-source platform for biological-image analysis. *Nature Methods, 9*(7), 676-682. doi: 10.1038/nmeth.2019. Repéré à https://doi.org/10.1038/nmeth.2019

Schlichting, K. W., Padture, N., Jordan, E., & Gell, M. (2003). Failure modes in plasma-sprayed thermal barrier coatings. *Materials Science and Engineering: A, 342*(1-2), 120-130.

Schulz, U., Leyens, C., Fritscher, K., Peters, M., Saruhan, B., Lavigne, O., . . . Caliez, M. (2003). Some Recent Trends in Research and Technology of Advanced Thermal Barrier Coatings. *Aerospace Science and Technology, 7*, 73-80. doi: 10.1016/S1270-9638(02)00003-2

Schulz, U., Menzebach, M., Leyens, C., & Yang, Y. (2001). Influence of substrate material on oxidation behavior and cyclic lifetime of EB-PVD TBC systems. *Surface and Coatings Technology, 146*, 117-123.

Schulz, U., Saruhan, B., Fritscher, K., & Leyens, C. (2004). Review on advanced EB-PVD ceramic topcoats for TBC applications. *International journal of applied ceramic technology, 1*(4), 302-315.

Seo, D., Ogawa, K., Suzuki, Y., Ichimura, K., Shoji, T., & Murata, S. (2008). Comparative study on oxidation behavior of selected MCrAlY coatings by elemental concentration profile analysis. *Applied Surface Science, 255*(5, Part 2), 2581-2590. doi: https://doi.org/10.1016/j.apsusc.2008.07.141. Repéré à https://www.sciencedirect.com/science/article/pii/S0169433208017765

Shen, Q., Li, S., Yang, L., Zhou, Y., Wei, Y., & Yuan, T. (2018). Coupled mechanical-oxidation modeling during oxidation of thermal barrier coatings. *Computational Materials Science, 154*, 538-546.

Shi, J., Zhang, T., Sun, B., Wang, B., Zhang, X., & Song, L. (2020). Isothermal oxidation and TGO growth behavior of NiCoCrAlY-YSZ thermal barrier coatings on a Ni-based superalloy. *Journal of Alloys and Compounds, 844*, 156093.

Shibata, M., Kuroda, S., Murakami, H., Ode, M., Watanabe, M., & Sakamoto, Y. (2006). Comparison of microstructure and oxidation behavior of CoNiCrAlY bond coatings prepared by different thermal spray processes. *Materials transactions, 47*(7), 1638-1642.

Sidhu, T., Prakash, S., & Agrawal, R. (2005). State of the art of HVOF coating investigations—A review. *Marine Technology Society Journal, 39*(2), 53-64.

Sloof, W., & Nijdam, T. (2009). On the high-temperature oxidation of MCrAlY coatings. *International Journal of Materials Research, 100*(10), 1318-1330.

Sloof, W. G., & Nijdam, T. J. (2009). On the high-temperature oxidation of MCrAlY coatings. *International Journal of Materials Research, 100*(10), 1318-1330. doi: doi:10.3139/146.110201. Repéré à https://doi.org/10.3139/146.110201

Smialek, J. (2000). Maintaining adhesion of protective Al 2 O 3 scales. *Jom, 52*, 22-25.

Standard, I. (1998). 4287: 1997: Geometrical product specifications (GPS)–Surface texture: profile method–Terms, definitions and surface texture parameters. *(No Title)*.

Stott, F. (1992). Developments in understanding the mechanisms of growth of protective scales on high-temperature alloys. *Materials characterization, 28*(3), 311-325.

Strehl, G., Naumenko, D., Al-Badairy, H., Rodriguez Lobo, L. M., Borchardt, G., Tatlock, G. J., & Quadakkers, W. J. (2000). The effect of aluminium depletion on the oxidation behaviour of FeCrAl foils. *Materials at High Temperatures, 17*(1), 87-92. doi: 10.1179/mht.2000.014. Repéré à https://doi.org/10.1179/mht.2000.014

Sun, J., Fu, Q.-G., Liu, G.-N., Li, H.-J., Shu, Y.-C., & Fan, G. (2015). Thermal shock resistance of thermal barrier coatings for nickel-based superalloy by supersonic plasma spraying. *Ceramics International, 41*(8), 9972-9979.

Sun, X., Li, X., Guo, S., Yu, X., Zhu, L., Teng, J., . . . Peng, R. L. (2024). Revealing microstructural degradation mechanism induced by interdiffusion between Amdry365 coating and IN792 superalloy. *Materials & Design*, 112937.

Sutton, M. A., Orteu, J. J., & Schreier, H. (2009). *Image correlation for shape, motion and deformation measurements: basic concepts, theory and applications*. Springer Science & Business Media.

Szala, M., Walczak, M., & Świetlicki, A. (2021). Effect of microstructure and hardness on cavitation erosion and dry sliding wear of HVOF deposited CoNiCrAlY, NiCoCrAlY and NiCrMoNbTa coatings. *Materials, 15*(1), 93.

Tamarin, Y. (2002). *Protective coatings for turbine blades*. ASM international.

Tammann, G. (1920). Über Anlauffarben von metallen. *Zeitschrift für anorganische und allgemeine Chemie, 111*(1), 78-89.

Tancret, F., Bhadeshia, H., & MacKay, D. (2003). Design of a creep resistant nickel base superalloy for power plant applications: Part 1-Mechanical properties modelling. *Materials Science and Technology, 19*(3), 283-290.

Tang, F., Ajdelsztajn, L., & Schoenung, J. M. (2004). Characterization of oxide scales formed on HVOF NiCrAlY coatings with various oxygen contents introduced during thermal spraying. *Scripta Materialia, 51*(1), 25-29.

Tao, C., Wang, L., & Song, X. (2017). High-temperature frictional wear behavior of MCrAlY-based coatings deposited by atmosphere plasma spraying. *International Journal of Minerals, Metallurgy, and Materials, 24*, 222-228.

Taylor, A., & Floyd, R. (1951). The Constitution of Nickel-rich Alloys ofthe Nicke-Chromium-Titanium System. *J. Inst. Met, 80*, 577-587.

Taylor, M., Evans, H. E., Gray, S., & Nicholls, J. R. (2011). A chromia forming thermal barrier coating system. *Materials and corrosion, 62*(7), 668-673.

Tejero-Martin, D., Rezvani Rad, M., McDonald, A., & Hussain, T. (2019). Beyond Traditional Coatings: A Review on Thermal-Sprayed Functional and Smart Coatings. *Journal of thermal spray technology, 28*(4), 598-644. doi: 10.1007/s11666-019-00857-1. Repéré à https://doi.org/10.1007/s11666-019-00857-1

Teng, J., Gong, X., Yang, B., Yu, S., Liu, J., & Li, Y. (2021). Influence of Ti addition on oxidation behavior of Ni-Cr-W-based superalloys. *Corrosion Science, 193*, 109882.

Terry, S. G. (1999). Elevated temperature coatings. *Science and Technology*.

Texier, D. (2013). *Measurement and evolution of the gradient of mechanical properties in MCrAlY coated MC2 nickel based superalloy system* (PhD thesis, INP Toulouse, Toulouse, 2013, 1–299).

Texier, D., Cadet, C., Straub, T., Eberl, C., & Maurel, V. (2020). Tensile behavior of air plasma spray MCrAlY coatings: Role of high temperature agings and process defects. *Metallurgical and Materials Transactions A, 51*(6), 2766-2777.

Texier, D., Ecochard, M., Gheno, T., Monceau, D., Salem, M., & Lours, P. (2021). Screening for Al2O3 failure in MCrAlY APS coatings using short-term oxidation at high temperature. *Corrosion Science, 184*, 109334.

Texier, D., Monceau, D., Crabos, F., & Andrieu, E. (2017). Tensile properties of a non-line-of-sight processed β-γ-γ′ MCrAlY coating at high temperature. *Surface and Coatings Technology, 326*, 28-36. doi: https://doi.org/10.1016/j.surfcoat.2017.07.026. Repéré à https://www.sciencedirect.com/science/article/pii/S0257897217307132

Texier, D., Monceau, D., Hervier, Z., & Andrieu, E. (2016). Effect of interdiffusion on mechanical and thermal expansion properties at high temperature of a MCrAlY coated Ni-based superalloy. *Surface and Coatings Technology, 307*, 81-90.

Texier, D., Monceau, D., Salabura, J. C., Mainguy, R., & Andrieu, E. (2016). Micromechanical testing of ultrathin layered material specimens at elevated temperature. *Materials at High Temperatures, 33*(4-5), 325-337. doi: 10.1080/09603409.2016.1182250. Repéré à https://doi.org/10.1080/09603409.2016.1182250

Thakare, J. G., Pandey, C., Mahapatra, M., & Mulik, R. S. (2021). Thermal barrier coatings—A state of the art review. *Metals and Materials International, 27*, 1947-1968.

Thornton, J., Slater, S., & Almer, J. (2005). The measurement of residual strains within thermal barrier coatings using high-energy X-ray diffraction. *Journal of the American Ceramic Society, 88*(10), 2817-2825.

Toma, D., Brandl, W., & Köster, U. (1999). Studies on the transient stage of oxidation of VPS and HVOF sprayed MCrAlY coatings. *Surface and Coatings Technology, 120*, 8-15.

Torkashvand, K., Poursaeidi, E., & Mohammadi, M. (2018). Effect of TGO thickness on the thermal barrier coatings life under thermal shock and thermal cycle loading. *Ceramics International, 44*(8), 9283-9293.

Toscano, J., Naumenko, D., Gil, A., Singheiser, L., & Quadakkers, W. (2008). Parameters affecting TGO growth rate and the lifetime of TBC systems with MCrAlY-bondcoats. *Materials and corrosion, 59*(6), 501-507.

Toscano, J., Vaβen, R., Gil, A., Subanovic, M., Naumenko, D., Singheiser, L., & Quadakkers, W. (2006). Parameters affecting TGO growth and adherence on MCrAlY-bond coats for TBC's. *Surface and Coatings Technology, 201*(7), 3906-3910.

Ullah, A., Khan, A., Bao, Z., Yu, C., Zhu, S., & Wang, F. (2020). Effect of vacuum annealing on initial oxidation behavior and alumina transition of NiCoCrAlY coatings. *Surface and Coatings Technology, 404*, 126441.

Vanderesse, N., Lagacé, M., Bridier, F., & Bocher, P. (2013). An Open Source Software for the Measurement of Deformation Fields by Means of Digital Image Correlation. *Microscopy and Microanalysis, 19*(S2), 820-821. doi: 10.1017/S1431927613006090. Repéré à https://www.cambridge.org/core/article/an-open-source-software-for-the-measurement-of-deformation-fields-by-means-of-digital-image-correlation/809DA43CB68038653C7F52A6E1E0DD99

Vanderesse, N., Richter, A., Nuno, N., & Bocher, P. (2018). Measurement of deformation heterogeneities in additive manufactured lattice materials by Digital Image Correlation: Strain maps analysis and reliability assessment. *J Mech Behav Biomed Mater, 86*, 397-408. doi: 10.1016/j.jmbbm.2018.07.010. Repéré à https://www.ncbi.nlm.nih.gov/pubmed/30029167

Vaßen, R., Kerkhoff, G., & Stöver, D. (2001). Development of a micromechanical life prediction model for plasma sprayed thermal barrier coatings. *Materials Science and Engineering: A, 303*(1-2), 100-109.

Vats, A., Kumar, A., Patnaik, A., & Meena, M. (2021). Influence of deposition parameters on Tribological Performance of HVOF Coating: A review. Dans *IOP Conference Series: Materials Science and Engineering* (Vol. 1017, pp. 012015). IOP Publishing.

Vialas, N., & Monceau, D. (2006). Effect of Pt and Al content on the long-term, high temperature oxidation behavior and interdiffusion of a Pt-modified aluminide coating deposited on Ni-base superalloys. *Surface and Coatings Technology, 201*(7), 3846-3851. doi: https://doi.org/10.1016/j.surfcoat.2006.07.246. Repéré à https://www.sciencedirect.com/science/article/pii/S0257897206007948

Vicente-Mendoza, M., Mora-García, A., Muñoz-Saldaña, J., & Juárez-López, F. (2023). High-Temperature Oxidation of MCrAlY Coating Modified by Alumina Deposited by an MOCVD Process. *High Temperature Corrosion of Materials, 100*(3), 193-207.

Voggenreiter, H., Huber, H., Beyer, S., & Spies, H. (1995). *Influence of particle velocity and molten phase on the chemical and mechanical properties of HVOF-sprayed structural coatings of Alloy 316L*. ASM International, Materials Park, OH (United States).

Wagner, C. (1933). Beitrag zur theorie des anlaufvorgangs. *Zeitschrift für physikalische Chemie, 21*(1), 25-41.

Waki, H., Kitamura, T., & Kobayashi, A. (2009). Effect of thermal treatment on high-temperature mechanical properties enhancement in LPPS, HVOF, and APS CoNiCrAlY coatings. *Journal of thermal spray technology, 18*, 500-509.

Wang, L., Zhao, Y., Zhong, X., Tao, S., Zhang, W., & Wang, Y. (2014). Influence of "island-like" oxides in the bond-coat on the stress and failure patterns of the thermal-barrier coatings fabricated by atmospheric plasma spraying during long-term high temperature oxidation. *Journal of thermal spray technology, 23*, 431-446.

Wang, L., Zhao, Y. X., Zhong, X. H., Tao, S. Y., Zhang, W., & Wang, Y. (2014). Influence of "Island-Like" Oxides in the Bond-Coat on the Stress and Failure Patterns of the Thermal-Barrier Coatings Fabricated by Atmospheric Plasma Spraying During Long-Term High Temperature Oxidation. *Journal of thermal spray technology, 23*(3), 431-446. doi: 10.1007/s11666-013-0008-7. Repéré à https://doi.org/10.1007/s11666-013-0008-7

Wefers, K., & Misra, C. (1987). *Oxides and hydroxides of aluminum* (Vol. 19). Alcoa Laboratories Pittsburgh.

Wei, Z.-Y., & Cai, H.-N. (2020). Comprehensive effects of TGO growth on the stress characteristic and delamination mechanism in lamellar structured thermal barrier coatings. *Ceramics International, 46*(2), 2220-2237.

Wei, Z.-Y., Cai, H.-N., Meng, G.-H., Tahir, A., & Zhang, W.-W. (2020). An innovative model coupling TGO growth and crack propagation for the failure assessment of lamellar structured thermal barrier coatings. *Ceramics International, 46*(2), 1532-1544.

Wei, Z.-Y., Cai, H.-N., & Zhao, S.-D. (2022). Comprehensive understanding of horizontal and vertical crack effects on failure mechanism of lamellar structured thermal barrier coatings. *Ceramics International, 48*(6), 8143-8154.

Wei, Z.-Y., Liu, Y., Cheng, B., & Tahir, A. (2022). Influence of non-uniform feature of thermally grown oxide thickness on the local stress state and cracking behavior in TBC. *Surface and Coatings Technology, 443*, 128607.

Weiser, M., Chater, R. J., Shollock, B. A., & Virtanen, S. (2019). Transport mechanisms during the high-temperature oxidation of ternary γ/γ′ Co-base model alloys. *NPJ Materials Degradation, 3*(1), 33.

Wellman, R., Scrivani, A., Rizzi, G., Weisenburger, A., Tenailleau, F., & Nicholls, J. R. (2007). Pulsed electron beam treatment of MCrAlY bondcoats for EB PVD TBC systems part 2 of 2: Cyclic oxidation of the coatings. *Surface and Coatings Technology, 202*(4-7), 709-713.

Whitehouse, D. J. (2002). *Handbook of surface and nanometrology*. Taylor & Francis.

Wilber, J. P., Bennett, M. J., & Nicholls, J. R. (2000). Life-time extension of alumina forming FeCrAl–RE alloys: influence of alloy thickness. *Materials at High Temperatures, 17*(1), 125-132. doi: 10.1179/mht.2000.019. Repéré à https://doi.org/10.1179/mht.2000.019

Wright, P., & Evans, A. G. (1999). Mechanisms governing the performance of thermal barrier coatings. *Current opinion in solid state and Materials Science, 4*(3), 255-265.

Wu, Y. N., Zhang, G., Feng, Z. C., Zhang, B. C., Liang, Y., & Liu, F. J. (2001). Oxidation behavior of laser remelted plasma sprayed NiCrAlY and NiCrAlY–Al2O3 coatings. *Surface and Coatings Technology, 138*(1), 56-60. doi: https://doi.org/10.1016/S0257-8972(00)01102-6. Repéré à https://www.sciencedirect.com/science/article/pii/S0257897200011026

Xiaofeng, Z., Kesong, Z., Huantao, C., Tao, H., Jinbing, S., & Min, L. (2015). Properties of Thermal Barrier Coatings Made of Different Shapes of ZrO2-7wt% Y2O3 Powders. *Rare Metal Materials and Engineering, 44*(6), 1301-1306.

Xie, Z., Liu, Q., Hu, X., Guo, J., & Zhu, W. (2024). On the Thermal Shock Resistance and Failure Mechanism of the Pt-Modified Aluminide Bond Coating. *Coatings, 14*(3), 326.

Xu, C., & Gao, W. (2000). Pilling-bedworth ratio for oxidation of alloys. *Materials Research Innovations, 3*(4), 231-235. doi: 10.1007/s100190050008. Repéré à

https://www.scopus.com/inward/record.uri?eid=2-s2.0-0009874095&doi=10.1007%2fs100190050008&partnerID=40&md5=3f958e12d6850ba341f5e75ead1a9e98

Xu, R., Fan, X. L., Zhang, W. X., & Wang, T. (2014). Interfacial fracture mechanism associated with mixed oxides growth in thermal barrier coating system. *Surface and Coatings Technology, 253*, 139-147.

Yang, M., Wang, X., Feng, W., Fu, Y., Jiang, Y., Chen, F., . . . Chen, Y. (2024). Effects of TGO growth on the interface stress distribution based on 3D pores in TBC ceramics layer. *Materials Today Communications, 38*, 107878.

Yao, J., He, Y., Wang, D., Peng, H., Guo, H., & Gong, S. (2014). Thermal barrier coating bonded by (Al2O3–Y2O3)/(Y2O3-stabilized ZrO2) laminated composite coating prepared by two-step cyclic spray pyrolysis. *Corrosion Science, 80*, 37-45.

Young, D. J. (2008). *High temperature oxidation and corrosion of metals* (Vol. 1). Elsevier.

Young, D. J., Chyrkin, A., He, J., Grüner, D., & Quadakkers, W. J. (2013). Slow Transition from Protective to Breakaway Oxidation of Haynes 214 Foil at High Temperature. *Oxidation of Metals, 79*(3), 405-427. doi: 10.1007/s11085-013-9364-4. Repéré à https://doi.org/10.1007/s11085-013-9364-4

Young, D. J., Chyrkin, A., & Quadakkers, W. J. (2012). A Simple Expression for Predicting the Oxidation Limited Life of Thin Components Manufactured from FCC High Temperature Alloys. *Oxidation of Metals, 77*(5), 253-264. doi: 10.1007/s11085-012-9283-9. Repéré à https://doi.org/10.1007/s11085-012-9283-9

Yuan, K., Peng, R. L., Li, X.-H., Johansson, S., & Wang, Y.-D. (2015). Some aspects of elemental behaviour in HVOF MCrAlY coatings in high-temperature oxidation. *Surface and Coatings Technology, 261*, 86-101.

Zhang, Y. (2015). *An Alternative Low-Cost Process for Deposition of MCrAlY Bond Coats for Advanced Syngas/Hydrogen Turbine Applications*. United States. doi: 10.2172/1253139. Repéré à https://www.osti.gov/biblio/1253139

https://www.osti.gov/servlets/purl/1253139

Zhao, H., Yu, F., Bennett, T. D., & Wadley, H. N. G. (2006). Morphology and thermal conductivity of yttria-stabilized zirconia coatings. *Acta materialia, 54*(19), 5195-5207. doi: https://doi.org/10.1016/j.actamat.2006.06.028. Repéré à https://www.sciencedirect.com/science/article/pii/S1359645406004782

Zhou, F., Wang, Y., Wang, L., Cui, Z., & Zhang, Z. (2017). High temperature oxidation and insulation behavior of plasma-sprayed nanostructured thermal barrier coatings. *Journal of Alloys and Compounds, 704*, 614-623.

Zhou, S., Xiong, Z., Dai, X., Liu, J., Zhang, T., & Wang, C. (2014). Microstructure and oxidation resistance of cryomilled NiCrAlY coating by laser induction hybrid rapid cladding. *Surface and Coatings Technology, 258*, 943-949.

Zhou, S., Xiong, Z., Lei, J., Dai, X., Zhang, T., & Wang, C. (2016). Influence of milling time on the microstructure evolution and oxidation behavior of NiCrAlY coatings by laser induction hybrid cladding. *Corrosion Science, 103*, 105-116.

Zou, Z., Jia, L., Yang, L., Shan, X., Luo, L., Guo, F., . . . Xiao, P. (2017). Role of internal oxidation on the failure of air plasma sprayed thermal barrier coatings with a double-layered bond coat. *Surface and Coatings Technology, 319*, 370-377.